ELSEVIER

Contents lists available at ScienceDirect

Radiation Physics and Chemistry

journal homepage: www.elsevier.com/locate/radphyschem





Determination of Photon Therapy Beam Spectra Using Transmission and Unfolding Techniques

Milomir Milaković ^a, Nikola Jovančević ^{a,*}, Dimitrije Maletić ^b, Miodrag Krmar ^a, David Knežević ^{b,c}, Strahinja Ilić ^d, Žarko Medić ^a, Jelena Bardak ^a, Bellona Bles ^a

- ^a Department of Physics, Faculty of Science, University of Novi Sad, Trg Dositeja Obradovica 3, Novi Sad, 21000, Serbia
- b Institute of Physics Belgrade, Pregrevica 118, Zemun, 100190, Serbia
- c Technische Universität München, Heinz Maier Leibnitz Zentrum (MLZ), Lichtenbergstr. 1, Garching, 85748, Germany
- d Faculty of Technical Sciences, University of Novi Sad, Trg Dositeja Obradovića 6, Novi Sad, 21000, Serbia

ARTICLE INFO

Keywords: Medical Linac Photon spectra Unfolding

ABSTRACT

For effective radiation therapy, it is crucial to understand the properties of the radiation being utilized. The challenge lies in the dose distribution within an irradiated inhomogeneous medium composed of various tissues, each with different attenuation characteristics. Consequently, it is essential to determine the mass energy absorption coefficient for each point within the irradiated volume and the incident beam spectrum of the therapeutic accelerator to accurately calculate the dose distribution in the treated body area. In this study, our objective was to determine the photon radiation spectrum of a medical linear accelerator using a measurement technique based on the transmission and unfolding method. The radiation spectrum of the Varian DHX therapeutic linear accelerator was analyzed using the attenuation (transmission) method. This study focused exclusively on the 6 MeV photon radiation spectrum. Radiation doses were measured after attenuation through materials such as water, aluminum, lead, iron, and copper. The photon radiation spectrum was determined using these measured data, the known attenuation coefficients for the materials, and the standard unfolding technique, which is well-established in neutron and photon activation measurements. The results of this study demonstrate that the applied technique can reliably provide information about the photon radiation spectrum characteristics of medical linear accelerators. The analysis reveals that the radiation doses calculated using the photon spectrum obtained via the unfolding method are more consistent with the measured values than those calculated using the standard Schiff spectrum.

1. Introduction

One of the most important techniques in radiation therapy is the use of megavoltage photon beams from linear accelerators. The prominent development of sophisticated computational techniques in therapy planning has opened up the need for knowledge of photon beam features. The energy spectrum of the photon beam is one of the most important accelerator characteristics. Since the intensities of therapeutic photon beams are very high, only a few results of direct spectroscopy can be found in the literature (Ali et al., 2012). One way to characterize a photon beam is through Monte Carlo simulations that take into account all interactions within the accelerator head (Sheikh-Bagheri and Rogers, 2002). Although simulation techniques may provide good estimations of beam energy spectra, it is necessary to provide experimental verification. Several indirect techniques have been developed for the reconstruction of the shape of the energy spectra of photon beams from

therapeutic machines with details explained in Refs. Ali and Rogers (2012), Ali et al. (2012), Catala et al. (1995) and Huang et al. (1983, 1982). Transmission analysis has proven to be very suitable for the indirect determination of the photon spectrum of the therapeutic beam in a clinical environment (Ali and Rogers, 2012).

Transmission analysis is a method wherein a collimated photon beam is passed through attenuators of different thicknesses, and the dose is measured at a selected point. The result of these measurements is an attenuation curve, i.e., the dose dependence on the thickness of the attenuator. To obtain a transmission curve, it is necessary to normalize the detected dose values (attenuation curve) with the dose measured when there were no attenuators in the beam. Based on the transmission data, it is possible to reconstruct the shape of the photon spectrum using various techniques. The most commonly used techniques include Laplace pairs, matrix inversion, or iterative unfolding. In some of these methods, it is desirable that the function

E-mail address: nikola.jovancevic@df.uns.ac.rs (N. Jovančević).

^{*} Corresponding author.

describing the energy dependence of the attenuation material decreases monotonically. The minimum of this function must be at an energy higher than the endpoint energy of the photon beam; therefore, in these experiments, mainly light materials were chosen, from graphite to copper, to collect transmission data. In some publications, the authors have described measurements where the desired photon beam attenuation characteristics were obtained by combining two materials, most commonly lead and some other light element (Catala et al., 1995; Huang et al., 1983, 1982).

This paper will focus on the transmission technique and the use of the unfolding procedure to reconstruct the energy spectrum of a photon beam, but in a slightly different way. The standard method uses unfolding to estimate the shape of the spectrum from a certain number of dose measurements with different thicknesses of one attenuator material (or a combination of two different ones). This paper investigates the possibility of reconstructing beam energy spectra utilizing a set of transmission data collected by an identical experimental procedure but using several different materials. Instead of several thicknesses of the same material, it is possible to perform measurements with several different materials and obtain a set of transmission data. The measured doses can be calculated as an integral of a function that also contains an unknown energy spectrum. Mathematically, this problem is reduced to Fredholm's equation of the first kind. This problem is often encountered in nuclear reactions with neutrons and photons (Jovancevic et al., 2014; Jovančević et al., 2016, 2017; Ilić et al., 2020; Medic et al., 2021; Jovančević et al., 2024; Medic et al., 2024), so several highly efficient unfolding codes have been developed in reactor physics. Some of them will be used to estimate the energy spectrum of photons in the beam of a therapeutic accelerator from a set of transmission data obtained with several different attenuators.

2. The method

Dose D_k of the well-collimated high energy x-ray beam in air after transmission in thickness x of chosen material can be expressed as:

$$D_{k} = \int_{0}^{E_{max}} \mu_{en}(E) \cdot E \cdot F(E) \cdot R(E)$$

$$\cdot exp(-\mu_{k}(E) \cdot x) \cdot dE$$
(1)

where μ_{en} is the mass-energy absorption coefficient of air, F(E) is the differential photon flounce at energy E (photon spectrum), R(E) is the energy response function of the ionization chamber, $\mu_k(E)$ is the linear attenuation coefficient of chosen attenuation material (which has same unit as μ_{en} , cm²/g) and E_{max} is the endpoint energy in the spectrum.

Expression (1) can be rewritten as:

$$D_k = \int_0^{E_{max}} E \cdot F_i \cdot \sigma_{ik} \cdot dE \tag{2}$$

It means that the dose for attenuation material, k, is proportional to the product of the $\sigma_{ik} = \mu_{en}(E) \cdot R(E) \cdot exp(-\mu_k(E) \cdot x)$ for a certain material (Eq. (1)), and the photon fluence rate defined as $E \cdot F_i$. To employ the unfolding method, it is essential to convert the integral equations into a set of discrete equations for a certain energy bin E_i .

$$D_k = \sum_{i}^{c} \boldsymbol{\Phi}_i \cdot \boldsymbol{\sigma}_{ik} \cdot \Delta E_i; \quad k = 1, 2, \dots, m$$
 (3)

where Φ_i is $\Phi_i = E_i \cdot F_i(E)$.

Measurements of multiple dose values D_k (m in Eq. (3)) using various materials (k) as attenuators, with an unknown photon fluence $\Phi_i(E)$, follow a procedure similar to that in neutron activation analysis. In the latter, the activities of several irradiated activation detectors are measured to determine the unknown quantities. Similarly, the unknown photon fluence $\Phi_i(E)$ can be resolved using standard unfolding procedures. The measured dose values can be normalized to one of the attenuators, as was done in this study. For the unfolding process, we utilized the MAXED, GRAVEL, and SAND-II algorithms (Matzke, 1994; McElroy et al., 1967; Reginatto and Goldhagen, 1999).

2.1. Unfolding algorithms

In this study, we utilized and compared three unfolding algorithms. The first was the SAND-II iterative algorithm (McElroy et al., 1967), followed by the GRAVEL algorithm, an enhanced version of SAND-II (Matzke, 1994). The third was the MAXED algorithm, which employs the maximum entropy principle to compute the unfolded function (Reginatto and Goldhagen, 1999).

Both the SAND-II and GRAVEL algorithms determine the $\Phi(E)$ function of photon spectra through iterative processes, beginning with an initial assumption about the spectrum. During the Jth iteration step of the photon fluence rate (Φ_i^J for the energy bin E_i), the subsequent iteration, Φ_i^{J+1} , is calculated as follows:

$$\boldsymbol{\Phi}_{i}^{J+1} = \boldsymbol{\Phi}_{i}^{J} \cdot f(D_{k}, \epsilon_{k}, \sigma_{ki}, \boldsymbol{\Phi}_{i}^{J}) \tag{4}$$

The function f is defined as:

$$f = exp\left(\frac{\sum_{ik} W_{ik}^{J} \log\left(\frac{D_{k}}{\sum_{i} \sigma_{ki} \Phi_{i}^{J}}\right)}{\sum_{k} W_{ik}^{J}}\right)$$
 (5)

The key difference between the SAND-II and GRAVEL algorithms lies in the definition of W_{ik}^J . In the SAND-II algorithm, W_{ik}^J is defined as follows:

$$W_{ik}^{J} = \frac{\sigma_{ki} \Phi_i^J}{\sum_i \sigma_{ki} \Phi_i^J},\tag{6}$$

while in GRAVEL it is defined as:

$$W_{ik}^{J} = \frac{\sigma_{ki} \Phi_i^J D_k^2}{\sum_i \sigma_{ki} \Phi_i^J \epsilon_k^2} \tag{7}$$

where W_{ik}^J is the weight factor, D_k is the measured dose, ε_k is the measurement uncertainty, and σ_{ki} is the response function (including the attenuation coefficient) of the kth attenuator in the energy bin E_i .

Unlike the SAND-II and GRAVEL algorithms, the MAXED algorithm calculates photon spectra by fitting the input data (measured dose D_k) to the function $\Phi(E)$ that maximizes the relative entropy, S:

$$S = -\int \left(\Phi(E) \ln \left(\frac{\Phi(E)}{\Phi_{def}(E)} \right) + \Phi_{def}(E) - \Phi(E) \right) dE$$
(8)

where $\Phi_{def}(E)$ is the default spectrum function.

3. Measurements

3.1. Materials

The attenuator plates were made of lead, copper, iron, aluminum, and a small water phantom. The thickness of each plate was selected to ensure that the incident beam from the linear accelerator, with an endpoint energy of 6 MeV, is attenuated to approximately 50% upon passing through the plate. Due to the varying electron densities of these materials, each plate has a different required thickness. The required thicknesses are as follows: 1 cm for lead, 1.55 cm for copper, 1.9 cm for iron, 6.1 cm for aluminum, and 13 cm for water. The attenuation coefficients for these materials (XCOM, 2024) are presented in Fig. 1.

3.2. Dose measurement

Measurements were performed using a multi-energy therapeutic linear accelerator, Clinac DHX (Varian Medical Systems) (varian, 2024), with an endpoint energy of 6 MeV. This linear accelerator is calibrated according to the TRS 398 (IAEA) protocol (Seriesa, 2004) and is licensed by the State Regulatory Agency for Radiation Safety of Bosnia

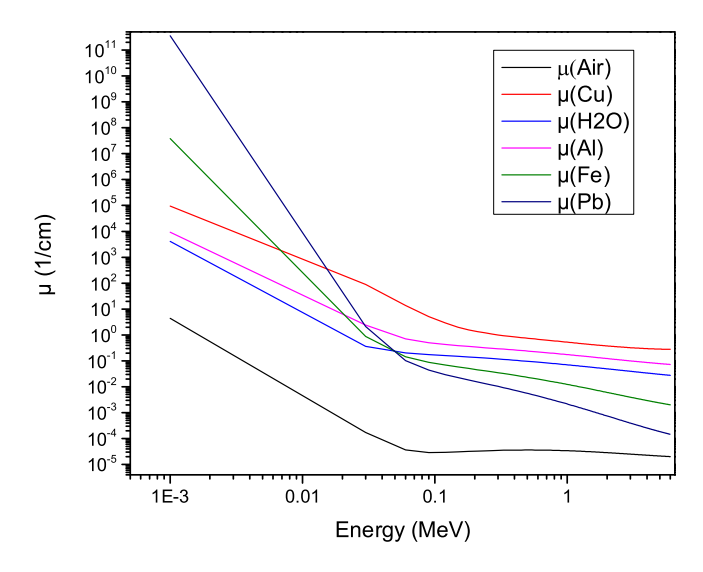


Fig. 1. Attenuation coefficients of selected materials (XCOM, 2024).

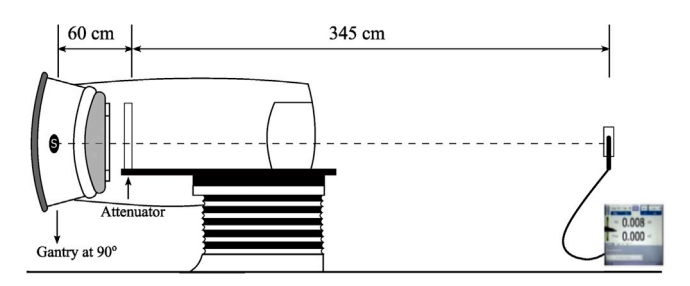


Fig. 2. Experimental setup.

and Herzegovina (State, 2024). Additionally, the dose delivery of this accelerator is verified by the IAEA Dosimetry Laboratory.

To achieve more reliable results, the delivered dose is 300 MU (3 Gy) for all attenuators, the distance from the source to the attenuated plates (SSD) is 60 cm, and from the attenuator to the ionization chamber is 345 cm (Fig. 2).

To obtain the most accurate measurement results, it is essential to minimize the contribution of scattered radiation to the total measured dose, as scattered photons reaching the ionization chamber can affect the readings. The measurements were conducted by placing the attenuators as close as possible to the accelerator's focus while positioning the ionization chamber at the maximum distance allowed by the room's size. Additionally, the collimator opening was adjusted so that the field width at the dosimeter location matched the dimensions of the build-up cap, creating a narrow geometry. This setup ensured that only a minimal volume of the attenuator was exposed to the primary beam, thereby reducing the impact of scattered radiation on the total measured dose. The large distance between the attenuator and the dosimeter further minimized this impact, as only a small fraction of scattered radiation, primarily that scattered at very small angles, could reach the dosimeter location.

Measurements were performed using an IBA Farmer-type ionization chamber equipped with a build-up cap and a SuperMAX 1000 electrometer (Standard Imaging) (https://www.standardimaging.com/products/exradin-a19-ion-chamber-waterproof-classic-farmer-0-62cc). The results for each attenuator are presented in Table 1. The measured dose values, expressed in nanocoulombs (nC), represent the ionization chamber's readout current.

Table 1 Characteristics of the used materials: ρ [g/cm³ - density; A/M - Relative atomic/molecular mass; Z -Atomic number; d [mm]- thickness of attenuator; D[nC] - measured dose.

Attenuator	ρ [g/cm ³]	A/M	Z	d [mm]	D[nC]
Air	$1.225 \cdot 10^{-3}$	28.96	7.5	4050.00(5)	2.947(3)
H_2O	1	18.0148	3.4	13.00(5)	1.5916(4)
Al	2.699	25.982	13	6.10(5)	1.472(4)
Fe	7.874	55.845	16	1.90(5)	1.1694(11)
Cu	8.96	93.546	29	1.55(5)	1.6352(7)
Pb	11.35	207.21	82	1.00(5)	1.6878(7)

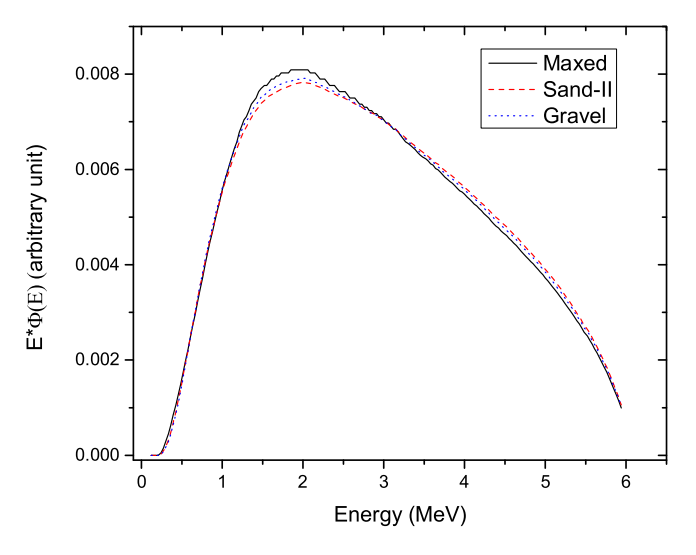


Fig. 3. Unfolding results from MAXED, Gravel and SAND-II algorithms. (The spectrum integral is normalized to unity.)

Table 2The S values for: 1. Default functions before unfolding procedures, 2. SAND-II results, 3. GRAVEL results and 4. MAXED results.

S			
Default function	Sand-II	Gravel	Maxed
0.00034	0.00023	0.00023	0.00023

4. Experimental results

4.1. Unfolding results

All unfolding methods used in this study require an initial or default spectrum to start the unfolding procedures. This spectrum should encompass all available known data about the shape of the spectrum. Various methods can be employed to construct this default spectrum. In this paper, the theoretical Schiff function was chosen as the default spectrum (Schiff, 1951) for the 6 MeV electrons producing bremsstrahlung radiation. This choice is considered a very good initial guess, and the final results should not deviate significantly from the initial spectrum.

Unfolding procedures were conducted over the energy range from 0 MeV to 6 MeV, grouped into discrete energy bins (200 bins). The results obtained by the SAND-II, GRAVEL, and MAXED algorithms using all selected default functions are presented in Fig. 3.

The validation of the unfolding results was performed by calculating the dose $(D_k^c = \sum \sigma(E_i) \cdot \Phi(E_i) \cdot \Delta E)$ and subsequently comparing it with the n measured data $(D_k^m$, Table 1). These calculations were carried out for the default function and for the three solutions obtained from the SAND-II, GRAVEL, and MAXED algorithms. The resulting σ values are presented in Table 2:

$$S = \frac{1}{n-1} \sum_{k=1}^{n} \left(\frac{D_k^c - D_k^m}{D_k^m} \right)^2 \tag{9}$$

These results suggest that the unfolding procedures improve the precision of reproducing the measured dose D_b .

As the final outcome, we present the averaged photon spectra obtained from all three unfolding algorithms. These results are depicted in Fig. 4, where the solid line represents the averaged photon spectra. The dashed lines indicate the maximum and minimum values of the photon spectra, representing the uncertainty corridor calculated directly from the spectrum unfolding.

4.2. Geant4 bremsstrahlung spectrum simulation

The simulation of gamma spectra of the central part of the beam coming from medical linac is done using Geant4 11.2.1 version (Agostinelli et al., 2003). Existing medical linac example (Caccia et al., 2020) simulation included in Geant4 advanced examples is using several main parts in simulation geometry, such as source of electrons, target, primary collimator, vacuum window and a flattening filter. The setup file included accelerator name, which was selected among implemented ones, which was "acc2", and that macro name containing specific data for accelerator chosen was modified one, based on "acc2_6MeV_3x3.mac". Geant4 Primary particles generator was a particle gun, and primary particles were electrons with mean energy of 6 MeV and with 0.127 MeV standard deviation in energy and 0.5 mm radius of the electron beam. The sampling of particles to create a resulting gamma spectrum is done in plane perpendicular to medical linac, i.e to the source, with center at 0,0,0 coordinates in x,y and z, with an arbitrary radius on same plane around the center of the incoming beam (Fig. 4).

5. Discussion

Fig. 5 compares the results obtained in this study using transparent measurement techniques and the unfolding process with Geant4 simulations. Additionally, it includes the theoretical Schiff spectrum corrected for attenuation in the accelerator head materials. The results demonstrate a good agreement between the measured, simulated, and theoretical values, although some deviations are noticeable.

At low energies, the measured values are smaller than both the theoretical and simulated ones. This discrepancy could be attributed to the limitations of the measurement technique or the accuracy of the unfolding process at lower energy ranges, for example, it can come from the contribution of scattered radiation to the low-energy part of the spectrum. The source of discrepancy could also be the accuracy of the unfolding process at lower energy ranges. Conversely, at higher energies, the measured values show a closer alignment with the simulated values than with the theoretical data, suggesting that the simulation model may be more reliable in predicting the photon spectrum at these energies.

Interestingly, the measured values indicate the peak of the spectrum at slightly higher energies than both the simulated and theoretical calculations. This could point to potential systematic shifts in the measurement process or inherent differences in how the experimental procedure determine the photon spectrum compared to the theoretical models and simulations.

These findings underscore the importance of continuous refinement in both experimental techniques and simulation models to enhance the accuracy of photon spectrum characterization in linear medical accelerators.

6. Conclusion

The comparisons of measured, simulated, and theoretical data suggest that the experimental technique used in this study can effectively characterize the photon radiation spectrum of linear medical accelerators. The measurement process is straightforward and time-efficient,

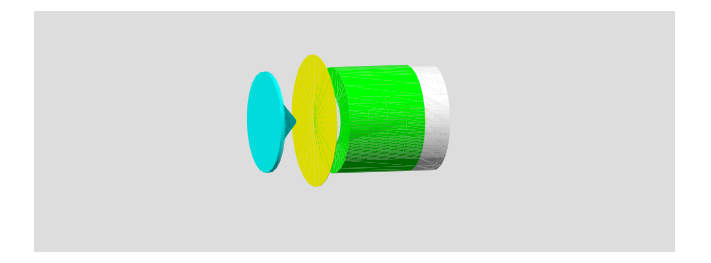


Fig. 4. Geant4 simulated geometry of medical linear accelerator head.

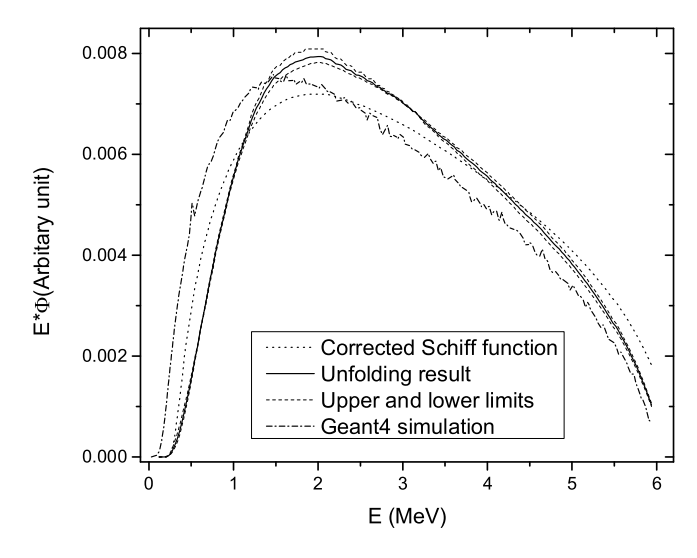


Fig. 5. Energy spectrum $E \cdot \Phi$ (arbitrary units) as a function of energy E (MeV). The dashed line represents the corrected Schiff function, the solid line shows the unfolding result, the dotted lines indicate the upper and lower limits, and the dash-dotted line corresponds to the Geant4 simulation. (The spectrum integral is normalized to unity.)

while the unfolding process can be automated, making this technique a promising option for routine beam quality control in clinical practice.

To fully realize its potential, standardization of the measurement and calculation processes is essential. This includes the optimal selection of attenuator materials, device miniaturization, and the refinement of unfolding algorithms. The application of machine learning techniques could play a important role in optimizing these factors.

The further development of this technique, as demonstrated for the first time in this work, will be the focus of future studies. These efforts aim to establish a reliable and efficient method for photon spectrum analysis, which is critical for ensuring the accurate and consistent operation of linear medical accelerators in clinical settings.

CRediT authorship contribution statement

Milomir Milaković: Writing – review & editing, Writing – original draft, Validation, Resources, Methodology, Investigation, Formal analysis, Data curation, Conceptualization. Nikola Jovančević: Writing – review & editing, Writing – original draft, Methodology, Investigation, Formal analysis, Conceptualization. Dimitrije Maletić: Writing – review & editing, Writing – original draft, Software, Investigation, Data curation. Miodrag Krmar: Writing – review & editing, Writing – original draft, Supervision, Resources, Methodology, Investigation, Formal analysis, Conceptualization. David Knežević: Writing – review & editing, Writing – original draft, Validation, Software, Formal analysis, Data curation. Strahinja Ilić: Writing – review & editing, Software, Data curation. Zarko Medić: Writing – review & editing, Formal analysis. Bellona Bles: Writing – review & editing, Formal analysis.

Declaration of competing interest

The authors declare that they have no known competing financial interests or personal relationships that could have appeared to influence the work reported in this paper.

Acknowledgment

The authors, NJ, MK, ZM, JB and BB, gratefully acknowledge the financial support of the Ministry of Science, Technological Development and Innovation of the Republic of Serbia (Grants No. 451-03-13/2025-03/200125 and 451-03-136/2025-03/200125). Two of the authors, N. Jovančević and M. Krmar, acknowledge financial support of the Provincial Secretariat for Higher Education and Scientific Research of Autonomous Province of Vojvodina (Grant No. 142-451-3139/2022-01/2).

Data availability

Data will be made available on request.

References

- Agostinelli, S., Allison, J., Amako, K., Apostolakis, J., Arau-jo, H., Arce, P., Asai, M., Axen, D., Banerjee, S., Barrand, G., 2003. GEANT4 a simulation toolkit. Nucl. Instrum. Methods Phys. Res. 506, 250–303.
- Ali, E.S.M., McEwen, M.R., Rogersc, D.W.O., 2012. Unfolding linac photon spectra and incident electron energies from experimental transmission data, with direct independent validation. Med. Phys. 39.
- Ali, E.S.M., Rogers, D.W.O., 2012. An improved physics-based approach for unfolding megavoltage bremsstrahlung spectra using transmission analysis. Med. Phys. 39.
- Caccia, B., Blideanu, V., Roy, M.L., Rabus, H., Tanner, R., 2020. A Model Validation Scheme for Monte Carlo Simulations of a Medical Linear Accelerator: Geometrical Description and Dosimetric Data Used in the "Linac Action", Vol. 2020. EURADOS Report, p. 05.
- Catala, A., Francois, P., Bonnet, J., Scouarnes, C., 1995. Reconstruction of 12 MV bremsstrahlung spectra from measured transmission data by resolution of the numeric AF=T. Med. Phys. 22.
- Huang, P.-H., Kase, K.R., Bjarngard, B.E., 1982. Simulation studies of 4-MV x-ray spectral reconstruction by numerical analysis of transmission data. Med. Phys. 9.
- Huang, P.-H., Kase, K.R., Bjarngard, B.E., 1983. Reconstruction of 4-MV bremsstrahlung spectra from measured transmission data. Med. Phys. 10.

- Ilić, S., Jovančević, N., Daraban, L., Stroh, H., Oberstedt, S., Hult, M., Bonaldi, C., Geerts, W., Hambsch, F.-J., Lutter, G., Marissens, G., Vidali, M., Knežević, D., 2020. The cross-sections for the ¹⁸⁷Re(n,p)¹⁸⁷W and ¹⁸⁵Re(n,3n)¹⁸³Re reactions in the energy range between 13.08 MeV and 19.50 MeV. Eur. Phys. J. A 56, 202.
- Jovancevic, N., Daraban, L., Oberstedt, S., 2014. Determination of the default curve for the unfolding procedure in the measurement of threshold neutron excitation functions. Nucl. Instrum. Methods Phys. Res. Sect. A: Accel. Spectrometers Detect. Assoc. Equip. 739, 68–74.
- Jovančević, N., Daraban, L., Stroh, H., Oberstedt, S., Hult, M., Bonaldi, C., Geerts, W., Hambsch, F.-J., Lutter, G., Marissens, G., et al., 2016. The neutron cross-section functions for the reactions ¹⁸⁷Re(n, α)¹⁸⁴Ta, ¹⁸⁷Re(n, 2n)¹⁸⁶Re and ¹⁸⁵Re(n, 2n)¹⁸⁴Re in the energy range 13.08-19.5 MeV. Eur. Phys. J. A 52 (5), 148.
- Jovančević, N., Daraban, L., Stroh, H., Oberstedt, S., Hult, M., Bonaldi, C., Geerts, W., Hambsch, F.-J., Lutter, G., Marissens, G., et al., 2017. The cross section functions for neutron induced reactions with Rhenium in the energy range 13.0–19.5 MeV. In: EPJ Web of Conferences. Vol. 146, EDP Sciences, p. 11025.
- Jovančević, N., Knežević, D., Krmar, M., Maletić, D., Zhemchugov, A., Milaković, M., 2024. Determination of the bremsstrahlung spectra by unfolding technique based on ²⁰⁹Bi(γ, xn) reactions. Radiat. Phys. Chem. 215, 111330. http://dx.doi.org/10. 1016/j.radphyschem.2023.111330.
- Matzke, M., 1994. Unfolding of Pulse Height Spectra: The Hepro Program System, Vol. L-IV. Report PTB-N-19. Physikalisch-Technische Bundesanstalt.
- McElroy, W.N., Berg, S., Crockett, T., 1967. A Computer-Automated Itera-tive Method for Neutron Flux-Spectra Determined byFoil Activation, Vol. I-IV. AFWL-TR-67-41, Los Alamos National Laboratory report.
- Medic, Z., Jovancevic, N., Maletic, D., Teterev, Y., Mitrofanov, S., Belov, A., Krmar, M., Hult, M., Oberstedt, S., 2021. The application of the unfolding technique for determination of photo-nuclear reaction cross-section with an example on the ¹¹⁵In(y, y') ^{115m}In reaction. Eur. Phys. J. A 57 (8), 258. http://dx.doi.org/10.1140/epia/s10050-021-00567-9.
- Medic, Z., Krmar, M., Jovancevic, N., Maletic, D., Teterev, Y., Mitrofanov, S., 2024.
 Photoactivation of the 391.69 keV isomer state of ^{113m}In by the (γ, 2n) reaction.
 Phys. Rev. C 109, 034607. http://dx.doi.org/10.1103/PhysRevC.109.034607.
- Reginatto, M., Goldhagen, P., 1999. Maxed, a computer code for maximum entropy deconvolution of multisphere neutron spectrometer data. Health Phys. 77 (5), 579–583.
- Schiff, L., 1951. Energy-angle distribution of thin target bremsstrahlung. Phys. Rev. 83 (2), 252.
- Seriesa, T.R., 2004. Absorbed Dose Determination in External Beam Radiotherapy, vol. 398. IAEA Vienna.
- Sheikh-Bagheri, D., Rogers, D.W.O., 2002. Monte Carlo calculation of nine megavoltage photon beam spectra using the BEAM code. Med. Phys. 29.
- State regulatory agency for radiation safety of bosnia and herzegovina. http://www.darns.gov.ba/ru/LegislationAndDocuments/Pravilnici.
- varian. https://www.varian.com.
- XCOM: Photon cross sections database. https://physics.nist.gov/PhysRefData/Xcom/html/xcom1.html.

Photoactivation of the 391.69 keV isomer state of 113m In by the $(\gamma, 2n)$ reaction

Z. Medic , ¹ M. Krmar, ² N. Jovancevic , ² D. Maletic , ¹ Y. Teterev , ³ and S. Mitrofanov . ¹Institute of Physics, Belgrade 11000, Republic of Serbia

(Received 28 September 2023; accepted 26 January 2024; published 12 March 2024)

Natural indium targets were exposed to high-energy bremsstrahlung radiation, from 9 MeV to 23 MeV. Using the measured γ spectra, the yield ratio of ^{113m}In and ^{115m}In was determined. It was checked to what extent the measured values of the yield ratio can be reproduced using the existing experimental data of cross sections of relevant photonuclear reactions, as well as cross sections obtained by TALYS calculations. The measured reaction yield ratio was used to reconstruct the energy differential cross section of 115 In(γ , 2n) 113m In using the unfolding procedure.

DOI: 10.1103/PhysRevC.109.034607

I. INTRODUCTION

Photonuclear reactions are appealing phenomena that occur when external radiation interacts with the nucleus through electromagnetic forces, without involving the nuclear force. The theoretical understanding of this phenomenon, particularly the giant dipole resonance (GDR), has been relatively successful [1]. As experimental techniques advanced, systematic data collection was initiated, primarily focusing on (γ, n) nuclear reactions. In these reactions, the nucleus releases excitation energy by emitting one neutron after interacting with electromagnetic radiation. A comprehensive systematic data set [2,3] exists in the form of energy differential cross sections for these reactions. However, there is a scarcity of experimental data for $(\gamma, 2n)$ reactions, and for (γ, xn) reactions involving more than two emitted neutrons. Energy differential cross sections are only available through theoretical estimation. Numerical codes, such as TALYS 1.9 [4], have been developed to estimate cross sections for various nuclear reactions based on theoretical assumptions.

Indium photoactivation, involving (γ, n) as well as (γ, γ') reactions, has been a subject of extensive research. Despite this, uncertainties persist regarding the photoexcitation of the ^{115m}In isomeric state, leading to variations in measured cross sections among different authors. To date, only one set of experimental measurements for the energy differential cross section of the $^{115}\text{In}(\gamma,2n)^{113m}\text{In}$ reaction has been published, dating back over 60 years [5]. Cross-section estimates for this reaction obtained using the TALYS 1.9 code differ slightly depending on the choice of functions describing the level density and radiation strength function.

This paper aims to compare the relative yields of the 115 In $(\gamma, 2n)$ 113m In reaction measured at several energies with calculated ones. Available cross-sectional data, both experimental and estimated using TALYS 1.9 were used. Furthermore, we will attempt to reconstruct the energy differential cross section for this reaction based on unfolding technique.

II. METHOD

Natural indium consists of two isotopes, ¹¹⁵In (95.7%) and ¹¹³In (4.3%). In high-energy photon beams with energies below 16.3 MeV, the only method to excite 113 In to its long-lived excited state at 391.69 keV is through the $^{113}\text{In}(\gamma, \gamma')$ ^{113m}In reaction. However, when the photon energy exceeds 16.3 MeV, the $^{115}\text{In}(\gamma, 2n)$ ^{113m}In nuclear reaction becomes dominant. Consequently, the formation of ^{113m}In can occur via two distinct reactions, and the total activity produced during irradiation is a result of the combined contribution of both of them. The probabilities of these mentioned reactions are determined by cross sections, denoted as $\sigma_{\gamma,2n}^{115}$ for $^{115}{\rm In}(\gamma,2n)^{113m}{\rm In}$ and $\sigma_{\gamma,\gamma'}^{113}$ for $In(\gamma,\gamma')^{113m}{\rm In}$, where the atomic number of the parent nuclei is indicated as a superscript. The yield of ^{113m}In can be expressed as follows:

$$Y(^{113m}\text{In}) = \frac{m_t}{M} N_A \left[0.957 \int_{E_t^{\gamma,2n}}^{E_{\text{max}}} \sigma_{\gamma,2n}^{115}(E) \Phi(E) dE + 0.043 \int_{E_t^{\gamma,\gamma}}^{E_{\text{max}}} \sigma_{\gamma,\gamma}^{113}(E) \Phi(E) dE \right], \tag{1}$$

where the mass of the exposed target is denoted by m_t , Mis the mass number and N_{av} is Avogadro's number. $E_t^{\gamma,2n}$ and $E_t^{\gamma,\gamma}$ are energy thresholds for the $^{115}\mathrm{In}(\gamma,2n)$ $^{113m}\mathrm{In}$ and $^{113}\mathrm{In}(\gamma,\gamma')$ $^{113m}\mathrm{In}$ reactions, respectively. The maximum energy of photons is denoted by E_{max} , and the flux of incident photons is $\Phi(E)$. The integrals in Eq. (1) are commonly referred to as saturation activity.

After irradiation, the γ spectra of the indium target should be recorded. The yield of 113m In can then be calculated by analyzing the intensity of the 391.69 keV γ line:

$$Y(^{113m}\text{In}) = \frac{N_{\gamma}(391)\lambda_{113}}{\epsilon(391)p_{\gamma}^{391}e^{-\lambda_{113}\Delta t}(1 - e^{-\lambda_{113}t_{\text{inr}}})(1 - e^{-\lambda_{113}t_{\text{m}}})}, \quad (2)$$

²Physics Department, Faculty of Sciences, University of Novi Sad, Novi Sad 21000, Republic of Serbia ³Flerov Laboratory of Nuclear Reactions, Joint Institute for Nuclear Research, Dubna 141980, Russia

where N_{γ} is detected number of 391.69 keV γ photons, λ_{113} is decay constant of 113m In, ϵ is the detector's efficiency at the observed energy. The quantum yield of the 391.69 keV transition is denoted by p_{γ}^{391} , and $t_{\rm irr}$, and $t_{\rm m}$ indicate how long the irradiation and measurement of the activated sample lasted, while Δt , so-called cooling time indicates how much time passed from the end of the irradiation to the beginning of the measurement. The above equation can be found in publications of other authors in a slightly different form [6].

The processing of the data obtained in the experiment can be significantly simplified by observing the relative yield of ^{113m}In. The optimal procedure involves normalizing the yield of ^{113m}In with the yield of some other isotope obtained from the same target and measured at the same time. The most suitable candidate for normalization is ^{115m}In, which forms through the photoactivation of the isomer state at 336.24 keV. The yield ratio of ^{113m}In and ^{115m}In can be expressed as follows:

$$\frac{Y(^{113m}\text{In})}{Y(^{115m}\text{In})} = \frac{\int_{E_{th}}^{E_{max}} \sigma_{\gamma,2n}^{115}(E)\Phi(E)dE}{\int_{E_{th}}^{E_{max}} \sigma_{\gamma,\gamma}^{115}(E)\Phi(E)dE} + \frac{0.043 \int_{E_{th}}^{E_{max}} \sigma_{\gamma,\gamma}^{113}(E)\Phi(E)dE}{0.957 \int_{E_{th}}^{E_{max}} \sigma_{\gamma,\gamma}^{115}(E)\Phi(E)dE}.$$
(3)

The cross section for the $^{115}\text{In}(\gamma,\gamma')^{115m}\text{In}$ reaction is denoted as $\sigma_{\gamma,\gamma'}^{115}$. Experimental data for this cross section, which are not always consistent, can be found in databases [7], along with the cross section for the $^{113}\text{In}(\gamma,\gamma')^{113m}\text{In}$ reaction.

The advantage of this approach is that no absolute photon flux is necessary. For the numerical procedure, only the shape of the photon spectra is required. It can be derived by simulation for a known geometry of bremsstrahlung production.

The experimentally obtained yield ratio of ^{113m}In to ^{115m}In can be expressed as follows:

$$\frac{Y(^{113m}\text{In})}{Y(^{115m}\text{In})} = \frac{N_{\gamma}(391)}{N_{\gamma}(336)} \frac{\lambda^{113}}{\lambda_{115}} \frac{\epsilon(336)}{\epsilon(391)} \frac{p_{\gamma}^{336}}{p_{\gamma}^{391}}.$$

$$\times \frac{e^{-\lambda_{115}\Delta t} (1 - e^{-\lambda_{115}t_{\text{irr}}}) (1 - e^{-\lambda_{115}t_{\text{m}}})}{e^{-\lambda_{113}\Delta t} (1 - e^{-\lambda_{113}t_{\text{irr}}}) (1 - e^{-\lambda_{113}t_{\text{m}}})}. \quad (4)$$

All quantities in Eq. (4) with the "336" index or "115" subscript have the same meaning as explained in Eq. (2), describing the decay of ^{115m}In. Importantly, this approach does not require the absolute value of the detector efficiency; instead, relative efficiency can be used.

Using the measured intensities of the corresponding γ lines in collected γ spectra, the experimental values of the $Y(^{113m}\text{In})/Y(^{115m}\text{In})$ yield ratio can be determined [Eq. (4)]. With the estimated shape of the photon bremsstrahlung spectra $\Phi(E)$, the same $Y(^{113m}\text{In})/Y(^{115m}\text{In})$ yield ratio can be obtained from Eq. (3), using theoretical or available experimental cross sections for observed photonuclear reactions. There are two ways in which Eq. (3) and Eq. (4) can be applied in the context of studying the photoactivation of ^{113}In :

(1) For several selected energies of the photon beam (denoted as $E_{\rm max}$), which are higher than the

threshold for the $(\gamma, 2n)$ reaction, the yield ratios of $Y(^{113m}{\rm In})/Y(^{115m}{\rm In})$ can be determined using the obtained γ spectra. Numerical codes like TALYS 1.9 can provide estimates of the cross sections for all three reactions in Eq. (3). Using the known experiment geometry, the shape of the photon flux $\Phi(E)$ can be obtained by simulation, as well as the integrals (saturation activities) appearing in Eq. (3). Based on calculated $Y(^{113m}{\rm In})/Y(^{115m}{\rm In})$ yield ratios, conclusions can be drawn regarding the model assumptions' capacity (level density and radiation strength function) to reproduce the experimental yields.

- (2) Cross sections corresponding to the three saturation activities in Eq. (3) can be found in databases. It can be used to estimate the yield ratio and compare it with the obtained measurement results, providing an additional assessment of the relevance of the existing experimental values of the observed reactions' cross sections. It should be noted that for ¹¹⁵In(γ, γ') and ¹¹³In(γ, γ'), measurements of cross sections were not conducted in the entire energy region covered by this experiment.
- (3) If the yield ratio of $Y(^{113m}\text{In})/Y(^{115m}\text{In})$ is determined for several different energies above the 16.3 MeV threshold, the cross section for the $^{115}\text{In}(\gamma, 2n)^{113m}\text{In}$ reaction can be determined using a suitable unfolding algorithm. It is noteworthy that only one available result of the $^{115}\text{In}(\gamma, 2n)^{113m}\text{In}$ cross-section measurement dates back more than 60 years ago [5].

III. MEASUREMENTS

A. Irradiation

The irradiation was carried out using MT25 Microtron [8] located in Flerow Laboratory of Nuclear reactions, JINR, Dubna. Technical details concerning used device and irradiation procedure are described in couple of previous publications [9].

Indium disks were exposed to bremsstrahlung with endpoint energies from 9 MeV to 23 MeV in steps of 1 MeV. For the photon production a 1 mm thick tungsten radiator was used. The distance between the tungsten radiator and an indium disk was 136 cm. The scheme of the experimental setup is presented in Fig. 1.

When high-energy photons interact with a tungsten target, fast neutrons are inevitably produced. The influence of and 113m In production by inelastic neutron scattering, 115 In(n,n') 115m In and 113 In(n,n') 113m In, especially at high photon energies was minimized by placing the indium disks at the center of a water container with a diameter of 18 cm. In this manner, fast neutrons resulting from photonuclear reactions in tungsten were thermalized. The number of neutrons created is highly dependent on the maximum bremsstrahlung energy. It was observed that the saturation activity of 116m In, produced by neutron capture, was about 130 times higher at a photon energy of 23 MeV than at the endpoint energy of 10 MeV when indium targets were placed in water. In order to check the degree of thermalization of neutrons, two

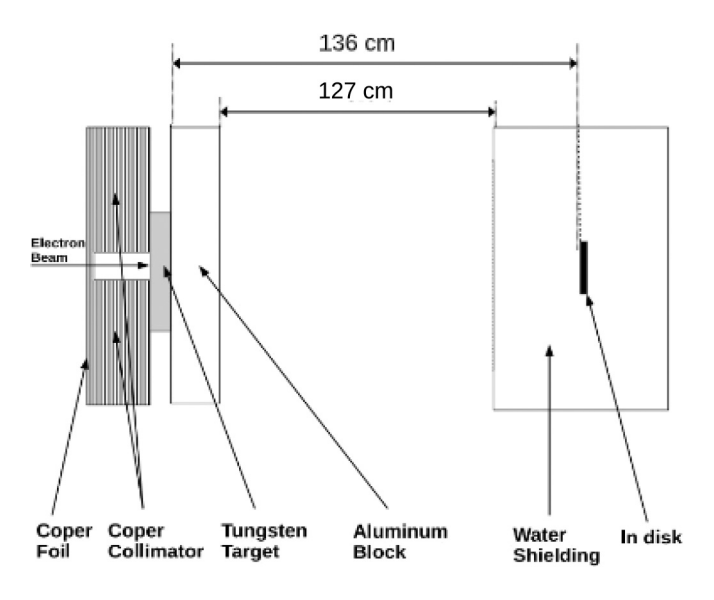


FIG. 1. Geometry of experimental setup (not in scale).

measurements were performed at energies of 21 MeV and 23 MeV where the indium samples were exposed in a photon beam with and without a water moderator. At both energies, the saturation activity of \$^{116m}\$In was ten times higher when the indium disk was in water. Significantly lower difference in \$^{115m}\$In saturation activities between exposures with and without water surrounding the indium samples was observed. A 14.5% higher saturation activity of \$^{115m}\$In was observed when the disk was exposed outside the water container at a maximum photon energy of 23 MeV compared to the saturation activity when the disk was positioned inside the water container. At an energy of 21 MeV, that difference was 16.8%.

In order to verify the possible influence of (n,n') reactions on the excitation of the observed isomeric states, a GEANT simulation was performed for the geometry shown in Fig. 1 and 50×10^6 incident electrons with an energy of 23 MeV. The total number of photons and neutrons in the energy region of interest, above the energy of metastable state of 115m In, at the site of the indium cylinder was monitored. It was found that the ratio of the number of photons to the number of neutrons is 1.03×10^5 . The same calculation was repeated for 18 MeV and it was obtained that the ratio of photons to neutrons is even higher and is equal to 3.54×10^5 . Although the cross section for the (n, n') reaction is almost three orders of magnitude higher than the cross section for (γ, γ') reactions, the large difference in the number of protons and neutrons gives a good basis for assuming that the inelastic scattering of neutrons does not lead to a significant excitation of the observed isomer. It was also estimated that the saturation activity 115m In should be about 15% lower in the case when the activation is performed by a 23 MeV bremsstrahlung beam that is attenuated in a 9 cm thick layer of water.

Another possible way of exciting the isomeric state of 115 In by (γ, γ') reaction was verified. There is a possibility that the photoneutrons created in the water and the indium sample

TABLE I. Irradiation characteristics for each indium disk: m: mass of disk; E_{max} : bremsstrahlung endpoint energy; Q: integral number of electrons striking tungsten target; t_{irr} : time of irradiation.

Disk No.	m[g]	E _{max} [MeV]	Q [mAs]	t _{irr} [s]
1	0.7711	9.00(5)	7000	1800.0(5)
2	0.6317	10.00(5)	6000	1800.0(5)
3	0.6813	11.00(5)	6000	1800.0(5)
4	0.6545	12.00(5)	6000	1800.0(5)
5	0.6533	13.00(5)	2700	1800.0(5)
6	0.6317	14.00(5)	2767	1800.0(5)
7	0.6685	15.00(5)	4000	1800.0(5)
8	0.6685	16.00(5)	4000	1800.0(5)
9	0.6813	17.00(5)	2700	1680.0(5)
10	0.6531	18.00(5)	2700	960.0(5)
11	0.6758	19.00(5)	2700	2100.0(5)
12	0.7233	20.00(5)	2700	1600.0(5)
13	0.7194	21.00(5)	3200	1600.0(5)
14	0.6778	22.00(5)	4000	1600.0(5)
15	0.7202	23.00(5)	3500	1600.0(5)

itself, experience inelastic scattering and bring ¹¹⁵In to an isomeric state. By tracking the events in the described simulation, where the sample was exposed to a photon beam at a distance of 136 cm, not a single such case was observed. For this reason, the simulation was repeated, with some differences in geometry: the sample was placed 20.6 cm from the tungsten converter, the diameter of the indium coin has been increased from 2 to 10 cm. In this way, the number of photons falling on the indium sample is increased by three orders of magnitude. A simulation was performed with 475×0^6 incident electrons having 23 MeV energy. It was found that out of the 41 115m In isomers, 39 of them are formed in (γ, γ') reaction and two through (n, n') reaction. For a result that would be statistically more reliable, it is necessary to perform a simulation with a larger number of incident electrons, but this result is also a good enough indication that the inelastic scattering of neutrons created in water and indium itself does not contribute more than 5% to the total activation of ¹¹⁵In isomer state. The irradiation times and intensities of bremsstrahlung beams (the integral numbers of accelerated electrons striking tungsten target Q) are presented in Table I.

B. γ spectroscopy measurements

After the exposition, the indium coins were measured using an HPGe detector with a relative efficiency of 25% and shielded by 5 cm of lead. The irradiated indium samples were placed directly on the vertical dipstick of the detector. The time between the end of irradiation and the start of measurement varied from 34 min to 221 min, depending on the activity of the exposed indium coins and the availability of the detector.

The cooling time for the samples irradiated at high energies was longer because the activity of 116m In, resulting from an increasing number of neutrons in the vicinity of the Microtron, significantly exceeded the activity of 115m In and 113m In. Considering that the half-life of 116m In ($T_{1/2} = 54.41$ min) is

shorter than the half-lives of 115m In ($T_{1/2}=4.468$ h) and 113m In ($T_{1/2}=1.658$ h), measurements were taken after the activity of 116m In had decreased to ensure low levels of dead time (up to 2%). Each indium sample was measured for a duration of 30 min, according to detector availability.

In all recorded spectra, a prominent 336.24 keV γ line, produced by the deexcitation of the isomer state of 115m In, was observed. However, the γ line of 113m In (391.69 keV) was very weak at low endpoint energies of the photon beam, and in some spectra, it exhibited a statistical uncertainty of up to 45%. Above 17 MeV energies, there was a rapid increase in the intensity of the 391.69 keV γ line as the 115 In(γ , 2n) 113m In reaction began to take place.

Furthermore, several strong γ lines emitted after the decay of 116m In, produced by neutron capture of 115 In, were visible in all recorded spectra. These γ lines were used to calculate the relative detection efficiency for the applied counting geometry. The relative efficiency was obtained using a combination of exponential and second-order polynomial functions. The GENIE 2000 software was employed to extract the intensities of the observed γ lines. Parts of detected of γ spectra are presented in Fig. 2.

C. Determination of relative yield

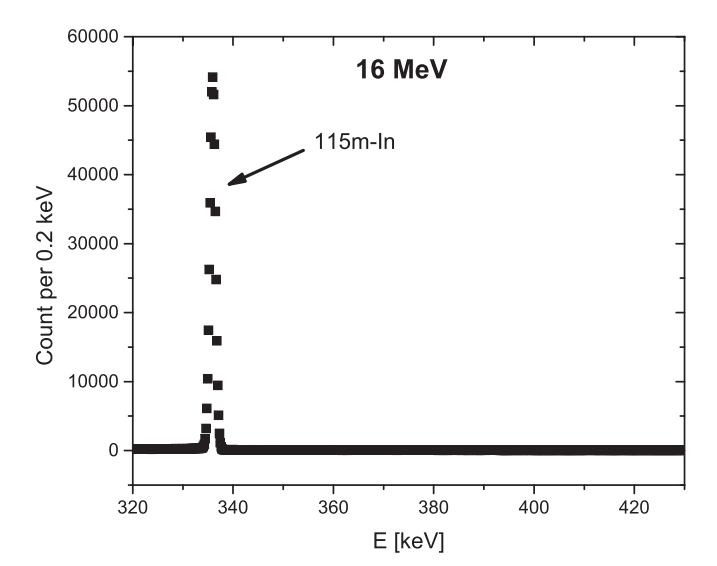
The intensities of the 336.24 keV and 391.69 keV γ lines were determined in all the recorded spectra. To obtain relative yields for all the used photon energies, Eq. (4) was applied. The results obtained from this analysis are presented in Fig. 3.

Based on the data depicted in Fig. 3, it is evident that the relative yield, as defined by Eq. (3), remains approximately constant over a wide range of energies, up to the threshold for the 115 In(γ , 2n) 113m In reaction. However, beyond this energy threshold, the yield ratio starts to increase rapidly.

In the lower-energy region, up to 17 MeV, the activity of 113m In is solely attributed to the photoactivation of the isomeric state [113 In(γ , γ') 113m In reaction], as described by the second term in Eq. (3). The mean value of the relative yield in the energy range from 9 MeV to 16 MeV was found to be 0.039(4).

To investigate whether this trend of the yield ratio between the photoactivation of ¹¹³In and ¹¹⁵In isomeric states persists at higher energies, TALYS 1.9 estimations of cross sections for the ${}^{113}\text{In}(\gamma, \gamma){}^{113m}\text{In}$ and ${}^{115}\text{In}(\gamma, \gamma){}^{115m}\text{In}$ reactions were calculated. The values of the second term in Eq. (3) were then determined for the energy range from 18 MeV to 23 MeV. Multiple models of level density were used for this test, and remarkably consistent results were obtained. For instance, with the TALYS 1.9 level density model 1 (constant temperature Fermi-gas model) and GLO (Kopecky-Uhl-generalized Lorentzian) model for the strength function, the second term in Eq. (3) varied between 0.0386 and 0.0388 in the mentioned energy range. Consequently, it can be inferred that the contribution of the second term in Eq. (3) remains constant throughout the entire energy interval depicted in Fig. 3, with the mean value of 0.039(4) serving as a reliable estimation.

The $Y(^{113m}\text{In})/Y(^{115m}\text{In})$ ratio was corrected using this value, and subsequently, the analysis focused on the first term in Eq. (3). In this simplified form, the corrected yield



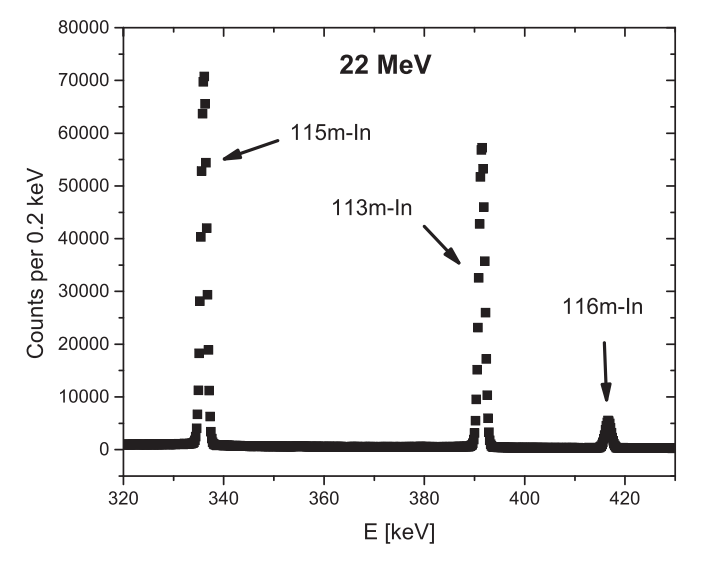


FIG. 2. Part of the γ -ray spectra collected after irradiation with 16 MeV and 22 MeV beams. The γ lines of interested are labeled. Energy width of one channel is 0.2 keV.

ratio reduces to the ratios of the saturation activities of the $^{115}\text{In}(\gamma, 2n)^{113m}\text{In}$ and $^{115}\text{In}(\gamma, \gamma')^{115m}\text{In}$ reactions.

D. Determination of photon flux

The calculation of relative yield Eq. (1) require knowing of bremsstrahlung photon spectra. For that purpose Monte Carlo (MC) simulations were used.

To estimate the flux of incident photons $\Phi(E)$ for the six used energies we employed GEANT4 (G4) version 11.01.p02 [10] with the experimental physics list QBBC. QBBC uses the standard G4 electromagnetic physics option without optical photon simulations and, the hadronic part of this physics list consists of elastic, inelastic, and capture processes. Each hadronic process is built from a set of cross sections and interaction models, which provide the detailed physics implementation. The simulated photon spectra are depicted in Fig. 4.

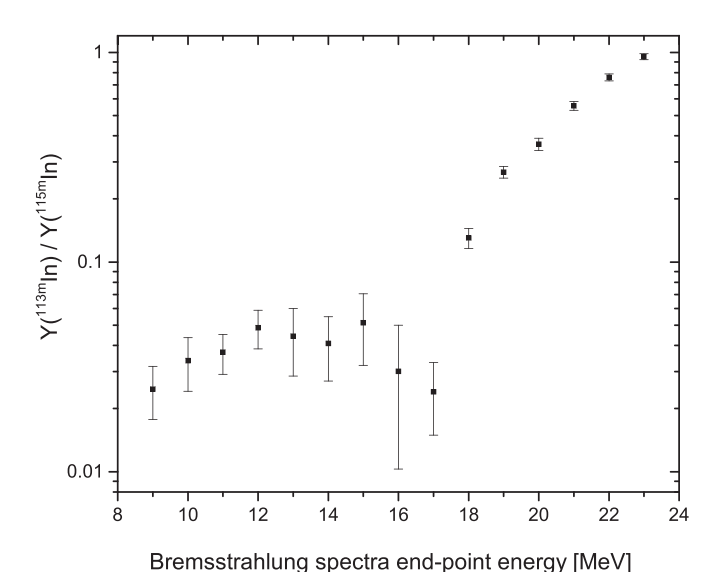


FIG. 3. Experimentally obtained relative yields $\frac{Y(^{113m}\ln)}{Y(^{115m}\ln)}$ for certain values of bremsstrahlung spectra end-point energy.

IV. RESULTS AND DISCUSSION

As it was mentioned in Sec. II, the set of obtained experimental data gives us two possibilities: (i) to check whether the theoretical and experimental cross-section values of the observed photonuclear reactions can reproduce the obtained results of measurement and (ii) to reconstruct the cross section for 115 In(γ , 2n) 113m In reaction.

A. Comparison of measured yield ratios with calculated ones

In the analysis of Eq. (3), we had the advantage of utilizing multiple data sets:

(1) Results obtained from TALYS 1.9 calculations for $\sigma_{\gamma,\gamma}^{115}$ and $\sigma_{\gamma,2n}^{115}$.

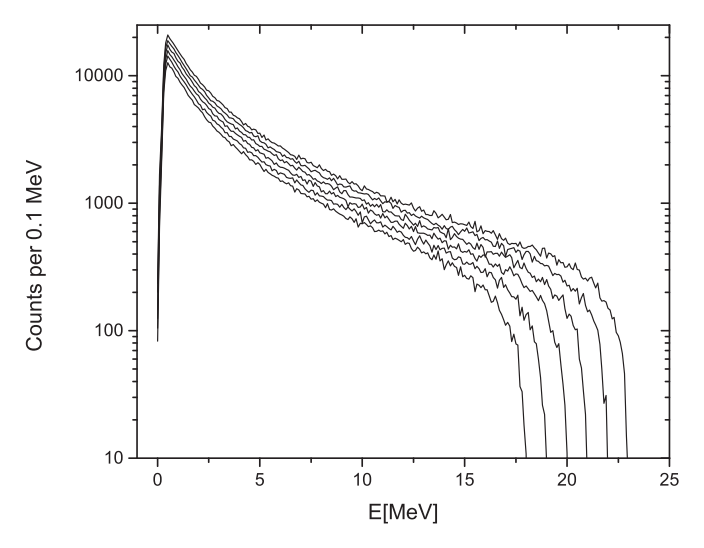


FIG. 4. Spectra of photon flux on the indium disks for electrons energies between 18 MeV and 23 MeV incident on the tungsten radiator. The electron energy corresponds to the end-point energy of the respective photon-flux spectrum ($E_{\rm max}$ in the Table I.)

- (2) Experimentally derived cross section for the $^{115}\text{In}(\gamma, 2n)^{113m}\text{In reaction}$.
- (3) Several measured cross sections for the photoactivation of ^{115m}In.

1. $\sigma_{\gamma,\gamma}^{115}$ and $\sigma_{\gamma,2n}^{115}$ estimated by TALYS 1.9

For the first check, TALYS 1.9 estimates of the cross sections of the observed reactions were chosen to be used. There were employed two different strength function models, and for each of them, cross sections for all six models describing the level density available in TALYS 1.9 were calculated. Available level density models in the TALYS 1.9 are [11–19]:

- (1) LD model 1: the constant temperature Fermi-gas model;
- (2) LD model 2: the back-shifted Fermi-gas model;
- (3) LD model 3: the generalized superfluid model;
- (4) LD model 4: the microscopic level densities based on the Goriely's tables;
- (5) LD model 5: Hilaire's combinatorial tables;
- (6) LD model 6: the temperature-dependent Hartree-Fock-Bogoliubov model, Gogny force.

The first cross-section estimation was performed using the GLO model for the radiation strength function, just as recommended in Ref. [20]. The reliability of the obtained results was checked by comparing the TALYS 1.9 results with the experimentally derived cross section of the 115 In (γ, γ') 115m In reaction. In this way, different models of the level density yield small differences in the cross section, but for all of them, it is common that the maximum value of the cross section is at 9.2 MeV, while the maximum value in the peak ranges from 0.865 mbarn to 1.14 mbarn. In most of the experimental results, the value of the cross section in the peak is around 1 mbarn. However, in Ref. [20], after careful measurements and calculation, it is obtained that the maximum value of the cross section could exceed 3 mbarn if some other model for the radiation strength function was chosen. For this reason, the decision was made to perform the calculations with cross sections obtained using another model of the strength function, which gives cross sections with a maximum value of around 3 mbarn. The Brink-Axel Lorentzian strength function (BAL) was used. In this case, the maximum cross-section value is at 9.2 MeV, and six different models of level density give peak values in the range from 2.96 mbarn to 3.66 mbarn. Six cross sections obtained using the GLO model and six cross sections obtained using the BAL model for the strength function are presented in Fig. 5.

The procedure was completely repeated for the $^{115}\text{In}(\gamma, 2n)^{113m}\text{In}$ reaction. Both the GLO and BAL strength function models were chosen, and for each of them, the cross sections with all six level density models were calculated. The results obtained are presented in Fig. 6.

From the graphical representation of the TALYS 1.9 cross section, it can be observed that there is a certain scatter in the shape of the function. However, unlike the case of the $^{115}\text{In}(\gamma, \gamma')^{115m}\text{In}$ reaction, no distinct separation into two clearly separated groups can be seen. The only existing measured cross section for this reaction [5] is depicted by the

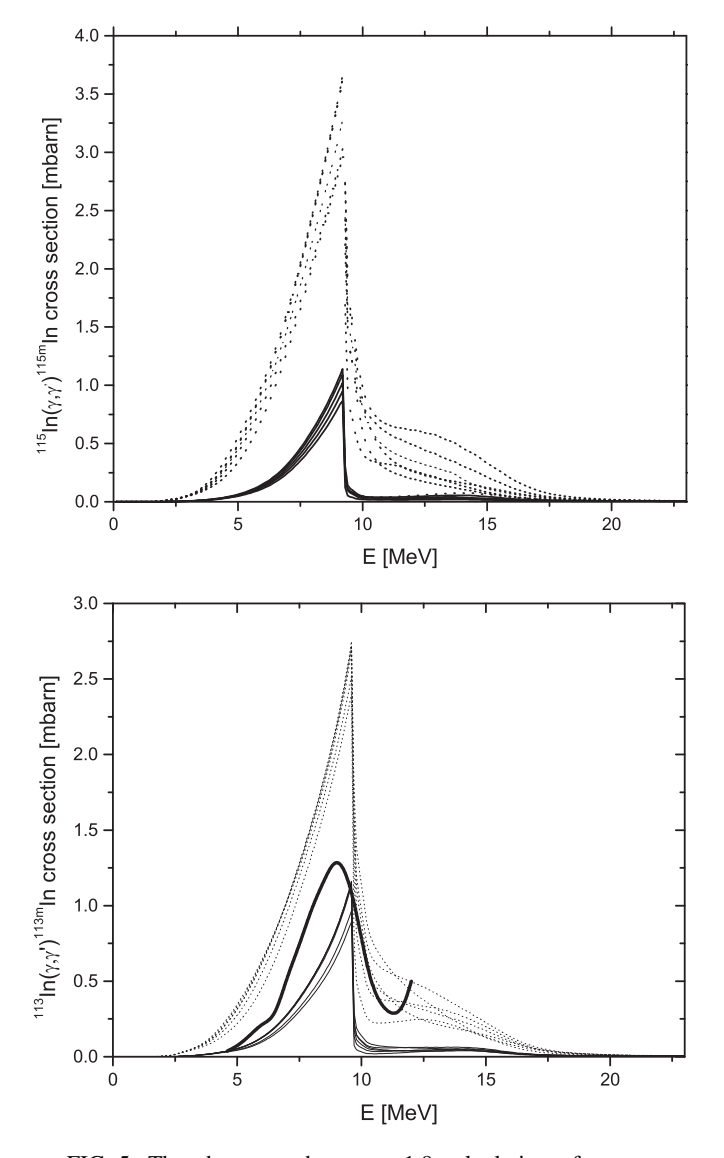


FIG. 5. The above graph: TALYS 1.9 calculation of cross sections for $^{115} \text{In}(\gamma,\gamma')\,^{115m} \text{In}$ reaction obtained using the GLO (solid line) and BAL (dotted line) models for radiation strength function and six models for level density. Bottom graph: TALYS 1.9 calculation of cross sections for $^{113} \text{In}(\gamma,\gamma')\,^{113m} \text{In}$ reaction obtained using the GLO (thin solid line) and BAL (dotted line) models for radiation strength function and six models for level density; thick line: experimental data with spline interpolation [21].

thick solid line in Fig. 6. A notable observation is that the measured cross-section values significantly differ from the cross sections obtained by TALYS 1.9 calculation.

The integrals (saturation activities) in the first term of Eq. (3) were calculated for several endpoint energies ranging from 18 MeV to 23 MeV using the obtained cross sections and G4 photon flux simulations. For each observed energy, six estimates for cross sections (and consequently, six values of saturation activities) were obtained for both the $(\gamma, 2n)$ and (γ, γ') reactions using one chosen model of the strength function.

Each saturation activity value obtained using one strength function model, for the $(\gamma, 2n)$ reaction was combined with

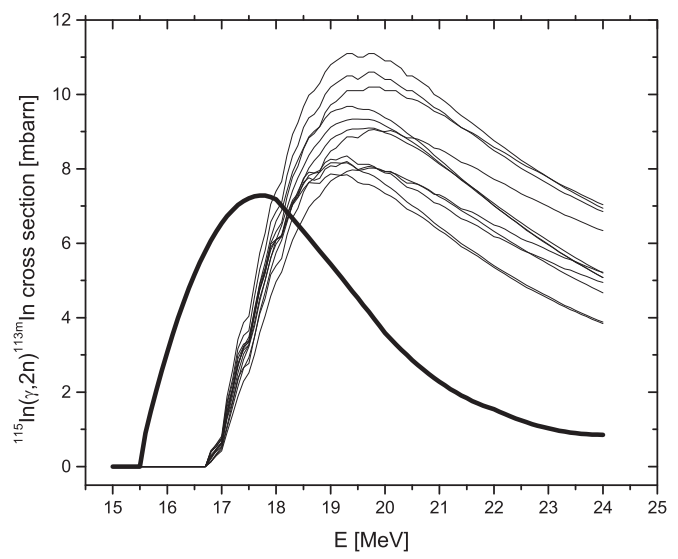


FIG. 6. Thin line: TALYS 1.9 calculation of cross sections for 115 In(γ , 2n) 113m In reaction obtained using the GLO and BAL models for radiation strength function and six models for level density; thick line: experimental data from Ref. [5].

each value for the (γ, γ') reaction, resulting in 36 estimates for one observed energy. The same procedure was repeated for a second model of the strength function, leading to another 36 combinations of saturation activity ratios. The outcomes of these calculations are presented in Fig. 7. At first glance, it can be seen that the obtained results of $Y(^{113m}\text{In})/Y(^{115m}\text{In})$ yield ratio are grouped into two bands, each obtained using one strength function. The upper band is obtained using GLO strength function model, while BAL model gives the lower cluster.

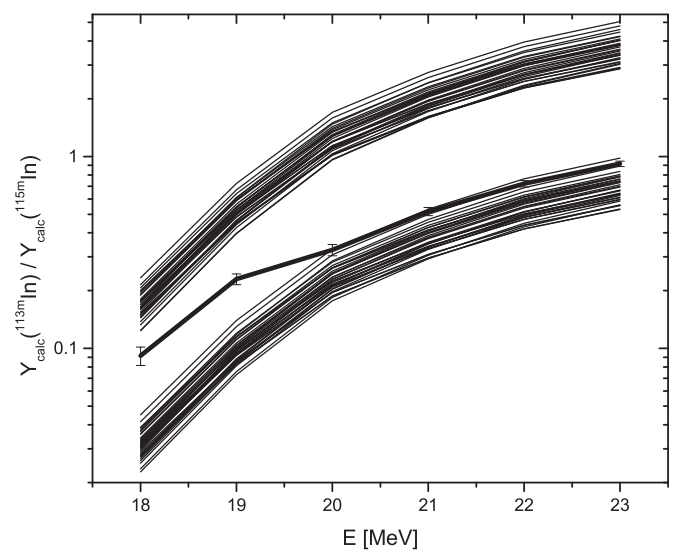


FIG. 7. Comparison of calculated yields $Y(^{113m}\text{In})/Y(^{115m}\text{In})$ using TALYS 1.9 results with measured ones presented by thick solid line. The top band consisting of 36 values of the $Y(^{113m}\text{In})/Y(^{115m}\text{In})$ yield ratio was obtained with the GLO model, while the bottom band contains yield values calculated using the BAL model.

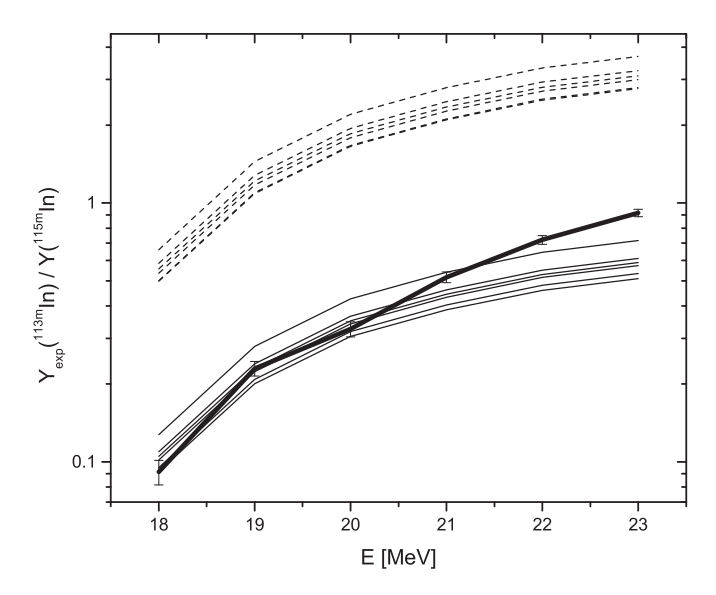


FIG. 8. Comparison of calculated yield ratios $Y(^{113m}\text{In})/Y(^{115m}\text{In})$ using TALYS 1.9 results available and experimental data [5] with measured ones. Top band is obtained using GLO model while the bottom one is calculated using BAL model.

It is important to note that the lines in Fig. 7, are provided solely as visual aids and do not result from a fit. The experimental results are represented by points and a thick line.

2. TALYS estimate for $\sigma_{\gamma,\gamma}^{115}(E)$ and experimentally determined $\sigma_{\gamma,2n}^{115}(E)$

Available data for the $^{115}\text{In}(\gamma, 2n)^{113m}\text{In}$ reaction cross section $\sigma_{\gamma,2n}^{115}(E)$ can be found in Ref. [5]. The saturation activities of this reaction were calculated for several endpoint energies from 18 MeV to 23 MeV of the using these cross section and reconstructed photon spectra $\Phi(E)$. Calculations of $\sigma_{\nu,\nu}^{115}(E)$ were performed using two different models of strength function, and all six models for level densities. For both groups of six cross section estimates, saturation activities were calculated, in the range between 18 MeV and 23 MeV. Ratios of saturation activities were calculated and obtained values are compared with experimentally derived values in Fig. 8. Thick solid line connects experimentally derived values $Y(^{113m}\text{In})/Y(^{115m}\text{In})$ ratios of reaction yields. Thin solid lines are obtained using GLO model of strength function, while thin dotted lines represent ratios of saturation activities calculated using cross sections estimated using BAL strength function model. Considering that two groups of cross sections for $\sigma_{\gamma,\gamma}^{115}(E)$ reactions differ significantly in amplitude depending on chosen model of strength function, as can be seen from Fig. 5, calculated ratios of reaction yields $Y(^{113m}\text{In})/Y(^{115m}\text{In})$ are grouped in two separated clusters.

3. Experimentally determined both $\sigma_{\gamma,\gamma}^{115}(E)$ and $\sigma_{\gamma,2n}^{115}(E)$

Although there are several published results of measurements of the cross section for the $^{115} In(\gamma,\gamma')^{115m} In$ reaction, none of them fully satisfy the requirements of this study. The primary reason is that the cross sections for the mentioned reaction were not measured across a sufficiently wide energy

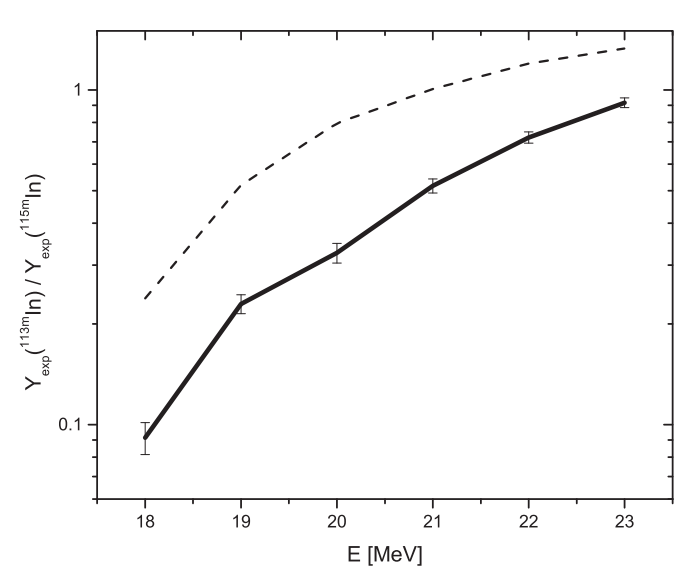


FIG. 9. Comparison of calculated yield ratios $Y(^{113m}\text{In})/Y(^{115m}\text{In})$ using available experimental data for the $^{115}\text{In}(\gamma,\gamma')^{115m}\text{In}$ reaction [22] and $^{115}\text{In}(\gamma,2n)^{113m}\text{In}$ reaction [5] with measured ones. Results of calculations are connected by dashed line.

range. The only paper presenting cross-section results at high energies [5] was rejected due to unrealistically high values of the cross section in the 20 MeV region. Consequently, the decision was made to utilize the cross sections published in Ref. [22], which demonstrate a reasonable agreement with the TALYS 1.9 estimates.

However, it should be noted that the main limitation of this data set is that the cross sections are only determined up to a maximum energy of 12 MeV. To accommodate the analysis, it is assumed that the cross-section values in the energy interval from 12 MeV to 23 MeV are not significantly large. Under this assumption, the absence of data in the high-energy region would not have a substantial impact on the value of the saturation activity. Figure 5 reveals that GLO model used for calculating the TALYS 1.9 cross section predicts a very small value of the cross section in the high-energy area.

Similarly, the saturation activity for the 115 In(γ , 2n) 113m In reaction was calculated using the experimental cross-sectional values published in Ref. [5]. The calculated values of the yield ratio are then compared with the experimental data in Fig. 9.

B. Cross section of 115 In(γ , 2n) 113m In reaction obtained by unfolding procedure

In this study, we applied the unfolding technique to obtain a more suitable cross section for the $^{115}\text{In}(\gamma,2n)^{113m}\text{In}$ reaction in the energy range from the reaction threshold up to 23 MeV. To derive the unfolding values of the phase cross section, the Eq. (3) was transformed as follows:

$$A_{k} = \frac{Y(^{113m}\text{In})}{Y(^{115m}\text{In})} \cdot \int_{E_{th}^{\gamma,\gamma}}^{E_{\text{max}_{k}}} \sigma_{\gamma,\gamma}^{115}(E) \Phi(E)_{k} dE$$

$$= \int_{E_{th}^{\gamma,2n}}^{E_{\text{max}_{k}}} \sigma_{\gamma,2n}^{115}(E) \Phi(E)_{k} dE, \qquad (5)$$

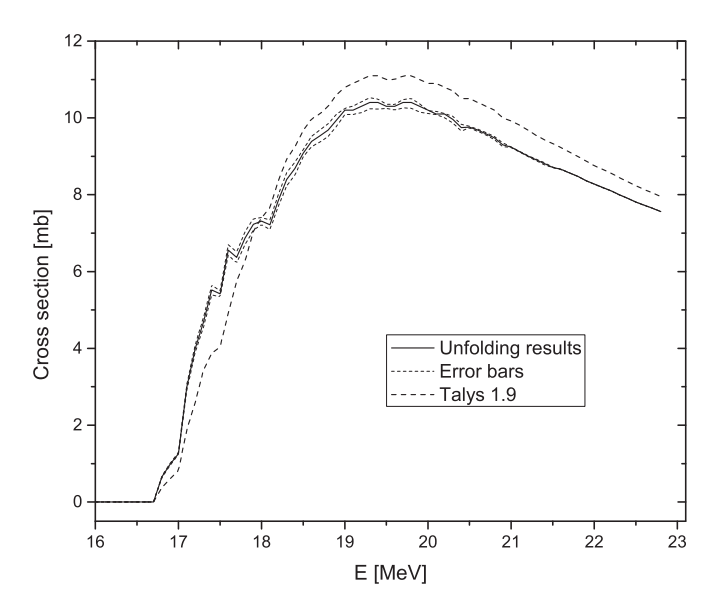


FIG. 10. Unfolded results for the 115 In(γ , 2n') 115m In cross section (line with a corridor of uncertainty) in comparison with default TALYS 1.9 function.

where the index k indicates the number of the irradiated disk and in this case it goes from 1–6 for six activated energies.

For the unfolding process, the input quantities included $A_k = Y_k(^{113m}\text{In})/Y_k(^{115m}\text{In}) \cdot \int_{E_{lh}^{Ny}}^{E_{max_k}} \sigma_{\gamma,\gamma}^{115}(E)\Phi(E)_k dE$ [saturation activity of $^{115}\text{In}(\gamma,\gamma')$ ^{115m}In multiplied by experimentally determined reaction yields]. In Eq. (5), A_k was calculated using the values of the cross section function for the $^{115}\text{In}(\gamma,\gamma')$ ^{115m}In reaction obtained by TALYS 1.9 calculations using model 6 for level density and BAL model for radiation strength function. This specific model combination was selected as it demonstrated the best agreement with experimentally determined yields (Fig. 7).

Similarly, in the unfolding procedure for the $^{115}\text{In}(\gamma,2n)^{113m}\text{In}$ reaction, the starting default function utilized TALYS 1.9 calculations with model 3 for level density and BAL for radiation strength function, as this combination also provided the best agreement with experimental results (Fig. 7). The unfolding procedure employed the MAXED algorithm [23], which utilizes input data of measured induced specific saturated activity A_k to derive a function $\sigma(E)$ maximizing the relative entropy S, defined as follows:

$$S = -\int \left(\sigma(E) \ln \left(\frac{\sigma(E)}{\sigma_{\text{def}}(E)}\right) + \sigma_{\text{def}}(E) - \sigma(E)\right) dE. \quad (6)$$

Here, $\sigma_{def}(E)$ represents the default cross-section function.

Unfolding procedures were conducted within the energy range of 16 MeV to 22.8 MeV, which was divided into 71 bins. The result obtained by employing the MAXED algorithm is depicted in Fig. 10. Corridor of uncertainty was calculated by MAXED algorithm and included influence of uncertainty of A to final cross-section values.

To validate the unfolding results, an induced activity $[A_{kc} = \sum \sigma(E_i) \cdot \Phi(E_i) \cdot \Delta E]$ was calculated and then compared with the measured data. This comparison was performed for default cross-section functions and the MAXED

results and the sum of the squared of relative deviation σ is calculated as:

$$S = \frac{1}{(k-1)} \sum_{1}^{k} \sigma^2 = \frac{1}{(k-1)} \sum_{1}^{k} \left(\frac{A_{kc} - A_{ke}}{A_{ke}} \right)^2. \tag{7}$$

The obtained values are S=0.13 for the default spectrum and S=0.08 for the unfolding results. This indicates that the unfolding outcomes provide a better description of the measured experimental data compared to the TALYS 1.9 calculations.

V. DISCUSSION

The first check was conducted by utilizing the cross-section values obtained by the TALYS 1.9 code for both reactions, $^{115}\text{In}(\gamma,2n)^{113m}\text{In}$ and $^{115}\text{In}(\gamma,\gamma)^{115m}\text{In}$. Each estimate for the $^{115}\text{In}(\gamma,2n)^{113m}\text{In}$ reaction was combined with each estimate obtained for the $^{115}\text{In}(\gamma,\gamma)^{115m}\text{In}$ reaction, resulting in 36 distinct values for the saturation activity ratios for a specific strength function choice.

It is evident that the 36 combinations of saturation activity ratios are grouped into two clusters. The lower cluster was obtained using the BAL radiation strength function, which provides higher cross-section values for the $^{115}{\rm In}(\gamma,\gamma')^{115m}{\rm In}$ reaction, approximately around 3 mbarn. Notably, at energies of 20 MeV and above, the highest estimated ratios of saturation activities align closely with the experimental results. However, at energies below 20 MeV, the experimental values slightly exceed the values obtained based on TALYS 1.9 sections.

On the other hand, the upper cluster comprises 36 combinations of saturation activity ratios obtained using the GLO model for the radiation strength function. It is evident that lower estimations of cross sections for the $^{115}\text{In}(\gamma,\gamma')$ ^{115m}In reaction, around 1 mbarn, lead to overestimated values of the yield ratio.

In summary, the analysis of these saturation activity ratios obtained through different radiation strength function models indicates that the BAL model tends to yield better agreement with experimental data at higher energies, while the GLO model tends to overestimate the yield ratio due to lower estimations of the cross sections for the $^{115}\text{In}(\gamma, \gamma')$ ^{115m}In reaction. If we focus on the energy region higher than 20 MeV, it can be observed that of the 36 TALYS combinations there are some that show good agreement with the experiment. It can be observed that the best agreement with the experiment is given by the combination in which the cross section for $^{115}\text{In}(\gamma, 2n)^{113m}$ In reaction is calculated using LD model 3 (the generalized superfluid model) and cross section of 115 In (γ, γ') 115m In reaction is estimated using LD model 6 (the temperature-dependent Hartree-Fock-Bogoliubov model, Gogny force).

In the second scenario, where one experimentaly established cross section was available in the databases for the $^{115} \text{In}(\gamma,2n)^{113m} \text{In}$ reaction, the comparison with the experimental results yielded similar outcomes. Notably, the cross section for the $^{115} \text{In}(\gamma,\gamma')^{115m} \text{In}$ reaction, calculated using the GLO radiation strength function in all six subvariants obtained by choosing the level density function, exhibited

significantly higher values of the saturation activity ratio compared to the measured values. The estimated ratios of saturation activities were found to be larger than the experimental ones when using cross sections for the 115 In(γ , 2n) 113m In reaction, which have maximum values around 1 mbarn.

Of particular interest was the comparison of the experimental values of the $Y(^{113m}In)/Y(^{115m}In)$ yield ratio with the calculated values when employing the BAL radiation strength function to estimate the cross section of the $^{115}\text{In}(\gamma, \gamma')$ ^{115m}In reaction. Remarkably, a much better agreement with the experimental data was achieved in this case. Figure 6 clearly illustrates that the experimental value of the cross section for the 115 In $(\gamma, 2n)$ 113m In reaction has a lower threshold compared to the prediction from TALYS 1.9 calculations. Consequently, the saturation activity calculated using this cross section increases more rapidly with increasing energy than the saturation activities obtained using the TALYS 1.9 cross sections for the same reaction in energy region up to 20 MeV. For this reason, it can be seen in Fig. 8 that the measured and calculated values of $Y(^{113m}In)/Y(^{115m}In)$ yield ratio coincide at lower energies, while the difference is observed at energies higher than 20 MeV. However, as the experimental cross section decreases significantly faster in high-energy region, compared to the TALYS 1.9 cross section, the ratio of saturation activities shows a slower increase with increasing energy. This effect is evident in Fig. 8, where the experimental values of the ratio of saturation activities at energies above 20 MeV are higher than the calculated ones.

In Fig. 9, it is evident that when calculating the ratio of saturation activities using experimentally established cross sections for both reactions, the obtained values significantly exceed the values measured in this experiment. This outcome was anticipated, as the cross section utilized for the $^{115} {\rm In}(\gamma,\gamma')\,^{115m} {\rm In}$ reaction has values similar to those obtained using the GLO model for the radiation strength function.

It was shown that, based on the measured $Y(^{113m}\text{In})/Y(^{115m}\text{In})$ yield ratio values, the unfolding technique can be used to estimate the energy differential cross section for the $^{115}\text{In}(\gamma,2n)^{113m}\text{In}$ nuclear reaction. The resulting estimate is shown in Fig. 10. This result is significantly different from the cross section shown in Ref. [5], however, it shows good agreement with the results of TALYS 1.9 calculations. Slight deviations from the smooth flow of the curve in the energy region around 18 MeV originate from some numerical effects in the unfolding procedure itself,

the most probable source of which is insufficient number and accuracy of the measured data.

VI. CONCLUSIONS

In this work, the $Y(^{113m}\text{In})/Y(^{115m}\text{In})$ yield ratio were measured in the energy interval from 18 MeV to 23 MeV, in order to verify the capacity of the existing methods for evaluating the cross section of relevant photonuclear reactions to reproduce the obtained experimental results. It was also checked whether it is possible to obtain agreement with the measured $Y(^{113m}\text{In})/Y(^{115m}\text{In})$ yield ratios with the available cross sections of the observed photonuclear reactions.

Comparisons of experimental values of $Y(^{113m}\text{In})/Y(^{115m}\text{In})$ yield ratio with the results of calculations based on TALYS 1.9 evaluated cross sections, showed that the best agreement is obtained if the cross section of $^{115}\text{In}(\gamma, \gamma')$ ^{115}In reactions is calculated in the way suggested in Ref. [20]. This raises the need to carefully check the cross section for $^{115}\text{In}(\gamma, \gamma')$ ^{115}In reaction, since most of the so far known measurements give lower values of the cross section than suggested in Ref. [20]. However, it was shown in this experiment that those lower cross section values for the $^{115}\text{In}(\gamma, \gamma')$ ^{115}In reaction, good agreement with the measured $Y(^{113m}\text{In})/Y(^{115m}\text{In})$ yield ratios is not obtained.

Based on cross sections for a given reaction, estimated using TALYS 1.9, $Y(^{113m}\text{In})/Y(^{115m}\text{In})$ yield ratios were and compared with measured ones. This study shows that the best agreement with the experimental data is obtained when the cross sections for the $^{115}\text{In}(\gamma,2n)^{113m}$ In reaction is estimated using generalized superfluid model for the level density calculation, and temperature-dependent Hartree-Fock-Bogoliubov model, Gogny force model for $^{115}\text{In}(\gamma,\gamma')^{115}\text{In}$ reaction. In both cases the BAL model of the radiation strength function is recommended. However, these results should only be conditionally accepted since there is a certain deviation between the experimental and calculated $Y(^{113m}\text{In})/Y(^{115m}\text{In})$ yield ratio values at lower energies.

Also in this paper, the estimation of cross sections for $^{115}\text{In}(\gamma,2n)^{113m}\text{In}$ reaction was performed using the unfolding method. The first results are encouraging and in much better agreement with the cross sections obtained by TALYS 1.9 calculations than the only cross section for this reaction that can be found in the literature. There is room to better determine this cross section in repeated measurements where the saturation activities would be determined for a larger number of energies in the energy interval of interest.

^[1] A. Zilges, D. Balabanski, J. Isaak, and N. Pietralla, Prog. Part. Nucl. Phys. 122, 103903 (2022).

^[2] T. Kawano, Y. Cho, P. Dimitriou, D. Filipescu, N. Iwamoto, V. Plujko, X. Tao, H. Utsunomiya, V. Varlamov, R. Xu, R. Capote, I. Gheorghe, O. Gorbachenko, Y. Jin, T. Renstrøm, M. Sin, K. Stopani, Y. Tian, G. Tveten, J. Wang *et al.*, Nucl. Data Sheets 163, 109 (2020).

^[3] S. S. Dietrich and B. L. Berman, At. Data Nucl. Data Tables 38, 199 (1988).

^[4] A. Koning and D. Rochman, Nucl. Data Sheets 113, 2841 (2012), special Issue on Nuclear Reaction Data.

^[5] O. Bogdankevich, L. Lazareva, and F. Nikolaev, J. Exp. Theor. Phys. 4, 320 (1957).

^[6] M. Erhard, A. R. Junghans, R. Beyer, E. Grosse, J. Klug, K. Kosev, C. Nair, N. Nankov, G. Rusev, K. D. Schilling, R. Schwengner, and A. Wagner, Eur. Phys. J. A 27, 135 (2006).

^[7] Janis nuclear data, https://www.oecd-nea.org/jcms/pl_39910/janis.

- [8] 25-microtron, http://flerovlab.jinr.ru/mt-25-microtron/.
- [9] M. Krmar, Y. Teterev, A. Belov, and S. Mitrofanov, Nucl. Instrum. Meth. Phys. Res. A 901, 133 (2018).
- [10] S. Agostinelli, J. Allison, K. Amako, J. Apostolakis, H. Araujo, P. Arce, M. Asai, D. Axen, S. Banerjee, G. Barrand, F. Behner, L. Bellagamba, J. Boudreau, L. Broglia, A. Brunengo, H. Burkhardt, S. Chauvie, J. Chuma, R. Chytracek, G. Cooperman et al., Nucl. Instrum. Meth. Phys. Res. A 506, 250 (2003).
- [11] A. Koning and J. Delaroche, Nucl. Phys. A 713, 231 (2003).
- [12] W. Hauser and H. Feshbach, Phys. Rev. 87, 366 (1952).
- [13] C. Kalbach, Phys. Rev. C 33, 818 (1986).
- [14] A. Gilbert and A. Cameron, Can. J. Phys. 43, 1446 (1965).
- [15] W. Dilg, Nucl. Phys. A 217, 269 (1973).
- [16] A. Zubov, G. Adamian, and N. Antonenko, Phys. Part. Nucl. 40, 847 (2009).

- [17] A. V. Ignatyuk, J. L. Weil, S. Raman, and S. Kahane, Phys. Rev. C 47, 1504 (1993).
- [18] S. Goriely, S. Hilaire, and A. J. Koning, Phys. Rev. C 78, 064307 (2008).
- [19] S. Hilaire, M. Girod, S. Goriely, and A. J. Koning, Phys. Rev. C 86, 064317 (2012).
- [20] M. Versteegen, D. Denis-Petit, V. Méot, T. Bonnet, M. Comet, F. Gobet, F. Hannachi, M. Tarisien, P. Morel, M. Martini, and S. Péru, Phys. Rev. C 94, 044325 (2016).
- [21] Z. M. Bigan, V. A. Zheltonozhsky, V. I. Kirishchuk, V. M. Mazur, D.N.Simochko, and P.N.Trifonov, Bull. Russ. Acad. Sci. Phys. 70, 292 (2006).
- [22] V. Mazur, I. Sokolyuk, Z. Bigan, and I. Kobal, Phys. At. Nucl. 56, 10 (1993).
- [23] M. Reginatto and P. Goldhagen, Health Phys. 77, 579 (1999).

ELSEVIER

Contents lists available at ScienceDirect

Applied Radiation and Isotopes

journal homepage: www.elsevier.com/locate/apradiso





Production of ^{117m}Sn and ^{119m}Sn by photonuclear reactions on natural antimony

M. Krmar ^{a,*}, N. Jovančević ^a, Ž. Medić ^b, D. Maletić ^b, Yu Teterev ^c, S. Mitrofanov ^c, K.D. Timoshenko ^c, S.I. Alexeev ^c, H. Marukyan ^d, I. Kerobyan ^d, R. Avetisyan ^d, R. Dallakyan ^d, A. Hakobyan ^d, L. Vahradyan ^d, H. Mkrtchyan ^d, A. Petrosyan ^d, H. Torosyan ^d

- ^a Physics Department, Faculty of Science, University Novi Sad, Serbia
- ^b Institute of Physics, Belgrade, Serbia
- ^c Flerov Laboratory of Nuclear Reactions, Joint Institute for Nuclear Research, Dubna, Russia
- ^d A.Alikhanyan National Science Laboratory (Yerevan Physics Institute), Yerevan, Armenia

ARTICLE INFO

Keywords: Photonuclear reactions ^{117m}Sn production 60 MeV bremsstrahlung

ABSTRACT

Natural antimony targets were irradiated in a 60 MeV bremsstrahlung beam and gamma spectrometric measurements were performed. The goal was to establish the yield of ^{117m}Sn , a radionuclide with great potential for application in medicine. Considering that ^{117m}Sn is predominantly produced through a photonuclear reaction in which an charged particle is emitted $(^{121}\text{Sb}(\gamma,p3n))$, the yield of this tin isotope is much lower than the yields of several antimony isotopes produced in (γ,xn) reactions. It has been estimated that photonuclear reactions on natural antimony could produce ^{117m}Sn activities needed for therapeutic applications, with accelerators having electron currents of the order of mA. For the used bremsstrahlung energy of 60 MeV, it was estimated how much ^{119m}Sn activity can be expected when exposing the antimony target.

1. Introduction

Photonuclear reactions represent a very interesting field in which the nucleus, as a system determined by a strong interaction, is subjected to electromagnetic forces. These reactions are conducted by the interaction of high-energy electromagnetic radiation (10 MeV and more) with nuclei of the selected target. The process of the highest probability is emission of one neutron. If the energy of the electromagnetic radiation is high enough, the excited nucleus can emit two or more neutrons, with lower probability. Protons and other charged particles can leave the nucleus, but with a much lower probability due to the effect of the Coulomb barrier.

Electromagnetic nature of interaction makes photonuclear reactions a suitable method for studies of the nucleus and some of its properties. Photonuclear reactions have become a convenient method in number of basic research (Pietralla et al., 2019; Zilges et al., 2022). Besides that, they could be quite acceptable way for production of radionuclides. The need for the production of radionuclides used in medicine is particularly important (Qaim, 2017). In currently established practice, a certain number of neutron-deficient radionuclides and positron sources are

usually produced by proton cyclotrons (IAEA radioisotopes and radiofarmaceuticals reports No, 2021). However, some of them can be obtained through photonuclear reactions (Starovoitova et al., 2015; Inagaki et al., 2019; Kazakov et al., 2021).

The main objective of this work is to check the feasibility of producing $^{117m} \mathrm{Sn}$ by photonuclear reactions. The tin isotope $^{117m} \mathrm{Sn}$ has shown extremely promising properties in the process of theranostics (Lewington, 2005). The 158.562 keV gamma radiation is emitted after de-excitation of the $^{117m} \mathrm{Sn}$ isomeric state. Moderate attenuation in soft tissues and large cross sections for interaction with NaI (XCOM, 2010) make 158.562 keV photons very suitable for SPECT diagnostic purposes. The large number of conversion electrons (113% emission probability), (Blachot, 2002) can provide a high local dose at some specific location where the radiopharmaceutical labeled with this isotope would be accumulated.

To obtain high specific activities of ^{117m}Sn, various nuclear reactions using charged particles were taken in consideration (Stevenson et al., 2015). The two most important directions are using proton beams (Ermolaev et al., 2009) and alpha particles (Maslov et al., 2011; Ditrói et al., 2016; Duchemin et al., 2016; Aikawa et al., 2018; Aslam et al.,

E-mail address: krmar@df.uns.ac.rs (M. Krmar).

^{*} Corresponding author.

2018). Photonuclear reactions for the production of 117m Sn are not frequently studied. A couple of attempts have been performed to get 117m Sn by (γ, γ) reaction on enriched 117 Sn target (Aksenov et al., 1992).

In the present paper, the possibility of producing ^{117m}Sn by photonuclear reactions on a target made of natural antimony with a 60 MeV bremsstrahlung beam has been investigated experimentally. One of the main goals is to estimate the yield of this radionuclide.

Natural antimony contains two isotopes, 121 Sb and 123 Sb. For the purposes of this study, the reactions 121 Sb(γ ,p3n) and 123 Sb(γ ,p5n) are considered. Photonuclear reactions in which no charged particles are emitted have higher cross sections than reactions with emission of charged particle (EXFOR Data Tables), due to the absence of a Coulomb barrier. Unfortunately, 121 Sb(γ ,4n) and 123 Sb(γ ,6n), do not lead to the creation of 117m Sn after beta decay (EC) of produced 117 Sb (Blachot, 2002).

It is inevitable that some other active radionuclides are formed during the exposure of a natural antimony target to a beam of high-energy photons. It is particularly interesting to see to what extent the produced $^{117m} \rm Sn$ would be contaminated by the activity of other products of possible photonuclear reactions. In this work, special attention is paid to $^{119m} \rm Sn$, which would be created through $^{121} \rm Sb(\gamma,pn)$ and $^{123} \rm Sb(\gamma,p3n)$ photonuclear reactions.

2. Materials and methods

2.1. Expected nuclear reactions

Natural antimony consists of two isotopes: ¹²¹Sb (57.36%) and ¹²³Sb (42.64%) (Chu et al., 1999). Relevant part of the isotope chart is presented in Fig. 1. During exposure of a natural antimony target to a flux of high-energy photons, several types of nuclear reactions occur.

a) (γ,n) and (γ,xn) reactions

Several antimony isotopes, (depending on the endpoint energy of the bremsstrahlung beam used in experiment) could be produced in reactions with emission of one or more neutrons. Both ground state and Sb isomers are created. Besides $^{122}\mathrm{Sb}$, which decays mostly (97.6%) to $^{122}\mathrm{Te}$ through the emission of a beta particle, all other Sb isotopes decay through electron capture (Chu et al., 1999). It can be seen (Fig. 1) that in this way stable tin nuclei will be formed. Two of the stable tin isotopes have isomers $^{117m}\mathrm{Sn}$ and $^{119m}\mathrm{Sb}$, however decays of $^{117}\mathrm{Sb}$ and $^{119}\mathrm{Sb}$ do not populate their metastable states. This means that no Sn activity should be expected after decay of antimony isotopes created in (γ,n) and (γ,xn) reactions. If Sn fraction is chemically extracted from the irradiated antimony target, the output of (γ,n) and (γ,xn) reactions can estimate how much non-active Sn would be obtained together with $^{117m}\mathrm{Sn}$,

produced in some other reactions.

b) (γ,p) and (γ,pxn) reactions

If one proton (with or without neutrons) is emitted during the irradiation of the Sb target, tin isotopes will be formed. All of Sn isotopes created in this way are stable, with the exception of ¹²¹Sn. This isotope is formed in the $^{123}\text{Sb}(\gamma,pn)$ reaction in the ground state, but also as an isomer. After decay of the ground state of ¹²¹Sn, beta radiation of relatively low energy (Q value: 390.1 keV) is emitted without the emission of gamma radiation. Considering that the time dynamics of the creation of a product of a nuclear reaction can be described by a function (1 $e^{-\lambda t_{irr}}$) and that $^{121 \mathrm{m}}$ Sn has a half-life of 55 years, low activity would be created in photon beam in some realistic case when the irradiation time is of the order of hours or shorter. Additionally, it could be expected that ^{119m}Sn and ^{117m}Sn isomers will be created (half lives 293.1 days and 13.6 days, respectively). 119m Sn can be formed in 121 Sb(γ ,pn) and 123 Sb $(\gamma,p3n)$ reactions. Another isomer, ^{117m}Sn can be produced in ¹²¹Sb $(\gamma,p3n)$ p3n) and 123 Sb(γ ,p5n) reactions, if the endpoint energy of bremsstrahlung is high enough.

^{117m}Sn has very suitable characteristics for use in medicine. The scheme of de-excitation of the metastable state is shown in Fig. 2. The gamma radiation energy emitted (158.56 keV) is almost ideal for SPECT diagnostic procedures (Duchemin et al., 2016). The transitions of 314.3 keV and 156.2 keV are almost entirely realized by the emission of conversion electrons. It was determined that 1.13 conversion electrons are emitted per one decay of ^{117m}Sn (Ermolaev et al., 2009; Aslam et al., 2018). Due to the low penetrating power, these electrons in the tissues

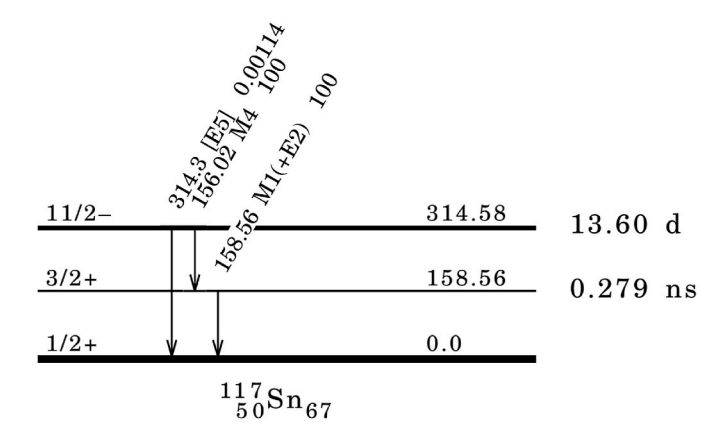


Fig. 2. Decay scheme of 117m Sn. For absolute intensities of transitions, multiply by 0.864 (Firestone 1996).

Sb116	Sb117	Sb118	Sb119	Sb120	Sb121	Sb122	Sb123
15.8 m	2.80 h	3.6 m	38.19 h	15.89 m	Stable	2.7238 d	Stable
3+	5/2+	1+	5/2+	1+	5/2+	2-	7/2+
EC	EC	EC	EC	EC	57.36 %	EC, β-	42.64 %
Sn115	Sn116	Sn117	Sn118	Sn119	Sn120	Sn121	Sn115
Stable	Stable	Stable	Stable	Stable	Stable	27.06 h	Stable
1/2+	0_{+}	1/2+	0_{+}	1/2+	0^{+}	3/2+	1/2+
0.34 %	14.53 %	7.68 %	24.23 %	8.59 %	32.59 %	β-	0.34 %
In114	In115	In116	In117	In118	In119	In120	In121
71.9 s	4.41E+14y	14.10 s	43.2 m	5.0 s	2.4 m	3.08 s	23.1 s
1+	9/2+	1+	9/2+	1+	9/2+	1+	9/2+
EC, β-	β ⁻ , 95.7 %	EC, β ⁻	β-	β-	β-	β-	β-

Fig. 1. Part of the isotope chart presenting Sb and Sn isotopes of interest (taken from Nuclear charts in (Chu et al., 1999)). Listed are, from top to bottom: isotope, half-life, ground state spin, and decay mode, or natural isotope abundance for stable ones.

deposit their energy in a small space around the location where the radiopharmaceutical labeled with $^{117m}\mathrm{Sn}$ accumulates (Lewington, 2005; Stevenson et al., 2015). In this way, a therapeutic dose can be deposited in a controlled area.

The decay scheme of ^{119m}Sn is shown in Fig. 3. During the deexcitation of the metastable state of 89.53 keV, gamma radiation of energy 23.87 keV is emitted. It is determined that 0.161 photons are emitted per decay (Symochko et al., 2009). Such low energy photon radiation has very little chance of leaving the patient's body, so it cannot be used for diagnostic purposes in nuclear medicine (half-value thickness of 23.98 keV gamma radiation in water is 1.25 cm according to (XCOM, 2010)). It was measured that the transitions shown in Fig. 3 are realized to the greatest extent by the emission of conversion electrons. It is determined that 1.83 conversion electrons are emitted per ^{119m}Sn decay (Symochko et al., 2009). These electrons could also play a significant role in radionuclide therapy.

c) (γ,α) , $(\gamma,\alpha n)$ and $(\gamma,\alpha xn)$ reactions

Additional interesting outcome of the photoreactions, which could be expected during exposition of antimony target in high energy photon beams, is emission of alpha particle, with or without neutrons. Reactions $(\gamma,\alpha),\,(\gamma,\alpha 2n),\,$ etc. will produce indium isotopes. In the simplest case, when just an alpha particle is emitted after interaction of high energy photons with ^{123}Sb , the ^{119}In isotope would be created. It is the heaviest isotope of indium that can be formed in this way. Considering that the half-life of ^{119}In is 2.4 min, it is unlikely that it will be identified in an off-line gamma radiation measurement. The same is with $^{118}\text{In},$ which has a half-life of 5 s. Just ^{117}In and lighter isotopes could be detected in some standard off-line gamma spectroscopy measurements. The decay of the ground state of ^{117}In populates the isomeric state ^{117m}Sn to a very small extent (0.344%), while the decay of the isomer ^{117m}In completely bypasses it (Blachot, 2002).

It should be emphasized that after the decay of ¹¹⁷Sb, as well as the decay of both the ground and isomer states of ¹¹⁷In, the emission of photon radiation of 158.56 keV occurs. This is also the only gamma radiation emitted after de-excitation of the 314.58 keV isomeric state of ^{117m}Sb, which complicates the interpretation of gamma spectra recorded immediately after the irradiation of the antimony target. The half-life of ¹¹⁷Sn is 2.8 days, while ¹¹⁷In and ^{117m}In have half-lives of 43.2 min and 116.2 min, respectively, which is significantly shorter than the half-life of ^{117m}Sn. In repeated measurements after a sufficiently long time interval, the presence of ^{117m}Sn in the irradiated sample can be determined.

d) (n,γ) reactions

The production of bremsstrahlung radiation with endpoint energies higher than the binding energy of neutrons in the nuclei of irradiated materials leads to the emission of neutrons. The sources of neutrons are

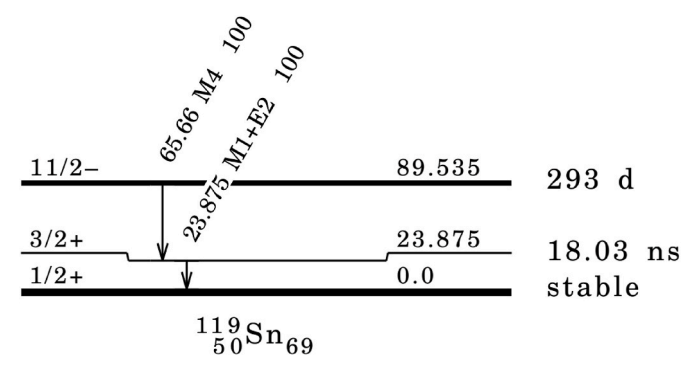


Fig. 3. Decay scheme of ^{119m}Sn (Firestone 1996).

usually a bremsstrahlung converter, collimators, filters and all other materials affected by the photon beam. These neutrons can be captured by the nuclei of the target material. It is most likely that $^{122}\mathrm{Sb}$ and $^{124}\mathrm{Sb}$ are formed in the interactions of neutrons with Sb target nuclei. The easiest way to assess the presence of neutrons at the location of the irradiated target is to identify the gamma lines of ¹²⁴Sb. The half-life of this radionuclide is 60.20 d, so for its identification purposes, the spectrum recorded three days after irradiation was used. Only two gamma lines of 602.73 keV and 1690.98 keV were observed in the spectrum. The quantum yields of these two lines are 97.8% and 47.3% respectively (Chu et al., 1999). The intensities of these gamma lines in the measured spectrum are four orders of magnitude lower than the ^{120m}Sb gamma lines, which have a similar quantum yield. In addition, in the spectrum of the gold foil exposed together with the Sb target, a gamma line of 411.8 keV can be observed. This gamma transition originates from ¹⁹⁸Au produced by the capture of neutrons on ¹⁹⁷Au. Based on these three very weak lines, it was estimated that the neutron capture does not give activities that can be compared with the activities obtained through photonuclear reactions and that the contribution of (n, γ) reactions can be neglected.

2.2. Reaction yields

Considering that natural antimony consist of two stable isotopes, $^{121}\mathrm{Sb}$ (57.36%) and $^{123}\mathrm{Sb}$ (42.64%), in some cases, one product of photonuclear reaction can be formed in two different ways. Total activity of observed product can be result of two reactions, whose probabilities are defined by the energy differential cross sections $\sigma_i^{121}(E)$ and $\sigma_i^{123}(E)$ for an observed *i*-th reaction. The atomic number of parent nuclei is denoted in superscript. The frequently used equation for calculating the saturation activity of the product obtained in a nuclear reaction (Krmar et al., 2004) can be somewhat corrected in the case of irradiation of an antimony target to express the yield of produced isotope:

$$\frac{m_{t}}{M}N_{av}\left(0.5726\int_{E_{i}^{t}}^{E_{max}}\sigma_{i}^{121}(E)\cdot\boldsymbol{\Phi}(E)\cdot dE + 0.4264\int_{E_{i}^{t}}^{E_{max}}\sigma_{i}^{123}(E)\cdot\boldsymbol{\Phi}(E)\cdot dE\right)$$

$$=\frac{N_{\gamma}\lambda}{\varepsilon\,p_{\gamma}e^{-\lambda\Delta t}\,(1-e^{-\lambda t_{irr}})(1-e^{-\lambda t_{m}})}$$
(1)

where m_t and M are the mass of the exposed target used in experiment and the atomic mass number, N_{av} is Avogadro number, E_t^i is the energy threshold for observed nuclear reaction and E_{max} is the maximal energy of photons, $\Phi(E)$ is flux of photons, N_{γ} is the number of detected gamma photons of chosen energy, λ is the decay constant, ε is absolute peak efficiency of the detector at the chosen energy, p_{γ} is the quantum yield of detected photons, Δt , t_{irr} and t_m are cooling, irradiation and measurement time, respectively.

For brevity, the above equation can be represented as:

$$\frac{m_t}{M} N_{av} \left(0.5726 \, R_i^{121} + 0.4264 \, R_i^{123} \, \right) = \frac{N_{\gamma} \, \lambda}{\varepsilon \, p_{\gamma} e^{-\lambda \Delta t} \, \left(1 - e^{-\lambda t_{irr}} \right) \left(1 - e^{-\lambda t_{m}} \right)} \tag{2}$$

Integrals denoted by symbol R are called saturation activities. A common way is to divide Equation (1) or Equation (2) by the term $\frac{m_i}{M}N_{av}$. In this way, the right-hand side of the equation yields the total saturation activity that can be determined from gamma spectroscopic measurements. In our case, it would be the sum of two saturation activities weighted by the abundances of isotopes 121 Sb and 123 Sb in the natural element.

Immediately after irradiation of the antimony target, several gamma spectra should be recorded, to identify short-living products of photonuclear reactions. It is very important to record gamma spectra of antimony target several days after irradiation, to get evidence about

long-living radionuclides. The next step would be to determine the intensities of the characteristic gamma lines in the spectrum, in order to determine the experimental values of the yields (or saturation activity) of the identified products based on the right side of Equation (1).

In this way, the output of all those photonuclear reactions that produce an unstable nucleus that emits gamma radiation of sufficiently high energy and intensity can be determined. There are several photonuclear reaction products whose yields cannot be determined from measured gamma spectra. Such is, for example, the isomer $^{119\mathrm{m}}\mathrm{Sn}$ reaching the ground state by the emission of low-energy gamma radiation of 23.87 keV, which could not be measured with the available detector. In this case, the yield of $^{119\mathrm{m}}\mathrm{Sn}$ can estimated computationally, as shown in the left side of Equation (1). For the purposes of this evaluation, it is necessary to have the energy differential cross sections $\sigma_i^{121}(E)$ and $\sigma_i^{123}(E)$ of the reaction that produces the observed nucleus, as well as the value of the photon flux $\Phi(E)$.

2.3. Ratio of 117mSb and 119mSb activities

The aim of this work is to check the possibility of producing ^{117m}Sb through photonuclear reactions. Based on Section 1.1, it can be expected that in the case of complete chemical separation of the tin fraction from the irradiated Sb target, the activity of ^{117m}Sn and the gamma line at 158.56 keV would remain. This certainly does not mean that ^{117m}Sn is the only active isotope of tin that can be expected in this experiment. During the exposure of the antimony target, ^{119}Sb is formed as a product of $^{121}Sb(\gamma,2n)$ and $^{123}Sb(\gamma,4n)$ reactions. The half-life of this antimony isotope is 38.19 h. It decays through an electron capture and populates the 23.87 keV excited state in ^{119}Sn . The gamma radiation emitted by the de-excitation of this state is not noticeable in the measured spectra due to the low efficiency of the available detector in the low-energy region. The ^{119}Sn nucleus has a metastable state of 89.53 keV, but it is not populated by the decay of ^{119}Sb .

There is a possibility that the creation of 119m Sn also occurs through 121 Sb(γ ,pn) and 123 Sb(γ ,p3n) reactions. Considering that the cross section for photonuclear reactions decreases very sharp with the number of emitted particles (Dietrich and Berman, 1988; Ermakov et al., 2010) it can be considered that the probability of creation of 119m Sn is higher than the probability of creation of 117m Sn.

The low energy of the photon radiation emitted by $^{119\text{m}}$ Sn did not provide the possibility to determine the yield of this isomer in the current experiment. The only possibility is to determine the activity ratio of the isotopes $^{117\text{m}}$ Sn and $^{119\text{m}}$ Sn with the help of theoretical estimates of the cross sections for the relevant nuclear reactions.

Equation (2) for the example of production ^{117m}Sn can be written in a slightly different form:

$$\frac{m_{t}}{M}N_{av}\left(1-e^{-\lambda_{117}t_{irr}}\right)\left(0.5726\,R_{\gamma,\mathrm{p3n}}^{121}+0.4264\,R_{\gamma,\mathrm{p5n}}^{123}\right) = \frac{N_{\gamma}\,\lambda_{117}}{\varepsilon p_{\gamma}e^{-\lambda_{117}\Delta t}(1-e^{-\lambda_{117}t_{m}})} \tag{3}$$

where the subscript of saturation activity R denotes the nuclear reaction producing the observed radionuclide. Both the left and right sides of Equation (3) give the activity of 117m Sn at the end of the irradiation. The left-hand side of Equation (3) provides a way to estimate the activity from known cross-section and photon flux values, while the right-hand side of Equation (3) allows the activity to be calculated using data obtained from the gamma spectrum.

An analogous equation can be written for the production of 119m Sn. The activity ratio of 117m Sn and 119m Sn can be represented as:

$$\frac{A_{119}}{A_{117}} = \frac{\lambda_{119}}{\lambda_{117}} \frac{0.5726 R_{\gamma,pn}^{121} + 0.4264 R_{\gamma,p3n}^{123}}{0.5726 R_{\gamma,p3n}^{121} + 0.4264 R_{\gamma,p5n}^{123}}$$
(4)

The above Equation (4) was written after the exponential function on the right-hand side of Equation (3) was developed into a series, discarding all but the linear terms. Considering that the sample irradiation time $t_{irr} = 30 \, m$ is significantly shorter than the half-life of the observed photonuclear reaction products (13.6 d and 293 d) second, the quadratic term is three orders of magnitude smaller than the linear one.

In order to obtain an estimate of the activity ratio, it is necessary to calculate the saturation integrals of the relevant nuclear reactions. For the bremsstrahlung production geometry used in this experiment, the photon flux is obtained by a GEANT4 simulation. Considering that it is necessary to determine the ratio of $^{119\rm m}{\rm Sb}$ and $^{117\rm m}{\rm Sn}$ activities, it is quite sufficient to know only the shape of the photon spectrum. The shape of the photon spectrum $\Phi(E)$ is obtained by using the GEANT4 software package [13], version v11.1.0, with standard G4 electromagnetic physics option selected. The simulation starts with creating 30·10⁶ of 60 MeV electrons in the beam, with a Gaussian spread in energy of 0.01 MeV. The photon spectrum is obtained at the place of irradiated sample based on the geometry used in this experiment.

There are no experimental values of the differential cross section for the observed nuclear reactions in EXFOR database, so the only possibility is to use theoretical estimates.

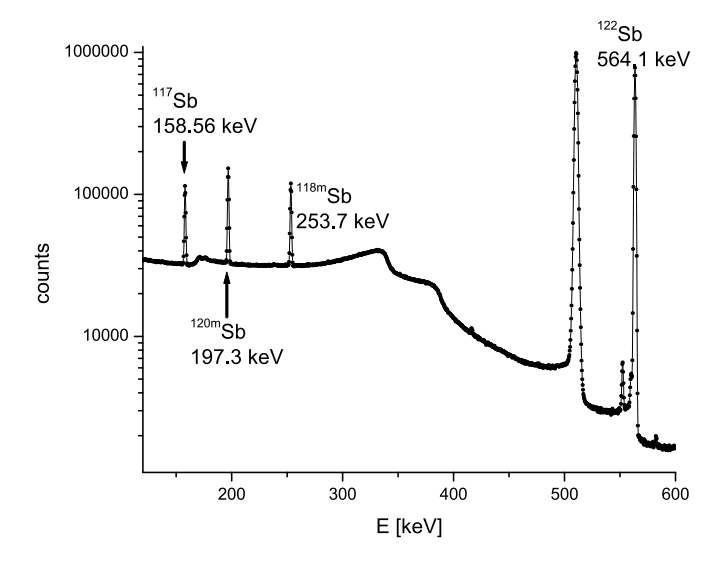
3. Measurements and results

A pure natural antimony target was exposed to a beam of brems-strahlung radiation with a maximum energy of 60 MeV. Only one endpoint energy was used in this experiment. The experiment was carried out using the linear electron accelerator LUE-75 located at A. Alikhanyn National Science Laboratory in Yerevan, Armenia. Accelerated electrons, after passing through a cylindrical collimator (length of 20 mm, diameter of 15 mm) strike a pure tungsten convertor. The thickness of the convertor was 2 mm. A 30 mm long aluminum cylinder was placed directly behind it. The function of the aluminum was to stop the electrons that penetrated the tungsten. At a distance of 60 mm from the tungsten plate, a disc-shaped antimony target (diameter of 1 cm and a mass of 0.5772 g) was placed. Duration of irradiation was $t_{irr}=1800\ s$. The current of accelerated electrons, monitored by Faraday cage was 1.2 μ A in average.

Exposed Sb disc was transferred to the room where the single vertical dipstick HPGe detector was located. Measurements were performed in geometry where Sb was placed 86 mm from the top of the detector. The spectrum used in this work was recorded for $t_m=53599~\rm s$, and cooling time was $\Delta t=1200~\rm s$. In the measured spectra, gamma lines from several Sb isotopes were identified, as well as several gamma lines of indium isotopes. Some relevant gamma lines used in further calculations are presented in Fig. 4.

The relative efficiency of the detector was determined using the ²⁰⁶Bi gamma lines. For the purposes of the experiment, simultaneously with the antimony target, a cylindrical bismuth sample of the same dimensions, weighing 1.1 g, was exposed in the photon beam, behind the Sb sample. Bismuth irradiation conditions are not overly significant since the only goal was to obtain measurable activity of the isotope ²⁰⁶Bi. The photonuclear reaction ²⁰⁹Bi(γ ,3n)²⁰⁶Bi gave sufficient activity to obtain a satisfactory number of very intense gamma lines in the spectrum recorded the next day for 24526 s. Nineteen gamma lines from the spectrum of ²⁰⁶Bi in the interval from 183.98 keV to 1878.65 keV were used to calculate the relative photo-peak efficiency of the HPGe detector for the used counting geometry. The relative efficiency curve was obtained by fitting a function that was a combination of an exponential and a third-order polynomial ($\varepsilon_{rel} = \exp(a + b \bullet E + c \bullet E^2 +$ $d \bullet E^3$)). With the ¹³⁷Cs calibration source, it was established that the absolute photopeak efficiency at the energy of 661.66 keV for the given geometry is 0.00147(1). This value was used to normalize the relative efficiency obtained with $^{206}\mathrm{Bi}.$

Three days (264960 s) after the first measurement, the second one was performed for a 65125 s. The time between the first and second measurements was long enough for $^{117}\mathrm{Sb},\,^{117}\mathrm{In}$ and $^{117m}\mathrm{In}$ to completely decay. In that case, all photons of energy 158.56 keV originate from the



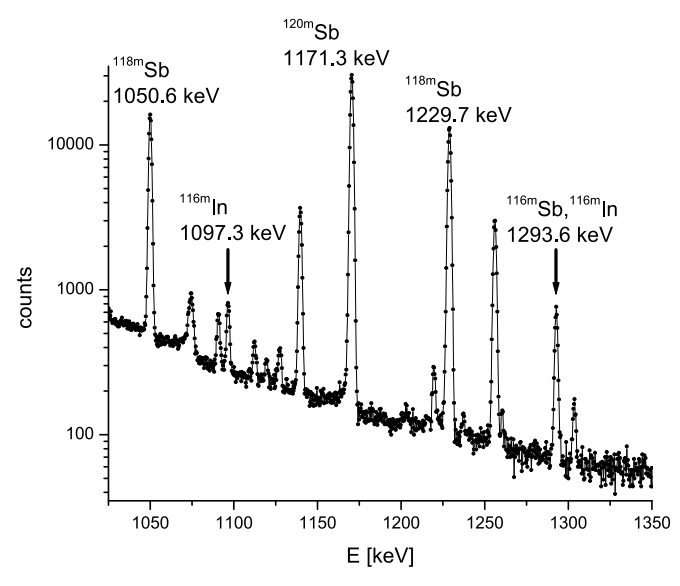


Fig. 4. Two segments of gamma spectra containing gamma lines used in calculations.

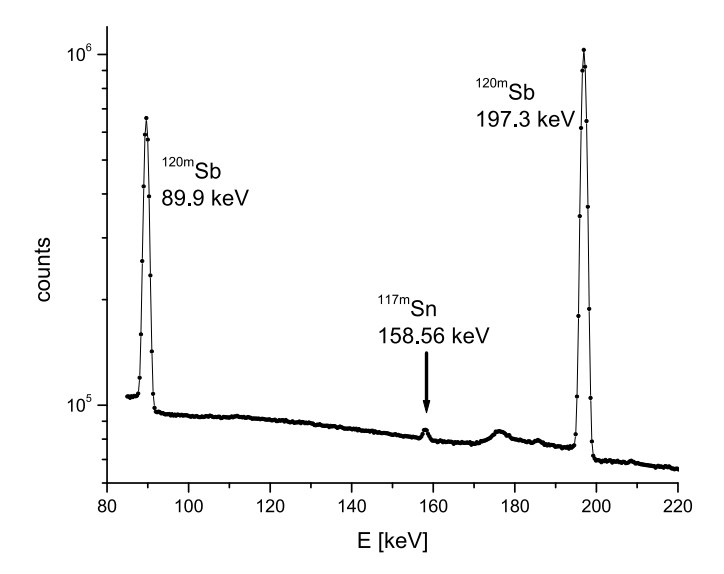


Fig. 5. Part of the gamma spectra recorded three days after irradiation of Sb target.

decay of 117m Sn only. Part of the spectra containing this line is depicted in Fig. 5.

The intensities of selected gamma lines were determined using the GENIE (Genie2000 Spectroscopy Software, 2004) software package. The yields of identified radionuclides were calculated as shown on the right side of Equation (1). Obtained results are depicted in Table 1. Uncertainties are given in parentheses. The main contribution to them is from the statistical uncertainty of the intensity of the observed gamma lines N_{γ} and from the uncertainty of the absolute detection efficiency ε . The exception is ¹¹⁷Sb, for which the gamma line intensity is determined by subtracting the estimated contribution of ^{117m}Sn, as explained later.

As could be expected, the highest yield among Sb isotopes has reaction products formed after the emission of the smallest number of neutrons. Table 1 shows that $^{122}\mathrm{Sb}$ and $^{120\mathrm{m}}\mathrm{Sb}$ have the highest yield. With the increasing number of emitted particles, the probability of a photonuclear reaction drops sharply, so the yield of lighter antimony isotopes is also lower.

The ^{116m}In yield was determined based on the obtained gamma line intensity of 1097.33 keV. Considering that both ^{116m}In and ^{116m}Sb populate the same excited states of ¹¹⁶Sn, 1293.56 keV gamma photons are emitted after the decay of both of these radionuclides. The yield of ^{116m}Sb was determined based on the intensity of the gamma line of 1293.56 keV, but the contribution of ^{116m}In was subtracted. Mentioned gamma lines can be seen in Fig. 4.

The yields of ¹¹⁷Sb and ^{117m}Sn were determined based on the intensity of the gamma line of 158.56 keV. In the first measurement, started 3 h and 20 min after the end of the irradiation, the largest contribution to this gamma line is from ¹¹⁷Sb. After three days, this radionuclide completely disappeared and all detected photons of this energy can be attributed to ^{117m}Sn. Based on the intensity of the gamma line of 158.56 keV from the second spectrum, it was determinate that count rate of ^{117m}Sn was 0.374 s⁻¹. The count rate of ^{117m}Sn three days earlier was calculated in order to assess the contribution of this tin isotope to the total intensity of the gamma line. It was obtained that the intensity of the gamma line of 158.56 keV came predominantly from the decay of ¹¹⁷Sb in the first spectrum. The contribution of ^{117m}Sn to the total intensity of the 158.56 keV gamma line is estimated at 0.7%, which is still an order of magnitude higher than its statistical uncertainty. Based on the intensity of the corrected 158.56 keV gamma line, the yield of ¹¹⁷Sb shown in Table 1 was determined.

The ratio of 119m Sn and 117m Sn activities was determined as shown in Equation (4). It is not necessary to know the absolute value of the photon flux. Only the shape of the photon spectrum obtained by GEANT4 simulation for a given geometry of bremsstrahlung production is necessary.

Cross sections for observed reactions were estimated using the

Table 1Yields and sum of saturation activities of identified products of photonuclear reactions.

	Half- life	Ways of production	Yield ⋅10 ⁶ [s ⁻¹]	Sat. Act. $\cdot 10^{-15} [s^{-1}]$	Activity10 ⁴ [s ⁻¹]
¹²² Sb	2.70 d	$^{123}{ m Sb}(\gamma, n) \\ + ^{121}{ m Sb}(n, \gamma))$	75.9(11)	26.6(5)	38.5(5)
^{120m} Sb	5.76 d	$^{121}{ m Sb}(\gamma, n) + ^{123}{ m Sb}(\gamma, 3n)$	6.05(9)	2.12(4)	1.53(2)
^{118m} Sb	5.00 h	121 Sb(γ ,3n) + 123 Sb(γ ,5n)	0.456(9)	0.160(3)	3.55(7)
¹¹⁷ Sb	2.80 h	121 Sb(γ ,4n) + 123 Sb(γ ,6n)	1.26(6)	0.44(2)	14.7(7)
^{116m} Sb	60.3 min	121 Sb(γ ,5n) + 123 Sb(γ ,7n)	0.026(1)	0.0091(4)	0.75(3)
^{116m} In	54.4 min	$^{121}\mathrm{Sb}(\gamma,\alpha\mathrm{n})$	0.0027 (2)	0.00095(6)	0.14(1)
^{117m} Sn	13.60 d	$^{121}{ m Sb}(\gamma, { m p3n}) + \ ^{123}{ m Sb}(\gamma, { m p5n})$	0.092(4)	0.0322(14)	0.0100(5)

TALYS 1.96/2.0 code (Koning et al., 2023). It has been shown (Gyürky et al., 2014) in the case of nuclear reactions in which isomers are created that TALYS estimates can differ from experimental results. Some scatter in the values of physical quantities determined using TALYS estimates can also be expected (Jovančević et al., 2024). But for a first estimate of the activity ratio A_{119}/A_{117} given in Equation (4), until the result of experimental measurements is obtained, the prediction based on TALYS can serve well. It could be expected that the choice of the strength function model has an impact on the estimation of the cross section, but this analysis is beyond the scope of this paper. It was decided to use SMLO model for a strength function. On the example of the creation of ^{113m}In in photonuclear reactions, it was shown that this model gives good results (Versteegen et al., 2016). Six different models of level density were employed in calculations. Cross sections were calculated using phenomenological ((1) The Fermi Gas Model + Constant Temperature Model, (2) The Back-shifted Fermi gas Model, (3) The Generalized Superfluid Model) and microscopic ((4) Skyrme-Hartree-Fock-Bogoluybov, (5) Gogny-Hartree-Fock-Bogoluybov and (6) Temperature-dependent Gogny-Hartree-Fock-Bogoluybov models) of level density. Default OMP was used in calculations. Different models for the densities of states give estimates of cross sections that can differ significantly from each other. In Figs. 6 and 7 are depicted the energy differential cross sections for the two reactions at \$\bar{1}21\$Sb which give ^{119m}Sn and ^{117m}Sn as a result.

The estimation of the activity ratio of 119m Sn and 117m Sn at the end of the irradiation was made using all six cross sections obtained by the TALYS code. The smallest value of 0.124 is obtained when the model of Fermi Gas + Constant Temperature Model is chosen for the density of states, while The Generalized Superfluid Model gives the highest ratio estimate of 0.268.

4. Discussion

Based on the results shown in Tables 1, it can be seen that $^{121}{\rm Sb}(\gamma, \rm p3n)$ and $^{123}{\rm Sb}(\gamma, \rm p5n)$ nuclear reactions, give a low yield of $^{117m}{\rm Sn}$ comparing to the activities of the produced antimony isotopes. The right side of Equation (3) is used to calculate the activities of radionuclides identified in the measured spectra. Obtained results are presented in Table 1, last column. During the irradiation of the antimony target, an activity of $^{117m}{\rm Sn}$ of about 100(5) Bq was obtained. This is three orders of magnitude less than the activity of Sb isotopes that have been identified. Considering that the formation of $^{117m}{\rm Sn}$ occurs with the emission

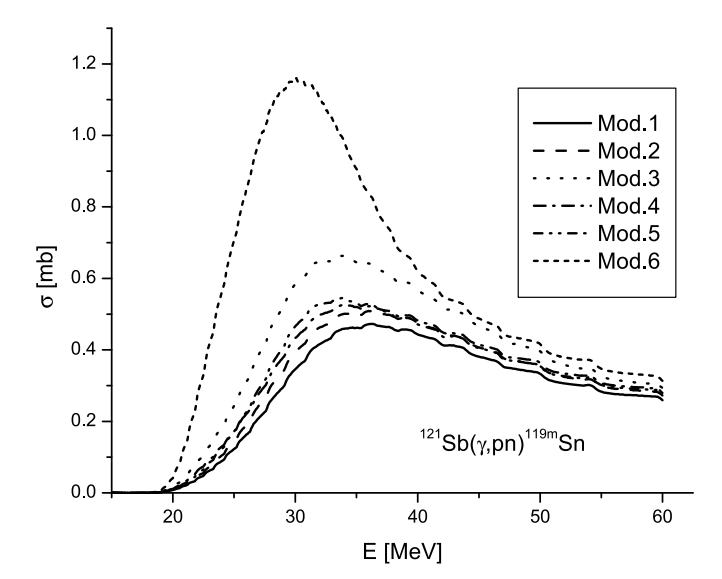


Fig. 6. Cross sections for $^{121}\text{Sb}(\gamma,pn)^{119m}\text{Sn}$ reaction estimated using TALYS code.

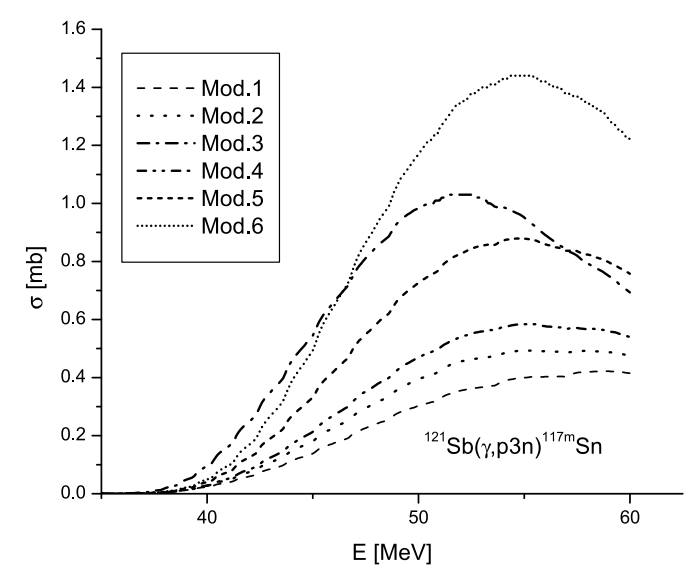


Fig. 7. Cross sections for $^{121}Sb(\gamma,p3n)^{117m}Sn$ reactions estimated using TALYS code.

of charged particles, such a low level of activity could be expected.

The method currently considered the most promising is the production of 117mSn by interactions of accelerated alpha particles with cadmium (natural Cd or ¹¹⁶Cd enriched) or indium targets (Maslov et al., 2011; Ditrói et al., 2016; Duchemin et al., 2016; Aikawa et al., 2018; Aslam et al., 2018), using. Since the range of alpha particles in these materials is very small, order of microns, the most common way to show the output of reaction is through the integral yield or Thick Target production Yield (TTY), as it is called by some authors. This quantity is expressed in units of kBq/µAh. A very complete review of theoretical predictions as well as known experimental results of 117mSn yields can be found in refs. (Rebeles et al., 2008; Ditrói et al., 2016; Aslam et al., 2018). The experimental results of ^{117m}Sn yields (Maslov et al., 2011) of 37.5 kBq/μAh and 410 kBq/μAh obtained on natural and enriched ¹¹⁶Cd targets, respectively, can be added to this review. The mechanism of photon interaction with metal targets is significantly different and they take place throughout the entire depth of the target and reaction yield depends on the target mass and thickness. However, from the estimated activity of ^{117m}Sn, a numerical value can be obtained that could somehow be equivalent to TTY, at least for the geometry used in experiment. With the experimental parameters listed in Section 2, it can be estimated that the production of ^{117m}Sn in photonuclear reaction is 0.174(8) $kBq/(\mu Ah)$.

Such an assessment could be expected taking into consideration the large difference in the values of the cross section for $^{116}\text{Cd}(\alpha,3n)^{117m}\text{Sn}$ and $^{121}\text{Sb}(\gamma,p3n)^{117m}\text{Sn}$ reactions. The maximum cross-section for the $^{116}\text{Cd}(\alpha,3n)^{117m}\text{Sn}$ reaction is about 1 b in the region of 35 MeV (Montgomery and Porile, 1969; Rebeles et al., 2008; Ditrói et al., 2016; Duchemin et al., 2016). From Fig. 6 it can be seen that the theory for the $^{121}\text{Sb}(\gamma,p3n)^{117m}\text{Sn}$ reaction predicts a cross section of less than 1 mb.

The experiment showed that with an antimony target weighing slightly more than half a gram, in a photon beam produced with an electron current of $1.2\,\mu\text{A}$ during 30 min of exposure, a very low activity of ^{117m}Sn is obtained, the order of magnitude being 0.1 kBq. For the purposes of medical application of this radionuclide, significantly greater activities are required. Standard therapy dose of ^{117m}Sn is usually 1 GBq for 70 kg patient (Srivastava et al., 1998). More ^{117m}Sn activity can be obtained by increasing: target mass, irradiation time and electron current. The obtained activity depends linearly on the mass and electron current and in this case also on the irradiation time, since the half-life of ^{117m}Sn is 13.6 days. It can be expected that an increase in the maximum bremsstrahlung energy can give a growth of the obtained

activity of the product of the photonuclear reaction as well. In any case, there is room for increasing the yield of ^{117m}Sn, which still needs to be investigated.

According to the estimates based on Equation (4), it can be expected that the activity of the long-lived $^{119m} Sn$ will be even lower and that in the bremsstrahlung beam of maximum energy of 60 MeV it will be up to 26% of the activity of $^{117m} Sb$. This ratio can be expected to be smaller at higher bremsstrahlung energies. It can be seen in Fig. 7, that some significant cross section component at energies higher than 60 MeV for the reaction $(\gamma,p3n)$ exist. Considering that the dominant way of production of $^{117m} Sn$ is through this reaction, a higher yield of this radionuclide can be expected at higher energies.

If there is an effective method to chemically separate the tin fraction from the antimony target, the activity of the 117m Sn and 119m Sn isotopes would be present in the obtained material only. This can be a very convenient way to produce two radionuclides of high specific activity (activity per unit mass), since a source of radiation without a carrier would be obtained. In photonuclear reactions on natural antimony, several isotopes of Sb are created. All of them, after decay give Sn nuclei as product. In this way, stable isotopes of tin with two active isomers 119m Sn and 117m Sn are created.

The mass of one of the isotopes of tin accumulated over time t by the decay of an unstable isotope of antimony created in a nuclear reaction could be expressed as:

$$m = \frac{M}{N_{av}} \frac{A_0}{\lambda} \left(1 - e^{-\lambda t} \right) \tag{5}$$

where A_0 is activity of observed Sb isotope at the end of irradiation. This activity can be calculated using right side of Equation (3).

The measured activities of ¹²²Sb, ^{120m}Sb, ^{118m}Sb, ¹¹⁷Sb and ^{116m}Sb were used for the approximate estimation of the amount of tin that is created from the decay of Sb isotopes. This estimation do not include all the ways of creating tin from the decay of antimony isotopes, but only those whose activity could be determined based on the measured gamma spectra. However, it can be enough to estimate the order of magnitude of the mass of tin. Relevant gamma lines in registered spectra can be seen in Fig. 4.

In a completely arbitrarily chosen case where the decay of the created antimony isotopes lasted 24 h after irradiation, it was found that the total mass of tin that was created by decay of $^{122}{\rm Sb},\,^{120m}{\rm Sb},\,^{118m}{\rm Sb},\,^{117}{\rm Sb}$ and $^{116m}{\rm Sb}$ is $8.1(4) \bullet 10^{-12}$ g. This means that by photonuclear reactions on natural antimony, very high specific activities of $^{117m}{\rm Sn}$ can be obtained, order of magnitude up to 10^7 MBq/g.

5. Conclusions

In the experiment described in this paper, photoactivation of a target made of natural antimony was performed in a bremsstralung beam with a maximum energy of 60 MeV, followed by gamma spectrometric measurements. As could be expected, the highest activity in the activated target was registered by neutron-deficient isotopes of antimony, obtained in (γ,xn) reactions.

These isotopes of antimony decay mainly through electron capture and give stable isotopes of tin as a product. The only tin activity detected in the experiment came from $^{117m}\mathrm{Sn}$. In the experiment $^{119m}\mathrm{Sn}$ was produced also, but the available detector could not detect it due to low-energy of emitted gamma radiation.

In the gamma spectroscopic measurement, which was performed after a few days, when all sources of interference disappeared, the activity of $^{117m}\mathrm{Sn}$, which was created in the irradiation of the target, was determined. In the described experiment, the yield of $^{117m}\mathrm{Sn}$ that was obtained (0.174(8) kBq/(µAh)) is about 2500 times lower than the yield of the same isotope obtained by $(\alpha,3n)$ reaction on enriched $^{116}\mathrm{Cd}$.

Such a large difference in yield can be explained by the fact that the cross section for the $^{116}\text{Cd}(\alpha,3n)^{117m}\text{Sn}$ reaction is significantly higher

than the cross sections of $^{123}\text{Sb}(\gamma,p5n)^{117m}\text{Sn}$ and $^{121}\text{Sb}(\gamma,p3n)^{117m}\text{Sn}$ of photonuclear reactions. However, this still does not mean that photonuclear reactions on antimony should be left out of consideration as a possible commercial source of ^{117m}Sn . There is still significant room to increase the yield of these photonuclear reactions. The yield can be significantly increased in photon accelerator beams that have higher electron currents.

In addition to ^{117m}Sn, some amount of ^{119m}Sn is also obtained in photonuclear reactions. Some of its characteristics, such as a large number of conversion electrons can contribute to the therapeutic effect. It was estimated that in the bremsstrahlung photon beam with a maximum energy of 60 MeV, the activity of ^{119m}Sn is obtained, which would less than 27% of the activity of ^{117m}Sn.

CRediT authorship contribution statement

M. Krmar: Writing – original draft, Supervision, Conceptualization. N. Jovančević: Investigation. Ž. Medić: Software, Formal analysis. D. Maletić: Software, Formal analysis. Yu Teterev: Project administration, Investigation. S. Mitrofanov: Resources, Funding acquisition. K.D. Timoshenko: Visualization, Data curation. S.I. Alexeev: Resources, Methodology. H. Marukyan: Investigation, Formal analysis. I. Kerobyan: Writing – original draft, Software, Investigation. R. Avetisyan: Resources, Investigation, Formal analysis. R. Dallakyan: Investigation. A. Hakobyan: Methodology. L. Vahradyan: Methodology. H. Mkrtchyan: Supervision, Investigation. A. Petrosyan: Resources, Data curation. H. Torosyan: Resources, Project administration, Resources, Project administration.

Declaration of competing interest

The authors declare that they have no known competing financial interests or personal relationships that could have appeared to influence the work reported in this paper.

Data availability

Data will be made available on request.

Acknowledgments

Two of authors (N. Jovancevic and M. Krmar) acknowledge financial support of the Provincial Secretariat for Higher Education and Scientific Research of Autonomous Province of Vojvodina (Grant No. 142-451-3139/2022-01/2).

References

Aikawa, M., Saito, M., Ukon, N., Komori, Y., Haba, H., 2018. Activation cross sections of alpha-induced reactions on natIn for 117mSn production. Nucl. Instrum. Methods Phys. Res. B 426, 18–21. https://doi.org/10.1016/j.nimb.2018.04.023.

Aksenov, V.L., Dikansky, N.A., Lomidze, V.L., Novokhatsky, A.V., Popov, YuP., Rudenko, V.T., Skrinsky, A.N., Furman, W.I., 1992. Proposal for the Construction of the New Intense Resonance Neutron Source (IREN), Communication of the JINR, E3-92-110. Dubna.

Aslam, M.N., Zubia, K., Qaim, S.M., 2018. Nuclear model analysis of excitation functions of α -particle induced reactions on in and Cd up to 60 MeV with relevance to the production of high specific activity 117m Sn. Appl. Radiat. Isot. 132, 181–188. https://doi.org/10.1016/j.apradiso.2017.12.002.

Blachot, J., 2002. Nuclear data sheets for A = 117. Nucl. Data Sheets 95, 679–836. https://doi.org/10.1006/ndsh.2002.0007.

Chu, S.Y.F., Ekström, L.P., Firestone, R.B., 1999. The Lund/LBNL Nuclear Data Search. http://nucleardata.nuclear.lu.se/toi/index.asp.

Dietrich, S.S., Berman, B.L., 1988. Atlas of photoneutron cross sections obtained with monoenergetic photons. Atomic Data Nucl. Data Tables 38 (1988), 199.

Ditrói, F., Takács, S., Haba, H., Komori, Y., Aikawa, M., 2016. Cross section measurement of alpha particle induced nuclear reactions on natural cadmium up to 52 MeV. Appl. Radiat. Isot. 118, 266–276. https://doi.org/10.1016/j.nimb.2016.08.016.
Duchemin, C., Essayan, M., Guertin, A., Haddad, F., Miche, I N., Métivier, V., 2016. How

Duchemin, C., Essayan, M., Guertin, A., Haddad, F., Miche, I N., Métivier, V., 2016. How to produce high specific activity tin-117 m using alpha particle beam. Appl. Radiat. Isot. 115, 113–124. https://doi.org/10.1016/j.apradiso.2016.06.016.

- Ermakov, A.N., Ishkhanov, B.S., Kapitonov, I.M., Makarenko, I.V., Orlin, V.N., 2010. Photodisintegration of heavy nuclei in the energy region above the Giant Dipole Resonance. Phys. Atom. Nucl. 73 (5), 737–745. https://doi.org/10.1134/
- Ermolaev, S.V., Zhuikov, B.L., Kokhanyuk, V.M., Abramov, A.A., Togaeva, N.R., Khamianov, S.V., Srivastava, S.C., 2009. Production of no-carrier-added ^{117m}Sn from proton irradiated antimony. J. Radioanal. Nucl. Chem. 280 (2), 319–324. https://doi.org/10.1007/s10967-009-0520-x.
- Experimental Nuclear Reaction Data (EXFOR) https://www-nds.iaea.org/exfor/. Firestone, R.B., 1996. Table of Isotopes. CD ROM Edition.
- Genie2000 Spectroscopy Software, 2004. Canberra Industries. Inc.
- Gyürky, Gy, Vakulenko, M., Fülöp, Zs, Halász, Y., Kiss, G.G., Somorjai, E., Szücs, T., 2014. Cross section and reaction rate of ⁹²Mo(p,γ)⁹³Tc determined from thick target yield measurements. T. Nucl. Phys. 922, 112–1125. https://doi.org/10.1016/j. nuclphysa.2013.12.003.
- IAEA radioisotopes and radiofarmaceuticals reports No.4, 2021. Alternative Radionuclide Production with a Cyclotron. IAEA, Viena, 978-92-0-103121-1.
- Inagaki, M., Sekimoto, S., Tanaka, W., Tadokoro, T., Ueno, Y., Kani, Y., Ohtsuki, T., 2019. Production of ⁴⁷Sc, ⁶⁷Cu, ⁶⁸Ga, ¹⁰⁵Rh, ¹⁷⁷Lu, and ¹⁸⁸Re using electron linear accelerator. J. Radioanal. Nucl. Chem. 322, 1703–1709. https://doi.org/10.1006/j.ci.010.07.010.06.004.g.
- Jovančević, N., Knežević, D., Krmar, M., Maletić, D., Zhemchugov, A., Milaković, M., 2024. Determination of the bremsstrahlung spectra by unfolding technique based on 209Bi(γ, xn) reactions. Radiat. Phys. Chem. 215, 111330. https://doi.org/10.1016/j. radphyschem.2023.111330.
- Kazakov, A.G., Ekatova, T.Y., Babenya, J.S., 2021. Photonuclear production of medical radiometals: a review of experimental studies. J. Radioanal. Nucl. Chem. 328, 493–505. https://doi.org/10.1007/s10967-021-07683-2.
- Koning, A., Hilaire, S., Goriely, S., 2023. TALYS: modeling of nuclear reactions. The European Physical Journal A 59 (2023), 131. https://doi.org/10.1140/epja/s10050-023-01034-3.
- Krmar, M., Ganezer, K., Pantelić, G., Krstonošić, P., 2004. Endpoint energy of linear medical accelerators. Nucl. Instrum. Methods Phys. Res. 532 (2004), 533–537. https://doi.org/10.1016/j.nima.2004.05.123.
- Lewington, V.J., 2005. Bone-seeking radionuclides for therapy. J. Nucl. Med. 46 (No. 1), 38S-47S. Suppl.
- Maslov, O.D., Starodub, G.Ya, Vostokin, G.K., Gustova, M.V., Dimitriev, S.N., Shvetsov, V.N., Szucs, Z., Jansen, D., Zeevaart, J.R., 2011. Production of ^{117m}Sn with

- high specific activity by cyclotron. Appl. Radiat. Isot. 69, 965–968. https://doi.org/10.1016/j.apradiso.2011.02.031.
- Montgomery, D.M., Porile, N.T., 1969. Reactions of ¹¹⁶Cd with intermediate energy ³He and ⁴He ions. Nucl. Phys. 130, 65–76.
- Pietralla, N., Isaak, J., Wernerc, V., 2019. Photonuclear reactions: achievements and perspectives. Eur. Phys. J. A 55, 237. https://doi.org/10.1140/epja/i2019-12857-4
- Qaim, S.M., 2017. Nuclear data for production and medical application of radionuclides: present status and future needs. Nucl. Med. Biol. 44, 31–59. https://doi.org/ 10.1016/j.nucmedbio.2016.08.016.
- Rebeles, R.A., Hermanne, A., Van den Winkel, P., Tárkányi, F., Takács, S., Daraban, L., 2008. Alpha induced reactions on 114Cd and 116Cd: an experimental study of excitation functions. Nucl. Instrum. Methods B 266 (21), 4731–4737. https://doi. org/10.1016/j.nimb.2008.07.013.
- Srivastava, S.C., H, L., Krishnamurthy, G.T., I Zanzi, I., Silberstein, E.B., Meinken, G., Mausner, L.F., Swailem, F., D'Alessandro, T., Cabahug, C.J., Lau, Y., Park, T., Madajewicz, S., 1998. Treatment of metastatic bone pain with tin-117m Stannic diethylenetriaminepentaacetic acid: a phase I/II clinical study. Clin. Cancer Res. 4 (1), 61–68. Jan.
- Starovoitova, V.N., Cole, P.L., Grimm, T.L., 2015. Accelerator-based photoproduction of promising beta-emitters 67Cu and 47Sc. J. Radioanal. Nucl. Chem. 305, 127–132. https://doi.org/10.1007/s10967-015-4039-z.
- Stevenson, N.R., George, G.St, Simón, J., Srivastava, S.C., Mueller, D.W., Gonzales, G.R., Rogers, J.A., Frank, R.K., Horn, I.M., 2015. Methods of producing high specific activity Sn-117m with commercial cyclotrons. Journal of Radioanalyitical Nuclear Chemistry 305, 99–108. https://doi.org/10.1007/s10967-015-4031-7.
- Symochko, D.M., Browne, E., Tuli, J.K., 2009. Nuclear data sheets for A=119. Nucl. Data Sheets 110, 2945–3105. https://doi.org/10.1016/j.nds.2009.10.003.
- Versteegen, M., Denis-Petit, D., Méot, V., Bonne, t T., Come, t M., Gobe, t F., Hannachi, F., Tarisien, M., Morel, P., Martini, M., Péru, S., 2016. Low-energy modification of the γ strength function of the odd-even nucleus 115In. Phys. Rev. C 94, 044325. https://doi.org/10.1103/PhysRevC.94.044325.
- XCOM, 2010. Photon Cross Section Database. https://physics.nist.gov/PhysRefData/X com/html/xcom1.html.
- Zilges, A., Balabanski, D.L., Isaak, J., Pietralla, N., 2022. Photonuclear reactions from basic research to applications. Prog. Part. Nucl. Phys. 122, 103903 https://doi.org/ 10.1016/j.ppnp.2021.103903.

STRUCTURE-PHASE STATUS OF THE HIGH-ENTROPY AININDTICO ALLOY

Y. A. Abzaev, ¹ Ž. Medić, ^{2,3} M. Koptsev, ² R. S. Laptev, ² A. M. Lider, ² and A. D. Lomygin, ² and A. A. Klopotov ¹

UDC 538.9, 669.9-127

Results of investigations of the structural state of the AlNiNbTiCo high-entropy alloy (HEA) obtained by mechanical synthesis of pure Al, Ti, Ni, Co, and Nb metals for 30, 40, and 50 min are presented. It is shown that the AlNiNbTiCo HEA belongs to stable structures near the melting temperature. By the method of inverse convex hulls (InveseHubWeb), the temperature interval of structure stability equal to $\Delta T = 1578-2935$ K has been found, and the lattice is created by predicting the structures in the USPEX code. The amorphous AlNiNbTiCo HEA structural state is determined by the simple AlNiNbTiCo-3 cubic lattice. It is shown that the AlNiNbTiCo-3 lattice dominates in the AlNiNbTiCo HEA synthesized for 30, 40, and 50 min.

Keywords: AlNiNbTiCo alloy, high-entropy alloys, X-ray diffraction techniques, mechanical alloying.

INTRODUCTION

Significant centrifugal forces in planetary ball mills stimulate fine and ultra-fine grinding of hard and superhard materials [1]. Under conditions of high local gradients of stresses and temperatures in high-entropy alloys of equiatomic and close-to-equiatomic compositions, new materials are formed by mechanochemical activation. The planetary ball mill method is promising here, because it allows synthesizing alloys with high melting points. The new class of high-entropy alloys (HEAs), in contrast to alloyed alloys based on iron, titanium, aluminum, etc. is characterized by high configurational entropy, the contribution of which to the solution stabilization is significantly higher. The characteristic HEA features include high entropy of the mixture, low atomic diffusion, lattice distortions, as well as formation of simple FCC, BCC, and HCP lattice structures [1, 2]. In particular, interest in the HEAs is also connected with their exceptional strength characteristics at high temperatures [3], ductility, impact toughness at cryogenic temperatures, combination of strength and ductility [4], and their application in the fields of hydrogen storage [2] and membrane hydrogen separation [3].

Fundamental studies of the HEAs have significantly expanded the list of single-phase high-entropy materials [6–8]. In multielement HEAs of 2nd generation, single-phase solid solutions based on simple cubic lattices (SCLs) are found both in crystalline and amorphous states [4, 5, 9–15]. In the latter case, as a rule, the complete structural information on the SCLs is unknown. It seems relevant to study the structure of the 5-element AlNiNbTiCo HEA – an equimolar (equiatomic) elemental composition [8, 9] in which single-phase solid solutions of amorphous type can be synthesized by mechanical stirring. Prediction of stable SCLs of the AlNiNbTiCo alloy is based on critical indices and InverseHubWeb methods [11] as well as on evolutionary prediction using the USPEX code [17, 18]. Detailed analysis of the content of amorphous-type SCLs in the AlNiNbTiCo HEA shwed that it is a function of the synthesis time in the ball mill.

The aim of this work is to study the structural state and stability of the AlNiNbTiCo alloy obtained by mechanical stirring in a ball mill for 30, 40 and 50 min, to determine a type of stable single-phase equiatomic state

¹Tomsk State University of Architecture and Building, Tomsk, Russia, e-mail: abzaev@tsuab.ru; ²Tomsk Polytechnic University, Department of Experimental Physics, Tomsk, Russia, e-mail: mok13@tpu.ru; laptevrs@tpu.ru; lider@tpu.ru; ³Institute of Physics in Belgrade, Belgrade, Serbia, e-mail: medic3@tpu.ru. Original article submitted November 24, 2023.

based on a set of Yum-Roseri critical indices, energy and entropy of mixing of binary alloys near the melting point within the framework of the Miedema model, as well as the mixing entropy of the 5-element AlNiNbTiCo composition, to predict the stable SCLs of the AlNiNbTiCo alloy by the evolutionary method, to estimate the stability temperature intervals using the InveseHubWeb code, and to determine the content of the equiatomic SCLs of semi-amorphous type based on calculations of the contributions of theoretical intensities to experimental diffraction patterns of the AlNiNbTiCo alloys synthesized for 30, 40, and 50 min.

MATERIALS AND RESEARCH METHODS

The synthesized AlNiNbTiCo alloy was chosen as the object of our study. Mechanical synthesis of AlNiNbTiCo alloy was carried out in a planetary mill AGO-2. Metal Al, Ti, Ni, Co, and Nb powders with purity of 99.5% and sizes from 10 to 70 μ m were mixed in equimolar ratio. The mass of the powders was 7 g. The mass ratio of grinding balls to powder was 10: 1. The powder and balls were loaded into a glove box in an argon environment. The drum rotational speed was 1260 rpm. To prevent overheating of the drums, grinding was stopped for 30 s every 2 min. Also, drums were water cooled during the grinding process. Grinding lasted 30, 40, and 50 min. The X-ray diffraction of the AlNiNbTiCo alloy was studied using a Shimadzu 7000 diffractometer with the tube having a copper anode in $K\alpha$ radiation according to the Bragg–Bretano scheme with a step of 0.0143° and exposure time per point of 0.5 s at anges in the range of 10° – 90° . The X-ray tube voltage was 40 kV, and the beam current was 30 mA.

Prediction of the stable composition of the AlNiNbTiCo HEAs was realized based on a set of critical Yum-Roseri indices [8-15]. The contributions of the following group of the paramaters to the free energy near the melting point of the binary alloys was considered in this work: lattice distortion δ , Pauling electronegativity χ , enthalpy H_{mix} , entropy S_{mix} , and valence electron concentration. The enthalpy and entropy of the mixture were found using the semiempirical Miedema method [15]. The critical indices allowed us to evaluate the stability as well as the class of the AlNiNbTiCo HEAs. In the next step, the evolutionary USPEX method was used to predict the lattices with complete structural information [17, 18]. According to the USPEX method, the enthalpy of lattices of fixed equiatomic composition of the AlNiNbTiCo alloy is considered. The fraction of generations generated from random structures and due to heredity were 0.3 and 0.5, respectively, and 0.2 from mutations. The fraction of the current generation that was used to generate the next generation was 0.6. In each generation, a population of 30 atoms was considered, the initial size of which was also equal to 30 atoms. Calculations were performed with 6 optimization steps using the VASP code. The lattice energy was calculated within the framework of the electron density functional in the gradient pseudopotential of the electron density in the generalized gradient approximation (GGA). The total lattice energies were determined at 0 K. The details of the code are given in [19, 20]. The orbitals of electronic states, the distribution of the one-electron density, and the ground state energy were calculated in a self-consistent manner. The wave functions of the valence electrons of phase atoms were analyzed in the plane wave basis with a kinetic energy cutoff radius of 330 eV. In this case, the total energy convergence was $\sim 0.5 \cdot 10^{-6}$ eV/atom.

In the InverseHubWeb method, the results of calculations of the temperature interval diagrams of the stability of single HEAs are proposed within a graphical representation. The HEA convex shell diagrams were constructed on the basis of benchmarks calculated in the Material Project [16] with (intermetallic) reactants in the temperature intervals of existence of stable and metastable alloys. In the InverseHubWeb method, *ab intio* estimations of the free energy of the lattices are made based on the cluster method used in [11] for the HEA.

The identification of the structural state and quantitative phase content (QPC) of the AlNiNbTiCo alloy on the basis of synthesized lattices (standards) was performed using reflex [19, 20]. In the Rietveld method, the relative difference between the integral (model) and experimental diffraction patterns is minimized by a nonlinear method depending on the variation of instrumental, profile, and structural parameters of the full-profile intensities. The maximum possible number of the parameters of reference gratings was varied. The background radiation on diffraction patterns was approximated by a polynomial of degree 20. The calculated X-ray intensity of the model phases in the work were evaluated in a self-consistent manner.

RESULTS AND DISCUSSIONS

In the process of mechanical synthesis of the AlNiNbTiCo HEAs, the formation of the stable single-phase material was observed. The identification of the stable HEAs was realized using the Yum-Roseri criteria, which include, in particular, distortion [12–15]

$$\delta = 100 \cdot \sqrt{\sum_{i=1}^{n} c_i} \left(1 - \frac{r_i}{\sum_{i=1}^{n} c_i r_i} \right)^2 , \tag{1}$$

where r_i is the radius of the atomic element, the difference of which should not exceed 8.5%. The criterion of HEA electronegativity is defined by the expression [12–15]

$$\Delta \chi_{mix} = \sum_{i=1}^{n} c_i \left(1 - \frac{\chi_i}{\sum_{i=1}^{n} c_i \chi_i} \right), \tag{2}$$

where χ_i is the electronegativity of the *i*th atomic element. Yeh [13, 14] also proposed the classification of stable highentropy alloys based on the entropy of the mixture:

$$S_{mix} = R \sum c_i \ln c_i \,, \tag{3}$$

where R is the universal gas constant, and c_i is the atomic concentration of elements. From the formula it follows that in the case of compounds of equiatomic composition, the total contribution to the entropy should be the largest. The enthalpy H_{mix} of the mixture is determined by the expression

$$H_{mix} = \sum_{i \neq j}^{n} 4c_i c_j \Delta H_{mix}^{AB} , \qquad (4)$$

where H_{mix}^{AB} is the enthalpy of the binary alloys near the melting point the AB elements of which are parts of the HEA compound. In the case of the AlNiNbTiCo alloy, it was necessary to use the following binary alloys with cubic lattice to estimate the enthalpy H_{mix} : AlNi, AlNb, AlTi, AlCo, NiNb, NiTi, NiCo, NbTi, NbCo, and TiCo. When calculating the enthalpy H_{mix} of the mixture, it was also necessary to know the melting point of the binary alloys determined by the formula

$$T_{molt} = \sum c_i T_i \,, \tag{5}$$

where T_i is the melting point of the pure elements. For the pure elements Al, Ni, Nb, Ti, and Co, the temperatures are $T_{melt} = 933.47$, 1728, 2750, 1941, and 1768 K, respectively [10–12]. The found effective melting temperatures of the binary alloys are summarized in Table 1. Based on the obtained T_{melt} values and the known elements, the enthalpy of the mixture as well as the entropic contribution to the free energy of the binary alloys were determined within the framework of the Miedema model [15]. The calculated results are summarized in Table 1. The effective enthalpy of the mixture found by formula (4) was $H_{mix} = -41.27$ kJ/mol, and the entropic contribution was $S_{mix} = -23.78$ kJ/mol. The results obtained indicate that the entropic contribution of the binary alloys accounts for a high fraction of the free energy. The critical indices used to evaluate the stability of the AlNiNbTiCo HEA are based on the enthalpy of the binary alloys [10–15] as well as the entropy of the 5-element composition given by formula (4). The entropy of the

TABLE 1. Effective Liquid Phase Temperature and Thermodynamic Properties of Binary Alloys

	AlNi	AlNb	AlTi	AlCo	NiNb	NiTi	NiCo	NbTi	NbCo	TiCo
T_{melt} , K	1330.7	1841.7	1437.2	1350.7	2239	1834.5	1748	2345.5	2259	1854.5
ΔH , kJ/mol	-4.44	-6.25	-7.60	-4.83	-3.61	-4.29	-1.65	-1.85	-3.11	-3.66
ΔS, kJ/mol	-3.21	-4.55	-6.28	-4.55	-1.54	-2.6	1.61	0.32	-1.02	-1.95

mixture is equal to $S_{mix} = 1.61R$; this implies that the compound under study, according to the classification presented in works [10–15], belongs to high-entropy alloys. The predicted melting temperature of the AlNiNbTiCo alloy was found to be $T_{mix} \approx 1824$ K, then $T_{mix}S_{mix} \approx 29184R$, which is much higher than the mixing enthalpy H_{mix} . For the investigated AlNiNbTiCo HEA, the critical parameters are: distortion $\delta \approx 6.97\%$, electronegativity $\Delta \chi \approx 0.20$, and valence electron concentration $VEC \approx 6.2$. The set of the critical parameters together with the mixing enthalpy and entropy allows us to conclude that the AlNiNbTiCo HEA belongs to the class of high-entropy materials: amorphous structures, solid solutions, and intermetallic compounds [10–15]. A comparative analysis of the critical indices with the literature data [10–15] shows that the high-entropy single-phase AlNiNbTiCo compound with the amorphous lattice is formed as a result of mechanical synthesis in the ball mill. Indeed, the indices $\Delta \chi \approx 0.20$, $\delta \approx 6.97\%$, $H_{mix} = -41.27$ kJ/mol, $S_{mix} \approx 13.4$ J/(K mol), and $VEC \approx 6.2$ correspond to the amorphous type formed as a result of mechanical synthesis in the ball mill. The critical values $\delta \approx 6.97\%$ and $H_{mix} = -41.27$ kJ/mol also correspond to the amorphous type according to the classification discussed in [15].

In the inverse convex hull method, the 2D diagram with the energy formation axes and zero level energy in the convex hull is proposed to visualize the results the level of which is determined by the driving force of the phase separation of the HEAs into low-component reactants. Alloys with mixing energy exceeding the zero level belong to quasi-stable structures. The vertices of the convex hull are stable phases (convex hull reactants) or intermetallic alloys found in the Material Project crystallographic database [12]. The composition of the phases at the qualitative level is captured by the shape and color gradation of the markers, while the arrows and their widths indicate the reactivity of neighboring alloys and the proportion of phases. The shape of the markers determines the number of components in the phase. The stability of alloys is determined by the expression [11]

$$\Delta G = \Delta H - TS \,, \tag{6}$$

$$\Delta Sss = k_B \sum_{i=1}^{n} x_i \ln x_i = R \ln(n), \qquad (7)$$

where G is the Gibbs free energy, ΔH is the enthalpy of mixing, ΔS_{ss} is the entropy of mixing of solid solutions, and x_i is the molar fraction of the *i*th element in the HEA. For the HEA, the separation of low-component reactants is taken into account, so that formula (7) should be modified as follows:

$$\Delta S_{ss} = R \ln \left(\frac{n}{n-1} \right). \tag{8}$$

The enthalpy ΔH of the *n*-atomic mixture is equal to

$$\Delta L = \sum_{i} \sum_{i>j} \Omega_{i,j} x_i x_j = \sum_{i} \sum_{i>j} \Omega_{i,j} \left(\frac{1}{n}\right)^2, \tag{9}$$

where $\Omega_{i,j}$ is the binary interaction that for the equiatomic composition is defined by the expression [11]

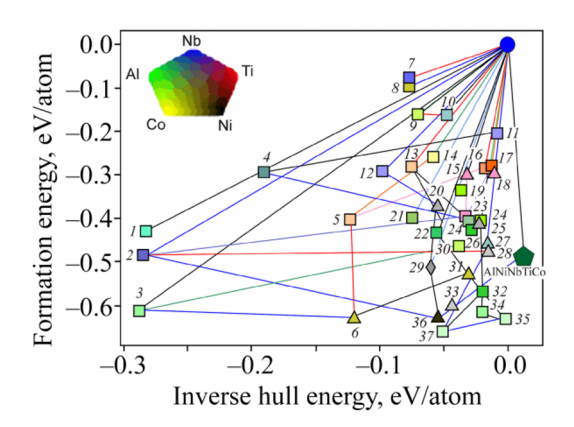


Fig. 1. Phase diagram of the AlNiNbTiCo alloy at T=1500 K. The numbers on the diagram correspond to the following connections: $I-Al_3Nb$, $2-Ni_3Ti$, $3-Al_3Co$, $4-Nb_3Ni$, 5-TiCo, $6-TiAlCo_2$, 7-NbTi, 8-NiCo, $9-NbCo_3$, $10-Nb_6Co_7$, 11-NbNi, $12-Nb_2Al$, $13-Ti_3Al$, $14-TiCo_3$, 15-NiNbTi, 16-NiNb, $17-Ti_2Ni$, $18-Ti_4CoNi$, $19-Al_9Co_2$, 20-AlNbTi, $21-Al_3Ti$, $22-AlNi_3$, 23-TiNi, $24-TiAl_2$, $25-Al_3Ni_2$, $26-TiAl_2$, 27-AlNiNb, 28-TiAlNi, 29-AlNiNbTi, $30-Al_5Co_2$, $31-Ti_{13}Al_8Co_8$, $32-Ti_{15}Al_{16}Ni_7$, 33-AlNiTi, $34-Al_3Ni_2$, $35-Al_4Ni_3$, $36-TiAlNi_2$, and 37-AlNi.

$$\Omega_{i,j} = 4 \left[E_{i,j}^{SQS} - \frac{1}{2} \left(E_i - E_j \right) \right], \tag{10}$$

where $E_{i,j}^{SQS}$ is the energy of the binary lattice determined from first principles within the cluster approximation in the ATAT code [10–15], and E_i and E_j are the lattice energies of the pure components. The results of stability calculations using formula (7) are shown in Fig. 1. Our calculations showed that the AlNiNbTiCo HEA after solidification is in the stable state in the temperature range $\Delta T = (1587–2935)$ K. The enthalpy of formation and mixing energy are negative in the specified temperature range, but with further temperature decrease, the AlNiNbTiCo alloy becomes quasi-stable and inclined to relaxation.

The X-ray diffraction analysis of the AlNiNbTiCo alloy synthesized in the ball mill showed that the diffraction patterns exhibit main reflections extended in the angular range the distribution of which is characteristic of simple cubic structures (Fig. 2), which indicates low crystallinity and high proportion of amorphous component in the registered intensity. Indeed, the crystallinity of the AlNiNbTiCo alloy on the diffraction patterns for 30, 40 and 50 min of stirring is 29.5%, 11.7%, and 15.8%, respectively. Identification of the structural state of the AlNiNbTiCo alloy by the Rietveld method is possible using the known reference lattices. In this work, the search for 5-element lattices of the known AlNiNbTiCo composition was realized by the evolutionary method in USPEX [24, 25]. During the prediction process, about 300 stable and quasi-stable reference lattices of fixed Al–Ni–Nb–Ti–Co composition were found, from which orthogonal class structures were selected for quantitative phase analysis (QPA).

Cubic class lattices were not detected in the prediction process. Qualitative phase analysis showed that among the detected lattices, the highest FoM (figure-of-merit) criterion corresponds to the simple cubic lattice with space group P1, the parameters of which are given in Table 2; for convenience, it is denoted as AlNiNbTiCo-3. The results of phase analysis of the AlNiNbTiCo alloy by the Rietveld method are shown in Fig. 2a-e, which illustrates the theoretical intensities of the AlNiNbTiCo-3 alloy (curves I), their experimental diffraction patterns (curves 2), and their differences (curve 3). The experimental diffraction patterns correspond to the AlNiNbTiCo HEA synthesized by stirring for 30 (Fig. 2a and b), 40 (Fig. 2c and d), and 50 min (Fig. 2e and f). As can be seen, the intensity difference indicates a good convergence of the theoretical diffraction patterns to the experimental ones (curve 3). The good convergence is also evidenced by the agreement criterion (according to Table 2, $R_{wp} \approx 1.57$, 1.54, and 1.35 %). The fraction of contributions

TABLE 2. Structural Lattice Parameters and Phase Fraction in the AlNiNbTiCo Alloy

t, min	Phases	<i>a</i> , 10 ⁻¹ nm	<i>b</i> , 10 ⁻¹ nm	c, 10 ⁻¹ nm	α	β	γ	$V, 10^{-3}$ nm ³	E, eV	Fraction of <i>I</i> , %	R_{wp} , %
0	AlNiNbTiCo-3	4.042	4.042	4.042	90.00	90.00	90.00	66.037	-5599.933	ı	_
30	AlNiNbTiCo-3	4.094	4.092	3.989	89.68	91.66	87.67	66.750	-5599.443	98.33	1.57
40	AlNiNbTiCo-3	4.051	4.093	3.909	90.30	90.03	89.48	64.809	-5598.506	97.31	1.54
50	AlNiNbTiCo-3	4.091	4.171	3.951	89.94	89.45	89.13	67.447	-5599.060	95.42	1.36

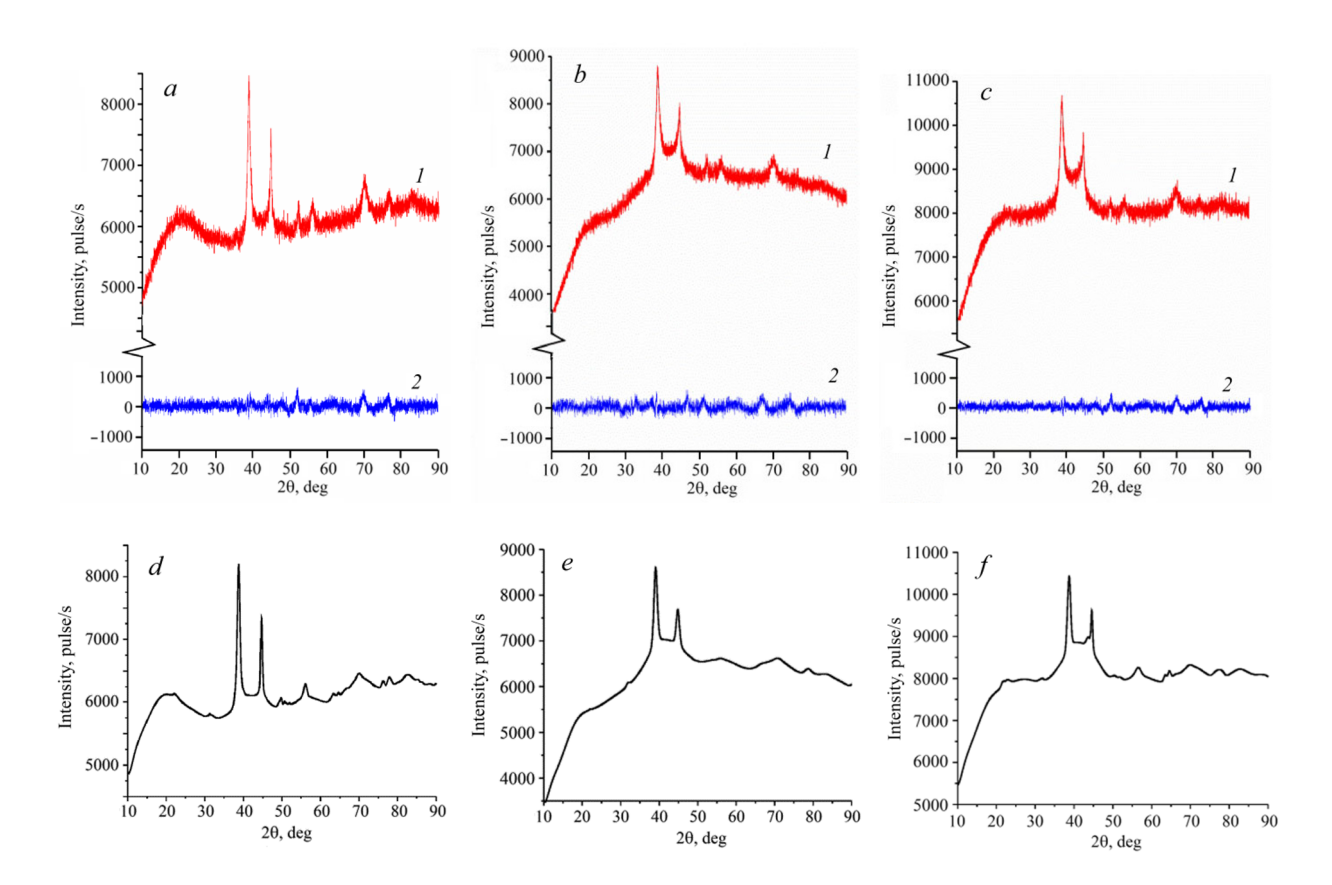


Fig. 2. Diffraction patterns of the AlNiNbTiCo alloys after stirring times of 30 (a and d), 40 (b and e), and 50 min (c and f). Here curves I in Fig. 2a–c show the experimental diffractin patterns, and curves 2 in Fig. 2a–c show the intensity difference. The theoretical AlNiNbTiCo-3 diffraction patterns are shown in Fig. 2 d–f.

to the integral intensity I of the lattices is given in Table 2; it is found to be dominant for all synthesis times and equal to 0.98, 0.97, and 0.95, respectively. The structural SCL parameters are given in Table 2, and the spatial distribution of atoms is shown in Fig. 3. Table 2 also presents the parameters in the initial state (0 min) and after refinement by the Rietveld method (30, 40, and 50 min) together with the lattice volume V.

It should also be noted that the coordinates of the atoms are known for all SCLs; however, because of the large volume, these data are not given in the paper. Table 2 also presents the AlNiNbTiCo-3 lattice energies (E < 0 eV), which indicate their at least quasi-stable state. Using the Rietveld method, it was found that the AlNiNbTiCo HEAs after 30, 40, and 50 min of stirring are dominated by the AlNiNbTiCo-3 lattice contributions to the experimental diffraction patterns, which are partially in the X-ray amorphous state. The results of full-profile refinement of the low-crystalline HEA diffraction patterns of the AlNiNbTiCo allow with a high degree of agreement ($R_{wp} < 1.6\%$) indicate

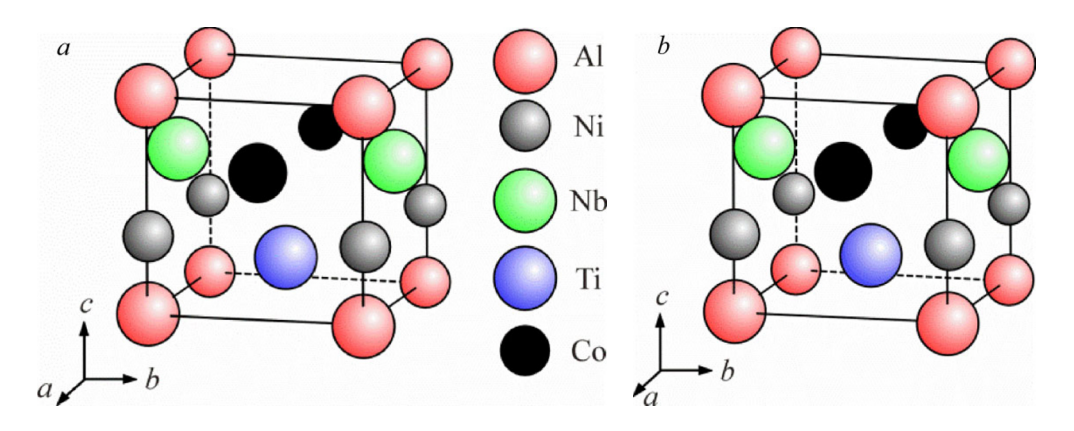


Fig. 3. Spatial distribution of atoms in the AlNiNbTiCo-3 alloy in the initial state (*a*) and after parameter refinement by the Rietveld method (*b*).

that the AlNiNbTiCo-3 lattice is in the X-ray amorphous state. From the results obtined it follows that the stirring time has almost no significant effect on the quantitative content of the main X-ray amorphous phase of the AlNiNbTiCo-3 allow. However, the specific energy (E/V) varies. The stirring time affects the internal energy and the structural parameters of the synthesized AlNiNbTiCo-3 lattice. The specific energy is found to be $E/V \approx -84.80$, -83.89, -86.38, -83.01 eV/Vol for stirring times of 30, 40, and 50 min, respectively, from which it follows that the optimal stirring time is 40 min. The change in the specific lattice energy due to redistribution of atoms is found to be more noticeable.

The results of calculations showed that the lattice parameters do not change during the optimization process, and they are kept equal to the initial state given in Table 2. Then, the specific energy is equal to $E/V \approx -84.88 \text{ eV/Vol}$, which is even higher than the specific energy of the alloy after stirring for 40 min. A comparison shows that the mechanical stirring in the planetary mill synthesizes both the semi-amorphous AlNiNbTiCo HEA and the alloy which tends to stabilize, in particular within 40 min. It should also be noted that the complete structural information on the AlNiNbTiCo-3 lattices can be used to study the thermodynamic properties of individual phases and AlNiNbTiCo HEAs.

CONCLUSIONS

Thus, the full group of critical indices has been used in the present work to study the structural state of the AlNiNbTiCo alloy identified as a stable single-phase amorphous high-entropy alloy. Using the above procedure as well as the inverse convex hull method (InvewrseHubWeb), the stability interval was determined $\Delta T = (1587-2935)$ K. The prediction of the lattices of equiatomic composition by the evolutionary method allowed us to create a 5-element (AlNiNbTiCo) crystallographic base of the AlNiNbTiCo alloy etalons composed of orthogonal lattices (etalons with P1). Using the Rietveld method, it was established with a high degree of reliability that the high-entropy AlNiNbTiCo alloy is dominated by the AlNiNbTiCo-3 SCL, for which the complete structural information was determined, including parameters, atom coordinates, node occupancy, and space group. Moreover, the AlNiNbTiCo-3 lattice is the main lattice in the AlNiNbTiCo HEAs synthesized by mechanical stirring for 30, 40, and 50 min. Our analysis of the geometrically optimized AlNiNbTiCo-3 lattice showed that not only stable amorphous-type HEAs are formed during stirring, but also the lattice relaxation towards its stabilization occurs during 40 min.

COMPLIANCE WITH ETHICAL STANDARDS

Author contributions

A.M.L. and R.S.L. conceived the study and were in charge of overall direction and planning; Y.A.A., Ž.M., and A.A.K. designed the model and the computational framework, analyzed the data, and wrote the paper with contribution from all authors. M.K. and A.D.L. contributed to sample preparation and performed the experiments and measurements. All authors have read and agreed to the published version of the manuscript.

Conflicts of interest

The authors declare that they have no known competing financial interests or personal relationships that could have appeared to influence the work reported in this paper.

Funding

This research was funded by the Governmental Program (Grant No. FSWW-2023-0005).

Financial interests

The authors have no relevant financial or non-financial interests to disclose.

Institutional review board statement

Applicable.

REFERENCES

- 1. B. Cantor, I. T. H. Chang, P. Knight, and A. J. B. Vincent, Mater. Sci. Eng. A, **375**, 213–218 (2004); https://doi.org/10.1016/j.msea.2003.10.257.
- M. Sahlberg, D. Karlsson, C. Zlotea, and U. Jansson, Sci. Rep., 6, 36770 (2016); https://doi.org/10.1038/ srep36770.
- 3. O. N. Senkov, G. B. Wilks, J. M. Scott, and D. B. Miracle, Intermetallics, **19**, 698–706 (2011); https://doi.org/10.1016/j.intermet.2011.01.004.
- 4. Z. Li, K. G. Pradeep, Y. Deng, D. Raabe, and C. C. Tasan, Nature, **534**, 227–230 (2016); https://doi.org/10.1038/nature17981.
- 5. X. Li, D. Liu, X. Liang, et al., J. Memb. Sci., 496, 165–173; https://doi.org/10.1016/j.memsci.2015.08.067.
- 6. R. Li, L. Xie, W.Y. Wang, et al., Front. Mater., 7, 290 (2020); https://doi.org/10.3389/fmats.2020.00290.
- K. Lee, M. V. Ayyasamy, P. Delsa, et al., Npj Comput. Mater., 8, 25 (2022); https://doi.org/10.1038/s41524-022-00704-y.
- 8. S. Rajendrachari, Alloys, 1, 116–132 (2022); https://doi.org/10.3390/alloys1020008.
- 9. A. Fourmont, S. Le Gallet, O. Politano, *et al.*, J. Alloys Compd., **820**, 153448 (2020); https://doi.org/10.1016/j.jallcom.2019.153448.
- 10. A. Rogachev, D. Kovalev, A. Fourmont, *et al.*, Int. J. Self-Propagating High-Temp. Synth., **31**, 62–68 (2022); https://doi.org/10.3103/S1061386222020078.

- 11. D. Evans, J. Chen, G. Bokas, *et al.*, Npj Comput. Mater., 7, 151 (2021); https://doi.org/10.1038/s41524-021-00626-1.
- 12. G. U. O. Sheng and C. T. Liu, Prog. Nat. Sci.: Mater. Int., **21**, 433–446 (2011); https://doi.org/10.1016/S1002-0071(12)60080-X.
- 13. J. W. Yeh, S. K. Chen, S. J. Lin, *et al.*, Adv. Eng. Mater., **6**, 299–303 (2004); https://doi.org/10.1002/adem.200300567.
- 14. J. W. Yeh, JOM, **65**, 1759–1771 (2013); https://doi.org/10.1007/s11837-013-0761-6.
- 15. Y. Zhang, Y. J. Zhou, J. P. Lin, *et al.*, Adv. Eng. Mater., **10**, 534–538 (2008); https://doi.org/10.1002/adem.200700240.
- 16. Crystallography Open Database, https://www.crystallography.net/cod/search.html (accessed on July 25, 2023).
- 17. A. R. Oganov and C. W. Glass, J. Chem. Phys., **124**, 244704 (2006); https://doi.org/10.1063/1.2210932.
- 18. A. R. Oganov, A. O. Lyakhov, and M. Valle, Acc. Chem. Res., 44, 227–237 (2011); https://doi.org/10.1021/ar1001318.
- 19. P, V. Kosmachev, Y. A. Abzaev, and V. A. Vlasov, Russ. Phys. J., **61**, 264–269 (2018); https://doi.org/10.1007/s11182-018-1396-4.
- 20. Y. F. Ivanov, Y. A. Abzaev, V. E. Gromov, *et al.*, AIP Conf. Proc., **2509**, 020087 (2022); https://doi.org/10.1063/5.0085244.

ELSEVIER

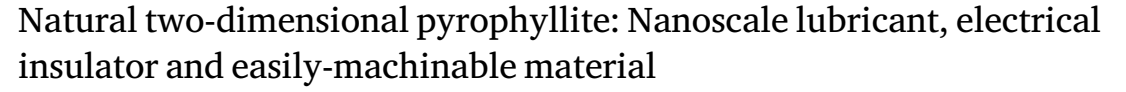
Contents lists available at ScienceDirect

Applied Surface Science

journal homepage: www.elsevier.com/locate/apsusc



Full length article



Borislav Vasić ^{a,*}, Radoš Gajić ^a, Ivana Milošević ^a, Žarko Medić ^a, Marina Blagojev ^b, Marko Opačić ^a, Aleksandar Kremenović ^c, Dejan Lazić ^d

- ^a Institute of Physics Belgrade, University of Belgrade, Pregrevica 118, 11080 Belgrade, Serbia
- ^b Faculty of Mining and Geology, University of Belgrade, Dušina 7, 11000 Belgrade, Serbia
- ^c Laboratory of Crystallography, Faculty of Mining and Geology, University of Belgrade, Đušina 7, 11000 Belgrade, Serbia
- d Biotech Engineering D.O.O, Golsvordijeva 32, 11000 Belgrade, Serbia

ARTICLE INFO

Keywords: Natural two dimensional materials Phyllosilicates Pyrophyllite Nanofriction and wear Insulating properties Atomic force microscopy

ABSTRACT

Pyrophyllite, with the chemical formula $Al_2Si_4O_{10}(OH)_2$, is a naturally occurring and abundant van der Waals mineral belonging to the group of phyllosilicates. It is very soft, layered crystal used for sculpting and an excellent electrical and thermal insulator aimed for the operation at high pressure and temperature. Here, for the first time, two-dimensional (2D) pyrophyllite obtained by both mechanical and liquid phase exfoliation is presented and investigated at the nanoscale. The layered structure provides low friction coefficient of around 0.1 as measured by friction force microscopy. The wear properties, studied by atomic force microscope (AFM) based scratching, are distinctly different from graphene. Since the wear is initiated at low normal forces, 2D pyrophyllite can be routinely carved by the AFM tip and it is suitable for scratching based nanolithography. According to our optical measurements, 2D pyrophyllite is an insulator with a band gap of ~ 5.2 eV. Local current measurements by conductive AFM reveal that 2D pyrophyllite flakes behave as efficient electrical insulators with a breakdown voltage of around 6 MV/cm. Therefore, the obtained results indicate possible applications of 2D pyrophyllite as a low-cost electric insulator and lubricant, as well as an easily-machinable material at the nanoscale.

1. Introduction

Layered materials are usually defined as a special crystal class existing in the form of weakly stacked atomic layers, like graphene in graphite. General property of these materials are the strong inplane bonds and very weak interactions perpendicular to the planes, typically of the van der Waals type. Therefore, layered materials that can be exfoliated into atomically thin layers are often called van der Waals materials. Two dimensional (2D) materials concerns crystalline solids consisting of a single or few atomic layers. Huge interest for them started when large graphene flakes were isolated for the first time in 2004 by Novoselov et al. using mechanical exfoliation [1]. Extraordinary properties of graphene [2] triggered the search for new 2D materials. Nowadays hundreds of different 2D materials beyond graphene have been devised and thoroughly investigated because of their extraordinary properties that are not present in corresponding counterpart bulk materials. As a result, 2D materials find numerous applications in nanoelectronics, nanophotonics and optoelectronics, spintronics, sensing and many other fields [3-5].

After the discovery of graphene, the second generation of 2D materials, which includes hexagonal boron nitride, 2D transition metal dichalcogenides (such as MoS₂, WS₂, MoSe₂, WSe₂, MoTe₂) and functionalized graphene, quickly appeared [6–11]. The third-generation of 2D materials includes elemental analogues of graphene such as silicene, germanene, stanene, phosphorene [12], as well as with 2D transition metal carbides and carbonitrides (MXenes) [13], 2D silicon dioxide [14], and minerals [15]. Interestingly, many of them were firstly discovered by numerical calculations, and afterwards, experimentally obtained [16].

The most of 2D materials are synthetic, for instance large-scale 2D materials are commonly prepared by chemical vapour deposition. On the other hand, natural van der Waals minerals exist in most classes of 2D materials like semi-metallic graphite and semiconducting molybdenite MoS_2 and tungstenite WS_2 . In recent years, a new family of 2D materials has appeared. It is based on layered natural minerals as a source of 2D materials [15]. This family includes 2D insulating materials based on phyllosilicates such as talc [18–24], muscovite (mica) [25],

E-mail address: bvasic@ipb.ac.rs (B. Vasić).

^{*} Corresponding author.

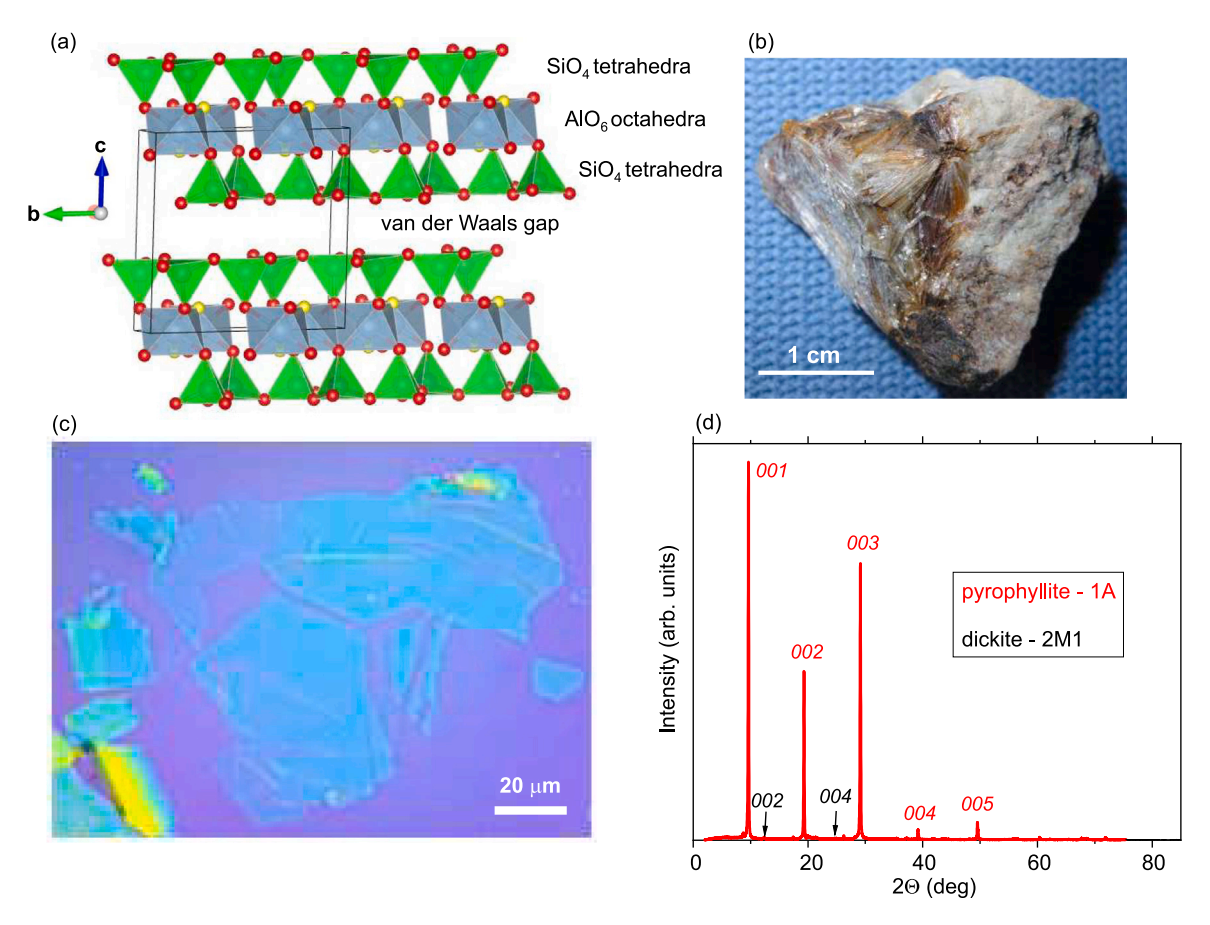


Fig. 1. (a) Polyhedral representation of pyrophyllite-1A structure: SiO_4 tetrahedra in green, AlO_6 octahedra in blue, oxygen atoms in red, OH group in yellow. The unit cell is outlined in black. VESTA program [17] was used for three-dimensional visualization of the crystal structure. (b) Optical image of the crystalline pyrophyllite used in this study. (c) Optical micrograph of mechanically exfoliated 2D pyrophillite flakes. (d) XRPD pattern of bulk pyrophyllite crystal which contains pyrophyllite-1A (PDF card # 01-075-0856) and small amount (near detection limit) of dickite-2M1 (PDF card # 00-058-2002). Most intense hkl reflections are marked.

biotite [26], vermiculite [27], clinochlore [28], and phlogopite [29], as well as 2D magnetic materials such as cylindrite [30] and ironrich talc [31]. Furthermore, semiconducting van der Waals mineral franckeite has been used for the exfoliation of 2D van der Waals heterostructures [32–34]. Therefore, 2D materials can be obtained directly from natural minerals by just simple exfoliation and without complex synthetic procedures. As a result, search of 2D materials among natural minerals can be particularly interesting. Furthermore, clay minerals are abundant in Earth crust and therefore they serve as cost-effective sources of 2D materials. This mainly concerns phyllosilicates or layered silicates such as talc, pyrophyllte, kaolinite, gibbsite, etc., which are the most common and abundant clays.

Pyrophyllite (from Greek pyro—fire and phyllos—a leaf) is natural van der Waals mineral which belongs to the talc-pyrophyllite family of phyllosilicates. It is a hydrous aluminum silicate with the chemical formula Al₂Si₄O₁₀(OH)₂. Single layer of pyrophyllite consists of the AlO₆ octahedral sheet sandwiched between two SiO₄ tetrahedral layers (Fig. 1(a)). Pyrophyllite is a chemically inert material, good electrical and thermal insulator with a high melting point [35] and with a fairly high dielectric constant [36,37]. As a clay mineral, it is abundant and inexpensive. Therefore, it is widely used in refractories, highgrade ceramics, electric insulators, and as a filler in order to improve properties of paper, plastic, rubber, paint and other mixtures [35]. As a van der Waals material, pyrophyllite has a lamellar structure which indicates good frictional properties and its applications as a lubricant [38]. It is very soft mineral [35] which provides easy machining and making of various profiles, while at the same time, it can withstand large pressures. Therefore, bulk pyrophyllite mineral exhibits interesting properties with a broad range of potential applications. Still,

its 2D form has not been studied so far, although small flakes of few layer pyrophyllite have been obtained by liquid phase exfoliation [39], whereas thermal exfoliation was investigated as well [40], but not in the context of 2D layers.

Here we present our report on 2D pyrophyllite with the focus on its properties related to potential applications as 2D electric insulator, lubricant and material suitable for nanolithography. Using mechanical and liquid phase exfoliation (LPE), we routinely fabricated few-layer pyrophyllite which can be exfoliated down to single-layer thickness. The initial characterization was done by X-ray powder diffraction (XRPD), Raman spectroscopy, UV–VIS spectroscopy, and optical microscopy. Afterwards, we focused on nanoscale mechanical and electrical properties of 2D pyrophyllite such as friction, wear, nanoscale machining, as well as insulating properties and dielectric breakdown, which were investigated by atomic force microscopy (AFM) based methods.

2. Experimental methods

2.1. Sample preparation

Here we used the crystalline pyrophyllite from Hillsborough, Orange County, North Carolina, USA (Fig. 1(b)). 2D pyrophyllite flakes were obtained by the mechanical exfoliation [41] onto ${\rm SiO_2/Si}$ substrate (with 300 nm thick ${\rm SiO_2}$). Briefly, thick pyrophyllite flakes were separated from the bulk crystal by an adhesive tape. These flakes were further thinned by multiple peeling against two pieces of the tape, and finally transferred onto the substrate. The flakes of interest were selected by optical microscopy (typical optical micrograph depicted in Fig. 1(c)).

The starting material for LPE of pyrophyllite was ground pyrophyllite crystal (Hillsborough mine, Orange County, North Carolina, USA). Its dispersion was obtained in N-N-Dimethylformamide (DMF, Sigma Aldrich, product no. D4551), while the initial concentration of pyrophillite was 10 mg/mL (in 10 mL cylindrical vial). The solution was then sonicated in a low-power ultrasonic bath for 12 h. The resulting yellowish dispersion was centrifuged for 15 min at 1000 rpm. In order to fabricate pyrophyllite films from the obtained dispersion, Langmuir-Blodgett Assembly (LBA) technique at a water-air interface was used. This technique was previously employed for the preparation of graphene films as well [42,43]. In the first step, a small amount of pyrophyllite dispersion in DMF was added at the water-air interface. Then, after the pyrophyllite film was formed at the interface, it was slowly picked up by desired substrate. Three different substrates were used: SiO₂/Si for AFM measurements (morphological characterization), Au-coated SiO₂/Si for C-AFM measurements (current maps and breakdown voltage), and quartz for UV-VIS spectroscopy.

2.2. XRPD measurements, Raman and UV-VIS spectroscopy

The structural characterization was done by XRPD which was conducted at room temperature on Rigaku Smartlab X-ray Diffractometer in $\theta-\theta$ geometry (the sample in the horizontal position) in parafocusing Bragg–Brentano geometry using D/teX Ultra 250 strip detector in 1D standard mode with CuK $\alpha_{1,2}$ radiation source (U = 40 kV and I = 30 mA). The XRPD pattern was collected in 2–90° 2θ range, with the step of 0.01°, and data collection speed of 6°/min. The pyrophyllite sample was spinning in the horizontal plane with the speed of 60 rounds per minute. The low background single crystal silicon sample holder was used to minimize the background. The PDXL2 integrated XRPD software (Version 2.8.30; Rigaku Corporation) was employed for XRPD data treatment.

Raman scattering measurements were performed on Tri Vista 557 Raman system, in backscattering micro-Raman configuration. The 514.5 nm line of an $\rm Ar^+/Kr^+$ gas laser was used as an excitation source. Laser power was less than 1 mW on a sample in order to minimize its local heating. A microscope objective with the 50x magnification was used for focusing the laser beam. All measurements were performed at ambient conditions.

Optical transmittance of the pyrophyllite film (obtained by liquid phase exfoliation) was measured by ultraviolet-visible (UV-VIS) spectrophotometer Beckman Coulter DU 720 in the range from 200 to 900 nm.

2.3. AFM measurements

The morphological characterization of 2D pyrophillite was done by imaging in the tapping AFM mode. Friction was measured using friction force microscopy, by recording the lateral force which corresponds to the lateral torsion of the AFM cantilever during scanning in the contact AFM mode. The friction signal was calculated as a half difference between lateral forces measured in forward and backward scan direction. The measurements were done using NSG01 probes (nominal stiffness 5 N/m) from NT-MDT, while the applied normal load was up to $\sim\!\!300$ nN, well below the threshold force needed to initiate wear. The wedge calibration of frictional forces was used in order to transform measured lateral signal into frictional forces [44].

Wear properties were studied by scratching the pyrophyllite flakes in the AFM contact mode. Square domains were scratched with an increased normal force (applied by the AFM tip) from the bottom to the top of the scan regions. The maximal normal load needed to initiate wear was around 1 μN . When a wear was initiated, the normal force was held constant. Mechanically robust and stiff, diamond coated probes DCP11 (nominal stiffness 11.5 N/m) from NT-MDT were used since they allowed high normal forces needed for scratching as well as subsequent imaging of scratched areas in the tapping AFM mode.

The AFM based nano-lithography was done using diamond coated probes HA HR DCP (nominal stiffness 35 N/m) from NT-MDT in three modes: nanoindentation and two lithographic modes, vector and raster. The nanoindentation mode is very similar to the measurement of forcedisplacement curves. The AFM scanner holding a sample was moved only vertically (without scanning in the horizontal plane) toward the AFM tip in order to induce a point-like deformation in pyrophyllite. For this purpose, the applied normal load was around 6 µN. In the lithographic modes, pyrophillite surface was scratched in the AFM contact mode according to predefined templates. In the case of the vector lithography, the templates were defined by discrete lines only, whereas in the case of the raster lithography, the square domains were taken for simplicity. During the nano-lithography, two force levels were applied. The low force level was applied along trajectories of the AFM tip which should stay intact (the movements between discrete line segments to be scratched, from the initial position to the first line segment, and from the last line segment back to the initial position). On the other hand, a high force level in the range $\sim 2-6$ µN was applied on segments which are to be scratched. The scratching velocity was around 0.2 µm/s. It was significantly decreased compared to the scanning speed in order to provide an efficient lithography.

The study of insulating properties and dielectric breakdown requires 2D pyrophyllite flakes placed between two metallic electrodes. In order to make possible study at the nanoscale, conductive AFM (C-AFM) was employed. For this purpose, the pyrophyllite flakes obtained by LPE method were deposited on a gold substrate. Then, a metallic AFM tip on the top of a pyrophyllite flake served as a top electrode, while the underlying gold was a bottom electrode. The bias voltage was applied on the gold, while the AFM tip in contact with the pyrophyllite flakes was (virtually) grounded. The current imaging was done by scanning in C-AFM mode, using highly doped and conductive, diamond coated probes DCP11, and simultaneously recording topography and local current. Dielectric breakdown was examined by measuring local I/V curves at single point, while the bias voltage was swept in a range $\pm 10~\rm V$.

3. Results and discussion

3.1. Structural and vibrational properties

The results of XRPD measurements presented in Fig. 1(d) show that the specimen predominantly contains crystalline pyrophyllite-1A (PDF (Powder Diffraction File) card # 01-075-0856), whereas a small amount (near detection limit) of dickite-2M1 (PDF card # 00-058-2002) was also identified. The most intense reflections in the XRPD pattern of the dominant phase are 00l (l = 1-5) which is in accordance with the layered structure of pyrophyllite-1A. The XRPD results indicate that a crystalline pyrophyllite sample (Fig. 1(b)) has a triclinic lattice and 2:1 structure (two tetrahedral sheets and one octahedral sheet) depicted in Fig. 1(a). The refined unit cell parameters for pyrophyllite-1A are the following (estimated standard deviations in parenthesis): $a = 5.14(2) \text{ Å}, b = 8.99(4) \text{ Å}, c = 9.28(4) \text{ Å}, \alpha = 91.88(8)^{\circ}, \beta =$ 99.36(15)°, $\gamma = 89.16(15)$ °, V = 423(3) Å³. The refined values, within an experimental error, are in a very good agreement with the values obtained for pyrophyllite-1A (OH group in the structure) in both single crystal XRD experiment [45] and powder XRD experiment [46].

Raman spectra of the bulk crystalline pyrophyllite are presented in Fig. 2 in the spectral ranges from 50 to $1100~\rm cm^{-1}$ and 3600 to 3750 cm⁻¹. The first range describes the fundamental vibrations of all phyllosilicates, whereas the second one displays the vibrations of the $\rm H_2O/OH$ group [47–49]. Our spectra are fully consistent with the previous published Raman spectra of crystalline pyrophyllite [47]. They contain all fundamental modes up to $1100~\rm cm^{-1}$ as well as $\rm H_2O/OH$ peak at $3670~\rm cm^{-1}$. Details and the full assignment of all modes could be found elsewhere [47].

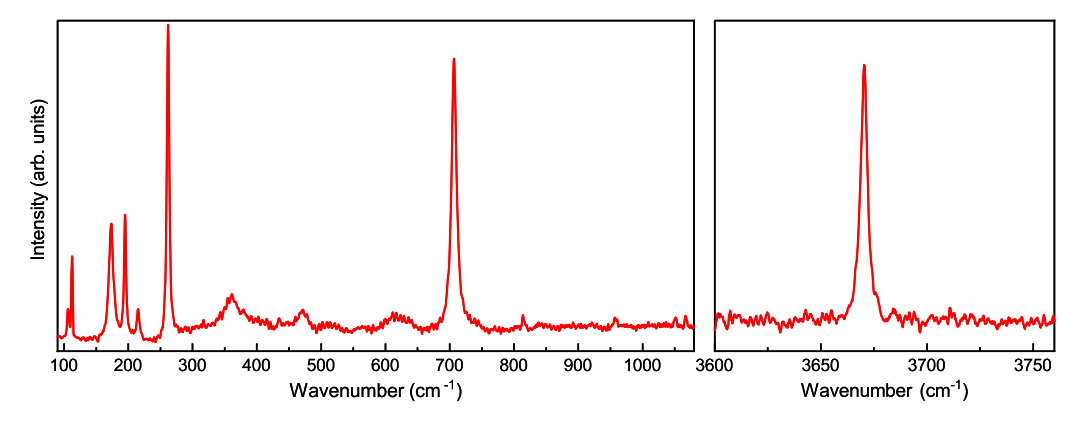


Fig. 2. Raman spectrum of a bulk pyrophyllite for two spectral ranges: the fundamental vibrations of phyllosilicates (left) and the H₂O/OH range (right).

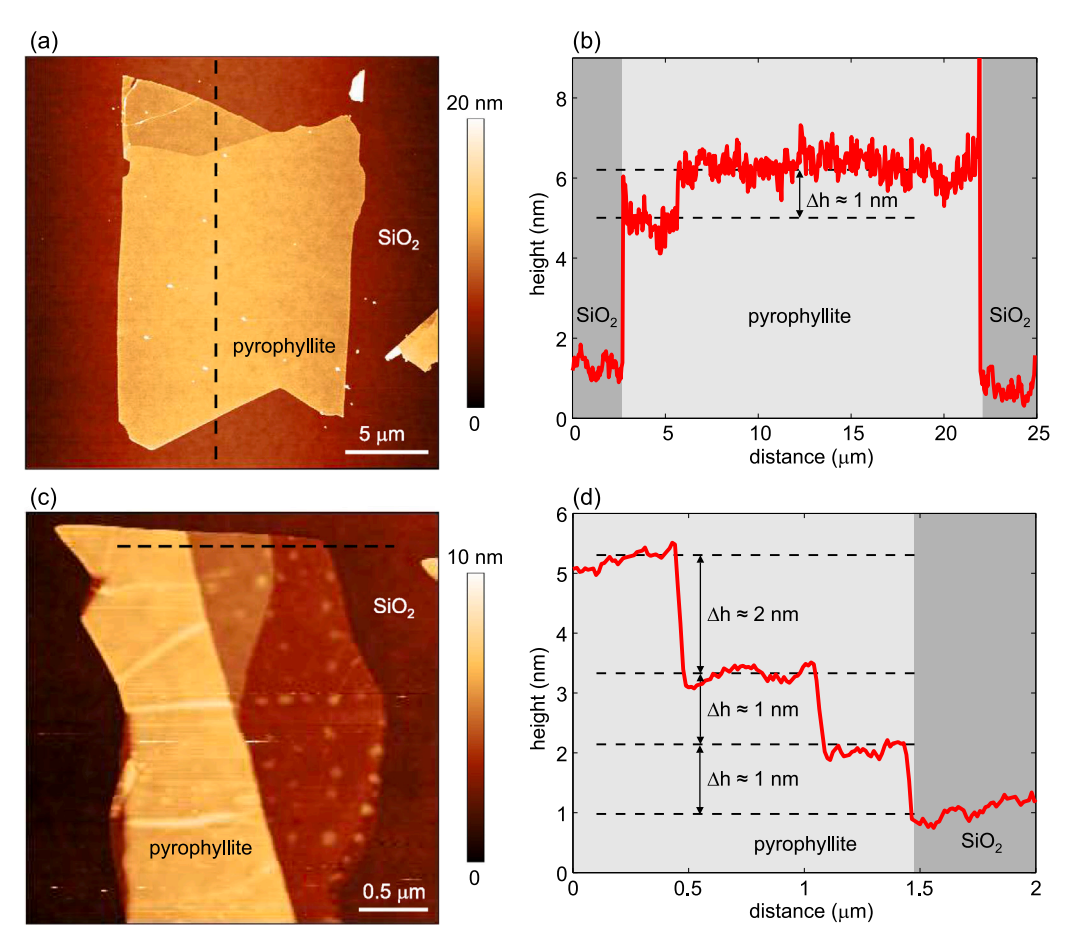


Fig. 3. (a), (c) Topographic images of pyrophillite flakes mechanically exfoliated on Si/SiO₂ with (b), (d) corresponding height profiles along dashed lines with indicated characteristic step heights.

3.2. Morphology

Fig. 3(a) depicts the topography of a typical flake obtained by mechanical exfoliation, with the height profile given in Fig. 3(b). It is a few-layer pyrophyllite with a thickness of ${\sim}5$ nm and an area of ${\sim}15\times20~\mu\text{m}^2$. The root-mean-square roughness calculated on $5\times5~\mu\text{m}^2$ areas is only 0.6 nm indicating atomically flat surface free of residues. The height profile (Fig. 3(b)) reveals that a step height between two domains is only ${\sim}1$ nm.

The trilayer structure of the pyrophyllite unit cell displayed in Fig. 1(a) consists of ${\rm AlO_6}$ octahedral sheet sandwiched between two ${\rm SiO_4}$ tetrahedral layers. According to XRPD results, the thickness of the neutral trilayer is 6.39 Å, whereas the thickness of van der Waals

gap is 2.76 Å [45], measuring from the center of oxygen ions (O²⁻). Accordingly, the effective thickness of the trilayer is around 9.2 Å, measuring from the top to bottom oxygen surfaces since we have to add two oxygen ion radii of 2.8 Å. Therefore, the thickness of single layer pyrophyllite measured by AFM should be around more or the same. The smallest thickness measured in our AFM experiments was always around 1 nm. The same minimal thickness was observed in AFM scratching based experiments as discussed below. Therefore, this value corresponds to the single layer of pyrophyllite. The small discrepancy between expected (around 9.2 Å) and measured thickness (around 1 nm) probably appears due to adsorbed water layer which is inevitable at ambient conditions and/or due to measurements done in

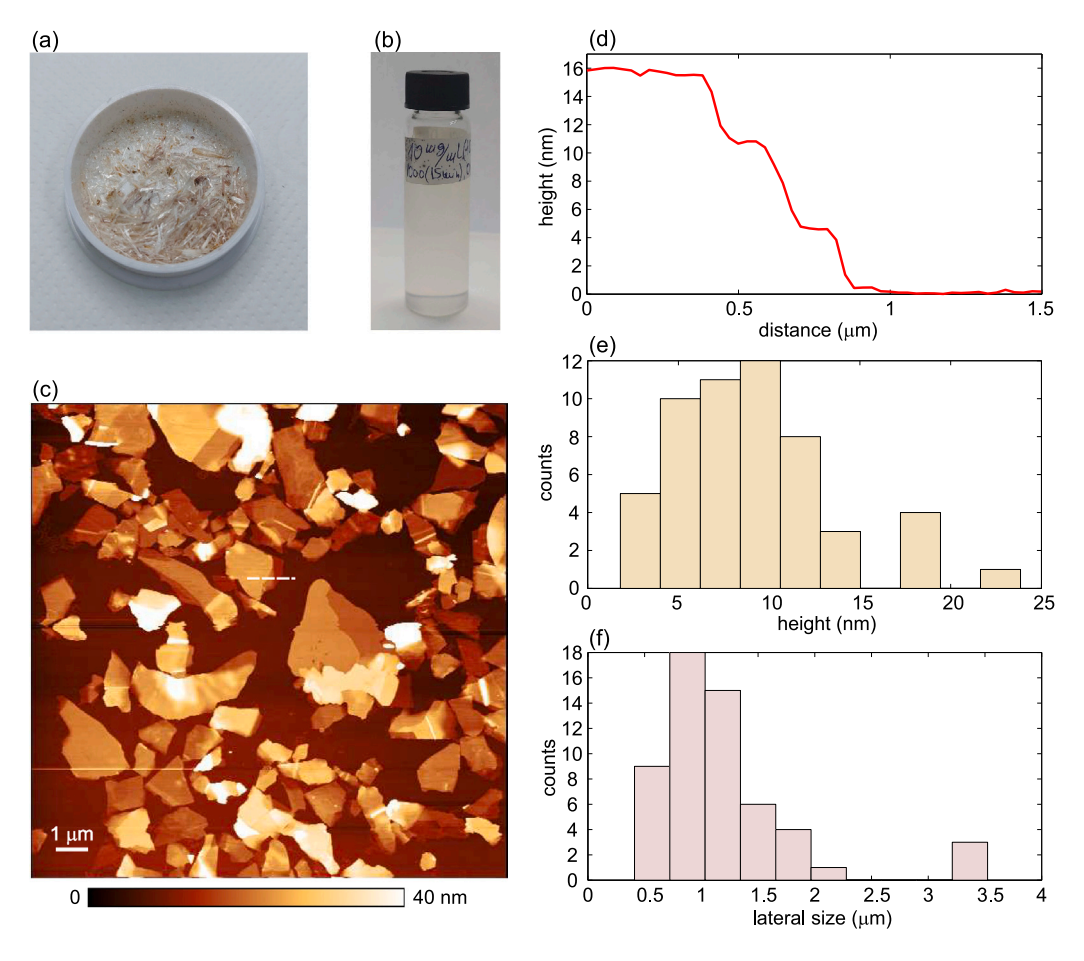


Fig. 4. (a) Ground pyrophyllite mineral used as a starting material for LPE and (b) the resulting dispersion employed for LBA. (c) Topographic image of pyrophillite flakes obtained by LPE and subsequent LBA on Si/SiO₂. (d) Height profile along the dashed line in (c). Histograms of (e) height and (f) lateral size of the flakes shown in (c).

tapping AFM mode, which commonly gives an increased step height on atomically thin layers [50].

Generally, we routinely exfoliated few layer pyrophillite flakes with the lateral size larger than 10 $\mu m.$ On the other hand, yield of single layers was low, while their size was significantly smaller. One example is illustrated in Fig. 3(c). The corresponding height profile in Fig. 3(d) displays two single-layer step heights of $\sim\!\!1$ nm, and the third step height of $\sim\!\!2$ nm which corresponds to double-layer flake. As can be seen, the area of the single layer pyrophyllite is only several square micrometers.

The ground pyrophyllite crystal and its yellowish dispersion used in LPE are depicted in Fig. 4(a) and (b), respectively. Topography of 2D pyrophyllite obtained by the LPE method is depicted in Fig. 4(c). The height profile in Fig. 4(d) displays three step heights of $\sim\!\!5$ nm. Samples produced by the LPE method consist of a network of flakes with a typical height of 5–15 nm (Fig. 4(e)) and lateral dimensions of $\sim\!\!1$ µm (Fig. 4(f)). The flakes have well defined shapes, flat surface and regular edges. Although they are thicker and smaller compared to those fabricated by the mechanical exfoliation, LPE method provides large scale production of 2D pyrophyllite. At the same time, the LPE method can be easily adapted to various substrates. This was employed below in the study of insulating properties and dielectric breakdown of 2D pyrophyllite, where the flakes were deposited on a gold substrate.

3.3. Friction

Friction properties are analyzed on a small segment of the pyrophyllite layer surrounded by SiO_2 as depicted in Fig. 5(a). In the friction force map displayed in Fig. 5(b), the pyrophyllite is represented by

a dark contrast, thus indicating decreased friction compared to SiO2. The height and friction force profiles from Fig. 5(c) reveal three times lower friction on the pyrophyllite. The same measurements were done for the normal force in the range ~30-330 nN. Average friction forces on both pyrophyllite and SiO₂ were calculated from the histograms of friction maps and the corresponding results are presented in Fig. 5(d). As can be seen, the friction force approximately linearly increases with the normal force in accordance with Amonton's law. The friction coefficients were calculated from the slopes of the linear fits (dashed lines in Fig. 5(d)). The obtained friction coefficient of the pyrophyllite flake $\mu_{\rm DVF} = 0.12$ is more than four times lower than the friction coefficient of surrounding silicon-dioxide substrate ($\mu_{SiO_2} = 0.5$). At the same time, μ_{pvr} is very similar to the friction coefficient of graphene grown by chemical vapour deposition [51] and 2D talc [21]. Therefore, the presented results indicate good lubricating properties of few-layer thick pyrophyllite.

Generally, mechanical and liquid phase exfoliation give 2D layers with the same physical properties. The main difference between two methods is morphology of produced layers, the lateral size of the flakes before all. Therefore, we expect the same friction properties of pyrophyllite obtained by both methods. Additional friction measurements on LPE pyrophyllite prove this predictions. The results presented in figure S1 of Supplementary material show that pyrophyllite flakes obtained by LPE has a low friction coefficient of around 0.14, that is, very similar to pyrophyllite obtained by the mechanical exfoliation (0.12). Compared to the surrounding silicon-dioxide substrate, the friction is again decreased by around four times.

In our previous manuscript [21] we investigated friction as a function of talc thickness in detail. Talc friction reduces with number of layers (talc thickness), which is similar to other 2D materials, since so

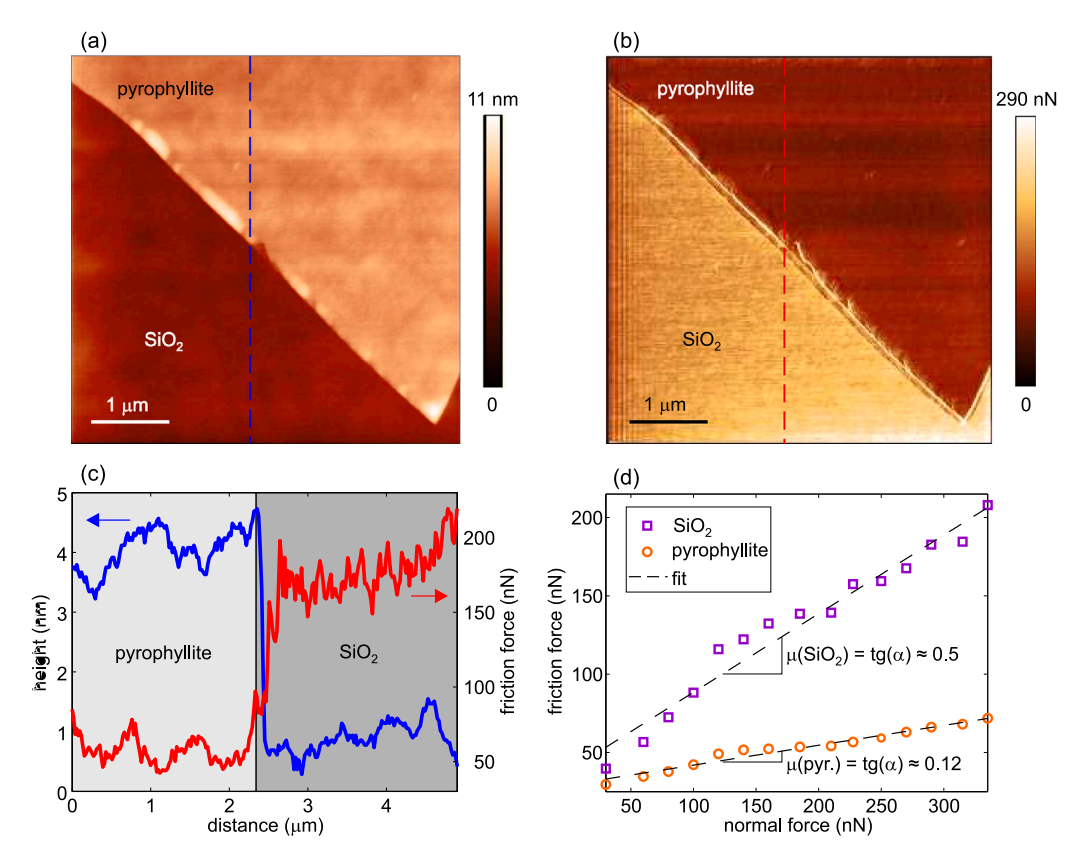


Fig. 5. (a) Topography and (b) friction force map of pyrophyllite flake on Si/SiO_2 . (c) Height and force profiles along dashed lines in (a) and (b), respectively. (d) Average friction force (calculated from histograms of friction maps such as the one presented in (b)) as a function of the normal force applied by the AFM tip. Friction coefficients were calculated as slopes of the linear fits represented by dashed lines.

called puckering effect, responsible for the friction of 2D materials, is less pronounced for thicker layers due to larger bending rigidity. In the case of talc, this dependence is rather weak, since single layer is 1 nm thick and already consists of three atomic planes. Pyrophyllite and talc belong to the family of 2:1 phyllosilicates. Their chemical formulas are almost identical (pyrophyllite - $Al_2Si_4O_{10}(OH)_2$, talc - $Mg_3Si_4O_{10}(OH)_2$) and they have practically the same structure (octahedral plane with metallic (Al or Mg) ion sandwiched between two tetrahedral SiO layers). The thickness of the single layer (around 1 nm) is similar in both materials. Therefore, dependence of the friction as a function of pyrophyllite thickness should be the same as for talc. This conclusion is further confirmed in figure S1(b) of Supplementary material depicting friction map of pyrophyllite flakes produced by LPE. Although their thicknesses vary in a broad range from only several nanometers to several tens of nanometers, the friction force on the pyrophyllite is associated with a single peak in the corresponding histogram given in figure S1(c) (the observed dispersion (width of the histogram peak) is very similar to the dispersion of the friction force measured on SiO2 substrate).

3.4. Wear

The next step was to analyze wear properties and behavior of 2D pyrophyllite for high normal load applied by the AFM tip during scanning in contact mode. Fig. 6(a) displays the topography recorded after the AFM scratching of the central square domain. From the right, left, and top side, the scratched domain is surrounded by walls (represented by a bright contrast) formed from the material deposited by the AFM tip. Enlarged topographic image of the scratched area is presented in Fig. 6(b) together with the characteristic height profile in Fig. 6(c). At the bottom of the figure, the pyrophyllite surface is flat and without visible wear scars due to low normal load. At the same

time, the lateral force recorded during the AFM scratching is low and approximately constant as depicted in Fig. 6(d) and (e). Since there is no wear, the lateral force corresponds to the friction between the AFM tip and pyrophyllite.

In the experiment, the normal load was increasing as the AFM tip was moving from the bottom to the top. For high enough normal load of around 1.1 µN, the wear was initiated and afterwards, the normal load was held constant. As a result of the wear, pyrophyllite surface became crumpled with many local holes and bumps. The holes present local depressions made by peeling pyrophyllite layers, while bumps are local hills formed out of the material previously peeled off (Fig. 6(c)). The height profile in Fig. 6(c) reveals several step heights of ~1 nm. They correspond to single layer of pyrophyllite which therefore indicates that the AFM scratching leads to layer-by-layer peeling. The lateral force during the scratching (Fig. 6(d) and (e)) is increased compared to the bottom area without wear scars. Although this is expected due to higher normal load applied by the AFM tip, the lateral force profile is not flat anymore, but strongly oscillating. Obviously, bright puddles in the force map (Fig. 6(d)) and peaks in the force profile (Fig. 6(e)) correspond to strongly increased lateral force required for tearing and peeling of pyrophyllite layers.

According to the presented results, during the AFM scratching, pyrophyllite behaves in a different manner compared to well known 2D materials such as graphene and transition metal dichalcogenides (MoS₂, and WS₂) [52,53]. The scratching of these materials is associated with wrinkling at the initial stage, while at higher normal loads, it is followed by a sudden tearing along the direction of the AFM tip movement, and finally by a peeling of large segments and their folding. On the other hand, in the case of pyrophillite, exfoliated segments made by the AFM scratching are small, not folded, and they form local bumps of irregular shapes. Recently, similar results have been obtained for muscovite (mica), another phyllosilicate van der Waals mineral, and

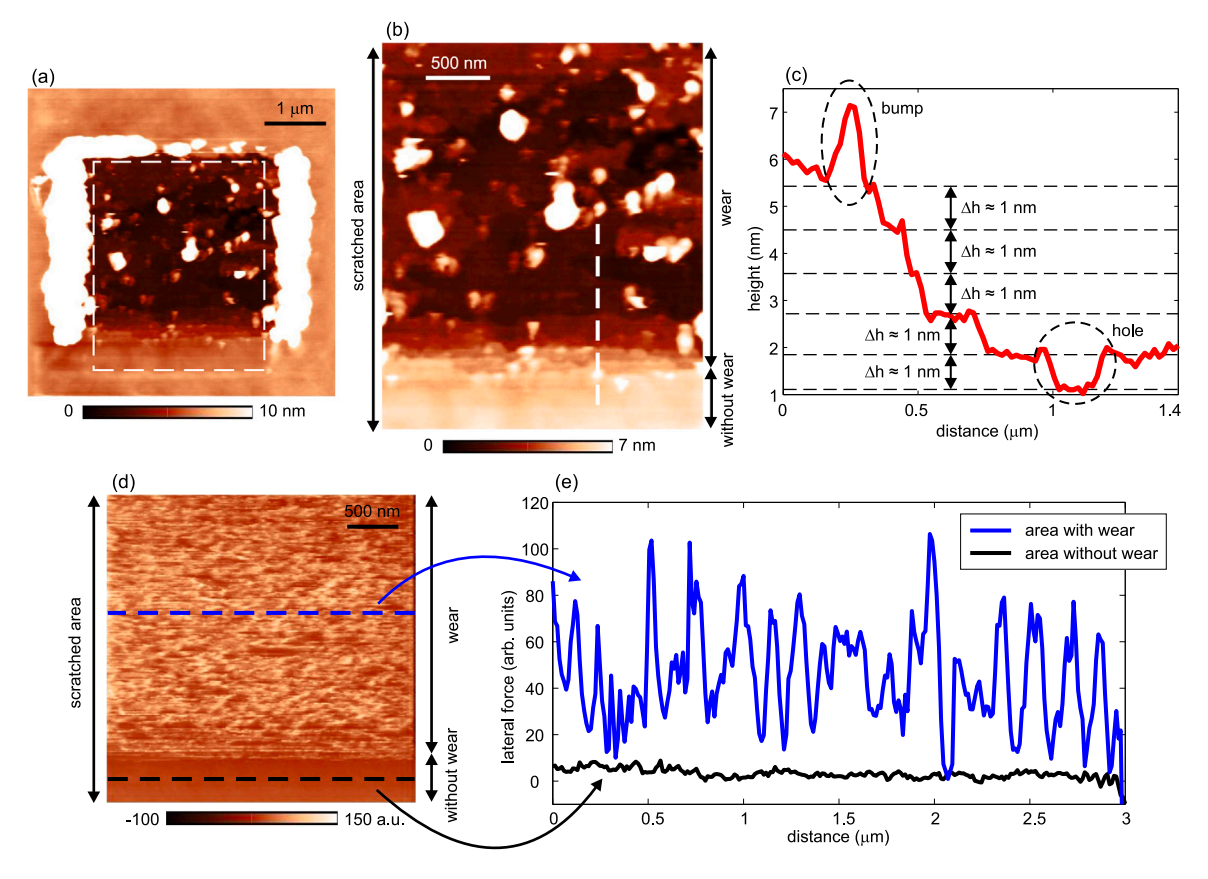


Fig. 6. (a) Topographic image of a pyrophyllite flake after the AFM scratching. (b) The topographic image of the domain encircled by the dashed line in (a) focusing on the scratched area only. (c) The height profile along the dashed line in (b) with indicated step heights of \sim 1 nm and local hole/bump (encircled by dashed lines). (d) The lateral force map recorded during the AFM scratching. (e) The lateral force profiles along two dashed lines in (d), standing for the area with and without wear.

the observed difference in wear properties were explained by different mechanical properties [53]. Accordingly, significant thickness of single layer of pyrophyllite (\sim 1 nm) and large bending rigidity of \sim 70 eV [54] limit its flexibility and folding. At the same time, Young's modulus (modulus of elasticity) of \sim 100 GPa [55,56] and tensile strength less than 10 GPa [56,57] are much lower than in the case of graphene and transition metal dichalcogenides, which indicates much brittle structure of pyrophyllite. This can be indirectly confirmed by comparing threshold normal loads needed to initiate wear. In the case of graphene and transition metal dichalcogenides, the threshold load is at least several μ N [52,53], while in the case of pyrophyllite, it is much lower, around 1 μ N. As a result, pyrophillite layers are easily torn into small pieces during AFM scratching.

Wear of 2D materials is always started from their edges (these are weak points for wear), and not on homogeneous (flat) 2D flakes [58]. Since LPE 2D materials are associated with small flakes and huge number of exposed edges, their wear resistance is determined by their edges [59], and it is always lower that the wear resistivity of 2D material itself. For this reason, wear of LPE pyrophyllite was not studied here.

3.5. Nanoscale machining and nanolithography

As mentioned in the previous section, the AFM scratching of graphene and transition metal dichalcogenides generally leads to their peeling, but not to local cutting along directions defined by the movement of the AFM tip. On the other hand, lower elasticity and tensile strength of 2D pyrophyllite indicate that it could be suitable material for AFM scratching based nanolithography. The results of the nanolithography of 2D pyrophyllite are presented in Fig. 7. Three basic shapes and characteristic height profiles are presented for the following

cases: the hole made by nanoindentation (Fig. 7(a–b)), the trench carved out by line scratching (Fig. 7(c–d)), and the square crater made by raster scratching (Fig. 7(e–f)). As can be seen, the AFM tip induces local carving of a pyrophyllite flake. This process is associated with the tearing of the pyrophyllite into small pieces, which are then deposited around the tip during its motion. The deposited material was then removed by several additional scans in contact AFM mode (not shown here). They were done at lower normal load, which was insufficient to cause pyrophyllite cutting and wear, but high enough to provide pushing of the deposited material by the AFM tip.

As can be seen, 2D pyrophyllite is efficiently carved by applying a local pressure at single point (Fig. 7(a)) as well as during AFM tip motion (Fig. 7(c)). Making of holes on wider areas is successfully achieved by AFM scratching along array of parallel lines (Fig. 7(e)). Depth of created objects was controlled by applied normal load as illustrated in Fig. 7(e-f) showing that a deeper crater was formed by a higher normal force. The width of the line trench in Fig. 7(c) is 150–300 nm. It is strongly influenced by the width of the diamond coated probes employed here, and it is reasonable to expect that a better resolution and more narrow features could be created with sharper AFM tips.

3.6. Electronic bandgap

Electronic bandgap was estimated from UV–VIS spectroscopic measurements. For that purpose, a large-area pyrophyllite film was obtained by LPE. The film thickness was around 20 nm as determined by AFM measurement. Transmittance through the pyrophyllite film for wavelengths in the range 200–900 nm is displayed in the inset of Fig. 8. As can be seen, the film is transparent with the transmittance in the visible region above 97%. The obtained transmittance spectrum allows the calculation of an intrinsic optical absorption coefficient

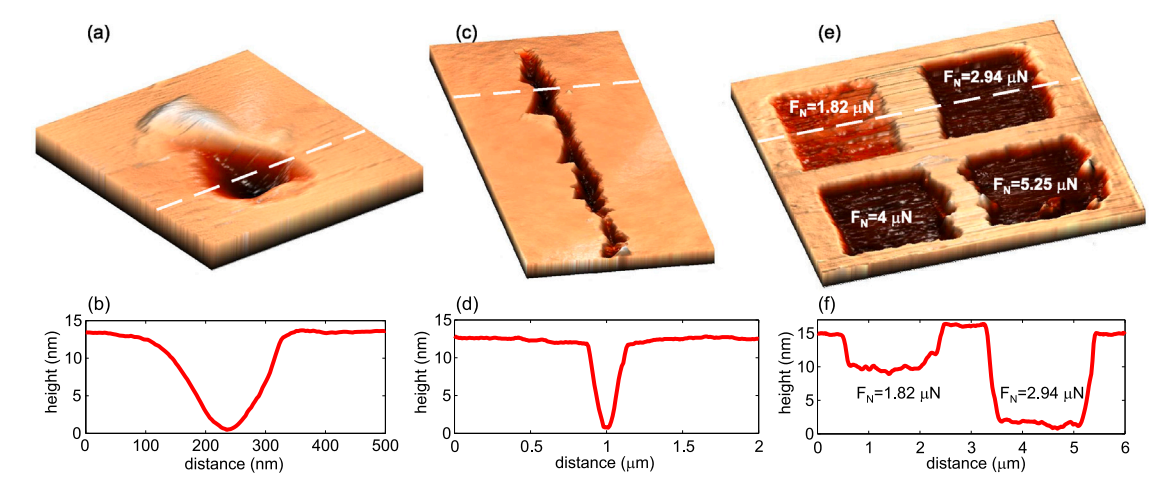


Fig. 7. The topographic images and the height profiles for three characteristic structures made by nanolithography of pyrophyllite: (a-b) single hole obtained by nanoindentation, (c-d) trench made by the AFM scratching along single line, (e-f) four square domains made by raster scratching.

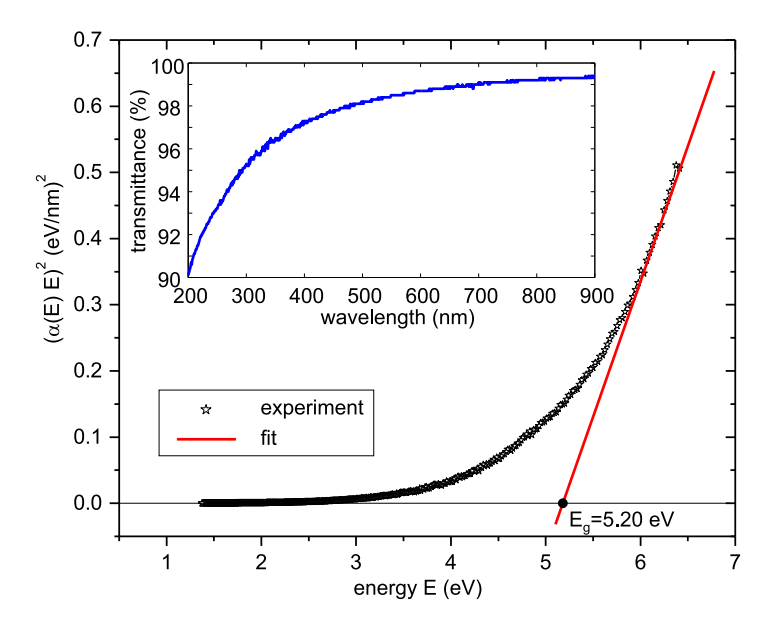


Fig. 8. The Tauc plot with estimated bandgap energy of \sim 5.20 eV obtained from the transmittance (plot in the inset) through \sim 20 nm thick pyrophyllite film obtained by LPE on a quartz substrate.

 $\alpha(E)$. Namely, the well known Bourguer–Lambert–Beer (BLB) law gives the absorption coefficient as $\alpha_{\rm BLB}(E)=(1/d)\ln(1/T)$, where d is the film thickness and T the measured transmittance [60]. This is the simplest law representing the optical absorption in semiconductors, and in practice the BLB law turned out to be more than a good enough approximation.

For the estimation of a direct optical bandgap E_g , we used the Tauc method [61] and the standard fitting procedure of the linear part of $(\alpha(E)E)^2$ (Tauc plot), i.e. $(\alpha(E)E)^2 = \mathrm{const} \cdot (E-E_g)$. The Tauc plot displaying $(\alpha(E)E)^2$ as a function of the energy of incident light E=hv (h is the Planck constant, v is the frequency of incident photon) is given in Fig. 8. The plot indicates that the pyrophyllite film has a direct band gap of around 5.20 eV (the value obtained as the intersection point of the linear fit of the Tauc plot and x-axis). The obtained value is consistent with the theoretical value of 5.42 eV [55], whereas to best of our knowledge, this is the first experimentally obtained value of the pyrophyllite bandgap. The measured value is also close to the band gap of 2D hexagonal boron nitride (\sim 6 eV) [62], which implies that pyrophyllite can be considered as efficient 2D insulator as well.

3.7. Insulating properties and dielectric breakdown

Hexagonal boron nitride has been a standard choice as insulator in 2D electronics [63–67]. Insulating properties and dielectric breakdown are usually explored by placing materials between two metallic electrodes in order to form a capacitor. Furthermore, C-AFM [68, 69] provides characterization at the nanoscale [63–65,70–72]. Recent studies have extended the family of 2D insulators to materials with improved properties, such as high-*k* van der Waals dielectrics [70].

In order to study dielectric properties, 2D pyrophyllite flakes obtained by LPE were deposited on a conductive substrate—thin gold film, which acted as a bottom electrode, while the AFM tip had a role of the top electrode. The topography image (Fig. 9(a)), corresponding current map (Fig. 9(b)), and characteristic profiles (Fig. 9(c)) reveal that pyrophyllite flakes with a thickness ranging from 3 nm to 22 nm are associated with a dark (black) contrast in the current map and zero current. The black color of pyrophyllite flakes in the current map in Fig. 9(b) is spatially homogeneous and therefore it does not contain current spikes which would indicate a possible dielectric breakdown. As a result, at the applied bias voltage U=2 V, several nanometer thick pyrophyllite behaves as 2D insulator.

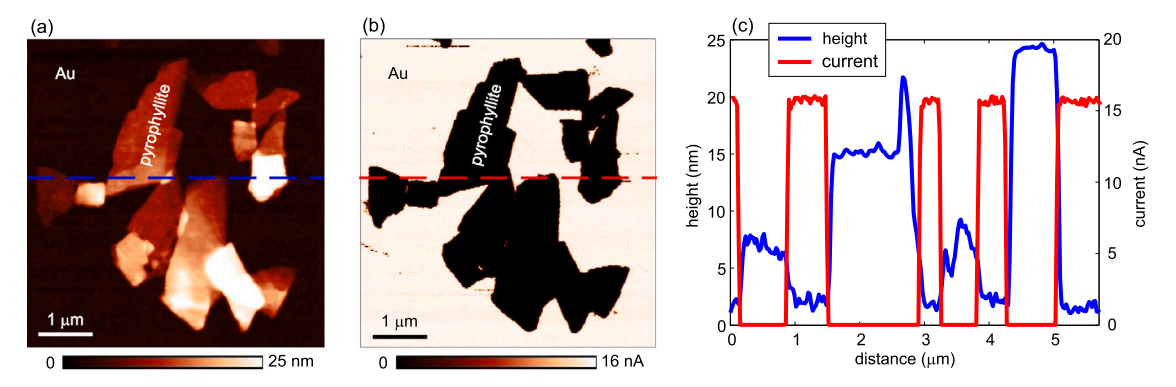


Fig. 9. (a) Topography and (b) the corresponding current maps of the pyrophillite flakes (obtained by LPE) deposited onto gold substrate. (c) The overlapped height and current profiles along the dashed lines in (a) and (b).

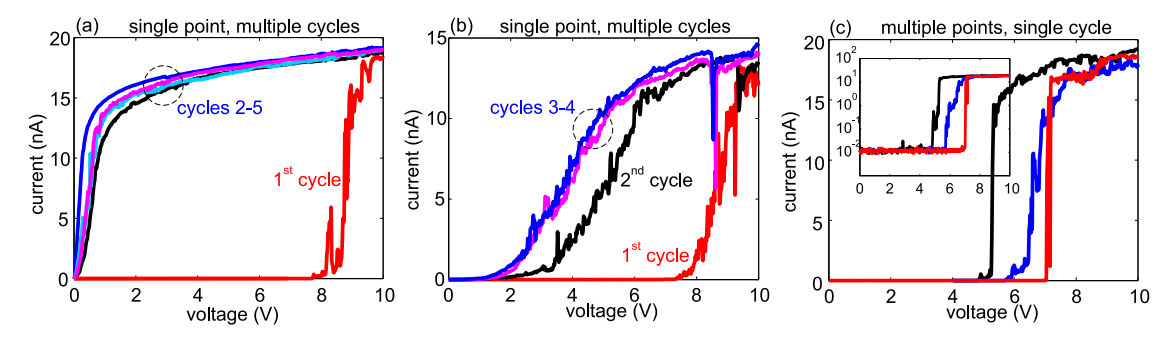


Fig. 10. (a) and (b) Successive cycles of the I/V curves measured at single point (but two different points). (c) The I/V curves (the first cycle only) measured at three different points of the same 10 nm thick pyrophyllite flake. The inset displays the I/V curves in semi-logarithmic scale.

In order to induce a dielectric breakdown, local I/V curves were measured in a wider voltage range. Typical results are given in Fig. 10(a) showing five successive cycles measured at the same point in the voltage range ± 10 V. In the first cycle, the current is zero for voltages below ~8 V. After reaching this threshold voltage, the current rapidly grows indicating dielectric breakdown. In the next cycles (2-5), for small voltages below ~0.5 V, the current practically linearly increases with the applied bias voltage without any threshold (small nonlinearities around the zero voltage indicate possible Schottky barriers at the tip-sample contact, whereas the decreased slope of I/V curves for the voltages higher than ~0.5 V is due to limitations of the current amplifier). Therefore, pyrophyllite does not behave as an insulator anymore and the metallic AFM tip is practically short circuited by the bottom gold electrode. In another case presented in Fig. 10(b), after the first cycle and dielectric breakdown, the region with zero (or near to zero) current becomes narrower indicating gradually decreasing the electronic bandgap of pyrophyllite.

Fig. 10(c) displays the I/V curves (only the first cycles shown) measured at three different points on the same flake. Rapid increase of the current is observed for threshold voltage in the range 5-7 V. The semilogarithmic scale displayed in the inset reveals that below the threshold voltage, the current is at almost constant level in the order of 10^{-2} nA. Taking into account that the thickness of examined pyrophyllite flake was ~10 nm, the dielectric breakdown strength of 2D pyrophyllite is around 6 MV/cm. Although the obtained value is slightly below the strength of 2D hexagonal boron-nitride (~8 MV/cm) [63], the presented results indicate that 2D pyrophyllite has good insulating properties and could be considered as an efficient 2D dielectric and gate oxide. One of the main issue with applications of hexagonal boron-nitride as 2D insulator is its low dielectric constant (~3.9) responsible for high leakage currents. Although dielectric measurements of pyrophyllite are very rare [36,37], it is reasonable to expect lower leakage currents due to larger dielectric constant of pyrophyllite of around 10, which is also similar to the permittivity of the second

member of 2:1 family of phyllosilicates—talc [73]. Still, this has to be confirmed in future studies since leakage currents are influenced by other factors, such as layers' quality (absence of structural defects) and the conduction/valence band discontinuity with respect to the substrate.

Morphological changes after the dielectric breakdown of phyrophyllite are illustrated in Fig. 11. Two- and three-dimensional images of the pyrophyllite flake (Fig. 11(a) and (b), respectively) are recorded in tapping mode after 30 I/V curves measured in the range ± 10 V at the point marked by the arrow. As can be seen, a small hole appeared at the point where the I/V curves were measured, while protrusions appeared around the hole. Height profile in Fig. 11(c) reveals that the hole depth is around 1 nm which corresponds to the thickness of single layer of pyrophyllite. The presented results demonstrate that high local electric fields causing dielectric breakdown lead to local fracture of 2D pyrophyllite. The hole depth equal to the thickness of single layer of pyrophyllite indicates that in the considered case, only the most top pyrophyllite layer was locally cut, while the pyrophyllite thickness is reduced at this point. Although additional measurements should be done in future studies, these results suggest layer-by-layer breakdown of pyrophyllite which was previously confirmed in the case of hexagonal boron nitride [65].

Friction measurements done after the induced dielectric breakdown demonstrate that the point where I/V curves were previously measured is associated with increased friction compared to the rest of pyrophyllite flake. The increased friction indicates some chemical and/or structural changes on the pyrophyllite surface which should be further explored in future studies.

4. Conclusions

In a summary, we have thoroughly characterized pyrophyllite crystal and then successfully fabricated 2D flakes by using both mechanical exfoliation and LPE. Pyrophyllite was exfoliated down to single layer.



Fig. 11. (a) Two-dimensional topographic image of the pyrophyllite flake after 30 I/V curves measured in the range ± 10 V at the point marked by the arrow. (b) Three-dimensional topographic image of the area marked by dashed square in (a). (c) Height profile along the dashed line marked in (a).

The lateral size of typical few-layer flakes was in the order of $10~\mu m$ in the case of the mechanical exfoliation, and 1 μm in the case of the LPE. 2D pyrophyllite has different wear properties compared to graphene and transition metal dichalcogenides. The wear is initiated at much lower normal loads while AFM based scratching leads to the tearing of pyrophyllite into small pieces, contrary to nano-exfoliation and folding, typically observed on graphene for example. Such wear properties provide easy machining at the nanoscale by the AFM tip which can be used as a tool for local carving and reshaping of pyrophyllite flakes. At the same time, 2D pyrophyllite has a low friction coefficient of ~ 0.1 and therefore, it joins the family of other van der Waals layered materials as a potential candidate for ultra-thin coatings aimed for solid lubrication in micro- and nano-mechanical devices. The optical measurements on thin (~20 nm) 2D pyrophyllite film obtained by the LPE reveal that it is transparent in the visible domain, with a large band gap of 5.2 eV. The local studies by C-AFM demonstrated that several nanometer thick pyrophyllite flakes behaves as 2D insulators with a high breakdown voltage of around 6 MV/cm, which is close to hexagonal boron-nitride. In addition, the larger dielectric permittivity of pyrophyllite compared to the boron nitride could provide lower leakage currents which needs to be confirmed in future studies.

CRediT authorship contribution statement

Borislav Vasić: Conceptualization, Investigation, Methodology, Formal analysis, Visualization, Writing – original draft. Radoš Gajić: Conceptualization, Investigation, Formal analysis, Resources, Supervision, Funding acquisition, Writing – review & editing. Ivana Milošević: Investigation, Visualization. Visualization. Visualization. Marko Opačić: Investigation, Formal analysis, Visualization. Aleksandar Kremenović: Investigation, Formal analysis, Visualization, Writing – review & editing. Dejan Lazić: Investigation, Formal analysis.

Declaration of competing interest

The authors declare that they have no known competing financial interests or personal relationships that could have appeared to influence the work reported in this paper.

Data availability

Data will be made available on request.

Acknowledgments

We acknowledge funding provided by the Institute of Physics Belgrade, through the grant of the Ministry of Education, Science, and Technological Development of the Republic of Serbia. A. K. acknowledges funding provided by the Ministry of Education, Science and Technological Development of the Republic of Serbia (contract No. 451-03-68/2022-14/200126).

Appendix A. Supplementary data

Supplementary material related to this article can be found online at https://doi.org/10.1016/j.apsusc.2022.155114.

References

- K.S. Novoselov, A.K. Geim, S.V. Morozov, D. Jiang, Y. Zhang, S.V. Dubonos, I.V. Grigorieva, A.A. Firsov, Electric field effect in atomically thin carbon films, Science 306 (2004) 666–669.
- [2] A.K. Geim, K.S. Novoselov, The rise of graphene, Nature Mater. 6 (2007) 183–191.
- [3] T.F. Avouris, P. nad Heinz, T. Low, 2D Materials, Cambridge University Press, 2017.
- [4] Y.M. Jhon, J.H. Lee, 2D Materials for Nanophotonics, Elsevier, 2021.
- [5] M. Houssa, A. Dimoulas, A. Molle, 2D Materials for Nanoelectronics, CRC Press, 2016
- [6] B. Radisavljevic, A. Radenovic, J. Brivio, V. Giacometti, A. Kis, Single-layer MoS₂ transistors, Nat. Nanotechnol. 6 (2011) 147–150.
- [7] M. Xu, T. Liang, M. Shi, H. Chen, Graphene-like two-dimensional materials, Chem. Rev. 113 (2013) 3766–3798.
- [8] S.Z. Butler, S.M. Hollen, L. Cao, Y. Cui, J.A. Gupta, H.R. Gutiérrez, T.F. Heinz, S.S. Hong, J. Huang, A.F. Ismach, E. Johnston-Halperin, M. Kuno, V.V. Plashnitsa, R.D. Robinson, R.S. Ruoff, S. Salahuddin, J. Shan, L. Shi, M.G. Spencer, M. Terrones, W. Windl, J.E. Goldberger, Progress, challenges, and opportunities in two-dimensional materials beyond graphene, ACS Nano 7 (2013) 2898–2926.
- [9] R. Ganatra, Q. Zhang, Few-layer MoS₂: A promising layered semiconductor, ACS Nano 8 (2014) 4074–4099.
- [10] S. Manzeli, D. Ovchinnikov, D. Pasquier, O.V. Yazyev, A. Kis, 2D transition metal dichalcogenides, Nat. Rev. Mater. 2 (2017) 17033.
- [11] K. Zhang, Y. Feng, F. Wang, Z. Yang, J. Wang, Two dimensional hexagonal boron nitride (2D-hBN): synthesis, properties and applications, J. Mater. Chem. C 5 (2017) 11992–12022.
- [12] S. Balendhran, S. Walia, H. Nili, S. Sriram, M. Bhaskaran, Elemental analogues of graphene: Silicene, germanene, stanene, and phosphorene, Small 11 (2015) 640–652.
- [13] M. Naguib, V.N. Mochalin, M.W. Barsoum, Y. Gogotsi, 25Th anniversary article: MXenes: A new family of two-dimensional materials, Adv. Mater. 26 (7) (2014) 002, 1005.
- [14] S. Shaikhutdinov, H.-J. Freund, Ultrathin silica films on metals: The long and winding road to understanding the atomic structure, Adv. Mater. 25 (2013) 40, 67
- [15] R. Frisenda, Y. Niu, P. Gant, M. Muñoz, A. Castellanos-Gomez, Naturally occurring van der waals materials, npj 2D Mater. Appl. 4 (2020) 38.
- [16] T. Gould, S. Lebègue, T. Björkman, J.F. Dobson, 2D structures beyond graphene: The brave new world of layered materials and how computers can help discover them, in: F. Iacopi, J. Boeckl, C. Jagadish (Eds.), 2D Materials, Academic Press, 2016, pp. 1–33, Ch. 1.
- [17] K. Momma, F. Izumi, VESTA3 for three-dimensional visualization of crystal, volumetric and morphology data, J. Appl. Crystallogr. 44 (2011) 1272–1276.
- [18] A.B. Alencar, A.P.M. Barboza, B.S. Archanjo, H. Chacham, B.R.A. Neves, Experimental and theoretical investigations of monolayer and few-layer talc, 2D Mater. 2 (2015) 015004.
- [19] A. Harvey, J.B. Boland, I. Godwin, A.G. Kelly, B.M. Szydłowska, G. Murtaza, A. Thomas, D.J. Lewis, P. O'Brien, J.N. Coleman, Exploring the versatility of liquid phase exfoliation: producing 2D nanosheets from talcum powder, cat litter and beach sand, 2D Mater. 4 (2017) 025054.
- [20] A.R. Cadore, E. Mania, A.B. Alencar, N.P. Rezende, S. de Oliveira, K. Watanabe, T. Taniguchi, H. Chacham, L.C. Campos, R.G. Lacerda, Enhancing the response of NH₃ graphene-sensors by using devices with different graphene-substrate distances, Sensors Actuators B 266 (2018) 438–446.

- [21] B. Vasić, C. Czibula, M. Kratzer, B.R.A. Neves, A. Matković, C. Teichert, Twodimensional talc as a van der Waals material for solid lubrication at the nanoscale, Nanotechnology 32 (2021) 265701.
- [22] D. Nutting, G.A. Prando, M. Severijnen, I.D. Barcelos, S. Guo, P.C.M. Christianen, U. Zeitler, Y. Galvão Gobato, F. Withers, Electrical and optical properties of transition metal dichalcogenides on talc dielectrics, Nanoscale 13 (2021) 15853–15858
- [23] G.A. Prando, M.E. Severijnen, I.D. Barcelos, U. Zeitler, P.C.M. Christianen, F. Withers, Y. Galvão Gobato, Revealing excitonic complexes in monolayer WS₂ on talc dielectric, Phys. Rev. Appl. 16 (2021) 064055.
- [24] A.C. Gadelha, T.L. Vasconcelos, L.G. Cançado, A. Jorio, Nano-optical imaging of in-plane homojunctions in graphene and MoS₂ van der Waals heterostructures on talc and SiO₂, J. Phys. Chem. Lett. 12 (2021) 7625–7631.
- [25] A. Castellanos-Gomez, M. Wojtaszek, N. Tombros, N. Agraït, B.J. van Wees, G. Rubio-Bollinger, Atomically thin mica flakes and their application as ultrathin insulating substrates for graphene, Small 7 (2011) 2491–2497.
- [26] X. Ji, Y. Kang, J. Ouyang, Y. Chen, D. Artzi, X. Zeng, Y. Xiao, C. Feng, B. Qi, N.Y. Kim, P.E. Saw, N. Kong, O.C. Farokhzad, W. Tao, 2D black mica nanosheets: Synthesis of ultrathin biotite nanosheets as an intelligent theranostic platform for combination cancer therapy, Adv. Sci. 6 (2019) 1970118.
- [27] Z. Huang, T. Lan, L. Dai, X. Zhao, Z. Wang, Z. Zhang, B. Li, J. Li, J. Liu, B. Ding, A.K. Geim, H.-M. Cheng, B. Liu, 2D functional minerals as sustainable materials for magneto-optics, Adv. Mater. 34, 2110464.
- [28] R. de Oliveira, L.A.G. Guallichico, E. Policarpo, A.R. Cadore, R.O. Freitas, F.M.C. da Silva, V. d. C. Teixeira, R.M. Paniago, H. Chacham, M.J.S. Matos, A. Malachias, K. Krambrock, I.D. Barcelos, High throughput investigation of an emergent and naturally abundant 2D material: Clinochlore, Appl. Surf. Sci. 559 (2022) 153959.
- [29] A.R. Cadore, R. de Oliveira, R. Longuinhos, V. de C. Teixeira, D.A. Nagaoka, V.T. Alvarenga, J. Ribeiro-Soares, K. Watanabe, T. Taniguchi, R.M. Paniago, A. Malachias, K. Krambrock, I.D. Barcelos, C.J.S. de Matos, Exploring the structural and optoelectronic properties of natural insulating phlogopite in van der waals heterostructures, 2D Mater. 9 (2022) 035007.
- [30] Y. Niu, J. Villalva, R. Frisenda, G. Sanchez-Santolino, L. Ruiz-González, E.M. Pérez, M. García-Hernández, E. Burzurí, A. Castellanos-Gomez, Mechanical and liquid phase exfoliation of cylindrite: a natural van der Waals superlattice with intrinsic magnetic interactions. 2D Mater. 6 (2019) 035023.
- [31] A. Matković, L. Ludescher, O.E. Peil, A. Sharma, K.-P. Gradwohl, M. Kratzer, M. Zimmermann, J. Genser, D. Knez, E. Fisslthaler, C. Gammer, A. Lugstein, R.J. Bakker, L. Romaner, D.R.T. Zahn, F. Hofer, G. Salvan, J.G. Raith, C. Teichert, Iron-rich talc as air-stable platform for magnetic two-dimensional materials, npj 2D Mater. Appl. 5 (2021) 94.
- [32] A.J. Molina-Mendoza, E. Giovanelli, W.S. Paz, M.A. Niño, J.O. Island, C. Evangeli, L. Aballe, M. Foerster, H.S.J. van der Zant, G. Rubio-Bollinger, N. Agraït, J.J. Palacios, E.M. Pérez, A. Castellanos-Gomez, Franckeite as a naturally occurring van der Waals heterostructure, Nature Commun. 8 (2017) 14409.
- [33] M. Velický, P.S. Toth, A.M. Rakowski, A.P. Rooney, A. Kozikov, C.R. Woods, A. Mishchenko, L. Fumagalli, J. Yin, V. Zólyomi, T. Georgiou, S.J. Haigh, K.S. Novoselov, R.A.W. Dryfe, Exfoliation of natural van der Waals heterostructures to a single unit cell thickness, Nature Commun. 8 (2017) 14410.
- [34] K. Ray, A.E. Yore, T. Mou, S. Jha, K.K.H. Smithe, B. Wang, E. Pop, A.K.M. Newaz, Photoresponse of natural van der Waals heterostructures, ACS Nano 11 (2017) 6024–6030
- [35] M.A. Ali, H.A.M. Ahmed, H.M. Ahmed, M. Hefni, Pyrophyllite: An economic mineral for different industrial applications, Appl. Sci. 11 (2021) 11357.
- [36] G.W. Timco, Z. Dvorak, H.H. Schloessin, Dielectric properties of pyrophyllite as a function of water vapor pressure, J. Appl. Phys. 47 (1976) 2232–2233.
- [37] E. Izci, The investigation of dielectric properties of pyrophyllite, Key Eng. Mater. 264–268 (2004) 1361–1364.
- [38] E.W. Bucholz, X. Zhao, S.B. Sinnott, S.S. Perry, Friction and wear of pyrophyllite on the atomic scale, Tribol. Lett. 46 (2012) 159–165.
- [39] E.L. Brightbill, Design Rules for Discovering 2D Materials from 3D Crystals, University of North Carolina at Chapel Hill, 2016.
- [40] M. Shamim, T.K. Mukhopadhyay, K. Dana, Kinetic pathway for thermal exfoliation of pyrophyllite, Appl. Clay Sci. 114 (2015) 40–47.
- [41] K.S. Novoselov, D. Jiang, F. Schedin, T.J. Booth, V.V. Khotkevich, S.V. Morozov, A.K. Geim, Two-dimensional atomic crystals, Proc. Natl. Acad. Sci. USA 102 (2005) 10451–10453.
- [42] A. Matković, I. Milošević, M. Milićević, T. Tomašević-Ilić, J. Pešić, M. Musić, M. Spasenović, D. Jovanović, B. Vasić, C. Deeks, R. Panajotović, M.R. Belić, R. Gajić, Enhanced sheet conductivity of Langmuir–Blodgett assembled graphene thin films by chemical doping, 2D Mater. 3 (2016) 015002.
- [43] I.R. Milošević, B. Vasić, A. Matković, J. Vujin, S. Aškrabić, M. Kratzer, T. Griesser, C. Teichert, R. Gajić, Single-step fabrication and work function engineering of Langmuir–Blodgett assembled few-layer graphene films with Li and Au salts, Sci. Rep. 10 (2020) 8476.
- [44] M. Varenberg, I. Etsion, G. Halperin, An improved wedge calibration method for lateral force in atomic force microscopy, Rev. Sci. Instrum. 74 (2003) 3362–3367.
- [45] J.H. Lee, S. Guggenheim, Single crystal X-ray refinement of pyrophyllite-1Tc, Am. Mineral. 66 (1981) 350–357.

- [46] R. Wardle, G.W. Brindley, The crystal structures of pyrophyllite, 1Te, and of its dehydroxylate, Am. Mineral. 57 (1972) 732–750.
- [47] A. Wang, J.J. Freeman, B.L. Jolliff, Understanding the Raman spectral features of phyllosilicates, J. Raman Spectrosc. 46 (2015) 829–845.
- [48] J. Kloprogge, Chapter 6 Raman spectroscopy of clay minerals, in: W.P. Gates, J.T. Kloprogge, J. Madejová, F. Bergaya (Eds.), Infrared and Raman Spectroscopies of Clay Minerals, in: Developments in Clay Science, vol. 8, 2017, pp. 150–199.
- [49] B. Lafuente, R.T. Downs, H. Yang, N. Stone, 1. The power of databases: The RRUFF project, 2015, pp. 1–30.
- [50] P. Nemes-Incze, Z. Osváth, K. Kamarás, L.P. Biró, Anomalies in thickness measurements of graphene and few layer graphite crystals by tapping mode atomic force microscopy, Carbon 46 (2008) 1435–1442.
- [51] K.-S. Kim, H.-J. Lee, C. Lee, S.-K. Lee, H. Jang, J.-H. Ahn, et al., Chemical vapor deposition-grown graphene: The thinnest solid lubricant, ACS Nano 5 (2011) 5107–5114.
- [52] B. Vasić, A. Matković, U. Ralević, M. Belić, R. Gajić, Nanoscale wear of graphene and wear protection by graphene, Carbon 120 (2017) 137–144.
- [53] A. Özoğul, E. Gnecco, M.Z. Baykara, Nanolithography-induced exfoliation of layered materials, Appl. Surf. Sci. Adv. 6 (2021) 100146.
- [54] Y.-T. Fu, G.D. Zartman, M. Yoonessi, L.F. Drummy, H. Heinz, Bending of layered silicates on the nanometer scale: Mechanism, stored energy, and curvature limits, J. Phys. Chem. C 115 (2011) 22292–22300.
- [55] X. Qin, J. Zhao, J. Wang, M. He, Atomic structure, electronic and mechanical properties of pyrophyllite under pressure: A first-principles study, Minerals 10 (2020) 778.
- [56] A. Castellanos-Gomez, M. Poot, A. Amor-Amorós, G.A. Steele, H.S.J. van der Zant, N. Agraït, G. Rubio-Bollinger, Mechanical properties of freely suspended atomically thin dielectric layers of mica, Nano Res. 5 (2012) 550–557.
- [57] G.D. Zartman, H. Liu, B. Akdim, R. Pachter, H. Heinz, Nanoscale tensile, shear, and failure properties of layered silicates as a function of cation density and stress, J. Phys. Chem. C 114 (2010) 1763–1772.
- [58] B. Vasić, A. Matković, R. Gajić, I. Stanković, Wear properties of graphene edges probed by atomic force microscopy based lateral manipulation, Carbon 107 (2016) 723–732.
- [59] R. Buzio, A. Gerbi, S. Uttiya, C. Bernini, A.E. Del Rio Castillo, F. Palazon, A.S. Siri, V. Pellegrini, L. Pellegrino, F. Bonaccorso, Ultralow friction of ink-jet printed graphene flakes. Nanoscale 9 (2017) 7612–7624.
- [60] M. Fox, Optical Properties of Solids, Oxford University Press, 2010.
- [61] P. Makuła, M. Pacia, W. Macyk, How to correctly determine the band gap energy of modified semiconductor photocatalysts based on UV-Vis spectra, J. Phys. Chem. Lett. 9 (2018) 6814–6817.
- [62] G. Cassabois, P. Valvin, B. Gil, Hexagonal boron nitride is an indirect bandgap semiconductor, Nat. Photonics 10 (2016) 262–266.
- [63] G.-H. Lee, Y.-J. Yu, C. Lee, C. Dean, K.L. Shepard, P. Kim, J. Hone, Electron tunneling through atomically flat and ultrathin hexagonal boron nitride, Appl. Phys. Lett. 99 (2011) 243114.
- [64] L. Britnell, R.V. Gorbachev, R. Jalil, B.D. Belle, F. Schedin, M.I. Katsnelson, L. Eaves, S.V. Morozov, A.S. Mayorov, N.M.R. Peres, A.H. Castro Neto, J. Leist, A.K. Geim, L.A. Ponomarenko, K.S. Novoselov, Electron tunneling through ultrathin boron nitride crystalline barriers. Nano Lett. 12 (2012) 1707–1710.
- [65] Y. Hattori, T. Taniguchi, K. Watanabe, K. Nagashio, Layer-by-layer dielectric breakdown of hexagonal boron nitride, ACS Nano 9 (2015) 916–921.
- [66] Y.Y. Illarionov, T. Knobloch, M. Jech, M. Lanza, D. Akinwande, M.I. Vexler, T. Mueller, M.C. Lemme, G. Fiori, F. Schwierz, T. Grasser, Insulators for 2D nanoelectronics: the gap to bridge, Nature Commun. 11 (2020) 3385.
- [67] K.K. Kim, H.S. Lee, Y.H. Lee, Synthesis of hexagonal boron nitride heterostructures for 2D van der Waals electronics, Chem. Soc. Rev. 47 (2018) 6342–6369.
- [68] F. Giannazzo, G. Fisichella, G. Greco, P. Fiorenza, F. Roccaforte, Conductive atomic force microscopy of two-dimensional electron systems: From AlGaN/GaN heterostructures to graphene and MoS₂, in: M. Lanza (Ed.), Conductive Atomic Force Microscopy: Applications in Nanomaterials, WILEY-VCH Verlag, Weinheim, Germany, 2017, pp. 163–186, Ch. 7.
- [69] F. Giannazzo, G. Greco, F. Roccaforte, C. Mahata, M. Lanza, Conductive AFM of 2D materials and heterostructures for nanoelectronics, in: U. Celano (Ed.), Electrical Atomic Force Microscopy for Nanoelectronics, Springer, Berlin, Germany, 2019, pp. 303–350, Ch. 10.
- [70] C.-Y. Zhu, J.-K. Qin, P.-Y. Huang, H.-L. Sun, N.-F. Sun, Y.-L. Shi, L. Zhen, C.-Y. Xu, 2D indium phosphorus sulfide (In₂P₃S₉): An emerging van der Waals high-k dielectrics, Small 18 (2022) 2104401.
- [71] Y. Ji, C. Pan, M. Zhang, S. Long, X. Lian, F. Miao, F. Hui, Y. Shi, L. Larcher, E. Wu, M. Lanza, Boron nitride as two dimensional dielectric: Reliability and dielectric breakdown, Appl. Phys. Lett. 108 (2016) 012905.
- [72] A. Ranjan, N. Raghavan, M. Holwill, K. Watanabe, T. Taniguchi, K.S. Novoselov, K.L. Pey, S.J. O'Shea, Dielectric breakdown in single-crystal hexagonal boron nitride, ACS Appl. Electron. Mater. 3 (2021) 3547–3554.
- [73] J.L. Rosenholtz, D.T. Smith, The dielectric constant of mineral powders, Am. Mineral. 21 (1936) 115–120.



Regular Article - Experimental Physics

Search for the evidence of 209 Bi(γ ,p5n) 203 Pb reaction in 60 MeV bremsstrahlung beams

M. Krmar^{1,a}, N. Jovančević¹, D. Maletić², Ž. Medić², D. Knežević², M. Savić², Yu. Teterev³, S. Mitrofanov³, K. D. Timoshenko³, S. I. Alexeev³, H. Marukyan⁴, I. Kerobyan⁴, R. Avetisyan⁴, L. Poghosyan⁴, R. Dallakyan⁴, A. Hakobyan⁴, L. Vahradyan⁴, H. Mkrtchyan⁴, A. Petrosyan⁴

Received: 2 June 2023 / Accepted: 11 July 2023 / Published online: 26 July 2023

© The Author(s), under exclusive licence to Società Italiana di Fisica and Springer-Verlag GmbH Germany, part of Springer Nature 2023

Communicated by Jose Benlliure

Abstract Samples made from natural bismuth were exposed in 60 MeV end-point bremsstrahlung beam. In this paper, a simple model for determination the share of two ways of 203 Pb formation: by the decay of 203 Bi, produced in 209 Bi(γ ,6n) 203 Bi reaction and by 209 Bi(γ ,5n) 203 Pb reaction is described. The method employs the ratio of 203 Pb and 203 Bi nuclei numbers and activities at the end of the exposure as the input value. This ratio was estimated from gamma spectra measured after irradiation of natural Bi sample. It was found that the rate of production of 203 Pb by 209 Bi(γ ,p) 203 Pb reaction is about 6% of the 203 Bi production rate in the 209 Bi(γ ,6n) 203 Bi reaction. Obtained result is compared with TALYS based estimation.

1 Introduction

The simplest photonuclear reaction (γ,n) usually takes place through the well-known mechanism of giant dipole resonance. For a large number of stable nuclei, the energy differential cross section of this reaction has been successfully measured [1, 2]. Data on photonuclear reactions can be found in available databases [3] also. The experimental evidence for the $(\gamma,2n)$ reaction is much poorer, while for reactions when three or more neutrons are emitted (usually denoted by (γ,xn)), the reaction cross sections can be obtained by mainly by theoretical calculations [4]. For reactions in which a charged particle, such as proton in the simplest case, is emitted (single or in addition to one or more neutrons) there is a much poorer experimental evidence. In the interactions of

high energy photons with nuclei, the probability of emission of a charged particle is significantly lower than the emission of neutrons due to the existence of the Coulomb barrier. It is a reason why experimental data concerning $(\gamma, p \times n)$ are insufficient in literature.

Cross sections for photonuclear reactions on natural bismuth (monoisotope ²⁰⁹Bi) with emission of one and two neutrons can be found in the reference [5]. In several recently published papers [6-11], photonuclear reactions with Bi target exposed in bremsstrahlung photon beams having endpoint energies up to 70 MeV were studied. Irradiation of such a heavy element by the high energy photons can give several products of (γ,xn) reactions. In these publications, the relative yield of photonucleated reactions on ²⁰⁹Bi was analyzed, while in reference [12] the cross section results for reactions (γ,n) , $(\gamma,2n)$, $(\gamma,3n)$ and $(\gamma,4n)$ were presented. The authors of reference [12] used natural bismuth target and quasimonochromatic laser Compton-scattering γ-ray beams with energies up to 40 MeV. In reference [11], reaction channel (γ,pxn) with emission of one proton along with several neutrons is accounted for.

In this paper, an attempt was made to establish experimental evidence for $^{209}\text{Bi}(\gamma,p\,5\text{n})^{203}\text{Pb}$ nuclear reaction by comparison of intensities of gamma lines following EC decay of ^{203}Bi and ^{203}Pb . Lead-203 can be formed by $(\gamma,p\,5\text{n})$ nuclear reaction, but it is certainly created after decay of ^{203}Bi , obtained in $^{209}\text{Bi}(\gamma,6\text{n})^{203}\text{Bi}$ reaction. After activation of the target made from natural bismuth by 60 MeV endpoint energy bremsstrahlung beam, several gamma spectra were successively measured. Gamma lines from the measured spectra were selected in order to estimate the ratio of created nuclei numbers of ^{203}Bi and ^{203}Pb in the moment



¹ Physics Department, Faculty of Science, University Novi Sad, Novi Sad, Serbia

² Institute of Physics, Belgrade, Serbia

³ Flerov Laboratory of Nuclear Reactions, Joint Institute for Nuclear Research, Dubna, Russia

⁴ A. Alikhanyan National Science Laboratory (Yerevan Physics Institute), Yerevan, Armenia

^a e-mail: krmar@df.uns.ac.rs(corresponding author)

170 Page 2 of 9 Eur. Phys. J. A (2023) 59:170

Fig. 1 Part of the chart containing relevant nuclides

Bi202	Bi203	Bi204	Bi205	Bi206	Bi207	Bi208	Bi209
1.72 h	11.76 h	11.22 h	15.31 d	6.243 d	31.55 y	3.68E5 y	Stable
5+	9/2-	6+	9/2-	6(+)	9/2+	(5)+	9/2-
EC,α	EC,α	EC	EC	EC	EC	EC	100%
Pb201	Pb202	Pb203	Pb204	Pb205	Pb206	Pb207	Pb208
9.33 h	5.24E4 y	51.873 h	1.4E17 y	1.53E7 y	Stable	Stable	Stable
5/2-	0+	5/2-	0+	5/2-	0+	1/2-	0+
EC	EC	EC	1.4%	EC	24.1%	24.1%	52.4%

when irradiation was stopped. Probability ratio for the occurrence of $(\gamma,6n)$ and $(\gamma,p\,5n)$ nuclear reactions can be obtained from these data.

For the purposes of this paper, the cross sections for the observed nuclear reactions were extracted using the TALYS code. These cross-sections were used to estimate the ratio of probabilities of nuclear reactions of interest in order to compare them with the values obtained by measurements.

2 Materials and methods

Considering that lead isotopes ^{206}Pb , ^{207}Pb and ^{208}Pb are stable (Fig. 1), $^{209}\text{Bi}(\gamma,\text{p3n})^{205}\text{Pb}$ is the very first photonuclear reaction on ^{209}Bi which can give active lead as a product. However, half life of ^{205}Pb is $1.57\cdot 10^7$ y and small amount of produced ^{205}Pb , would be very difficult to detect. Moreover, this isotope does not emit gamma radiation.

The next candidate which can be used to verify if (γ,pxn) on natural bismuth can yield measurable amounts of reaction products is 204m Pb. Half life of 204m Pb is 67.2 min and deexcitation of isomer state takes place through several gamma transitions having high quantum yield. However, 204m Pb can be created by decay of 204 Bi, produced in $(\gamma,5n)$ photonuclear reaction. This means that de-excitation of the isomeric state of 204m Pb created in $(\gamma,p$ 4n) results in gamma transitions that are almost the same as those occurred after the 204 Bi decay. It is very difficult to estimate how 204 Bi decay and 204m Pb de-excitation contribute to the total intensity of some of measured gamma lines.

Another possibility to check if irradiation of 209 Bi by high-energy photons results in proton emission together with several neutrons is lead isotope 203 Pb. This isotope can be created by $(\gamma,p 5n)$ reaction. Half-life of 203 Pb is 51.873 h and after decay two intensive lines in gamma spectra can be observed. A study of gamma photons originating from the decay of 203 Pb could be a good way to determine if $(\gamma,p 5n)$ reaction can give measurable amount of 203 Pb during irradiation of the natural bismuth target by high energy photons. But in order to do that, it is necessary to estimate, in some way, how much of the 203 Pb activity comes from decay of 203 Bi.



In interactions of 209 Bi nuclei with high energy photons, several bismuth isotopes can be created through (γ, xn) reactions. Suppose that a bismuth isotope 203 Bi, we have chosen to analyze, is formed at a constant rate q in a photon beam. The change of the number of nuclei of observed bismuth isotope can then be described by the following differential equation:

$$\frac{dN_{Bi}}{dt} = q - \lambda_{Bi} N_{Bi} \tag{1}$$

 λ_{Bi} is decay constant of ²⁰³Bi, created in (γ ,6n) photonuclear reaction. The number of created ²⁰³Bi nuclides after irradiation time t_{irr} is:

$$N_{Bi} = \frac{q}{\lambda_{Bi}} (1 - \exp(-\lambda_{Bi} t_{irr})) \tag{2}$$

The dynamics of the number of 203 Pb nuclei created exclusively by the decay of 203 Bi can be expressed as:

$$\frac{dN_{Pb}}{dt} = \lambda_{Bi} N_{Bi} - \lambda_{Pb} N_{Pb} \tag{3}$$

The very same 203 Pb isotope can additionally be produced through the $(\gamma, p 5n)$ nuclear reaction. In the case when the production of 203 Pb occurs, process can be described by the following equation:

$$\frac{dN_{Pb}}{dt} = \lambda_{Bi} N_{Bi} + p - \lambda_{Pb} N_{Pb} \tag{4}$$

where p denotes a constant rate of 203 Pb production through the $(\gamma, p 5n)$ nuclear reaction. It can be considered that at the very beginning (t = 0), there were no 203 Pb nuclei. The solutions of differential Eqs. 3 and 4 describing time evolution of the number of 203 Pb isotopes are:

$$N_{Pb} = q \left[\frac{1}{\lambda_{Pb}} (1 - \exp(-\lambda_{Pb} t_{irr})) + \frac{1}{\lambda_{Pb} - \lambda_{Bi}} (\exp(-\lambda_{Pb} t_{irr}) - \exp(-\lambda_{Bi} t_{irr})) \right]$$
(5)



Eur. Phys. J. A (2023) 59:170 Page 3 of 9 170

in the case when ²⁰³Pb originates from the decay of ²⁰³Bi, and

$$N_{Pb} = q \left[\frac{1 + \frac{p}{q}}{\lambda_{Pb}} (1 - \exp(-\lambda_{Pb} t_{irr})) + \frac{1}{\lambda_{Pb} - \lambda_{Bi}} (\exp(-\lambda_{Pb} t_{irr}) - \exp(-\lambda_{Bi} t_{irr})) \right]$$
(6)

when production of ^{203}Pb through $(\gamma,p\ 5n)$ can not be neglected.

Using Eqs. 2 and 5 ratio $N_{Pb}(t_{irr})/N_{Bi}(t_{irr})$ of produced numbers of ²⁰³Pb and ²⁰³Bi nuclei, in the case when ²⁰³Pb is produced only by the ²⁰³Bi decay, can be determined as:

will decrease according to a well-known exponential law

$$N_{Bi}(t) = N_{Bi}^{0} \exp(-\lambda_{Bi} t) \tag{9}$$

while the dynamics of the time change of ²⁰³Pb activity will be determined by the rate of its simultaneous decay and creation from ²⁰³Bi. It is well known that a number of daughter nuclei in the case of simultaneous decay can be described as:

$$N_{Pb}(t) = \frac{\lambda_{Bi}}{\lambda_{Pb} - \lambda_{Bi}} N_{Bi}^{0}(\exp(-\lambda_{Bi}t) - \exp(-\lambda_{Pb}t)) + N_{Pb}^{0}\exp(-\lambda_{Pb}t)$$
(10)

$$\frac{N_{Pb}(t_{irr})}{N_{Bi}(t_{irr})} = \frac{\frac{\lambda_{Bi}}{\lambda_{Pb}}(1 - \exp(-\lambda_{Pb}t_{irr})) + \frac{\lambda_{Bi}}{\lambda_{Pb} - \lambda_{Bi}}(\exp(-\lambda_{Pb}t_{irr}) - \exp(-\lambda_{Bi}t_{irr}))}{1 - \exp(-\lambda_{Bi}t_{irr})}$$
(7)

It can be seen from Eq. 7 that the ratio of 203 Pb and 203 Bi nuclei numbers does not depend on the rate q at which Bi is generated in photonuclear reaction.

In a similar way, using Eqs. 2 and 6, it can be determined the 203 Pb/ 203 Bi nuclei number ratio for the case when the 203 Pb isotope is formed by decay of 203 Bi and the direct 209 Bi(γ ,p. 5n) reaction as well.

Let's assume that the recording of the gamma spectrum started at the moment t_1 after the end of the irradiation, and that the measurement was stopped at the moment t_2 . In that time interval, the number of decayed 203 Bi nuclei is:

$$\frac{N_{Pb}(t_{irr})}{N_{Bi}(t_{irr})} = \frac{(1 + \frac{p}{q})\frac{\lambda_{Bi}}{\lambda_{Pb}}(1 - \exp(-\lambda_{Pb}t_{irr})) + \frac{\lambda_{Bi}}{\lambda_{Pb} - \lambda_{Bi}}(\exp(-\lambda_{Pb}t_{irr}) - \exp(-\lambda_{Bi}t_{irr}))}{1 - \exp(-\lambda_{Bi}t_{irr})}$$
(8)

From the above Eq. 8, we can see that the ratio p/q, ie. the production rate of 203 Bi by the emission of six neutrons and the rate of production of 203 Pb by $(\gamma,p 5n)$ nuclear reaction affects ratio of these two isobars. It can be seen that, if there is no proton emission, ie. if p = 0, Eq. 8 turns into Eq. 7.

All the above equations, as well as those that will follow in which the ratios of the nuclei of the observed two isotopes N_{Pb}/N_{Bi} can be written in the form where the ratios of their activities A_{Pb}/A_{Bi} appear.

2.2 Decay measurement

At the moment when the irradiation is completed, there will be some number of both radionuclides in the bismuth sample: $N_{Pb}(t_{irr})$ and $N_{Bi}(t_{irr})$. After the end of the irradiation, it is possible to register gamma spectra of irradiated sample and $N_{Pb}(t_{irr})$ and $N_{Bi}(t_{irr})$ can be considered as the initial numbers of ²⁰³Bi and ²⁰³Pb. Let's denote them as N_{Bi}^{0} and N_{Pb}^{0} . Starting from the end of irradiation, activity of ²⁰³Bi

$$N_{Bi}^{D} = N_{Bi}^{0}(\exp(-\lambda_{Bi}t_1) - \exp(-\lambda_{Bi}t_2))$$
 (11)

By integrating the function that describes the temporal change of ²⁰³Pb activity within the same time limits, it is obtained that the total number of ²⁰³Pb nuclei that decayed is:

$$N_{Pb}^{D} = \frac{\lambda_{Bi}}{\lambda_{Bi} - \lambda_{Pb}} N_{Bi}^{0} (\exp(-\lambda_{Pb}t_1) - \exp(-\lambda_{Pb}t_2))$$
$$-\frac{\lambda_{Pb}}{\lambda_{Bi} - \lambda_{Pb}} N_{Bi}^{0} (\exp(-\lambda_{Bi}t_1) - \exp(-\lambda_{Bi}t_2))$$
$$+ N_{Pb}^{0} (\exp(-\lambda_{Pb}t_1) - \exp(-\lambda_{Pb}t_2)) \tag{12}$$

From Eqs. 11 and 12 the values of N_{Bi}^0 and N_{Pb}^0 can be estimated, but in some cases it is more convenient to analyze the ratio of the number of decays of the observed two nuclides:



170 Page 4 of 9 Eur. Phys. J. A (2023) 59:170

$$\frac{N_{Pb}^{D}}{N_{Bi}^{D}} = \frac{\lambda_{Bi}}{\lambda_{Bi} - \lambda_{Pb}} \frac{\exp(-\lambda_{Pb}t_{1}) - \exp(-\lambda_{Pb}t_{2})}{\exp(-\lambda_{Bi}t_{1}) - \exp(-\lambda_{Bi}t_{2})} - \frac{\lambda_{Pb}}{\lambda_{Bi} - \lambda_{Pb}} + \frac{N_{Pb}^{0}}{N_{Bi}^{0}} \frac{\exp(-\lambda_{Pb}t_{1}) - \exp(-\lambda_{Pb}t_{2})}{\exp(-\lambda_{Bi}t_{1}) - \exp(-\lambda_{Bi}t_{2})}$$
(13)

As can be seen from Eq. 13, if the ratio of the decay numbers of 203 Pb and 203 Bi is known, it is possible to estimate the ratio of the initial numbers of these two nuclides N_{Ph}^{0}/N_{Bi}^{0} .

In order to determine the ratio of the number of decays N_{Pb}^D/N_{Bi}^D in a selected time interval, two gamma lines, one from ²⁰³Pb and another from ²⁰³Bi should be selected their intensities should be determined. Let's denote registered intensities with N_{Bi}^R and N_{Pb}^R . Ratio N_{Pb}^D/N_{Bi}^D can be determined as:

$$\frac{N_{Pb}^{D}}{N_{Bi}^{D}} = \frac{N_{Pb}^{R}}{N_{Bi}^{R}} \frac{\varepsilon_{Bi} p_{\gamma}^{Bi}}{\varepsilon_{Pb} p_{\gamma}^{Pb}}$$
(14)

The quantum yields of the observed gamma transitions of ^{203}Bi and ^{203}Pb are denoted by p_{γ}^{Bi} and p_{γ}^{Pb} while ε_{Bi} and ε_{Pb} are the absolute detection efficiency at the selected energies. From Eq. 14 it can be seen that it is sufficient to know the relative efficiency of the detector system for the used geometry.

2.3 Procedure of the results extraction

And finally, let's summarize the procedure that can be used to prove whether a measurable contribution of $(\gamma, p \ 5n)$ reaction could be expected:

- (a) the ratio of 203 Pb and 203 Bi nuclei numbers, expected at the end of irradiation, without contribution of (γ ,p 5n) reaction, could be calculated using Eq. 7;
- (b) intensities of selected gamma lines should be obtained. The N_{Ph}^D/N_{Ri}^D ratio can be calculated using Eq. 14;
- (c) Equation 13 should be used to obtain the ratio of initial nuclei numbers N_{Pb}^0/N_{Bi}^0 , created during exposition in the photon beam;
- (d) obtained N_{Pb}^0/N_{Bi}^0 ratio can be compared with the result derived from Eq. 7. If the obtained values coincide within the interval of experimental error, it can be concluded that the reaction $(\gamma, p, 5n)$ does not give a measurable contribution to the activity of 203 Pb. However, if the contribution of the reaction $(\gamma, p, 5n)$ to the total number of 203 Pb cannot be neglected, the N_{Pb}^0/N_{Bi}^0 ratio obtained by Eq. 13 should be greater than the ratio acquired from Eq. 7
- e) and finally, if the ratios N_{Pb}^0/N_{Bi}^0 differ, it is possible to find the value of the parameter p/q in Eq. 8 which gives the N_{Pb}^0/N_{Bi}^0 ratio experimentally established.

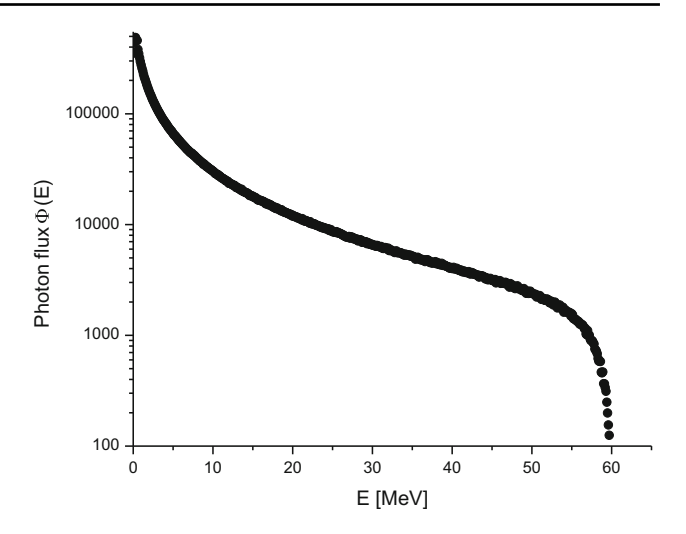


Fig. 2 The shape of the photon spectrum $\Phi(E)$ obtained for 30 M incident electrons

The described procedure can give confirmation about contribution of the $(\gamma, p \ 5n)$ reaction to the total activity of ²⁰³Pb and to estimate the value p/q.

2.4 Theoretical calculations

The rate of some nuclear reaction at the selected target is directly proportional to the product of the cross section and the number of incident particles. This means that the quantities p and q would be proportional to the saturation activities of observed reactions:

$$q \sim \int_{E_{\star}}^{E_{max}} \sigma_{6n}(E) \Phi(E) dE \tag{15}$$

$$p \sim \int_{E_t}^{E_{max}} \sigma_{p,5n}(E) \Phi(E) dE \tag{16}$$

where $\Phi(E)$ is photon fluency, E_t is energy threshold for observed nuclear reaction and E_{max} is end-point energy of the photon spectra (in our case 60 MeV). By $\sigma_{6n}(E)$ and $\sigma_{p,5n}(E)$ cross-sections for $(\gamma,6n)$ and $(\gamma,p,5n)$ nuclear reactions are denoted respectively.

The simplest way to check the obtained result for the p/q ratio would be to calculate the saturation activities for these two reactions using Eqs. 15 and 16 and compare them with the experimental result.

The shape of the photon spectrum $\Phi(E)$ is obtained by using Geant4 software package [13], version v11.1.0, with standard G4 electromagnetic physics option selected. The simulation starts with creating 30 M of 60 MeV electrons in the beam, with very small Gaussian spread in energy of 0.01 MeV. The photon spectrum, obtained at the place of irradiated sample based on the geometry described in the next section is presented in Fig. 2.



Eur. Phys. J. A (2023) 59:170 Page 5 of 9 170

There is no experimental evidence of the cross sections of ²⁰⁹Bi (γ,6n) and ²⁰⁹Bi (γ,p 5n) nuclear reactions in literature. Related information can be obtained using some numerical code for evaluation of the cross sections for nuclear reactions. In this experiment, TALYS 1.9 code was used to estimate cross sections for 209 Bi(γ ,p 5n) 203 Pb and ²⁰⁹Bi(γ,6n)²⁰³Bi reactions. It was decided to use SMLO model for a strength function. It can be expected that the choice of the strength function model has an impact on the estimation of the cross section, but that analysis is beyond the scope of this paper. Six different models of level density were employed in calculations. Cross sections were calculated using phenomenological (1. The Fermi Gas Model + Constant Temperature Model, 2. The Back-shifted Fermi gas Model, 3. The Generalized Superfluid Model) and microscopic (4. Skyrme-Hartree-Fock-Bogoluybov, 5. Gogny-Hartree-Fock-Bogoluybov and temperature-dependent 6. Gogny-Hartree-Fock-Bogoluvbov models) of level density [14].

3 Measurements

One coin-shaped sample of natural bismuth (high purity 99.999%), 1 cm diameter and mass of 1.1 g, was exposed in bremsstrahlung photon beam having maximal energy of 60 MeV. The source of the photon beams was the linear electron accelerator LUE-75 located at A. Alikhanyan National Science Laboratory in Yerevan, Armenia. Accelerated electrons, after passing through a cylindrical collimator (length of 20 mm and a diameter of 15 mm) strike a pure tungsten converter. The thickness of the converter was 2 mm, and a 30 mm long aluminum cylinder was placed directly behind it. The function of the aluminum was to stop the electrons that passed through the tungsten. At a distance of 60 mm from the tungsten plate, a Bi coin was placed. Duration of exposition was 30 min.

After 22 min., exposed Bi coin was placed 86 mm from the end cap of HPGe detector. Measurement setup is presented in Fig. 3. Activity of measured samples was high enough and no detector shielding was used. Sample was fixed by tape to the holder ring above detector. First 5400 s spectrum was measured and second one was collected during 79,463 s. In the measured spectra, gamma lines from several Bi isotopes were identified. The lightest one was ²⁰²Bi. Gamma line intensities were determined using the GENIE software package.

The most intense ²⁰³Pb gamma transition of 279.2 keV (quantum yield 81%) was selected for calculation procedure. In both collected spectra, a prominent single 279.2 keV gamma line appeared. For example, in the first spectrum, intensity of this line was 5.87(28)·10³ counts. In the second spectrum, intensity of this line was 3.71(2)·10⁵ detected



Fig. 3 Measurement setup

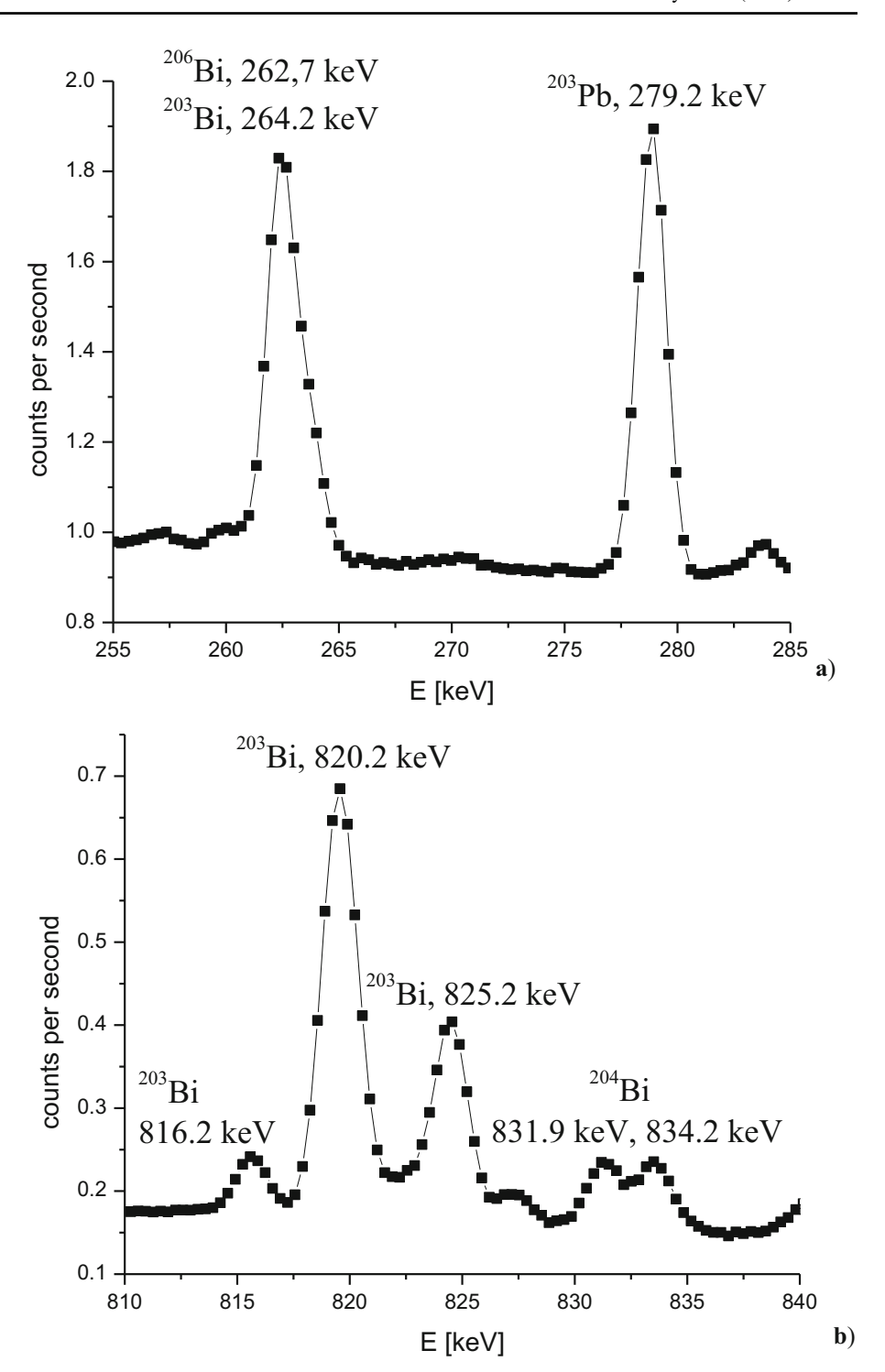
counts. Several strong gamma lines of ²⁰³Bi were identified in spectra, however almost all of them are parts of doublets or even multiplets. In order to avoid errors caused during the numerical procedure in separation of the intensity of individual lines in doublets, several gamma transitions of ²⁰³Bi were chosen for calculation. Ratio of decayed nuclei N_{Ph}^D/N_{Ri}^D was calculated using Eq. 14 and intensities of 264.2 keV, 816.2 keV and 1033.8 keV gamma lines of ²⁰³Bi and mean average was calculated. For example, in the first spectrum intensity of 264.2 keV gamma line was 3.63(7)·10⁴ detected counts. Considering that activity of ²⁰³Bi decreased all the time, while the activity of ²⁰³Pb increased, intensity 264.2 keV gamma line was smaller than 279.2 keV gamma line of ²⁰³Pb in second spectra. Intensity of 264.2 keV gamma line was 1.015(15)·10⁴ counts. Two segments of measured gamma spectra are depicted in Fig. 4.

It can be seen from the Eq. 14 that the N_{Pb}^D/N_{Bi}^D ratio can be obtained using the relative efficiency of the detection system. The best way to get relative efficiency is to use gamma lines of $^{206}\mathrm{Bi}$. Half-life of this isotope is 6.243 days and there are many intensive gamma transitions from 183.98 to 2 MeV. The longer spectrum was used and 16 gamma lines of $^{206}\mathrm{Bi}$, starting from 183.98 keV to 1878.65 keV were selected to get relative efficiency. Combination of an exponential function and a second order polynomial was used in fit procedure.



170 Page 6 of 9 Eur. Phys. J. A (2023) 59:170

Fig. 4 Two parts of gamma spectra: **a**) low energy part containing ²⁰³Pb gamma line (279.2 keV) and ²⁰³Bi/²⁰⁶Bi doublet; **b**) multiplet containing three ²⁰³Bi lines



4 Results and discussion

4.1 Experiment

The estimation of the $N_{Pb}(t_{irr})/N_{Bi}(t_{irr})$ ratio at the moment when irradiation was stopped can be obtained from the Eq. 7.

This equation describes output of the $(\gamma,6n)$ reaction, without proton emission. It was obtained that the ratio of created 203 Pb and 203 Bi nuclei is $N_{Pb}(t_{irr})/N_{Bi}(t_{irr}) = 0.0148$. If no $(\gamma,p 5n)$ reaction occurs, it could be expected that number of 203 Pb created nuclei is 1.48% of the number of 203 Bi nuclei, after 30 min of irradiation. Ratio of activities of two



Eur. Phys. J. A (2023) 59:170 Page 7 of 9 170

Table 1 ²⁰³Pb/²⁰³Bi activity ratio at the end of irradiation

	$N_{Pb}(t_{irr})/N_{Bi}(t_{irr})$	$A_{Pb}(t_{irr})/A_{Bi}(t_{irr})$
Without proton emission ((γ,6n) only), Eq. 7	0.0148	0.00335
Experimental based values, Eq. 13	0.0758(8)	0.0172(2)

mentioned nuclei after irradiation is $A_{Pb}(t_{irr})/A_{Bi}(t_{irr}) = 0.00335$.

The intensities of the selected gamma lines were determined in both measured spectra. Relative efficiency of detection was calculated using gamma lines of 206 Bi. Ratio of 203 Pb and 203 Bi nuclei that decayed in the observed time interval was evaluated as shown in Eq. 14. Obtained N_{Pb}^D/N_{Bi}^D ratio was used to calculate value of N_{Pb}^0/N_{Bi}^0 ratios by Eq. 13. The ratio of activities at the moment when irradiation was stopped was calculated as well. Both registered spectra gave ratio results that agreed within experimental error. In the continuation of the paper, the results obtained from gamma lines measured in a longer spectrum will be presented, due to better counting statistics. The calculated and experimental values are presented in Table 1.

It can be seen from the data presented in Table 1 that the ratio of the numbers of created ^{203}Pb and ^{203}Bi nuclei, as well as their activity ratio, at the end of irradiation, extracted from the measured spectra, differs significantly from the estimation based on the assumption that no proton is emitted in photonuclear reaction. This leads us to the conclusion that the production of ^{203}Pb by some other process, probably (γ,p) 5n), in addition to the decay of ^{203}Bi can have a significant contribution.

After the experimental confirmation of the possibility that $(\gamma, p 5n)$ nuclear reaction can make a measurable contribution to total 203 Pb activity, the very next step is to estimate p/q ratio. Equation 8 gives such a possibility. If the irradiation time was 30 min and experimentally obtained ratio of 203 Pb and 203 Bi nuclei is 0.0758(8), it was estimated using Eq. 8, that p/q factor is 0.060(1). This means that the rate of production of 203 Pb by 209 Bi $(\gamma, p 5n)$ reaction is 6% of the rate of 209 Bi $(\gamma, 6n)$ 203 Bi (Fig. 5).

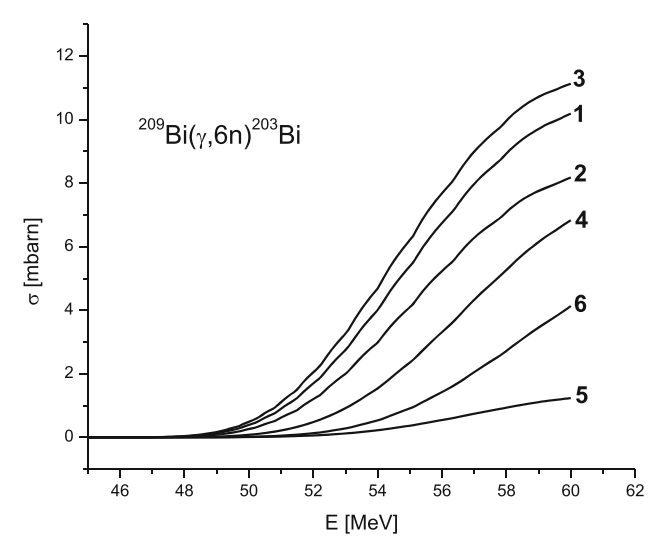


Fig. 5 TALYS estimations for cross section of $^{209}\text{Bi}(\gamma,6\text{n})^{203}\text{Bi}$ reaction. The numbers indicate the level density model as numbered in Sect. 2.4

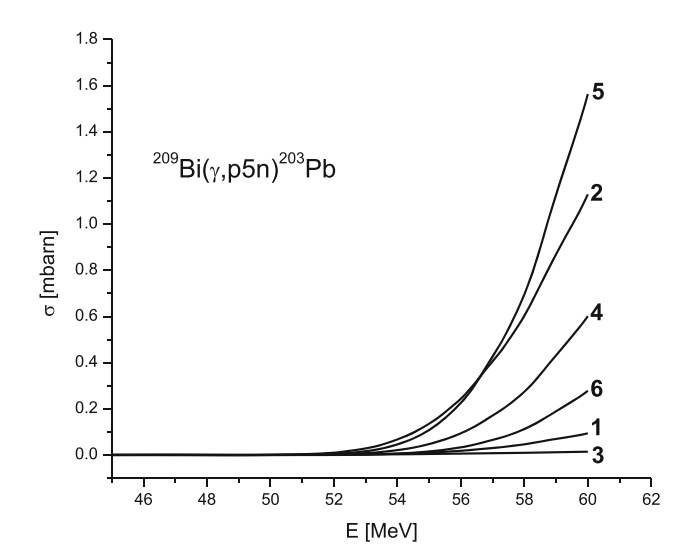


Fig. 6 TALYS estimations for cross section of 209 Bi(γ ,p 5n) 203 Pb reaction. The numbers indicate the level density model as numbered in Sect. 2.4

4.2 Calculated ratio of 209 Bi(γ ,p 5n) and 209 Bi(γ ,6n) reaction probabilities

And finally, in order to estimate ratio of probabilities of 209 Bi(γ ,p 5n) and 209 Bi(γ ,6n) reactions, denoted as p and q, it is necessary to calculate the energy differential cross section for both reactions using the TALYS code. The obtained results, for all six models of level densities are shown in Figs. 5 and 6. As might be expected, the cross section for a reaction without emission of positive charged particle is significantly larger than cross section for emission of one proton in addition to five neutrons. It should also be noted that the



170 Page 8 of 9 Eur. Phys. J. A (2023) 59:170

Table 2 Ratio p/q obtained using measured activities and simulation performed with six different models of level densities (in the same order as stated in Sect. 2.4)

	p/q ratio
Estimated using TALYS cross sections	0.00278
	0.0472
	0.000698
	0.0329
	0.5077
	0.0295
Estimated from Eq. 8	0.060(1)

estimated cross sections for both observed reactions can be very different from each other, depending on which density of states model is chosen.

With the obtained values of cross section and chosen bremsstrahlung function it is possible to calculate p/q ratio using both Eqs. 15 and 16. The result of TALYS estimations are depicted in Table 2, together with results of calculations based on measured data.

It is referred that the results obtained in the photoactivation experiments on 208 Pb and 209 Bi [7, 8] are in good agreement with the calculations performed using the TALYS code. Some examples can be found in the literature [15, 16] that the results of TALYS calculations do not completely match the results of measurements. For the purpose of analyzing the obtained results, it is particularly important to emphasize that one of the conclusions presented in reference [11] is that the shares of 209 Bi(γ ,p 4n) and 209 Bi(γ ,p 5n) reaction are not negligible. The authors estimated that the yield of the 209 Bi(γ ,p 4n) reaction obtained experimentally at 55.6 MeV bremsstrahlung beam was almost 15 times higher than the yield estimated using the TALYS code. In the case of 209 Bi(γ ,p 5n) reaction, this difference is even greater.

Here, it is particularly important to point out that, based on the results presented in reference [11], it can be concluded that the yield of $^{209} Bi(\gamma, p\,5n)^{203} Pb$ reaction is about 9.4 times higher than the yield of reaction $^{209} Bi(\gamma,6n)^{203} Bi$. As can be seen from Table 2, in this paper it is estimated that the yield of $^{209} Bi(\gamma,6n)^{203} Bi$ reaction is over 16 times higher than the yield of $^{209} Bi(\gamma,p)^{203} Pb$ reaction. It is most likely that the Coulomb barrier significantly reduces the probability of reactions in which a charged particle is emitted.

According to the data presented in Table 2, it is difficult to get general conclusion concerning agreement between TALYS estimation and experimental results. As can be seen, TALYS estimations can be almost two orders of magnitude smaller than the experimentally obtained p/q value, as well as one order of magnitude higher.



In this study, an attempt was made to check if 203 Pb is formed in photonuclear reactions on 209 Bi exclusively from the decay of 203 Bi formed in $(\gamma,6n)$ reaction or $(\gamma,p,5n)$ reaction also plays a part in it, as indicated in reference [11]. It has been shown that this estimation can be made if the ratio of 203 Pb and 203 Bi nuclei numbers, at the moment when the exposure of the Bi target in the photon beam is completed, is known.

Irradiation of the target from natural bismuth was performed at 60 MeV bremsstrahlung beam. Induced activity was measured in standard off-beam experiment. Registered spectra were used to extract numbers of created ²⁰³Bi and ²⁰³Pb nuclei. The obtained ratio of nuclei numbers indicates that ²⁰³Pb is formed in some other way, other than from the decay of 203 Bi. The most likely mechanism is the (γ ,p 5n) reaction. Based on the experimentally estimated ²⁰³Pb/²⁰³Bi nuclei number (or activity) ratio at the moment when the irradiation was stopped, it is possible to estimate how much of the 203 Pb activity originates from (γ ,p 5n) reaction. It was obtained that the number of produced ²⁰³Pb nuclei is about 7.6% of the number of ²⁰³Bi nuclei. Based on this value, it was established that the rate of production of ²⁰³Pb through (γ,p 5n) reactions is about 6% of the rate of production of 203 Bi by (γ ,6n) reaction. This is significantly less than presented in reference [11].

In order to verify the obtained results, a TALYS simulation of cross-sections for $(\gamma, p \ 5n)$ and $(\gamma, 6n)$ reaction was performed. According to the obtained cross-sections, ratio of reaction rates of both reactions was calculated using one model of strength function and six models of level density function. Due to large scatter of TALYS cross sections for both reactions obtained results of ratios of reaction rates differ significantly.

This approach neither verified nor contradicted certain indications [11] that TALYS code underestimates the probability of photonuclear events in which a proton is realized in addition to neutrons. A new experiment that primarily makes advantage of wider range of energies, preferably higher than 60 MeV and a more detailed analysis of theoretical results and TALYS simulations may eliminate this doubt. The new measurements will also help to resolve the dilemma of whether the yield of 209 Bi(γ ,p 5n) 203 Pb reaction is significantly higher than the yield of the 209 Bi(γ ,6n) 203 Bi reaction, as stated in reference [11], or whether this ratio is significantly lower, as obtained in the measurements described in this paper. The method described in this study is not limited to the case of 209 Bi, and can be applied to other targets and products of photonuclear reactions.

Data Availability Statement This manuscript has no associated data or the data will not be deposited. [Authors' comment: This manuscript has no associated data.]



Eur. Phys. J. A (2023) 59:170 Page 9 of 9 170

References

- Handbook on Nuclear Activation Data, Technical Report Series 273, IAEA Vienna (1987)
- Handbook of photonuclear data for applications: Cross sections and spectra, IAEA TECDOC 1178, IAEA Vienna (2000)
- Experimental Nuclear Reaction Data (EXFOR) https://www-nds. iaea.org/exfor/
- A.J. Koning, D. Rochman, Nucl. Data Sheets 113(12), 2841–2934 (2012)
- R.R. Harvey, J.T. Caldwell, R.L. Bramblett, S.C. Fultz, Phys. Rev. 136(1B), 126–131 (1964)
- H. Naik, A.V.R. Reddy, S. Ganesan, D. Raj, K. Kim, G. Kim, Y.D. Oh, D.K. Pham, M.H. Cho, I.S. Ko, W. Namkung, J. Korean Phys. Soc. 52(3), 934–939 (2008)
- H. Naik, S. Singh, A.V.R. Reddy, V.K. Manchanda, S. Ganesan, D. Raj, M.S. Rahman, K.S. Kim, G. Kim, Y.D. Oh, H.-S. Lee, M.-H. Cho, I.S. Ko, W. Namkung, Eur. Phys. J. A 41, 323–334 (2009)
- 8. H. Naik, S. Singh, A. Goswami, V.K. Manchanda, G. Kim, K.S. Kim, M.-W. Lee, M.S. Rahman, D. Raj, S. Ganesan, S. Suryanarayana, M.-H. Cho, W. Namkung, Nucl. Instrum. Methods Phys. Res. B **269**, 1417–1424 (2011)
- A.N. Ermakov, B.S. Ishkhanov, I.M. Kapitonov, I.V. Makarenko, V.N. Orlin, Phys. At. Nucl. 73(5), 737–745 (2010)
- S.S. Belyshev, A.N. Ermakov, B.S. Ishkhanov, V.V. Khankin, A.S. Kurilik, A.A. Kuznetsov, V.I. Shvedunov, K.A. Stopani, Nucl. Instrum. Methods Phys. Res. A 745, 133–137 (2014)

- S.S. Belyshev, D.M. Filipescu, I. Gheoghe, B.S. Ishkhanov, V.V. Khankin, A.S. Kurilik, A.A. Kuznetsov, V.N. Orlin, N.N. Peskov, K.A. Stopani, O. Tesileanu, V.V. Varlamov, Eur. Phys. J. A 51, 67 (2015)
- I. Gheorghe, H. Utsunomiya, S. Katayama, D. Filipescu, S. Belyshev, K. Stopani, V. Orlin, V. Varlamov, T. Shima, S. Amano, S. Miyamoto, Y.-W. Lui, T. Kawano, S. Goriely, Phys. Rev. C 96, 044604 (1917) Erratum Physical Review C 99, 059901 (2019)
- 13. S. Agostinelli et al., Geant4—a simulation toolkit. Nucl. Instrum. Meth. A **506**, 250–303 (2003)
- A. Koning, S. Hilaire, S. Goriely, Simulation of nuclear reactions, TALYS-1.96/2.0, https://www-nds.iaea.org/talys/tutorials/talys_v1.96.pdf
- O.S. Deiev, I.S. Timoshenko, S.N. Olejnik, V.A. Kushnir, V.V. Mytrochenko, S.A. Perezhogin, Phys. Rev. C 106, 024617 (2022)
- A.N. Vodin, O.S. Deiev, I.S. Timoshenko, S.N. Olejnik, M.I. Ayzatskiy, V.A. Kushnir, V.V. Mytrochenko, S.A. Perezhogin, Eur. Phys. J. A 57, 208 (2021)

Springer Nature or its licensor (e.g. a society or other partner) holds exclusive rights to this article under a publishing agreement with the author(s) or other rightsholder(s); author self-archiving of the accepted manuscript version of this article is solely governed by the terms of such publishing agreement and applicable law.



ELSEVIER

Contents lists available at ScienceDirect

Materials Today Communications

journal homepage: www.elsevier.com/locate/mtcomm





Study on the formation mechanism of oxide film of pure titanium during the cutting process

Jinquan Li ^{a,*}, Ning Cao ^a, Roman Laptev ^{b,*}, Haolun Shen ^a, Kuznetsov Pavel ^b, Zarko Medic ^b, Anton Lomygin ^b, Jian Cui ^b

- a School of Mechanical Engineering, Shenyang Ligong University, No.6 Nanping Center Road, Hunnan New District, Shenyang 110159, China
- b Division for Experimental Physics, National Research Tomsk Polytechnic University, Lenina Ave. 43, Tomsk 634050, Russia

ARTICLE INFO

Keywords: Titanium Oxide film High-speed cutting First-principles

ABSTRACT

The industrial pure titanium (TA2) can be oxidized to produce the dense oxide film acted by the effect of thermal-mechanical coupling on the machined surface during the cutting process, which influences its mechanical properties. The characteristics of oxide film were investigated by a single factor cutting test. The phase analysis of the oxide film was carried out. The topography of the oxide film was observed. The formation mechanism of oxide film was studied by the first-principles. The oxide film is uneven, which its roughness increases with the increase of feed rate. The oxide film is mainly composed of TiO₂, and the intensity of the TiO₂ diffraction peak increases with the increase of feed rate, that is, the amount of TiO₂ also increases gradually. When TA2 is oxidized at high temperature, O atoms are adsorbed by Ti atoms to the machined surface to form the corresponding O-Ti covalent bond. The bonding ability between O atoms and Ti atoms is gradually weakened from the machined surface to the inside of the matrix.

1. Introduction

The TA2 with a single α phase and its alloys have been widely used in aerospace, shipbuilding, biomedicine and other fields because of its advantages of low density, high melting point, strong corrosion resistance, good mechanical properties and biocompatibility [1–4].

Ti atoms are chemically active and can be oxidized at high temperature to produce the dense oxide film on the machined surface, which can prevent further oxidation to improve the corrosion resistance of TA2 [5]. The density, phase composition and thickness of oxides can influence the diffusivity of oxygen atoms[6]. Some oxide films are unstable and split with the matrix or even flake off [7]. Therefore, it is of great significance to study the characteristics and formation mechanism of oxide films in order to improve the physical properties of TA2 materials.

At present, a lot of research has been done on the characteristics of oxide film. Bailey et al. [8] conducted thermal oxidation of TA2 at 625/20 h $^{\circ}\text{C}$ and found that an oxide film with a thickness of about 0.98 μm was formed on its surface, and the surface hardness increased from 298HV0.05 to 766HV0.05. Kikuchi S et al. [9] found that with the increase of temperature, the wear resistance of TA2 was greatly improved and the friction coefficient was greatly reduced. Mohamed et al. [10]

found that the oxide film generated at 750°C and 850 °C for Ti-6Al-4 V titanium alloy was mainly composed of TiO_2 and Al_2O_3 . Ferraris et al. [11] presented a chemical surface treatment designed for titanium and its alloys to produce an oxide layer with a peculiar sponge like nanotexture coupled with high density of hydroxyl group. The dip-coating sol–gel method was utilized to cap the grown silver nanostructures by a thin TiO_2 layer. Thickness of the TiO_2 films was measured about 30 nm by a profilometer [12].

Higher temperature produced during the dry cutting process meets the conditions for the generation of oxide film. The titanium alloy cutting generally involves a large amount of plastic deformation and is coupled thermomechanical process on the machined surface layer. It always comes with grain refinement and phase transformation on the machined surface [13,14]. Peng et al. [15] observed the cross section of titanium alloy at different cutting speeds by SEM to find shear slip and severe plastic deformation grains in the oxide film area.

When cutting TA2, the uneven residual deformation occurs on the machined surface along the cutting direction to produce hardening layer, which has a great influence on fatigue strength and surface quality [16]. The surface topography fluctuation generally increases with the increase of the feed rate, but is less affected by the cutting speed [17].

E-mail addresses: li_jinquan@163.com (J. Li), laptevrs@tpu.ruu (R. Laptev).

^{*} Corresponding authors.

The cutting temperature can be controlled by selecting appropriate cutting parameters to form different bioactive oxide film on the surface of TA2 [18,19].

Wang et al. [20] conducted TEM, EBSD and XRD experiments on the machined surface of titanium alloy, which shown that nano-twins formed with the increase of cutting speed to enhance the hardness of machined surface, and the volume fraction of twins increased with the increase of cutting speed. The phase transition occurs from α phase to β phase during the cutting process, and β phase is decomposed into secondary α phase during the cooling process.

At present, the study of oxide film in the cutting process is generally focused on phase analysis, oxidation characteristics and physical properties based on the experimental result. In this paper, the first principle is applied to investigate the action mechanism of O and Ti atoms at atomic scale based on the experimental analysis.

2. Experimental

The test material was TA2 treated by annealing. The length of the sample is 300 mm and the diameter is 90 mm. Its chemical composition is shown in Table 1. Dry cutting test with single factor (only feed rate was changed) was carried out on CA6140A lathe. The physical vapor deposition (PVD) coated blades made by Sandvik were used. The diagram of experimental setup is shown in Fig. 1. The type of blade is CCMT09T308-MF1105. The tool cutting edge angle is $K_r = 95^{\circ}$, tool cutting edge inclination angle is $\lambda_s = 0^\circ$, tool rake angle is $\lambda_0 = 0^\circ$, tool rear angle is $\alpha_0 = 7^{\circ}$, corner radius is $r_{\varepsilon} = 0.8$ mm. The sample is segmented into several sections with the corresponding cutting parameter along the length direction of the workpiece. The cutting parameter of each section is shown in Table 2. After cutting, the phase analysis of the sample surface was carried out by Shimadzu X-ray diffraction (XRD)– 7000S diffractometer in Bragg-Brentano geometry from 20° to 75° with scanning rate of 5.0 deg/min at Copper K- α radiation $(\lambda = 1.54 \text{ Å})$ [10.3390/met10040447]. Current - 30 mA, voltage -40 kV. Laser scanning confocal microscopy (LSM700) was used to measure a three-dimensional shape of the machined surface sample. The characteristic parameters of three-dimensional topography are shown in Table 3.

3. Results and discussion

3.1. The characteristic of morphology of oxide film on machined surface

Fig. 2 shows the three-dimensional topography of the oxide film under different feed rates. The machined surface is rough and uneven. The distance between the peak and the trough increases with the increase of the feed rate. The depth of the furrows also gradually deepens. During the cutting process, the workpiece rotates and the tool feeds along the axial direction. The feed rate is the distance that the tool moves forward along the axis per rotation of the workpiece, which forms a spiral cutter mark. Therefore, the width between the two furrows approximates the value of the feed rate, which the larger the feed rate, the wider the furrow, as shown in Table 3.

3.2. The phase analysis of oxide film

Fig. 3 shows the XRD diffraction pattern of the machined surface of TA2 under different feed rates. The diffraction peak of TA2 is mainly composed of $\rm Ti_6O$ and $\alpha\text{-Ti}$ before cutting. The stability of $\rm Ti_6O$ oxide formed at low temperature is poor. After cutting, with the increase of

Table 1
The chemical composition of TA2 (wt%).

materials	С	Fe	N	О	Н	V	Al	Ti
TA2	0.10	0.3	0.05	0.20	0.015	\		blance

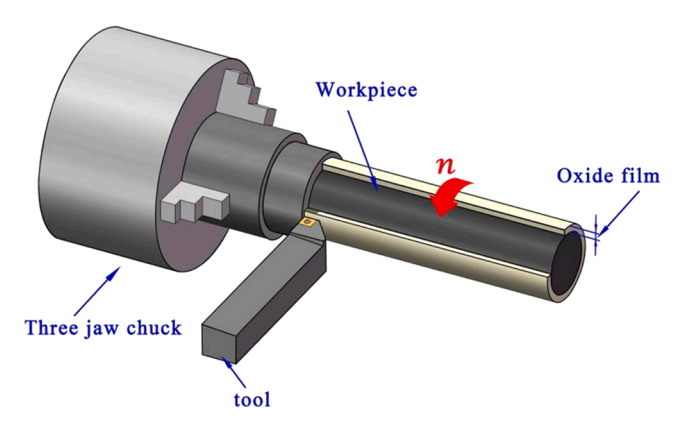


Fig. 1. The diagram of experimental setup.

Table 2The cutting parameter of different section.

Numbered list	Cutting speed (v)	Feed rat (f)	Cutting dept (a_p)		
	(m/min)	(mm/r)	(mm)		
1	111	0.10	0.20		
2	111	0.20	0.20		
3	111	0.30	0.20		

feed rates, the cutting temperature gradually increases. Therefore, the oxide composition also changes due to the influence of the temperature that is achieved in a given cutting mode. TiO $_2$ has relatively stable chemical properties at high temperature and its formation speed is faster than other low valence oxides. Therefore, Ti $_6$ O is further oxidized to high valence TiO $_2$. The diffraction peak is mainly composed of TiO $_2$ and α -Ti. With the increase of feed rate, the intensity of diffraction peak of TiO $_2$ gradually increases, indicating that the content of TiO $_2$ gradually increases. The apparent activation energy required for the oxidation is about 300 kJ/mol[21]. TiO $_2$ surface has good hydrophilicity in lighting conditions. The hydrophilicity properties are mainly determined by the presence of titanium dioxide TiO $_2$.

3.3. The formation mechanism of oxide film

3.3.1. The model construction

The Cambridge Serial Total Energy Package program in Material Studio software was used to perform all the calculations according to the first-principles method based on the density functional theory (DFT). The three TA2 structure models were constructed as shown in Fig. 4. Fig. 4(a) shows the cell model of α -Ti, whose space group is P63/MMC and lattice parameters are a=b=2.95 Å, c=4.767 Å, $\alpha=\beta=90^\circ$, $\gamma=120^\circ$. Due to the small number of atoms in the cell model of α -Ti, it was expanded to a $2\times2\times2$ supercell to increase the accuracy of the calculation, as shown in Fig. 4(b). A 10 Å (1 nm = 10 Å) vacuum layer was added above the supercell to construct the TA2 surface model, as shown in Fig. 4(c).

In the structural model of TA2 system, the energy band of the cell of Ti atom is shown in Fig. 5 and the energy band of the surface structure of Ti atom is shown in Fig. 6. Conduction and valence bands of the two energy bands across the Fermi level (E_f), namely 0 point, indicating that two structures have a quality of strong metal. The energy distribution of the energy band structure of Ti metal cell is mainly concentrated in -5 eV to 20 eV, and the energy distribution of the energy band structure of Ti metal surface is mainly concentrated in -5 eV to 13 eV. The surface structure of Ti metal has more metal atoms, so the energy is stronger, the energy band distribution is denser, and the conduction band distribution is more concentrated.

Table 3The characteristic parameters of three-dimensional topography of TA2 surface profile.

Feed rate	Arithmetic mean deviation	Mean height of profile elements	Root mean square deviation	Maximum profile peak height	Maximum profile valley depth	Total height of profile
f (mm/ r)	Pa (μm)	Pc	Pq(μm)	Pp(μm)	Pν(μm)	Pt(µm)
f = 0.1	1.126	2.656	1.300	2.412	3.065	5.477
f = 0.2	2.540	6.573	3.100	6.971	5.807	12.778
f = 0.3	5.523	11.585	6.517	10.848	12.457	23.305

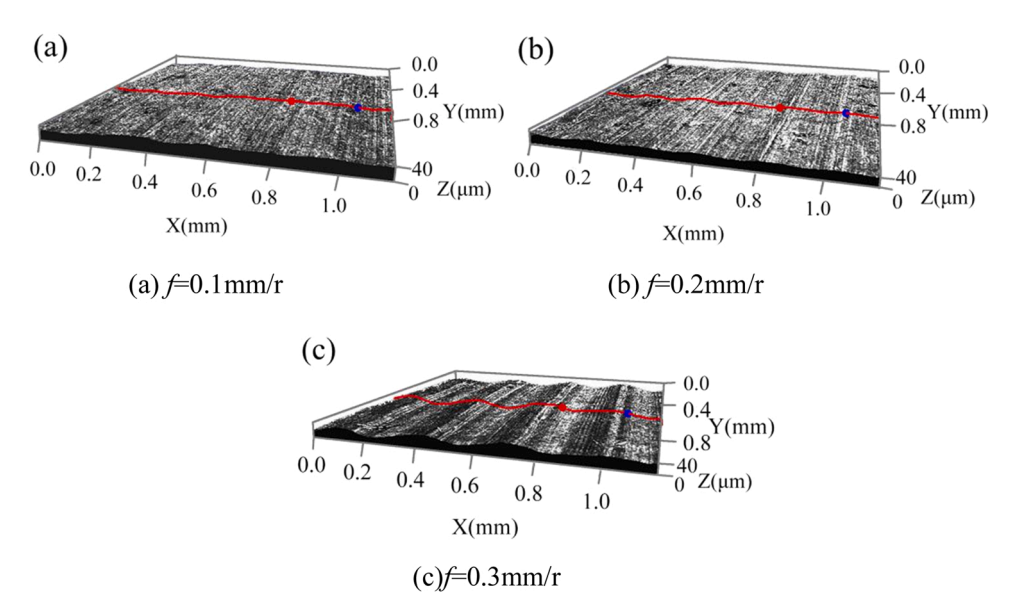


Fig. 2. The three-dimensional topography of the oxide film under different feed rate.

3.3.2. The oxidizing process of TA2 system

To ensure the occurrence of the oxidation reaction, the O atoms were placed 2.45 Å from the surface of TA2 to construct the surface structure of TA2. The distance between adjacent Ti atoms in the uppermost layer of TA2 surface structure is 1.75 Å. The Ti atoms in the two adjacent layers above and below are equally spaced, as shown in Fig. 7.

The temperature was set to 1000 K to simulate high-temperature oxidation. After simulated oxidation, O atoms were adsorbed from 2.45 Å away from the surface to 0.467 Å away from the surface (as shown in Fig. 8), indicating that Ti atoms have a strong adsorption effect on O atoms, and the O-Ti bond is easily formed at high temperature.

After simulated oxidation, the distance between adjacent Ti atoms in the surface layer was expanded from 1.75 Å to 2.508 Å. The distance between Ti atoms in two adjacent layers gradually decreases from top to bottom, that is 2.604 Å, 2.578 Å and 2.455 Å, respectively, as shown in Fig. 8. It shows that the adsorption of Ti atoms on O atoms decreases gradually from the surface to the interior of matrix.

3.3.3. Charge density difference (CDD)

After simulated oxidation, O atoms were adsorbed to the surface of TA2 by Ti atoms. Due to the small radius of O atoms, they existed in the form of interstitial atoms to produce a new form of bonding with Ti atoms.

Fig. 9 shows the CDD of TA2 oxide structure after simulated oxidation. Blue means losing electrons, red means gaining electrons. It can be seen from the Fig. 9 that the O atoms in the surface layer of TA2 gain more charge lost by Ti atoms in the uppermost layer, indicating that there exists charge transfer between Ti atoms and O atoms to form stronger O-Ti covalent bonds. The bonding characteristics of Ti-O bond formed by the combination of O atoms and Ti atoms gradually weaken from top to bottom. There is also some charge transfer between Ti atoms in different layers. The charge lost by Ti atoms decreases layer by layer

from the surface to the inside. The uppermost Ti1 and Ti3 lose more charge. Ti8 and Ti6 gain some of the charge lost by Ti1 and Ti3, meanwhile, they also lose some of the charge. Ti2 and Ti4 also gain a small amount of charge from Ti8 and Ti6 while losing some of their charge. Ti7 and Ti5 at the lowest layer do not basically lose charge, on the contrary, they gain part of the charge from Ti2 and Ti4, indicating that Ti-Ti covalent bond can also be formed in the oxidation structure of TA2, but Ti-Ti covalent bond inside TA2 is more stable and not to be easily oxidized. Therefore, the bonding ability between O atoms and Ti atoms decreases gradually from top to bottom. It can be inferred that the O atoms are easier to react with Ti atoms in the surface layer to form the O-Ti covalent bond, but after entering the TA2, the bonding ability of the O atoms with the Ti atoms is gradually weakened. The above analysis results are consistent with the XRD results in this paper.

The results of Mulliken population analysis for the Ti atom on the surface oxidation structure are shown in Table4, in which the distribution of electrons in atomic orbitals is exhibited to study the bonds between atoms. As can be seen from Table 4, among the s,p and d orbitals of Ti atom, 3p6 orbitals contribute the most charge, followed by 3d2, and 3s2 and 4s2 contribute the least charge. In general, the amount of charge transfer in the system is relatively balanced. However, the O atoms gain 0.69 charge, most of which is due to the charge lost by Ti1 and Ti3 on the upper surface (0.41). That is, O atoms are more likely to bond to Ti atoms in the upper layer.

According to the above analysis, O atoms are easily adsorbed to the matrix surface and combine with Ti atoms on the surface to generate oxides. At the same time, O atoms continue to penetrate into the matrix, but the binding ability of the inner Ti atom and O atom is weaker than that of the surface Ti atom, that is, the Ti atom inside the matrix is more stable and not easy to be oxidized. Therefore, TA2 oxides are easier to form on the surface.

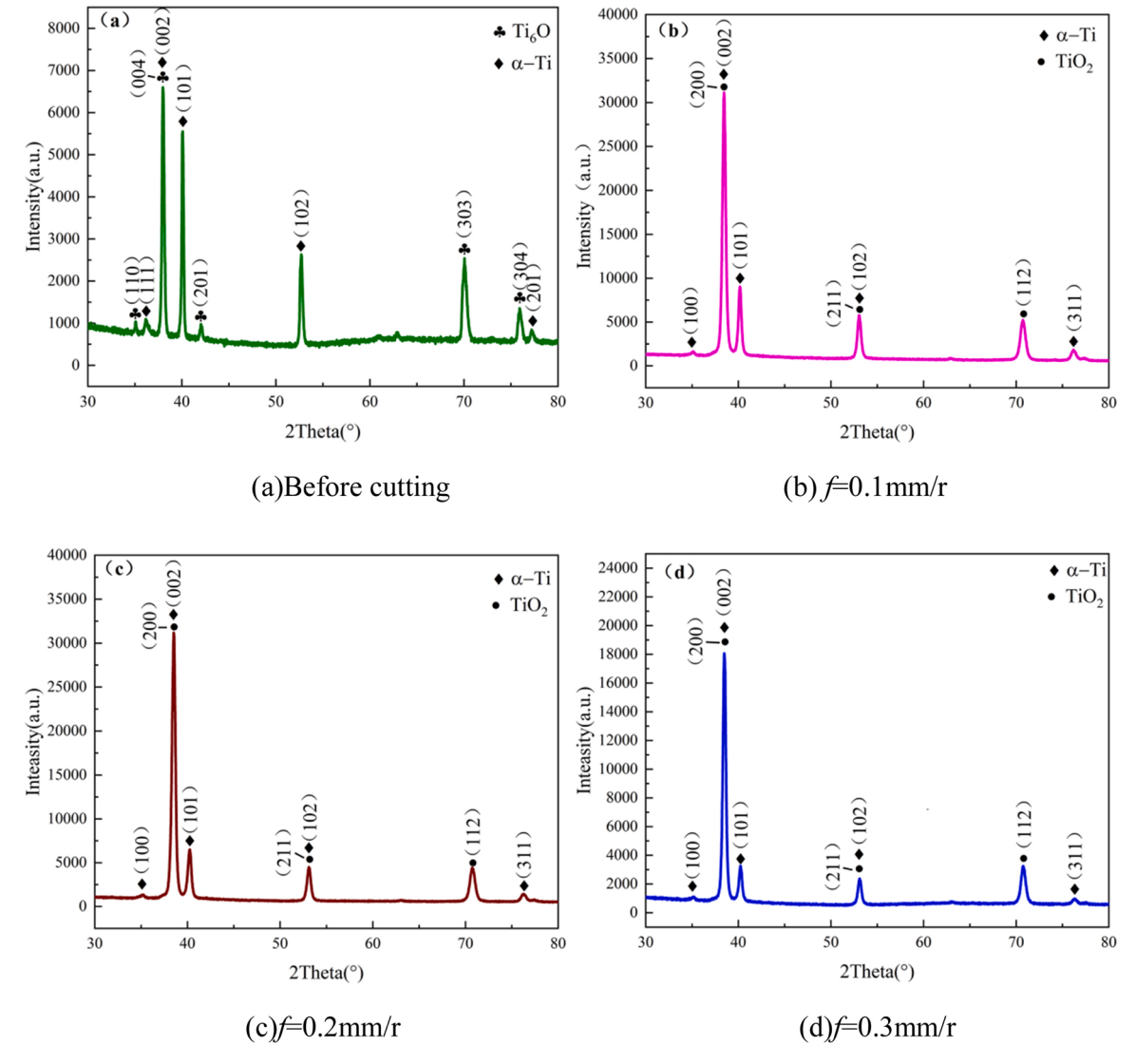


Fig. 3. XRD diffraction pattern of TA2 surface under different feed rates.

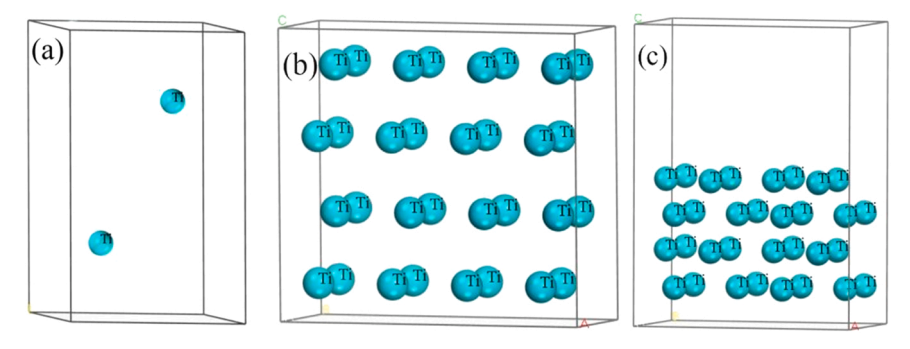


Fig. 4. Three structure models of TA2.

3.3.4. Density of states (DOS)

Fig. 10 (a), (b) show the DOS of the surface structure and the crystal cell structure of TA2, respectively.

At the Fermi level E_f = 0, the value of total density of state is still high, indicating that the system still has a strong metal property mainly resulting from the electrons contributed by the d and p orbital of Ti atoms. It can be seen that the s, p and d orbital are all hybridized for the two structures at the Fermi level. The s orbital of Ti metal surface

structure (Fig. 10a) is involved in more hybridization than that of Ti metal cell structure (Fig. 10b) because the outer 4s2 orbital is more likely to lose electrons.

The DOS of O atoms and Ti atoms on the surface structure is greater than that of the crystal cell structure, indicating that the electronic structure of O atoms and Ti atoms inside the crystal cell structure is more stable and the Ti atoms inside the crystal cell structure are difficult to be oxidized, that is, O atoms are easier to be oxidized on the surface.

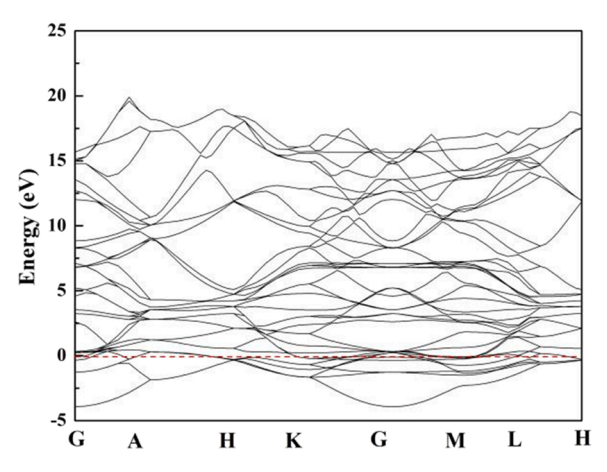
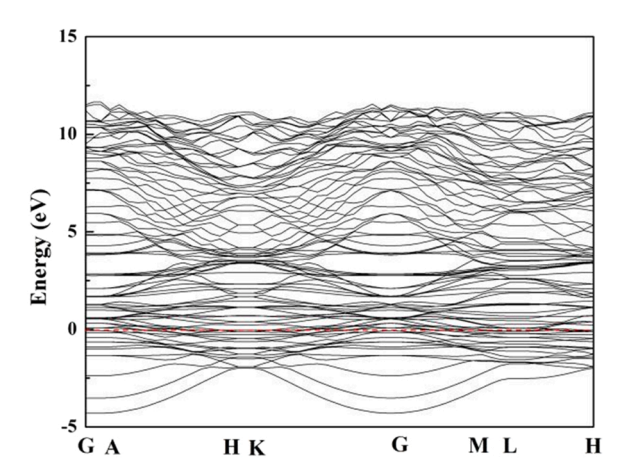


Fig. 5. Energy band of Ti metal unit cell.



 $\textbf{Fig. 6.} \ \ \textbf{Energy band of Ti metal surface structure.}$

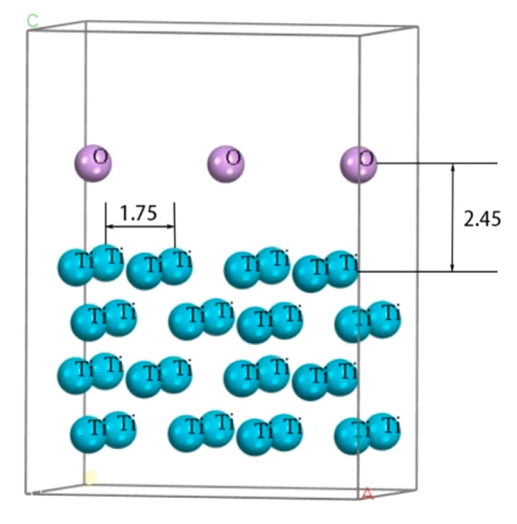


Fig. 7. TA2 surface model.

4. Energy analysis of TA2

The adsorption energy, surface energy and interface energy of O atoms in TA2 metal system are obtained by calculation. The oxidation mechanism of TA2 was analyzed from the perspective of interatomic energy.

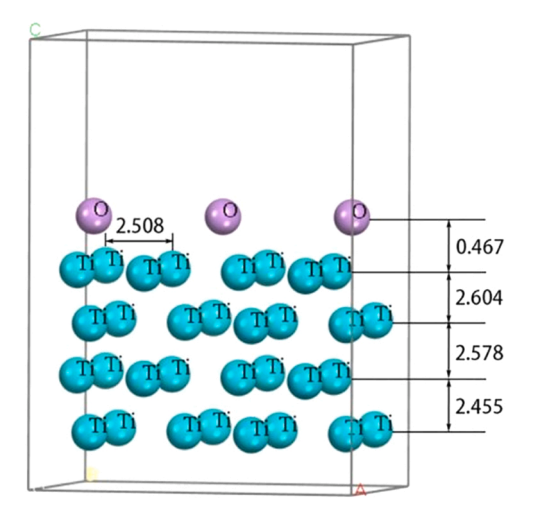


Fig. 8. Surface oxidation structure of TA2 after simulating.

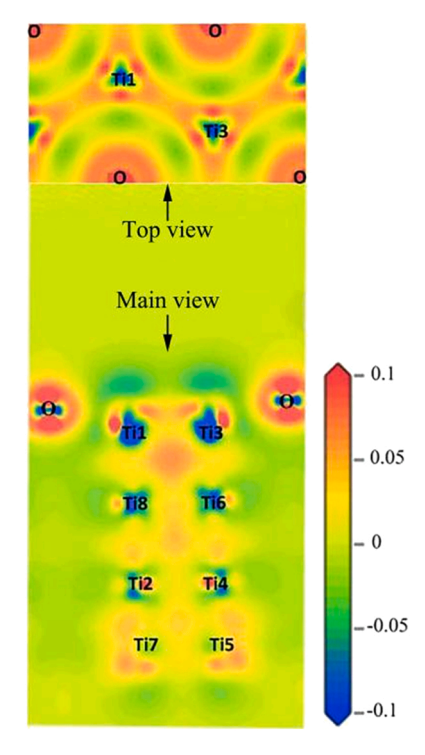


Fig. 9. Differential charge density of oxidized structure on TA2 surface.

Table 4Mulliken population analysis of the surface oxidation structure.

Atom	Orbital ch	Orbital charge							
	s	p	d	Total	Net (e)				
0	1.91	4.77	0	6.69	-0.69				
Ti1	2.47	6.34	2.78	11.59	0.41				
Ti2	2.48	6.57	2.90	11.95	0.05				
Ti3	2.47	6.34	2.78	11.59	0.41				
Ti4	2.48	6.57	2.90	11.95	0.05				
Ti5	2.73	6.43	2.89	12.05	-0.05				
Ti6	2.53	6.69	2.85	12.07	0.07				
Ti7	2.73	6.43	2.89	12.05	-0.05				
Ti8	2.53	6.69	2.85	12.07	0.07				

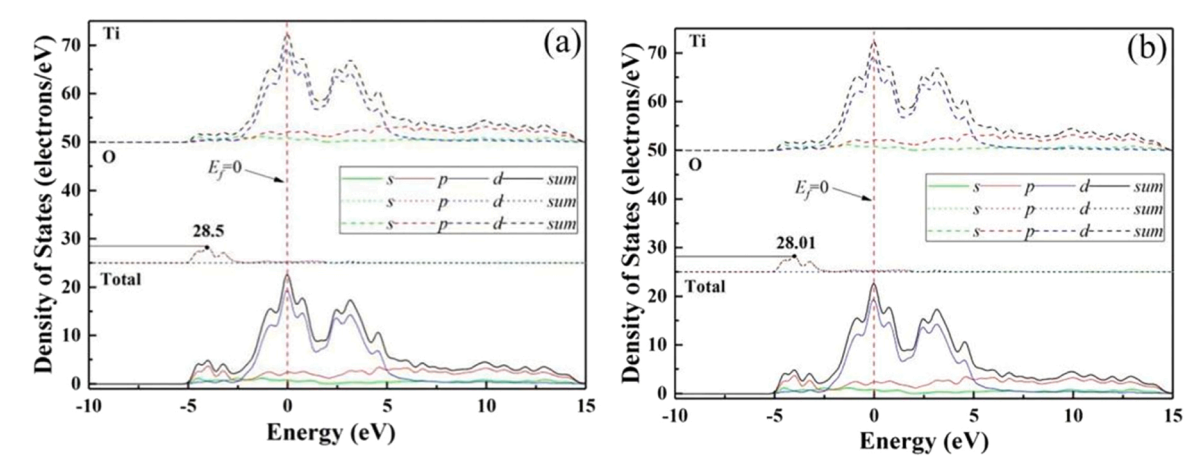


Fig. 10. The DOS of oxidation structure on the surface of TA2 (a) the DOS of the surface structure, (b) the DOS of the crystal cell structure.

$$\sigma_{\text{surface}}(\mu_i) = \frac{1}{2S} \left[E_{\text{system}} - \sum Num_i \cdot \mu_i(p_i, T) \right]$$
 (1)

Where σ surface is the surface energy of the atom, S is the atomic surface area, E_{system} means system energy, Num_i represents the number of atoms, μ_i is the energy of the atom.

$$W_{\rm ad} = \frac{E_{\rm sur} + E_{\rm ele} - E_{\rm int}}{S} \tag{2}$$

$$\gamma_{\rm int} = \frac{E_{\rm sys} - E_{\rm Ti} - E_{\rm O}}{2S} - \sigma_{\rm Ti}$$
 (3)

Where Wad means adsorption energy, Esur, Eele and Eint are the energy of the surface system, the energy of adsorbed atoms and the energy of interface system, respectively, S represents the surface area of the system, γ_{int} is the system interface energy, σ_{Ti} is the surface energy of TA2.

The calculation results in Table 5 show that the adsorption energy of oxygen is greater than 0, indicating that the O atoms are adsorbed by the surface of Ti atom to undergo the oxidation reaction.

The interfacial energy is less than 0.5, indicating that the oxidation reaction occurs on the surface and the O atoms will penetrate into the interior of matrix.

5. Conclusions

- (1) The surface of the oxide film is uneven. The distance between peaks and valleys increases with the increase of feed rate.
- (2) The oxide film produced on the machined surface of TA2 is mainly composed of TiO_2 , the intensity of the TiO_2 diffraction peak increases with the increase of feed rate, indicating that the content of TiO_2 also increases gradually.
- (3) During the process of the formation of oxide film, the O atoms are adsorbed to the machined surface by Ti atoms. There exists charge transfer between the O atoms and Ti atoms to form the corresponding O-Ti covalent bonds. The O atoms gain more charges from Ti atoms on the uppermost layer and are more likely to react with them to form stronger covalent bonds, but after entering the TA2, the bonding ability of the O atoms with the Ti atoms is gradually weakened from the surface to the inside of the matrix.

Funding

The research was supported by the National Natural Science Foundation of China (Grant No. 51775357), RFBR (project number 21-58-53039) and the Training Program of the National Defense Science and Technology Innovation Team of Shenyang Ligong University (project

Table 5Energy parameters of TA2 metal system.

Materials	S (Å2)	Adsorption energy (eV)	Surface energy (eV/Å2)	Interfacial energy (eV/Å2)
Ti-O	16.34	0.4933	1.27	0.25

number SYLUGFTD202102).

CRediT authorship contribution statement

All authors have seen and approved the final version of the manuscript being submitted. They warrant that the article is the authors' original work, has not received prior publication and is not under consideration for publication elsewhere.

Declaration of Competing Interest

The authors declare that they have no known competing financial interests or personal relationships that could have appeared to influence the work reported in this paper.

References

- [1] Z. Guo, R. Liu, C. Wang, Y. He, Y. He, Y. Ma, X. Hu, Compressive mechanical properties and shock-induced reaction behavior of a Ti-29Nb-13Ta-4.6 Zr alloy, Met. Mater. Int. 26 (2020) 1498-1505, https://doi.org/10.1007/s12540-019-00414-z.
- [2] R. Delgado-Ruiz, G. Romanos, Potential causes of titanium particle and ion release in implant dentistry: a systematic review, Int. J. Mol. Sci. 19 (2018) 3585, https://doi.org/10.3390/ijms19113585.
- J. Frankcombe, Proposed mechanisms for the catalytic activity of Ti in NaAlH4, Chem. Rev. 112 (2012) 2164–2178.
- [4] O. Akhavan, A. Moshfegh, Thickness dependence on thermal stability of sputtered Ag nanolayer on Ti/Si(100), Appl. Surf. Sci. 254 (2007) 548–551.
- [5] K. Aniolek, M. Kupka, A. Barylskl, G. Dercz, Mechanical and tribological properties of oxide layers obtained on titanium in the thermal oxidation process, Appl. Surf. Sci. 357 (2015) 1419–1426, https://doi.org/10.1016/j.apsusc.2015.09.245.
- [6] M. Kalienko, A. Volkov, M. Leder, A. Zhelnina, Study of oxygen content in titanium alloys after exposure at elevated temperature, MATEC Web Conf. 321 (2020) 11068
- [7] H. Li, Y. Sun, J. Zhang, Effect of ZrO2 particle on the performance of micro-arc oxidation coatings on Ti6Al4V, Appl. Surf. Sci. 342 (2015) 183–190, https://doi. org/10.1016/j.apsusc.2015.03.051.
- [8] R. Bailey, Y. Sun, Corrosion and tribocorrosion performance of thermally oxidized commercially TA2 in a 0.9% NaCl solution, J. Mater. Eng. Perform. 24 (2015) 1669–1678, https://doi.org/10.1007/s11665-015-1441-1.
- [9] S. Kikuchi, A. Ueno, H. Akebono, Combined effects of low temperature nitriding and cold rolling on fatigue properties of commercially TA2, Int. J. Fatigue 139 (2020), 105772, https://doi.org/10.1016/j.ijfatigue.2020.105772.

- [10] L. Mohamed, S. Elmomen, S. El-Hadad, Influence of the oxidation behavior of Ti-6Al-4V alloy in dry air on the oxide layer microstructure, Chem. Pap. 76 (2022) 1627–1638, https://doi.org/10.1007/s11696-021-01976-2.
- [11] S. Ferraris, A. Cochis, M. Cazzola, M. Tortello, A. Scalia, S. Spriano, L. Rimondini, Cytocompatible and anti-bacterial adhesion nanotextured titanium oxide layer on titanium surfaces for dental, Front. Bioeng. Biotechnol. 7 (2019) 1–12.
- [12] O. Akhavan, E. Ghaderi, Capping antibacterial Ag nanorods aligned on Ti interlayer by mesoporous TiO2 layer, Surf. Coat. Technol. 203 (2009) 3123–3128.
- [13] L. Zhou, X. Pan, X. Shi, T. Du, L. Wang, S. Luo, W. He, P. Chen, Research on surface integrity of Ti-6Al-4V alloy with compound treatment of laser shock peening and shot peening, Vacuum 196 (2022), 110717, https://doi.org/10.1016/j. vacuum.2021.110717.
- [14] G. Liu, D. Zhang, C. Yao, Research progress of the microstructure on machined surface of titanium alloys, J. Mech. Eng. 57 (2021) 231–245.
- [15] Z. Peng, X. Zhang, D. Zhang, Improvement of Ti–6Al–4V surface integrity through the use of high-speed ultrasonic vibration cutting, Tribol. Int. 160 (2021), 107025, https://doi.org/10.1016/j.tripoint.2021.107025.

- [16] G. Wang, X. Cheng, Research on cutting fluid used in processing medical TA2 implants, Chin. J. Oral. Implantol. 04 (1999) 1–4.
- [17] T. Jaingam, C. Kaminaga, T. Sawa, M. Anzai, Tool wear and surface roughness characteristics in the high-speed milling of pure Ti and Ti alloy using TiAlN coated carbide radius end mill, Int. J. Autom. Technol. 16 (2022) 230–237, https://doi. org/10.20965/ijat.2022.p0230.
- [18] R. Zhang, Y. Wan, X. Ai, G. Wang, B. Men, Development of oxygen-rich supply system applied in biomedical titanium alloy cutting, Mater. Sci. Forum 770 (2014) 410–413, https://doi.org/10.4028/www.scientific.net/MSF.770.410.
- [19] I. Karaokutan, G. Ozel, Effect of surface treatment and luting agent type on shear bond strength of titanium to ceramic materials, J. Adv. Prosthodont. 14 (2) (2022) 78–87, https://doi.org/10.4047/jap.2022.14.2.78.
- [20] Q. Wang, Z. Liu, Plastic deformation induced nano-scale twins in Ti-6Al-4V machined surface with high speed machining, Mater. Sci. Eng.: A 675 (2016) 271–279, https://doi.org/10.1016/j.msea.2016.08.076.
- [21] J. Małecka, Oxidation activation energy of titanium alloy based on tial(γ) intermetalic phase, Adv. Mater. Sci. 18 (2018) 5–10, https://doi.org/10.1515/adms-2017-0027.

THE EUROPEAN PHYSICAL JOURNAL A



Regular Article - Experimental Physics

The application of the unfolding technique for determination of photo-nuclear reaction cross-section with an example on the $^{115}\text{In}(\gamma,\gamma')^{115m}$ In reaction

Z. Medic¹, N. Jovancevic^{1,a}, D. Maletic², Y. Teterev³, S. Mitrofanov³, A. Belov³, M. Krmar¹, M. Hult⁴, S. Oberstedt⁴

- ¹ Physics Department, Faculty of Sciences, University of Novi Sad, Novi Sad, Serbia
- ² Institute of Physics, Belgrade, Serbia
- ³ Flerov Laboratory of Nuclear Reactions, Joint Institute for Nuclear Research, Dubna, Russia
- ⁴ European Commission, Joint Research Centre (JRC), Geel, Belgium

Received: 13 April 2021 / Accepted: 25 July 2021 / Published online: 24 August 2021 © The Author(s), under exclusive licence to Società Italiana di Fisica and Springer-Verlag GmbH Germany, part of Springer Nature 2021 Communicated by Robert Janssens

Abstract The cross-section function for the 115 In(γ , γ') 115m In reaction was determined in the energy range up to $E_{\gamma} = 9.6$ MeV using the bremsstrahlung facility at the MT25 Microtron, JINR, Dubna. Natural indium disks were irradiated with bremsstrahlung, each disk with a beam of different endpoint energy. To the measured saturation activity built up in the wide-energy photon beam we applied the unfolding technique, developed recently at the JRC-Geel with the primary purpose of being used in neutron activation. The results were compared with TALYS 1.9 calculations and existing experimental data. Our results suggest that the application of existing unfolding technique allow determining unknown excitation functions of photon-induced reactions.

1 Introduction

Experimental data obtained in nuclear reactions induced by photons on various materials are important for a number of different applications. High-energy photons are used to produce radionuclides for medicine and other applications. They are used in radiotherapy, industry, activation analysis and play significant roles in astrophysical processes and in the dynamics of nuclear reactors [1]. Therefore, cross-sections of photo-nuclear reactions are often studied in a wide energy region. The rich amount of experimental results obtained, can be found in several databases such as Refs. [2–8].

The aim of this paper is to apply the NAXSUN technique (Neutron Activation X-Section determined using UNfolding) to determine the differential cross section for the excitation of the 336.2 keV isomer in ¹¹⁵In as a function of the photon

energy, using photons from bremsstrahlung beams of several different endpoint energies. The NAXSUN technique was developed at the JRC-GEEL and utilized to obtain neutron-induced reaction cross sections as a function of incident neutron energy [9–13]. For the photo-activation measurements we adapted the NAXSUN technique and examined its applicability in photon-induced reactions.

There are several reasons why the excitation of ¹¹⁵In isomer state was chosen to test the possibility of extending the NAXSUN technique to the field of photo-nuclear reactions. Natural indium is a mixture of two isotopes 113 In (4.3%) and 115 In (95.7 %) [14]. It is a soft metal that is easy to shape in the desired irradiation and detection geometry. It can be used in several different ways as an activation detector for neutrons or photons. The high thermal neutron cross section of 160 b [15] has made 115 In a frequently used nuclide for neutron monitoring. The excitation of the 336.2 keV [14] isomeric state by non-elastic neutron scattering, $^{115}In(n,n')^{115m}In$, is recognized as one of the most common reactions for detection and monitoring of fast neutrons. Moreover, detection of photons having energies higher than 9 MeV (produced by LINACs used in radiotherapy, for example), which is the threshold energy for the photo-nuclear reaction 115 In(γ ,n) 114 In, is possible by using activation foils made of natural indium. And finally, high-energy photons may excite the isomeric state via the reaction $^{115}\text{In}(\gamma,\gamma')^{115m}\text{In}$.

All these reactions make indium the material of choice in experimental circumstances, when it is necessary to register the presence of neutrons and photons at the same location. For neutron reactions on 115 In cross sections are well known, and reliable data on the differential cross section for the 115 In(γ ,n) 114 In reaction are available, too. There are several experimental data sets [16–20], included in database [8],



^a e-mail: nikola.jovancevic@df.uns.ac.rs (corresponding author)

258 Page 2 of 14 Eur. Phys. J. A (2021) 57:258

for photo-excitation of the 115 In isomeric state. The cross-section values of the 115 In(γ,γ') 115m In reaction and the shape of the cross-section function in those several sources differ somewhat (datasets are shown in Fig. 12). Furthermore, data available in literature [8], show discrepancy with TALYS 1.9 [21,22] calculations, as can be seen in Figs. 11 and 12, below in this text. Additional objective of this paper is to report on a new measurement of the 115 In(γ,γ') 115m In cross section.

Possible applicability of NAXSUN techniques in photnuclear reactions can open a broad research field. Differential cross sections for (γ,n) reactions are well documented with reliable experimental material. However, at higher photon energies, when two or more neutrons are emitted, the results of measuring the flux-weighted averaged cross section and measurements with quasi-monoenergetic photon beam can be found in the literature [2,3,8]. For a specific channel of (γ,xn) nuclear reactions, energy differential cross-sections can be obtained using theoretical calculations only. The introduction of the NAXSUN techniques could make it possible to measure energy differential cross-sections for these nuclear reactions as well.

2 The method

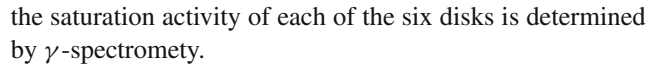
The NAXSUN technique is based on irradiation of several identical metal disks in different, but overlapping, neutron fields. It is followed by gamma-spectrometric measurements and unfolding procedures. This method has solely been used for measuring cross section curves for neutron-induced reactions [11–13].

The yield of activation products from some nuclear reactions, here the photo-excitation of the first excited and metastable state in 115 In in a bremsstrahlung beam, can be quantified by its saturation activity (maximum equilibrium activity when the rate of production of reaction product equals the rate of decay) A:

$$A = \int_{E_{cl}}^{E_{max}} \sigma(E) \cdot \Phi(E) \cdot dE \tag{1}$$

where $\sigma(E)$ is the cross section for the studied nuclear reaction, $\Phi(E)$ is the flux spectrum of incident photons and E is the photon energy. E_{th} is the energy threshold for the nuclear reaction and, E_{max} is the endpoint energy of the bremsstrahlung beam. After exposure to the photon beam, the induced activity of 115m In is measured by a high energy resolving γ -spectrometer.

One indium disk at the time was exposed in a bremsstrahlung beam of particular endpoint energy. The endpoint energies ranged from 5 to 10 MeV. In this way disks were exposed to different but overlapping photon fields, similar to the measurements performed in our previous work, where broadenergy neutrons fields were applied [11–13]. After irradiation



If the photon flux-spectrum, $\Phi(E)$ can be estimated, as shown in Section III D. in this paper, the general task comes down to the solution of six integral equations (Eq. 1) for each irradiated sample, and the determination of the unknown function $\sigma(E)$, which describes the cross section of the photonuclear reaction. Having six known values of saturation activity, A, the problem can be transformed into a system of discretized equations:

$$A_k = \sum_{i}^{c} \Phi_{ik} \cdot \sigma_i \cdot \Delta E_i; \quad k = 1, 2, ...m$$
 (2)

where A_k is the measured saturation activity of each irradiated disk, k, with m activated disks, k running from 1 to 6. The photon flux for a certain energy bin, E_i and disk k is described by Φ_{ik} . ΔE_i is the width of energy bin i, and c is the number of energy bins. σ_i represents the sought cross section function. Since c is larger than m the system of equations is under-determined and an unfolding procedure needs to be applied. In this work, we used three unfolding algorithms, SANDII, GRAVEL and MAXED [23–27], to take into account corresponding systematic uncertainties.

3 Measurements

3.1 Material

Six identical metal disks of indium with natural isotopic abundances were used. The material has a high level of purity with 99.9% of natural indium. Disks had an identical shape with a diameter of 20.0(1) mm and and an average thickness of 0.210(1) g cm⁻¹. Two more indium discs were used to check influence of neutrons on excitation of ¹¹⁵In isomer state. Sources of neutrons are described in next section.

3.2 Irradiation

All experimental activities were performed at the Flerov Laboratory of Nuclear Reactions of the JINR, Dubna. The MT25 Microtron [28] was used to produce the bremsstrahlung beams for irradiation of the indium disks. A more detailed description of the Microtron and the experimental setup can be found in Ref. [29]. Indium disks were exposed to bremsstrahlung with endpoint energies from 5 to 10 MeV in steps of 1 MeV (Table 1). For the photon production we used a 1 mm thick tungsten radiator. The distance between the the radiator and an indium disk was 60 cm.

An 8 mm thick beryllium plate was placed in front of the In sample, 52.5 cm far from the tungsten radiator, to serve in another study [29]. The influence of the beryllium plate on



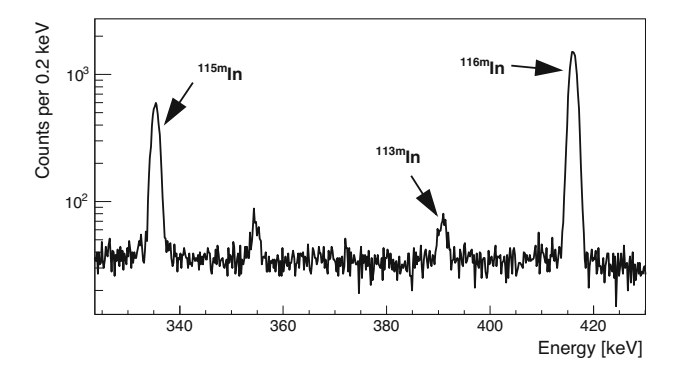


Fig. 1 Part of the γ -ray spectrum collected after irradiation of indium disk No. 6. The γ lines of interested are labelled. Energy width of one channel is 0.2 keV

the photon flux was corrected by Monte Carlo simulation as described below. The scheme of the experimental set up is presented in the Fig. 2.

Energy thresholds for photo-disintegration of ⁹Be (followed by emission of neutron) and $^{183}W(\gamma,n)^{182}W$ are 1.7 MeV and 6.2 MeV respectively [30]. In order to minimize the influence of inelastic neutron scattering, 115 In(n,n') 115m In reaction, the indium disks were placed in the center of a water container with a diameter of 15 cm. In this way, fast neutrons created in photo-nuclear reactions in beryllium and tungsten are thermalized. The need for such an action was confirmed by a noticeable difference in 115m In activity, after exposure with and without water around the indium disk. At a maximum photon energy of 23 MeV the saturation activity of 115m In in the disk exposed outside the water container was 15% higher than the saturation activity of 115m In, when the disk was located inside the water container. Furthermore, we may expect significantly lower parasitic neutron production at lower energies. We observed too that the saturation activity of ¹¹⁶In produced by neutron capture is about 130 times lower at a photon-energy of 10 MeV than at endpoint energy of 23 MeV. This means that there is an insignificant influence of non-elastic scattering of high-energy neutrons on the excitation of the isomeric state in ¹¹⁵In with samples placed in the water container.

The irradiation time was longer for lower photon-energies and ranged from 14 min at 10 MeV to 98 min at 5 MeV. The Microtron electron current varied from 2 to 7 μ A. The integral number of electrons striking the tungsten radiator (Q) is summarized in the Table 1.

3.3 Gamma spectroscopy measurements

After exposure, the decay spectra of the indium disks were measured using an HPGe detector. The relative efficiency of the detector was 25% and, it was passively shielded by 5 cm of lead. The irradiated indium disks were located directly on

the vertical end-cap of the detector. The elapsed time between the end of the irradiation and the start of each measurement was between 6 min and 2 h depending on detector availability. Considering that the half life of 115m In is $T_{1/2}=4.468$ h [14], in the worst case, more than 73% of initial activity remained. The measurement time for each activated disk was 30 min that was sufficient to obtain good counting statistics. For example, in the spectrum of that indium disk exposed to the 7 MeV bremsstrahlung beam the statistical uncertainty of the 115m In gamma line was about 3% at 1 σ .

The recorded spectra have very simple structure (part of the γ -ray spectrum collected after irradiation of indium disk No. 6. is presented in Fig. 1). In all of them the prominent 336.2 keV gamma line from the de-excitation of the isomeric level in 115m In is observed. The gamma line of the isomeric state of 113m In, $E_{\nu} = 391.7$ keV [14], is noticeable in some of measured spectra, especially in the spectrum from the indium disk exposed at 10 MeV endpoint energy as depicted in Fig. 1. In the γ -ray spectrum of the disk exposed to the 5 MeV bremsstrahlung, the 391.7 keV gamma line is not observed at all. The reason is the low abundance of ¹¹³In in natural indium, i.e. 4.3 % in combination with the small flux at 5 MeV. Several other gamma lines (416.9 keV, 1097.3 keV and 1293.5 keV [14]) emitted after the decay of ^{116m}In, produced by neutron capture of ¹¹⁵In, appeared only in spectra of those indium disks exposed at higher endpoint energies.

The saturation activity of 115m In can be determined from the peak area of the 336.2 keV gamma line according to:

$$A_{k} = \frac{N_{\gamma} \cdot M\lambda}{m \cdot N_{A} \cdot \epsilon \cdot \eta \cdot p_{\gamma} \cdot e^{-\lambda \Delta t} \cdot (1 - e^{-\lambda t_{irr}}) \cdot (1 - e^{-\lambda t_{m}})}$$
(3)

where N_{γ} is the number of detected γ rays with $E_{\gamma} = 336.2$ keV, λ is the decay constant, M and m are the mass number and the mass of the In disk used, N_A is Avogadro constant, ϵ is the total efficiency of the detector at 336.2 keV, η is the natural abundance of ¹¹⁵In, p_{γ} is a gamma emission probability, Δt , t_{irr} and t_m are cooling, irradiation and measurement time, respectively. Total efficiency was determined using calibration sources and LabSOCS software. Since indium is a soft metal, our samples were designed to match existing detector calibrations.

We notice that the saturation activity for $E_{max} = 5$ MeV is almost 150 times lower than the one at $E_{max} = 10$ MeV. All saturation activities, A_k , are summarized in Table 3. The statistical uncertainty at 5 MeV and at 6 MeV is about 10 % and, above 7 MeV the statistical uncertainty is up to 4 %.



258 Page 4 of 14 Eur. Phys. J. A (2021) 57:258

Table 1	Irradiation characteristics for each indium	disk: 1	E_{max}	bremsstrahlung endpoint energy,	Q integral	l number of electrons	striking	tungsten
target, t	rr time of irradiation							

Disk no.	E_{max} (MeV)	Q (mAs)	t_{irr} (s)
1	5.00(5)	12	5880.0(5)
2	6.00(5)	10	1320.0(5)
3	7.00(5)	12	1740.0(5)
4	8.20(5)	3.5	1680.0(5)
5	9.00(5)	7	1020.0(5)
6	10.00(5)	6	840.0(5)

3.4 Determination of photon flux

3.4.1 Monte Carlo simulation

The application of unfolding procedures to our problem requires information about the Φ_{ik} from Eq. 1, i.e. shape and intensity of the bremsstrahlung photon spectra. This was obtained using Monte Carlo (MC) simulations and the measured values of the integral number of electrons striking the tungsten radiator.

To estimate the flux of incident photons $\Phi(E)$ for the six used energies we employed Geant4 (G4) version 10.05.p01 [31] with the experimental Physics list QBBC. QBBC uses the standard G4 electromagnetic physics option without optical photon simulations and, the hadronic part of this physics list consists of elastic, inelastic, and capture processes. Each hadronic process is built from a set of cross sections and interaction models, which provide the detailed physics implementation.

Figure 2 depicts the setup geometry as entered to the Geant4 simulations. Elements of simulations are starting from the electron beam, shown to the left of the figure, going to the indium disk placed in the water container on the right. In the G4 simulations electron beam starting position is 10 cm before Cu foil.

The geometry of the Geant4 simulations consists of an electron beam of six energies, assuming a \pm 1% uncertainty (k = 1) for all energies. Then, on the beam path comes first a 70 μm thick copper foil followed by a copper cylindrical collimator with a 12 mm-wide circular hole. Next comes a 1 mm thick tungsten radiator followed by a 2 cm thick aluminium block. The distance between the tungsten radiator and the indium disk is 60 cm. In front of the indium disk we placed an 8 mm thick beryllium sheet and the water shielding. We simulated about 2×10^8 electrons for six different electron beam energies. From the simulation we obtained the integral number of photons, spectrum shape and the distribution of photons on the surface of an indium disk for each energy. To get approximation of integral number of gammas, which hit the indium sample, the number of photons from the simulation were scaled, having in mind that the number

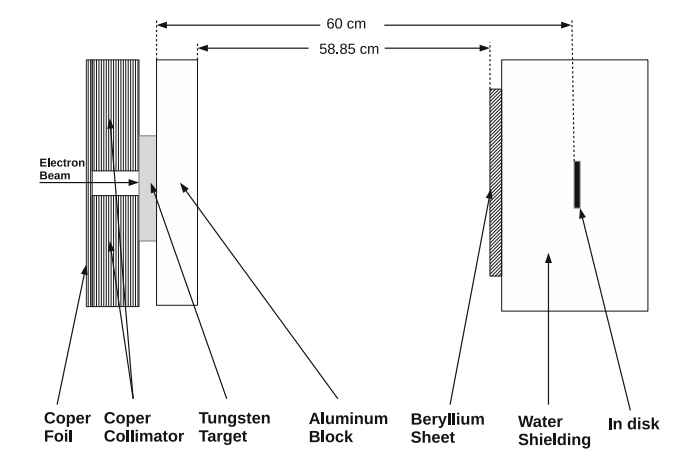


Fig. 2 Geometry of experimental setup (not in scale)

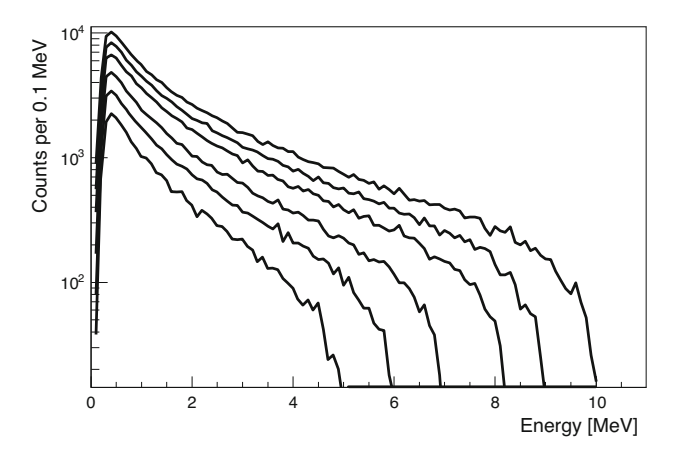


Fig. 3 Spectra of photon flux on the indium disks for all electrons energies incident on the tungsten radiator. The electron energy corresponds to the end-point energy of the respective photon-flux spectrum (E_{max} in the Table 1)

of electrons per mAs is 6.242×10^{15} and that each beam energy had a different number of electrons per second. The estimated integral number of photons hitting an indium disk at the particular endpoint energy is shown in the last column of Table 2. The simulated photon spectra are depicted in Fig. 3.



Eur. Phys. J. A (2021) 57:258 Page 5 of 14 258

Fig. 4 The photon distribution on the surface of an indium disk, simulated for the endpoint energy 10 MeV

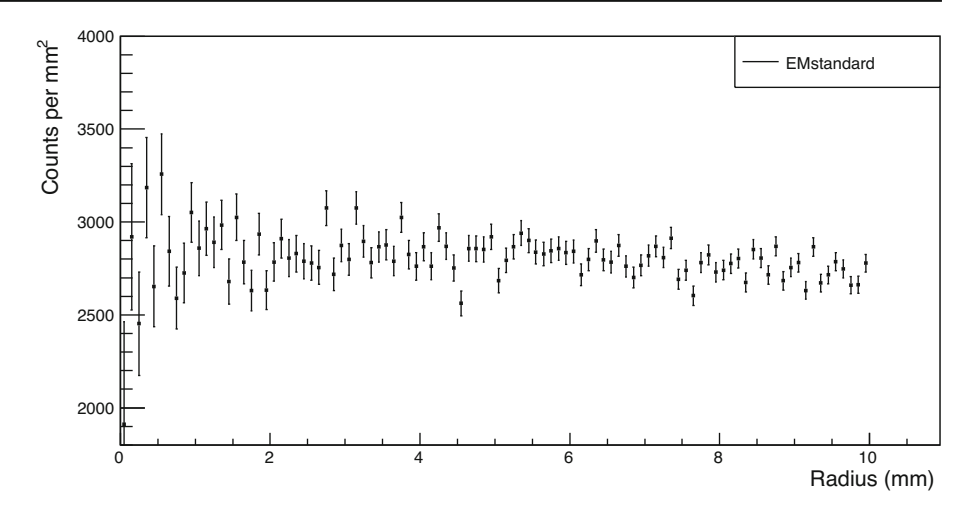


Table 2 Irradiation characteristics of the indium disks: E_{max} endpoint energy, $N_{e,S}$ simulated number of electrons, $N_{\gamma,S}$ simulated number of photons, S scaling factor, $N_{\gamma,Scaled}$ scaled number of photons

E (MeV)	$N_{e,S}$ (10 ⁶)	$N_{\gamma,S}$	S (10 ⁷)	$N_{\gamma Scaled} \ (10^{12})$
5.00(5)	200	25312	3.12	9.48
6.00(5)	199	43163	3.14	13.54
7.00(5)	194	65120	3.22	25.14
8.20(5)	192	99595	3.25	11.33
9.00(5)	192	129258	3.25	29.42
10.00(5)	187	165313	3.34	33.11

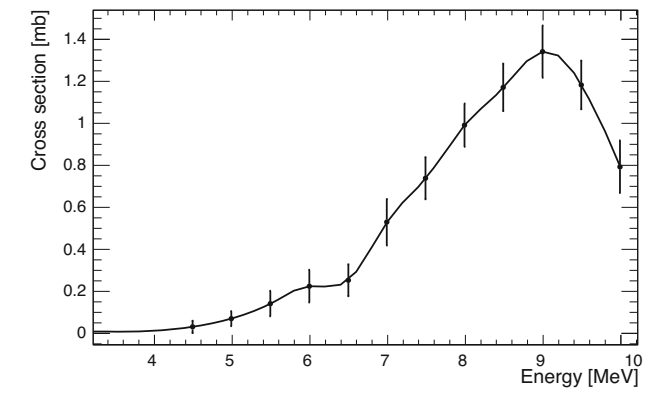


Fig. 5 Cross section for $^{113}In(\gamma, \gamma')^{113m}In$ reaction (points – measured data [32], line – spline interpolation)

In Fig. 4 the simulated areal distribution of the photon flux on the indium disks is shown for the 10 MeV endpoint energy. The distribution is flat across the entire disk. Corresponding results were obtained for the other endpoint energies.

3.4.2 Normalization of photon flux

To obtain absolute cross section values, it is necessary to have accurate values of the photon flux at the place of the exposed indium disks. In our experimental setup, the total number of

electrons striking the tungsten radiator, expressed in mAs in Table 1, could only serve as a relative measure. For the absolute calibration of the Monte-Carlo simulated photon spectra, it was necessary to use another nuclide with well-known photo-activation cross section. In the absence of some wellaccepted standard, it was decided to use the photo-activation of ¹¹³In for spectrum normalisation. As can be seen in Fig. 1, the characteristic gamma line of 113m In is present in the spectrum after irradiation of the indium samples at higher energies. The cross section function for the reaction 113 In(γ , γ')^{113m}In was taken from Ref. [32] as depicted in Fig. 5. In this study, samples of natural indium were irradiated in the range of 4-12 MeV with 0.5 MeV increments. The cross section was calculated using Penfold-Leis method [33]. Photon flux was determined using an absolutely calibrated ionization chamber with a build-up cap of appropriate thickness.

Saturation activity for 113 In(γ,γ') 113m In reaction at some chosen energy, A_c , can be calculated based on the Eq. 2. Photon flux spectra were calculated using Monte-Carlo simulation with a number of incident electrons specified in Table 2. Simulated spectra were corrected by Microtron electron current Q, as a relative measure, taken from Tab. 1. Interpolated values of the cross-section from Fig. 5 were taken to calculate the saturation activity A_c for the 10 MeV photon beam. The measured values of the saturation activities for the



258 Page 6 of 14 Eur. Phys. J. A (2021) 57:258

Disk No.	Energy [MeV]	$A_k[10^{-18} \text{ Bq/atom}]$
1	5.00(5)	0.0090(9)
2	6.00(5)	0.044(5)
3	7.00(5)	0.161(7)
4	8.20(5)	0.191(5)
5	9.00(5)	0.87(3)
6	10.00(5)	1.33(3)

Table 3 Saturation activity, A_k , for a given endpoint energy, E_{max} calculated according to Eq. 3

 A_m obtained using the intensity of the 391.7 keV gamma line detected for 10 MeV was $1.10(18) \times 10^{-18}$ Bq/atom. Based on that, a normalization factor of $r = A_m/A_c = 6.2(11)$ was obtained and used to normalise photon spectra, which were used in unfolding procedures.

4 Experimental results

4.1 Default functions for unfolding procedures

Cross-section unfolding procedures require an initial guess of the sought function, the so-called default function, to proceed further with the unfolding calculation. This function should be a reasonably good guess of the real cross-section function. In this work we used the TALYS 1.9 code [22] for determining this default functions.

TALYS 1.9 is a computer code for the simulation of nuclear reactions. A detailed description of TALYS 1.9 can be found in Ref. [22]. By this code it is possible to calculate various physical quantities for all possible outgoing reaction channels using different physical models in the calculations. In this work we calculated the cross section for the $^{115}\text{In}(\gamma, \gamma')^{115m}\text{In}$ reaction, for incident photon energies ranging from 0 to 10 MeV. All parameters of calculations were code-default values except level density parameters. Available level density models in the TALYS 1.9 are [34–42]:

- LD model 1. the constant temperature Fermi-Gas model;
- LD model 2. the back-shifted Fermi gas model;
- LD model 3. the generalised super-fluid model;
- LD model 4. the microscopic level densities based on the Goriely's tables;
- LD model 5. Hilaire's combinatorial tables;
- LD model 6. the temperature dependent Hartree-Fock-Bogoliubov model, Gogny force.

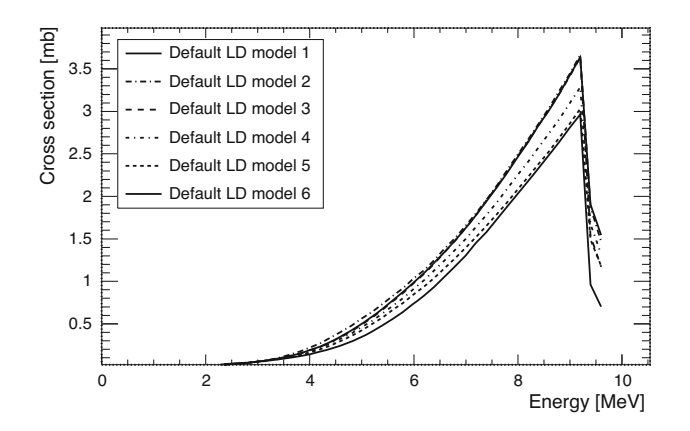


Fig. 6 Default functions for the 115 In(γ , γ') 115m In cross-section obtained by TALYS 1.9 for six different level density models (for details see text)

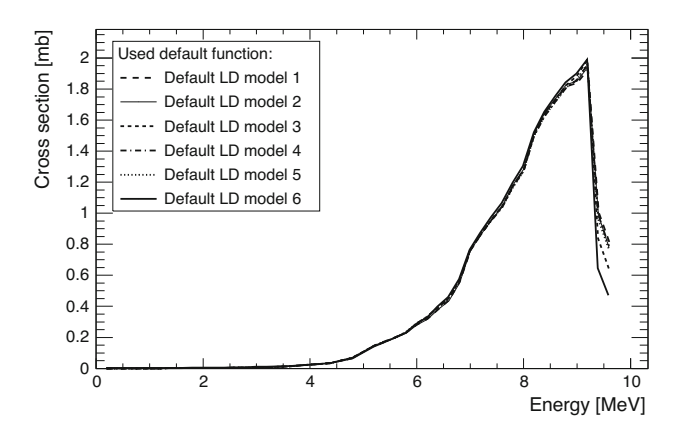


Fig. 7 Unfolded $^{115}\text{In}(\gamma, \gamma')^{115m}\text{In}$ cross-section for each default function, produced using the SANDII unfolding algorithm

Six different excitation functions for the 115 In(γ , γ ') 115m In reaction were obtained (see Fig. 6) and used as default functions for the unfolding procedures.

Other parameters such as photon strength functions (PSF) can also have a significant impact on cross-section values. However, detailed theoretical analysis was not part of this study and those parameters are not change from the default values given by the TALYS 1.9., which are for example the standard Lorentzian (Brink-Axel model) for PSF.



Eur. Phys. J. A (2021) 57:258 Page 7 of 14 258

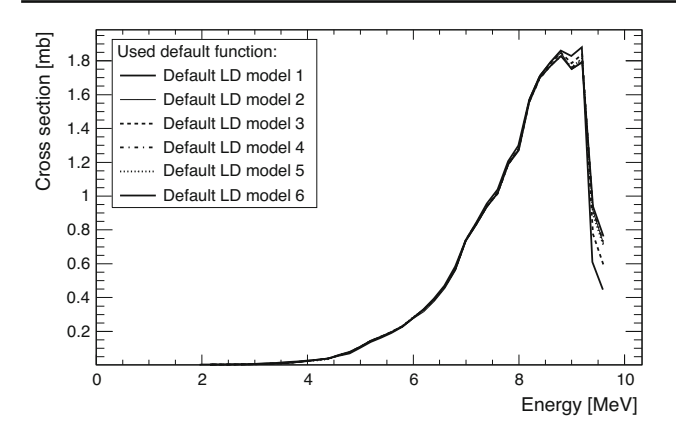


Fig. 8 Unfolded $^{115}\text{In}(\gamma, \gamma')^{115m}\text{In}$ cross-section for each default function, produced using the GRAVEL unfolding algorithm

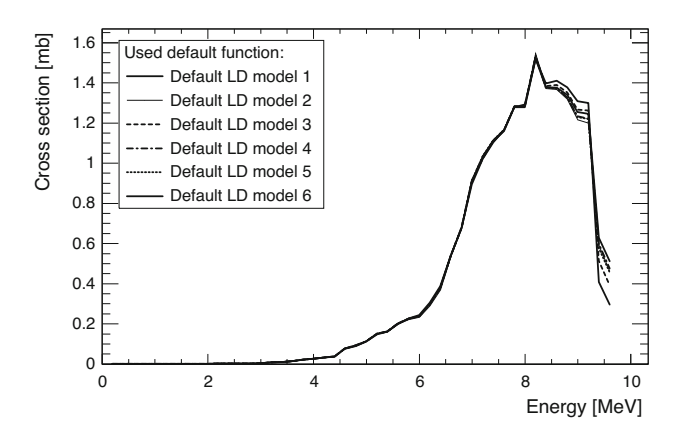


Fig. 9 Unfolded $^{115}\text{In}(\gamma, \gamma')^{115m}\text{In}$ cross-section for each default function, produced using the MAXED unfolding algorithm

4.2 Unfolding results

Three unfolding algorithms were used in this work and their results were compared. The first one was the SANDII iterative algorithm [27], the second was the GRAVEL algorithm, which is an improved version of SANDII [26] and, the third one was the MAXED algorithm that uses the maximum entropy principle to calculate the unfolded function [23].

The SANDII and GRAVEL algorithm give the solution:

$$\sigma_{i}^{J+1} = \sigma_{i}^{J} f(A_{k} \epsilon_{k} \Phi_{ki} \sigma_{i}^{J})$$

$$f = \exp\left(\frac{\sum_{k=1}^{m} W_{ik}^{J} \ln\left(\frac{A_{k}}{\sum_{i=1}^{n} W_{ik}^{J} \sigma_{i}^{J}}\right)}{\sum_{k=1}^{m} W_{ik}^{J}}\right), i = 1, 2...n$$
(4)

where in the case of the SANDII W_{ik}^{J} is:

$$W_{ik}^{J} = \frac{\Phi_{ki}\sigma_i^J}{\sum_{i=1}^n \Phi_{ki}^J}.$$
 (5)

and in the case of the GRAVEL W_{ik}^{J} is:

$$W_{ik}^{J} = \frac{\Phi_{ki}\sigma_i^J}{\sum_{i=1}^n \Phi_{ki}^J} \frac{A_k^2}{\epsilon_k^2}.$$
 (6)

 A_k is measured saturated activity, ϵ_k is measured uncertainty, cross-section for energy bin E_i is σ_i and photon flux is Φ_{ki} when irradiating k disk at energy bin E_i , J is number of the iteration step, m is number of activated discs and n is number of energy bins.

The MAXED algorithm provides by the fitting input data (measured induced specific saturated activity A_k), a function $\sigma(E)$ that maximizes the relative entropy:

$$S = -\int \left(\sigma(E) \ln \left(\frac{\sigma(E)}{\sigma_{def}(E)}\right) + \sigma_{def}(E) - \sigma(E)\right) dE$$
(7)

where $\sigma_{def}(E)$ is the default cross section function.

Unfolding procedures were performed in the energy range between 0 and 9.6 MeV grouped into 48 bins. The results obtained by the SANDII, GRAVEL and MAXED algorithms for all used default functions are presented in Figs. 7, 8 and 9.

4.3 Analysis of uncertainties

We will analyse here following sources of uncertainties that could have affect the final results: the measurement of saturated gamma activity, determination of normalisation factor, Monte Carlo calculation of photon spectra and unfolding procedures.

4.3.1 Gamma activation measurement

The uncertainty values of saturated gamma activity were determinated by taking into account contribution of uncertainties of all parameters from Eq. 3, and obtained values are presented in Table 3. Those uncertainties are dominated by statistical error of measurement of gamma peak intensity. Uncertainties of gamma activation measurement are affected the final results. However, only the MAXED algorithm gives the possibility to estimate the error of the cross section values depending on the error of the measured activity, while for the other two algorithms such an error analysis is not possible [43]. Cross section uncertainty of the MAXED code due to saturated gamma activity measurement uncertainty is presented in the first column of Table 5 in the case of the LD model 6 used as default function. Similar results were obtained for other 5 default functions. The influence of the measured gamma activity uncertainty on the error of the final results using other algorithms requires additional analyses that are not part of this study.



258 Page 8 of 14 Eur. Phys. J. A (2021) 57:258

Fig. 10 Spectra of photon flux on the indium disks for 10 MeV endpoint energy obtained by different models: EMstandard, EM standard_opt3, EMLivermore and EMPenelope

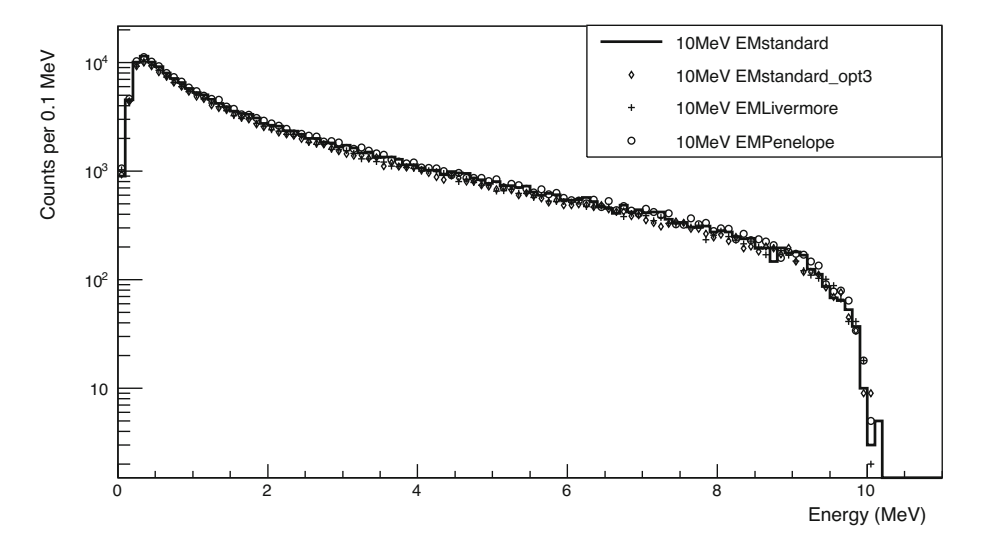
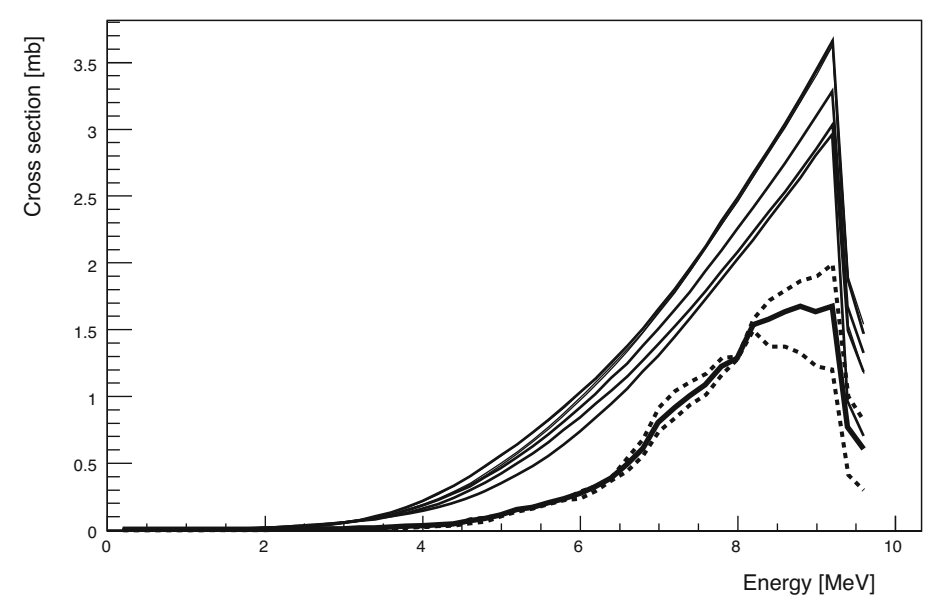


Fig. 11 Unfolded results for the 115 In(γ , γ') 115m In cross-section (line with a corridor of uncertainty) in comparison with default TALYS 1.9 functions (Fig. 6)



4.3.2 Normalisation factor

The cross section values for the $^{113}In(\gamma,\gamma')^{113m}In$ reaction taken from Ref. [32] were determined with uncertainty that varied form 50 % at low energy to 10% at higher energy. That lead to uncertainty of 17% for normalisation factor which introduced additional uncertainty of the final results obtained in this study. This problem can be solved by introducing precise measurement of photon flux as a part of this technique or by selecting another reaction (with well-known efficient cross-sections) as the standard for normalization.

4.3.3 Monte Carlo calculation of photon spectra

In this study, the QBBC model which is recommended for medical and space physics simulations was used [44,45]. Analysis of possible systematic uncertainty introduced by

the choice of the model in the Geant4 simulation was done by comparing results from other available models.

EM standard option model used in the QBBC physics list, as well as previously studied models [46], EM standard option3, Livermore and Penelope, predict the correct absolute scale and are able to reproduce the shape of the energy spectra at forward emission angles, which make the leading contribution to the total radiated energy. Nevertheless, all models over-estimate the bremsstrahlung emission in the backward hemisphere and predict a harder energy distribution than measured [46], which is not the case here, where all bremsstrahlung emission are in the narrow forward region. Obtained results by comparing different models are presented in the Fig 10. Based on those results we consider that the uncertainty introduced by the choice of the model in the Geant4 simulation is negligible.



Eur. Phys. J. A (2021) 57:258 Page 9 of 14 258

Fig. 12 Comparison of the $^{115}\text{In}(\gamma,\gamma')^{115m}\text{In}$ cross-section obtained in this work (line with uncertainty bars) with existing experimental data (white circle – [16], black filled square – [17], black filled circle – [18], black filled triangle [19], white square – [20])

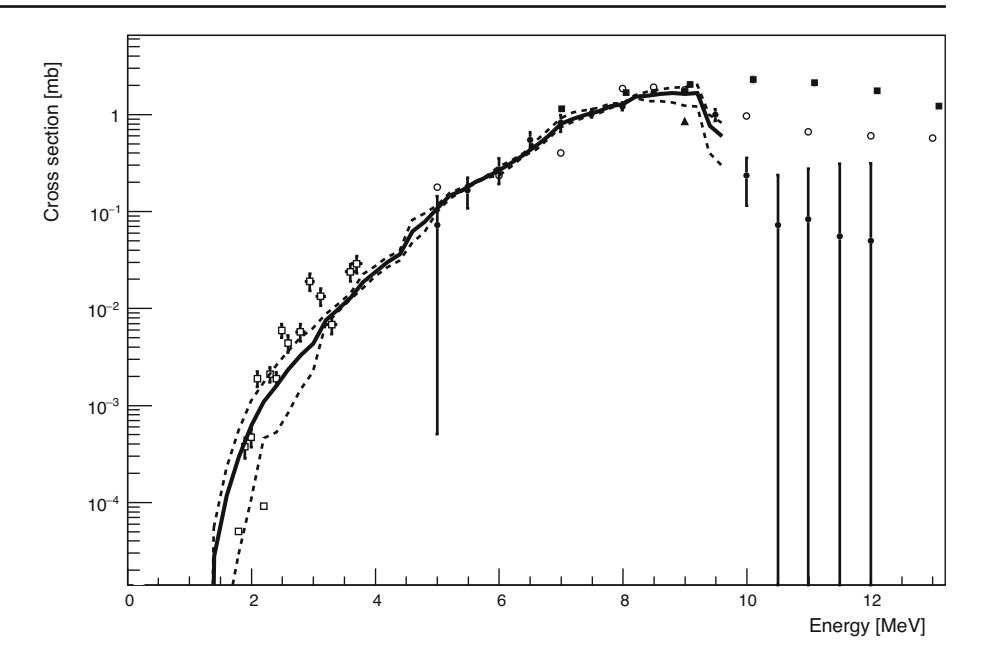


Table 4 The χ^2 values 8 for: 1. Default functions before unfolding procedures, 2. SANDII results, 3. GRAVEL results and 4. MAXED results

χ^2							
Energy (MeV)	Ld model 1	Ld model 2	Ld model 3	Ld model 4	Ld model 5	Ld model 6	
1. Default functions	5						
5.00(5)	253.03	280.01	252.84	272.95	282.51	297.59	
6.00(5)	33.40	39.41	32.73	34.67	34.81	30.09	
7.00(5)	107.44	116.33	105.32	107.33	106.26	87.90	
8.20(5)	0.03	0.31	0.02	0.14	0.21	0.38	
9.00(5)	112.89	132.55	110.05	120.70	123.58	112.17	
10.00(5)	120.07	144.36	119.75	130.04	133.45	117.23	
2. SANDII results							
5.00(5)	0.16	0.14	0.28	0.30	0.32	0.54	
6.00(5)	0.58	0.51	0.62	0.64	0.66	0.90	
7.00(5)	2.56	2.53	2.69	2.75	2.72	1.90	
8.20(5)	0.08	0.04	0.06	0.06	0.07	0.11	
9.00(5)	6.55	6.72	7.27	7.77	7.62	5.62	
10.00(5)	0.76	0.79	0.34	0.39	0.38	0.50	
3. GRAVEL results							
5.00(5)	0.77	0.52	0.80	0.93	1.00	2.57	
6.00(5)	0.24	0.21	0.27	0.25	0.26	0.32	
7.00(5)	4.80	4.46	4.45	4.70	4.61	3.59	
8.20(5)	0.31	0.21	0.30	0.31	0.31	0.26	
9.00(5)	4.47	4.25	4.14	4.44	4.40	3.95	
10.00(5)	1.01	1.15	0.91	0.97	0.96	0.79	
4. MAXED results							
5.00(5)	0.06	0.05	0.06	0.07	0.07	0.10	
6.00(5)	0.35	0.28	0.35	0.34	0.35	0.41	
7.00(5)	2.73	2.62	2.72	2.64	2.60	2.76	
8.20(5)	3.64	3.72	3.64	3.76	3.76	3.56	
9.00(5)	3.06	2.85	2.88	2.87	2.84	2.85	
10.00(5)	2.16	2.50	2.33	2.32	2.40	2.33	



258 Page 10 of 14 Eur. Phys. J. A (2021) 57:258

Table 5 Analysis of uncertainties

Energy (MeV)	$\sigma_{MAXEDAc}$ (%)	σ_{SANDII} (%)	σ_{GRAVEL} (%)	σ_{MAXED} (%)	σ_U (%)	σ_D (%)
0.2	8568.00	10.94	14.21	25.59	100.49	99.99
0.4	3561.00	10.79	14.45	45.28	105.83	100.00
0.6	341.20	10.98	14.17	35.66	105.17	100.00
0.8	227.50	11.11	14.32	25.27	101.48	99.99
1	171.70	11.03	14.04	19.87	98.56	99.78
1.2	149.10	10.96	14.32	16.56	96.92	99.56
1.4	123.20	11.13	14.16	13.57	95.09	98.14
1.6	85.50	11.12	14.00	12.44	86.72	94.71
1.8	81.27	10.98	14.15	10.82	85.21	90.20
2	52.99	11.10	13.98	12.17	74.33	83.02
2.2	55.47	10.89	13.68	8.35	56.57	58.67
2.4	47.59	10.92	13.71	10.13	61.19	66.70
2.6	44.83	10.51	12.97	10.26	56.38	63.56
2.8	31.66	9.47	12.17	10.88	48.19	57.08
3	36.10	7.68	10.34	8.25	40.95	49.71
3.2	20.04	5.59	7.92	4.86	14.57	11.22
3.4	17.51	3.23	5.60	3.03	11.16	6.88
3.6	13.32	1.44	3.54	1.58	8.85	5.50
3.8	10.30	1.42	1.72	1.07	20.42	13.81
4	7.42	2.59	1.54	1.30	12.16	12.01
4.2	7.73	3.68	2.26	1.60	10.48	13.41
4.4	8.01	4.36	2.67	2.28	8.58	13.76
4.6	15.53	4.03	3.26	2.58	29.84	24.26
4.8	13.53	3.86	3.20	2.08	21.77	20.88
5	16.38	2.84	2.88	0.85	6.23	8.65
5.2	12.87	2.17	2.73	0.89	4.87	8.13
5.4	9.82	1.57	2.03	0.47	4.20	4.11
5.6	7.14	0.89	1.47	0.38	1.26	4.09
5.8	9.05	0.75	0.94	0.64	1.74	2.63
6	11.47	1.07	0.61	1.26	7.86	12.82
6.2	11.67	1.72	1.09	1.32	4.67	8.03
6.4	8.48	1.61	1.03	1.38	2.64	4.03
6.6	6.55	1.53	0.86	0.14	11.59	9.67
6.8	4.47	1.35	1.03	0.33	12.83	8.67

4.3.4 Unfolding procedures

The validation of the unfolding results was done by calculating an induced activity $(A_c = \sum \sigma(E_i) \cdot \Phi(E_i) \cdot \Delta E)$ and subsequent comparison with the measured data $(A_k$, Table 3). This was done for all default cross-section functions and for all three algorithms, SANDII, GRAVEL and MAXED. In Table 4, the χ^2 values are presented:

$$\chi^2 = \frac{(A_c - A_k)^2}{\sigma_{A_k}^2} \tag{8}$$



These results suggested that unfolding results can reproduce the measured values of A_k much more accurately than the default functions.

For all three unfolding algorithms averaged cross sections for all variants of default function were calculated. The standard deviations from average values for algorithms are presented in Table 5. The objective of this study was not to judge which of the three unfolding algorithms would give most realistic results. Therefore, we treated all obtained cross sections with equal weights in the following. The final result, depicted in Fig. 11, represents the cross section averaged over all 18 variants, i.e. three unfolding codes and six default functions.

Table 5 continued

Energy (MeV)	$\sigma_{MAXEDAc}$ (%)	σ_{SANDII} (%)	σ_{GRAVEL} (%)	σ_{MAXED} (%)	σ_U (%)	σ_D (%)
7	7.04	0.21	0.21	0.81	14.30	8.32
7.2	6.02	0.46	0.53	0.63	13.90	8.67
7.4	4.55	0.64	0.62	0.34	11.14	6.61
7.6	3.69	0.78	0.74	0.19	8.43	5.87
7.8	5.62	0.81	0.62	0.23	5.81	4.21
8	3.46	0.77	0.66	0.34	1.45	0.81
8.2	7.03	0.67	0.53	0.61	3.01	2.64
8.4	5.60	0.67	0.43	0.58	9.07	12.84
8.6	5.19	0.70	0.60	1.06	9.94	16.22
8.8	5.06	0.62	0.59	1.48	11.44	20.89
9	6.35	1.05	1.51	2.39	16.41	25.35
9.2	5.12	1.18	1.65	2.65	18.73	28.26
9.4	3.83	14.44	13.97	13.30	31.07	46.82
9.6	3.79	17.09	16.59	16.29	36.01	50.74

 $\sigma_{MAXEDAc}$ cross section uncertainty of MAXED code due to measurement uncertainty, σ_{SANDII} standard deviation of average SANDII results, σ_{GRAVEL} standard deviation of average GRAVEL results, σ_{MAXED} standard deviation of average MAXED results, σ_{U} upper limit of final results, σ_{D} down limit of final results

The solid line represents the averaged cross section. Dashed lines depict the maximum and minimum values of the cross sections representing uncertainty corridor obtained directly from the spectrum unfolding which is also presented in Table 5 (σ_U and σ_D).

It turns out that the LD model 2 of the MAXED code gives the lowest estimation of the cross section. The maximum amplitude of the unfolded cross section is obtained with SANDII code using the LD model 4. In this way the region of the most probable values for the 115 In(γ , γ') 115m In reaction cross section, i.e. the uncertainty, was estimated.

In this way, the direct contributions to the uncertainty of the final result from the the measured gamma activity and the normalization factor were not taken into account and that will be part of a future study during the development of this technique.

5 Discussion

According to the TALYS 1.9 calculations, the cross section for a selected nuclear reaction channel can be calculated using different nuclear level density models. In Fig. 6 all TALYS 1.9 calculations of the $^{115}\text{In}(\gamma, \gamma')^{115m}\text{In}$ differential cross-section have a very similar shape. The only difference may be observed in the amplitude of the functions. It is evident, all TALYS 1.9 calculated cross sections show an exponential growth with increasing energy. When the process of neutron emission starts to compete with the process of de-excitation through electromagnetic transition, the cross section for the $^{115}\text{In}(\gamma, \gamma')^{115m}\text{In}$ reaction drops

sharply. According to TALYS 1.9, this happens at around 9 MeV.

Results obtained with three different unfolding algorithms are depicted individually in Figs. 7, 8 and 9. One can see a very interesting trend on them. Differences in the calculated cross sections, presented in Fig. 6, which are not large but still visible, do not produce a significant scatter in the values of the cross section obtained by one single code. For example, different default functions, when used as an input for the SANDII unfolding procedure, give very similar functions describing the cross section (Fig. 7). The same can be seen with the other two codes (Figs. 8, 9). Comparison of the results of three different algorithms, shows that SANDII and GRAVEL give functions of a very similar shape, with a small difference just at maximum energy. Results obtained by the MAXED code predicts slightly different form of the energy differential cross section for the $^{115}\text{In}(\gamma, \gamma')^{115m}$ In reaction. The maximum of the MAXED function is shifted towards 8 MeV, while SANDII predicts that the maximum crosssection value could be at 9 MeV, very similar to the TALYS 1.9 calculations.

Sharp peaks and small discontinuities can be noticed in the results obtained by applying the GRAVEL and the MAXED codes in high energy region above 6 MeV. With a reasonable assumption that the cross section of the $^{115} \text{In}(\gamma, \gamma')^{115m} \text{In}$ reaction should be smooth in the region where a giant dipole resonance is dominant mechanism of excitation of nuclei, it may be concluded that these peaks originate from some numerical phenomena related to the algorithm itself. The number and amplitude of these peaks increase in cases, where



258 Page 12 of 14 Eur. Phys. J. A (2021) 57:258

the reconstruction of the cross section is performed with a larger number of bins.

It can be seen in Fig. 11 that in the energy interval up to 8 MeV there is a very nice agreement between average, smallest and largest estimation of the cross section, leaving us with a very small systematic uncertainty introduced by the different unfolding algorithms. The differences appear in the region between 8 and 10 MeV. The same figure shows all six results from TALYS 1.9 calculations used as default functions. It can be seen that, without special adjustments, TALYS 1.9 gives significantly higher predictions for the cross-section than that obtained from the unfolding of our data. For this reason, there is a large difference between the saturation activities measured and calculated using the cross section estimated on the basis of the TALYS 1.9 calculations, as shown by χ^2 in Table 4.

The obtained average function was compared with existing experimental data from literature, which are unfortunately not very abundant. Figure 12 depicts the comparison of our results (full line) with data from different authors [16– 20], presented by symbols. Most of the data generally shows the same trend, i.e. a growth up to 9 MeV, after which the cross section sharply decrease. In the low-energy region, up to about 4 MeV, our results show the same trend as the data from Ref. [20]. This data is scattered around the line representing our data, obtained by the unfolding technique. The biggest difference between our data and the one from Ref. [20] is around 3 MeV, where our estimation is five times smaller. There is still some room for improvements by using for irradiation photon spectra with endpoint energy less then 5 MeV. It should be noted here that in low-energy region, up to 3 MeV where the excitation of individual levels is possible, some structural effects in the cross section curve should be expected. It is probably a reason of the scatter of the measurements published in reference [20]. Initial TALYS 1.9 function did not take into account the structural effects at low energies.

In the energy region between 5 MeV and 10 MeV the agreement between unfolding results and previous measurements is much better. For example, cross-sections obtained in this project and values published in Ref. [18], presented by closed circles on Fig. 12, are consistent within experimental uncertainties declared by the authors in Ref. [18] and our corridor defined by highest and lowest estimation as presented in Fig. 11. A distinct difference appears at 9 MeV only, where our estimation of the cross-section is 30 % lower. The point at 5 MeV in reference [18] was determined with very large uncertainty. Cross-section values published in reference [17], presented by black squares at Fig. 12 differ from our results up to 35 %. In energy region above 6.5 MeV our values are systematically lower, however, it is interesting to note that in measurements referred in this reference, there is no sharp drop of the cross-section after neutron emission threshold energy at all. The maximum of cross section function presented in this publication is at 10 MeV and minimum of the cross section peak is in energy region between 15 MeV and 18 MeV. Authors used 63 Cu(γ ,n) 62 Cu and absolute ionisation chamber gor calibration and control of bremsstrahlung beam. Authors used [33] algorithm for calculation. The results published in the reference [16] show maximum of cross section peak at 9 MeV, with the drop at energies higher than the binding energy of neutrons, although not so sharp as presented in reference [18]. Values presented in this reference (o—in Fig. 12) are scattered around our results with a maximum deviation of 50 %. Authors of publication [16] used NaI detectors for gamma spectra measurements and ionisation chamber with 7.5 cm thick aluminium walls for reconstruction of photon flux spectra. No information related to calculation cross section function were not presented.

To reveal possible factors, which could affect the cross-section values obtained in this study, we can start from the function describing the flux of the bremsstrahlung photons in Eqs. 1 and 2. This function was obtained by simulation with a reasonable number of incident electrons, from the point of view of the duration of a typical GEANT4 simulation. The amplitude of this function was calculated by normalization based on the measured intensity of 113m In gamma line of $E_{\gamma} = 391.7$ keV in obtained spectra. This was the only way to determine the flux of photons striking the target and, probably, some new method should be developed in a subsequent measurement campaign. Best candidates for new normalisation procedure could be the (γ, γ') reaction on 11 B or the 115 In $(\gamma, n)^{114m}$ In reaction.

6 Conclusions

The results presented in this work demonstrates the successful application of the NAXSUN technique also in the field of photonuclear reactions. We suggest that this method has potential in reconstructing energy differential cross sections using activation data from photonuclear reactions. The method was tested in the low-energy region, up to an endpoint energy of 10 MeV, on the example of photoactivation of the ¹¹⁵In isomeric state, where it was sufficient to monitor the intensity of only one nicely isolated gamma line in the spectrum. If additional checks confirm the potential of this method, one of the possible applications could be in determining the cross section functions of (γ,xn) photonuclear reactions with the emission of more than one neutron, for a number of irradiated nuclei and reaction products (having sufficiently long half-life). For now, only average crosssections can be found in literature for these nuclear reactions [2,3,47,48], and there are no experimentally established energy differential cross-sections for photonuclear reactions with multiple neutron emission at all.



In this paper, TALYS 1.9 calculations are used to construct the default functions, and the question remains for future work, whether it is possible to expand the method of determining the default function using mean values of efficient cross section as in the case of neutron induced nuclear reactions presented in our previous work [11]. This might be an interesting attempt, although the results of this work shows that the impact of a different choice of a default function obtained by only one selected code on the final result is not crucial.

In our analysis, different results were observed by three different algorithms. Differences are the most significant between the MAXED and the other two of the algorithms (Figs. 7, 8, 9). The obtained results are encouraging enough, but they also open the necessity of subsequent experimental activities in which it will be possible to check, which of the used unfolding codes gives the most reliable approximation to the real cross-section value.

Although the differential cross-section of 115 In(γ,γ') 115m In was not of primary interest in this project, it is worth to notice that good agreement with previously published results was obtained. Some of the existing measurement results are quite different, especially at energies higher than $10 \, \text{MeV} \, [16-18]$, but it has been observed that they show quite good agreement in the energy range from 5 to 10 MeV. In the same area, our results are fully consistent with literature data.

Data Availability Statement This manuscript has no associated data or the data will not be deposited. [Authors' comment: The data can be available on request sent to the corresponding author.]

References

- T. Kawano, Y. Cho, P. Dimitriou, D. Filipescu, N. Iwamoto, V. Plujko, X. Tao, H. Utsunomiya, V. Varlamov, R. Xu, R. Capote, I. Gheorghe, O. Gorbachenko, Y. Jin, T. Renstrøm, M. Sin, K. Stopani, Y. Tian, G. Tveten, J. Wang, T. Belgya, R. Firestone, S. Goriely, J. Kopecky, M. Krtička, R. Schwengner, S. Siem, M. Wiedeking, Nucl. Data Sheets 163, 109 (2020a). https://doi.org/10.1016/j.nds. 2019 12 002
- Experimental nuclear reaction data (exfor). https://www-nds.iaea. org/exfor/exfor.htm. Accessed 22 July 2021
- N. Otuka, E. Dupont, V. Semkova, B. Pritychenko, A. Blokhin, M. Aikawa, S. Babykina, M. Bossant, G. Chen, S. Dunaeva, R. Forrest, T. Fukahori, N. Furutachi, S. Ganesan, Z. Ge, O. Gritzay, M. Herman, S. Hlavač, K. Katō, B. Lalremruata, Y. Lee, A. Makinaga, K. Matsumoto, M. Mikhaylyukova, G. Pikulina, V. Pronyaev, A. Saxena, O. Schwerer, S. Simakov, N. Soppera, R. Suzuki, S. Takács, X. Tao, S. Taova, F. Tárkányi, V. Varlamov, J. Wang, S. Yang, V. Zerkin, Y. Zhuang, Nucl. Data Sheets 120, 272 (2014)
- The ENDF, evaluated nuclear data file. https://www-nds.iaea.org/ exfor/endf.htm. Accessed 22 July 2021
- D. Brown, M. Chadwick, R. Capote, A. Kahler, A. Trkov, M. Herman, A. Sonzogni, Y. Danon, A. Carlson, M. Dunn, D. Smith, G. Hale, G. Arbanas, R. Arcilla, C. Bates, B. Beck, B. Becker, F. Brown, R. Casperson, J. Conlin, D. Cullen, M.-A. Descalle, R. Firestone, T. Gaines, K. Guber, A. Hawari, J. Holmes, T. John-

- son, T. Kawano, B. Kiedrowski, A. Koning, S. Kopecky, L. Leal, J. Lestone, C. Lubitz, J.M. Damián, C. Mattoon, E. McCutchan, S. Mughabghab, P. Navratil, D. Neudecker, G. Nobre, G. Noguere, M. Paris, M. Pigni, A. Plompen, B. Pritychenko, V. Pronyaev, D. Roubtsov, D. Rochman, P. Romano, P. Schillebeeckx, S. Simakov, M. Sin, I. Sirakov, B. Sleaford, V. Sobes, E. Soukhovitskii, I. Stetcu, P. Talou, I. Thompson, S.V.D. Marck, L. Welser-Sherrill, D. Wiarda, M. White, J. Wormald, R. Wright, M. Zerkle, G. Žerovnik, Y. Zhu, Nucl. Data Sheets 148, 1 (2018)
- IAEA photonuclear data. https://www-nds.iaea.org/photonuclear/ pdfilelist.html. Accessed 22 July 2021
- T. Kawano, Y. Cho, P. Dimitriou, D. Filipescu, N. Iwamoto, V. Plujko, X. Tao, H. Utsunomiya, V. Varlamov, R. Xu, R. Capote, I. Gheorghe, O. Gorbachenko, Y. Jin, T. Renstrøm, M. Sin, K. Stopani, Y. Tian, G. Tveten, J. Wang, T. Belgya, R. Firestone, S. Goriely, J. Kopecky, M. Krtička, R. Schwengner, S. Siem, M. Wiedeking, Nucl. Data Sheets 163, 109 (2020b). https://doi.org/10.1016/j.nds. 2019.12.002
- Janis nuclear data. https://www.oecd-nea.org/jcms/pl_39910/ janis. Accessed 22 July 2021
- G. Lövestam, M. Hult, A. Fessler, T. Gamboni, J. Gasparro, W. Geerts, R. Jaime, P. Lindahl, S. Oberstedt, H. Tagziria, Nucl. Instrum. Methods Phys. Res. Sect. A Accel. Spectrom. Detect. Assoc. Equip. 580, 1400 (2007)
- L. Daraban, N. Jovančević, S. Oberstedt, F.-J. Hambsch, Phys. Procedia 59, 138 (2014)
- N. Jovancevic, L. Daraban, S. Oberstedt, Nuclear Instrum. Methods Phys. Res. Sect. A Accel. Spectrom. Detect. Assoc. Equip. 739, 68 (2014)
- N. Jovančević, L. Daraban, H. Stroh, S. Oberstedt, M. Hult, C. Bonaldi, W. Geerts, F.-J. Hambsch, G. Lutter, G. Marissens et al., Eur. Phys. J. A 52, 148 (2016)
- S. Ilić, N. Jovančević, L. Daraban, H. Stroh, S. Oberstedt, M. Hult,
 C. Bonaldi, W. Geerts, F.-J. Hambsch, G. Lutter, G. Marissens, M.
 Vidali, D. Knežević, Eur. Phys. J. A 56, 202 (2020)
- E. Browne, R. Firestone, *Table of Radioactive Isotopes* (Wiley, New York, 1986)
- J. Kopecky, J. Sublet, J. Simpson, R. Forrest, D. Nierop, Atlas of neutron capture cross sections (International Atomic Energy Agency (IAEA). INDC(NDS)-362 (1997)
- O. Bogdankevich, L. Lazareva, F. Nikolaev, J. Exp. Theor. Phys. 4, 320 (1957)
- V. Bokhinyuk, A.I. Guthy, A.M. Parlag, M.T. Sabolchy, I.V. Sokolyuk, I.V. Khimich, Ukr. J. Phys. 51, 657 (2006)
- V. Mazur, I. Sokolyuk, Z. Bigan, I. Kobal, Phys. At. Nuclei 56, 10 (1993)
- N. Demekhina, A. Danagulyan, G. Karapetyan, Phys. At. Nuclei 64, 1796 (2001)
- W. Tornow, M. Bhike, S. Finch, A. Krishichayan, Phys. Rev. C 98, 064305 (2018)
- Talys nuclear code. https://tendl.web.psi.ch/tendl_2019/talys. html. Accessed 22 July 2021
- A. Koning, D. Rochman, Nucl. Data Sheets 113, 2841 (2012). https://doi.org/10.1016/j.nds.2012.11.002. (special Issue on Nuclear Reaction Data)
- 23. M. Reginatto, P. Goldhagen, Health Phys. 77, 579 (1999)
- W.L. Goffe, Stud. Nonlinear Dyn. Econom. 1(3), (1996). https://doi.org/10.2202/1558-3708.1020
- 25. R. Behrens, J. Instrum. 4, P03027 (2009)
- 26. M. Matzke, Report PTB-N-19 I-IV (1994)
- W.N. McElroy, S. Berg, T. Crockett, Los Alamos National Laboratory report, AFWL-TR-67-41 I-IV (1967)
- 25-microtron. http://flerovlab.jinr.ru/mt-25-microtron/. Accessed
 July 2021



258 Page 14 of 14 Eur. Phys. J. A (2021) 57:258

 M. Krmar, Y. Teterev, A. Belov, S. Mitrofanov, Nucl. Instrum. Methods Phys. Res. Sect. A Accel. Spectrom. Detect. Assoc. Equip. 901, 133 (2018). https://doi.org/10.1016/j.nima.2018.06.028

- B. Forkman, R. Petersson, *Photonuclear cross-sections in Hand-book on Nuclear Activation data* (Technical Reports Series No. 273, IAEA, Vienna, 1987)
- 31. S. Agostinelli, J. Allison, K. Amako, J. Apostolakis, H. Araujo, P. Arce, M. Asai, D. Axen, S. Banerjee, G. Barrand, F. Behner, L. Bellagamba, J. Boudreau, L. Broglia, A. Brunengo, H. Burkhardt, S. Chauvie, J. Chuma, R. Chytracek, G. Cooperman, G. Cosmo, P. Degtyarenko, A. Dell'Acqua, G. Depaola, D. Dietrich, R. Enami, A. Feliciello, C. Ferguson, H. Fesefeldt, G. Folger, F. Foppiano, A. Forti, S. Garelli, S. Giani, R. Giannitrapani, D. Gibin, J. Gómez Cadenas, I. González, G. Gracia Abril, G. Greeniaus, W. Greiner, V. Grichine, A. Grossheim, S. Guatelli, P. Gumplinger, R. Hamatsu, K. Hashimoto, H. Hasui, A. Heikkinen, A. Howard, V. Ivanchenko, A. Johnson, F. Jones, J. Kallenbach, N. Kanaya, M. Kawabata, Y. Kawabata, M. Kawaguti, S. Kelner, P. Kent, A. Kimura, T. Kodama, R. Kokoulin, M. Kossov, H. Kurashige, E. Lamanna, T. Lampén, V. Lara, V. Lefebure, F. Lei, M. Liendl, W. Lockman, F. Longo, S. Magni, M. Maire, E. Medernach, K. Minamimoto, P. Mora de Freitas, Y. Morita, K. Murakami, M. Nagamatu, R. Nartallo, P. Nieminen, T. Nishimura, K. Ohtsubo, M. Okamura, S. O'Neale, Y. Oohata, K. Paech, J. Perl, A. Pfeiffer, M. Pia, F. Ranjard, A. Rybin, S. Sadilov, E. Di Salvo, G. Santin, T. Sasaki, N. Savvas, Y. Sawada, S. Scherer, S. Sei, V. Sirotenko, D. Smith, N. Starkov, H. Stoecker, J. Sulkimo, M. Takahata, S. Tanaka, E. Tcherniaev, E. Safai Tehrani, M. Tropeano, P. Truscott, H. Uno, L. Urban, P. Urban, M. Verderi, A. Walkden, W. Wander, H. Weber, J. Wellisch, T. Wenaus, D. Williams, D. Wright, T. Yamada, H. Yoshida, D. Zschiesche, Nucl. Instrum. Methods Phys. Res. Sect. A Accel. Spectrom. Detect. Assoc. Equip. 506, 250 (2003). https://doi.org/ 10.1016/S0168-9002(03)01368-8
- Z. Bigan, V. Zheltonozhsky, V. Kirishchuk, A.D.S.V.M. Mazur, P. Trifonov, Bull. Russ. Acad. Sci. Phys. 70, 292 (2006)

- 33. A. Penfold, J. Leiss, Phys. Rev. 114, 1332 (1959)
- 34. A. Koning, J. Delaroche, Nucl. Phys. A **713**, 231 (2003)
- 35. W. Hauser, H. Feshbach, Phys. Rev. 87, 366 (1952)
- 36. C. Kalbach, Phys. Rev. C 33, 818 (1986)
- 37. A. Gilbert, A. Cameron, Can. J. Phys. 43, 1446 (1965)
- 38. W. Dilg, Nucl. Phys. A 217, 269 (1973)
- A. Zubov, G. Adamian, N. Antonenko, Phys. Particles Nuclei 40, 847 (2009)
- A. Ignatyuk, J. Weil, S. Raman, S. Kahane, Phys. Rev. C 47, 1504 (1993)
- 41. S. Goriely, S. Hilaire, A.J. Koning, Phys. Rev. C 78, 064307 (2008)
- S. Hilaire, M. Girod, S. Goriely, A.J. Koning, Phys. Rev. C 86, 064317 (2012)
- M. Reginatto, P. Goldhagen, S. Neumann, Nucl. Instrum. Methods Phys. Res. Sect. B Beam Interact. Mater. Atoms 476, 242–246 (2002)
- A.V. Ivantchenko, V.N. Ivanchenko, J.-M.Q. Molina, S.L. Incerti, Int. J. Radiat. Biol. 88(1–2), 171–175 (2011). https://doi.org/10. 3109/09553002.2011.610865
- Geant4-userdoc. https://geant4-userdoc.web.cern.ch/UsersGuides /PhysicsListGuide/BackupVersions/V10.6c/html/reference_PL /QBBC.html. Accessed 22 July 2021
- L. Pandola, C. Andenna, B. Caccia, Nucl. Instrum. Methods Phys. Res. Sect. B Beam Interact. Mater. Atoms 350, 41 (2015)
- H. Naik, G. Kim, K. Kim, M. Zaman, A. Goswami, M.W. Lee, S.-C. Yang, Y.-O. Lee, S.-G. Shin, M.-H. Cho, Nucl. Phys. A 948, 28 (2016). https://doi.org/10.1016/j.nuclphysa.2016.01.015
- M. Zaman, G. Kim, H. Naik, K. Kim, Y.-S. Cho, Y.-O. Lee, S.-G. Shin, M.-H. Cho, Y.-R. Kang, M.-W. Lee, Nucl. Phys. A 960, 22 (2017). https://doi.org/10.1016/j.nuclphysa.2017.01.008





Contents lists available at ScienceDirect

Nuclear Instruments and Methods in Physics Research A

journal homepage: www.elsevier.com/locate/nima



Presence of neutrons in the low-level background environment estimated by the analysis of the 595.8 keV gamma peak



Brankica Anđelić, David Knežević, Nikola Jovančević, Miodrag Krmar, Jovana Petrović, Arpad Toth, Žarko Medić, Jan Hansman

Department of Physics, Faculty of Science, University of Novi Sad, Trg Dositeja Obradovica 3, 2100 Novi Sad, Serbia

ARTICLE INFO

Keywords: Low-background gamma spectroscopy Neutron capture Inelastic scattering of neutrons HPGe detector Evaporated neutron spectra

ABSTRACT

In order to explore possible improvements of the existing techniques developed to estimate the neutron fluence in low-background Ge-spectroscopy systems, gamma spectra were collected by a HPGe detector in the presence of the 252 Cf spontaneous fission neutron source. The spectra were taken with and without a Cd envelope on the detector dipstick, with different thicknesses of plastic used to slow down neutrons. We have analyzed the complex 595.8 keV gamma peak, as well as several more gamma peaks following the neutron interactions in the detector itself and surroundings materials. The investigation shows that some changes of the initial neutron spectra can be monitored by the analysis of the 595.8 keV gamma peak. We have found good agreement in the intensity changes between the long-tail component of the 595.8 keV and the 691 keV gamma peak (72 Ge(n,n') 72 Ge reaction), usually used for the estimation of the fast neutron fluence. Results also suggest that the thermal neutrons can have a stronger influence on creation of the Gaussian-like part of 595.8 keV peak, than on the 139 keV one following 74 Ge(n, 7) 75 Ge reaction and used in the standard methods (Škoro et al., 1992) [8] for determination of the thermal neutron flux.

1. Introduction

Reduction of different background effects induced by neutrons is very important in different types of low background gamma measurements, such as dark mater search experiments, rare nuclear events research or measurements of the low level environmental activity [1–7]. Consequently, efforts are made in order to improve methods that are used for estimation of the level of neutron presence in the Gespectroscopy systems during low-level background gamma measurements. [8–10]. Except for the low-background measurements, it is also important to know the background neutron contribution in different types of prompt neutron activation experiments [11].

Neutrons in the low-background gamma spectroscopy systems usually come from muon interactions, spontaneous fission of heavy elements and (α,n) reactions of α -emitters of the U- and Th-series with light elements in the surrounding rocks [12]. In the ground level laboratory, neutrons are mainly produced by muon capture in a lead shield of the gamma-ray spectroscopy systems [13]. There are a number of studies about the neutron induced activity during gamma spectroscopy measurements [8,13–17]. All of those analyses show that gamma peaks following neutron capture and scattering reactions with the detector itself (and surrounding materials) can give measurable contribution to the background spectra.

Peaks created in the neutron interactions with the detector and surroundings materials can be used for the determination of the neutron presence during gamma spectroscopy measurements. Methods for determination of the slow neutron flux, using intensity of the 139.9 keV gamma peak (following the $^{74}{\rm Ge}(n,\gamma)^{75{\rm m}}{\rm Ge}$ reaction) and the intensity of the 691.0 keV gamma peak for fast neutrons (the $^{72}{\rm Ge}(n,n')^{72}{\rm Ge}$ reaction), were proposed in Ref. [8]. However, results of the study [10] suggested that, alongside thermal neutron capture, excitation of the 139.9 keV level in $^{75{\rm m}}{\rm Ge}$ can also take place via some other mechanisms (for example, fast neutron interactions).

To investigate the possibility of using certain gamma peaks to estimate the presence of the neutrons, we performed measurements with the ²⁵²Cf neutron source placed near the HPGe detector. The ²⁵²Cf neutron energy spectrum is a standard evaporation spectrum. Its shape is very similar to the energy spectrum of background neutrons in deep underground laboratories, although in a sea level laboratory fast component of background neutron spectrum is not negligible [18–20]. In this work, investigation of the neutron induced gamma peaks in different neutron fluence was done by moderation of the original ²⁵²Cf spontaneous fission neutron spectra with PVC plastic sheets. It was the easiest way to obtain different measurement conditions concerning the number of neutrons reaching the active volume of the HPGe detector. Different intensities of the neutron induced gamma peaks obtained in different measurements geometries (thickness of plastic sheets) were thereby analyzed.

Here, we have studied the possibility of using the 595.8 keV gamma peak for estimation of the neutron presence in the HPGe detector

system. The gamma quanta, having the above-mentioned energy, can be emitted through the prompt de-excitation of the 74Ge nuclei following two different processes: the neutron captures on the 73Ge and the inelastic neutron scattering on the ⁷⁴Ge. The study [10] suggests that in the detected spectra a standard narrow Gaussian shape 595.8 keV gamma peak appears only when there is significant presence of the thermal neutrons. Fast neutrons will interact through inelastic scattering, producing a broad, long tail peak. The presence of this long tail peak is the underlying reason why the 595.8 keV gamma peak in collected gamma spectra has a characteristic structure, being a result of overlapping of a standard Gaussian shape peak, from the capture reaction, and a long tail peak following the neutron inelastic scattering on the Ge nuclei inside the detector. Therefore, in one relatively complex peak one can find the integral contribution of the thermal and also fast neutrons. For the analysis of the complex 595.8 keV gamma peak, the fitting procedure [3,21,22] was employed to differentiate between the contributions of the capture, on one hand, and the inelastic scattering on the other hand, to the overall peak intensity. A number of different gamma peaks were created in the interactions of Ge and surrounding materials with thermal neutrons, as well as in the interactions with fast neutrons. The intensities of those peaks depend on the measurement geometry (i.e. thickness of the plastic covering the neutron source). Obtained intensities of resolved components of the 595.8 keV gamma peak were compared with intensities of other gamma peaks to check whether they follow the same trends.

2. Experimental setup

The experimental setup was located in the low-background laboratory of the Department of Physics in Novi Sad (80 m amsl). The coaxial closed end HPGe detector with horizontal dipstick and a relative efficiency of 22.3 %, was used in the measurements. The HPGe is placed inside a cube chamber made of pre-World War II iron with a useful cube-shaped inner volume of $1 \, \mathrm{m}^3$. Iron walls are 25 cm thick and the total mass of the shield is approximately 20 tons [10,17].

Detector was exposed to the $^{252}\mathrm{Cf}$ spontaneous fission neutrons. The source strength was 4.5×10^3 neutrons per second into 4π sr. The $^{252}\mathrm{Cf}$ source was located in simple paraffin collimator. This was done to prevent some neutrons, which are not initially emitted in the direction of the detector, to reach active volume of the detector after scattering inside low-background iron chamber. The $^{252}\mathrm{Cf}$ source was placed in a Marinelli container (inner diameter 10.6 cm, outer diameter 16.0 cm, height 20.5 cm, bottom thickness 3.0 cm) with wall thickness of 2 mm. The Marinelli container was filled with melted paraffin and located below the HPGe detector (Fig. 1). Some degree of neutron collimation was obtained in this geometry by 17.5 cm long paraffin tube in very

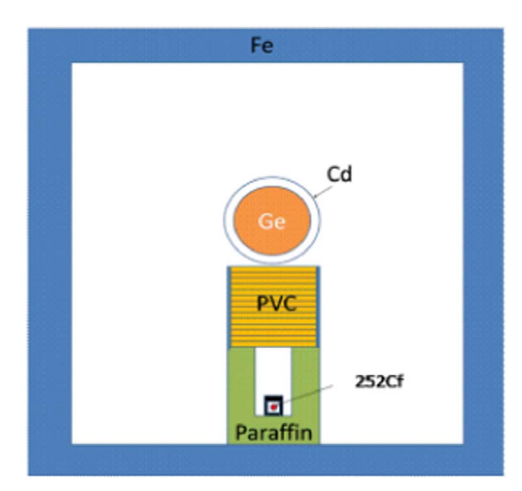


Fig. 1. Scheme of the experimental setup (not in scale).

narrow space of the low-background iron chamber. According to very simplified calculation based on measured values of the TVL for different light materials as paraffin or polyethylene [23], it was estimated that in the 3 cm thick walls of the Marinelli container about 50% of neutrons will be absorbed. To attenuate the gamma radiation of the accumulated fission products, the neutron source was placed in a 2 cm thick iron box. The measurements were carried out with different thicknesses of the PVC plates placed between the detector and the neutron source. The purpose of the PVC plates was to absorb and slow down neutrons. Thus, we obtained the simplest setup in which the detector was exposed to different neutron fluences. Six different thicknesses of the PVC plates (7 mm, 14 mm, 26 mm, 45 mm, 68 mm and 93 mm) were used. The measurements were performed for every thickness of the PVC plastic with and without the Cd envelope over the detector dipstick. Cadmium envelope served as an efficient absorber of the thermal neutrons. In this experimental configuration influence of the thermal neutrons was detected. The collection time for all spectra was approximately the same ~150,000 s.

3. Measurements and results

3.1. Rough insight in neutron fluence

Experimental setup presented in Fig. 1 was the simplest one which exposes the HPGe detector to different numbers of neutrons. It can be expected that the number (and energy spectra) of neutrons reaching detector is a result of a trade-off between thermalization and attenuation of neutrons. Intensities of several gamma lines emitted after neutron interactions in the surrounding materials can be used as a kind of an index showing how adding PVC attenuators can affect the number of neutrons striking active volume of the detector.

In the spectra recorded with the cadmium cap located around the detector dipstick, 651.1 keV and 558.4 keV peaks, following neutron capture on ^{113}Cd are detected. Detected intensity of both gamma lines following $^{113}\text{Cd}(n,\gamma)^{114}\text{Cd}$ reaction can be useful for a rough estimation of the slow neutron number at the very place of the active volume of the detector. Obtained values of the 558 keV and 651.3 keV gamma peaks intensities are presented in Fig. 2.

It can be seen that the count rates of the cadmium peaks do not change significantly with the thicknesses of the PVC plates. Measured intensities vary just up to 20% in the full range of the plastic thicknesses. The cross section for $^{113}\text{Cd}(n,\gamma)^{114}\text{Cd}$ reaction in the thermal region is a couple order of magnitude higher than the cross section in the resonant region. Thus, it can be expected that the results presented in Fig. 2 indicate, that the number of thermal neutrons does not changes significantly and the Ge crystal in the detector dipstick is exposed to thermal neutron fluence which is not dependent on thickness of the plastic attenuators. One possible explanation for a nearly constant number of thermal neutrons striking the detector, which should be verified, is that they result from a trade-off between two effects: the thermalization of fast neutrons and the neutron absorption. This can be found in detail for different moderator materials in the study Ref. [24].

In all recorded spectra, prominent 846.8 keV gamma peak was observed. The origin of this peak is the ⁵⁶Fe(n,n') gamma reaction. This reaction took place in the walls of the iron shield. Considering that for an inelastic neutron scattering neutron energy should be higher than some threshold energy, the intensity of this peak could be a good indicator for monitoring the presence of fast neutrons. The detected intensity of the 846.8 keV ⁵⁶Fe(n,n') peak measured for different thicknesses of the plastic plates is presented in Fig. 3. Count rates of this gamma peak decrease with the increase of the thickness of the PVC because of the slowing down of the neutrons in the PVC. It is evident that plastic PVC attenuators can reduce the number of fast neutrons. The change in the intensity of the 846.8 keV ⁵⁶Fe(n,n') peak has the same trend in presence of the Cd layer since the interactions of slow

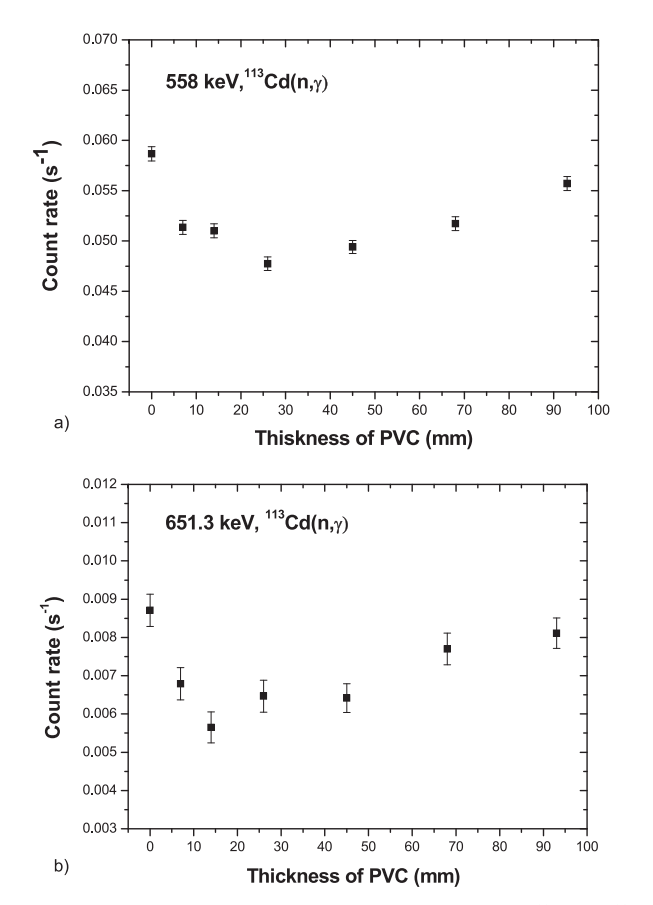


Fig. 2. Detected intensity of a) 558 keV and b) 651.3 keV for the $^{113}\text{Cd}(n.\gamma)^{114}\text{Cd}$ reaction.

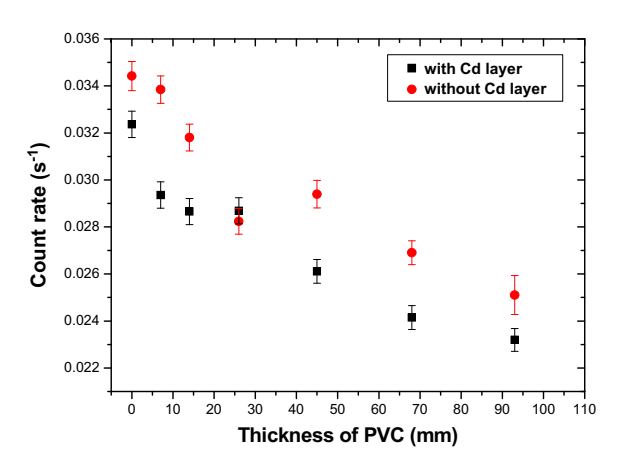


Fig. 3. Detected intensity of the 846.8 keV ⁵⁶Fe(n,n') gamma peak for different thickness of PVC plastic with and without Cd layer around HPGe detector.

neutrons do not have an influence on the detection of this gamma peak. We have to mention here that in our analysis we considered just the statistical uncertainty of detected gamma peaks. However, the jump in the count rate at 45 mm of PVC Fig. 6 can come from some systematic error. We do not have the possibility to repeat those measurements at the current time, but these results can be basis for future investigation.

3.2. Analysis of 595.8 keV gamma peak

The analysis of the 595.8 keV gamma peak was of particular interest in this work. As already noted, gamma quanta having this energy can be emitted thought a prompt de-excitation of the 74 Ge nuclei following two different processes: a) the slow neutron captures on the 73 Ge, b)

the inelastic neutron scattering on the 74 Ge. Thus, this gamma peak, in collected gamma spectra, has a characteristic structure; due to the summation of a standard Gaussian shape peak from the capture reaction and a long tail peak following the neutron inelastic scattering on the Ge nuclei inside the detector. It is necessary to deconvolute this structure by a fitting procedure and to separate the contribution to the overall counts detected in interactions of slow and fast neutrons. Resolved intensities of the narrow Gaussian-shape and the long tail peaks obtained by the deconvolution of the 595.8 keV gamma peak can provide an insight into the presence of fast and slow neutrons in the area of the active volume of the Ge detector.

The most important problem which should be addressed in the deconvolution procedure is the overlapping of the $Ge(n,\gamma)$ and Ge(n,n') and interference of the background peaks. This particular issue arises from choosing the function for fitting the asymmetric peaks induced by fast neutrons. This problem was already discussed by other authors [3,22] and in our analysis the neutron induced peaks were fitted by the following function:

$$C(E) = a_0 ERFC \left[-\frac{(E - E_0)}{\sigma_0} \right] \cdot Exp \left[-\frac{(E - E_0)}{\Delta} \right] + \sum_{i=1}^n a_i$$

$$\cdot Exp \left[-\frac{1}{2\sigma_i^2} (E - E_i)^2 \right] + F$$
(1)

where the first term corresponds to the Ge(n,n') peak; in the second term, the expression inside the summation is a Gaussian function which corresponds to any symmetric gamma peak in the fitting region; the parameter F refers to the background (here to be a linear function). The Gaussian symmetric gamma peaks can be the $Ge(n,\gamma)$ gamma peaks or any other gamma peak corresponding to the detection of some background gamma line. The parameters of the fit are: a_O , a_i , E_O , E_i , σ_O , σ_i and Δ . E_O and E_i and they correspond to the energy of the detected gamma peaks; a_O and a_i are the maximum amplitudes of those peaks. Parameters σ_O and σ_i should correspond to the energy resolution of the detector and they were determined by the peak full-width at half-maximum (FWHM). The characteristic of the exponential tail of Ge(n,n') peaks is determined by the Δ parameter.

First step in the fitting procedure is to fix the level of the background continuum. It was shown in Ref. [3] that the quality of the results obtained by the fit of the Ge(n,n') peaks depends on the energy region chosen for the fit. The next step was the variation of the fitting region for certain energy of the asymmetric peak. The energy region was varied between 30 keV and 40 keV. Different values of the level of the background continuum and energy region were used to get the fit which give the value of χ^2/NDF as close to 1 as possible. Furthermore, the uncertainties of fitting parameters were analyzed to get the optimal set of values. The gamma peaks were fitted by ROOT data analysis toolkit [25]. Fitting procedure was applied on the 691 keV $^{72}\text{Ge}(n,n')$ gamma peak, which has the simplest structure, with one well developed peak (723.3 keV ^{154}Eu , product of ^{252}Cf fission, contained in sealed source). The result of the fit is depicted on Fig. 4.

The same technique was used for deconvolution of the 595.8 keV gamma peak. It can be seen in Fig. 5 that, in the observed energy region, except for the standard narrow $^{73}{\rm Ge}(n,\gamma)$ and broad $^{74}{\rm Ge}(n,n')$ gamma lines, three additional background gamma peaks appeared (609.3 keV $^{214}{\rm Bi}(U)$, 603 keV from fission product $^{154}{\rm Eu}$ and 641 keV from fission product $^{145}{\rm Ba}$). The contribution of the background continuum, as well as the background gamma peaks, were subtracted and the intensities of $^{73}{\rm Ge}(n,\gamma)$ and $^{74}{\rm Ge}(n,n')$ gamma peaks were obtained.

3.3. Ge(n,n') component of the 595.8 keV gamma peak

The intensities of the 74 Ge(n,n') component of the 595.8 keV gamma peaks, obtained after deconvolution are presented in Fig. 6. It can be seen that the intensity of the long tail 595.8 keV gamma peak,

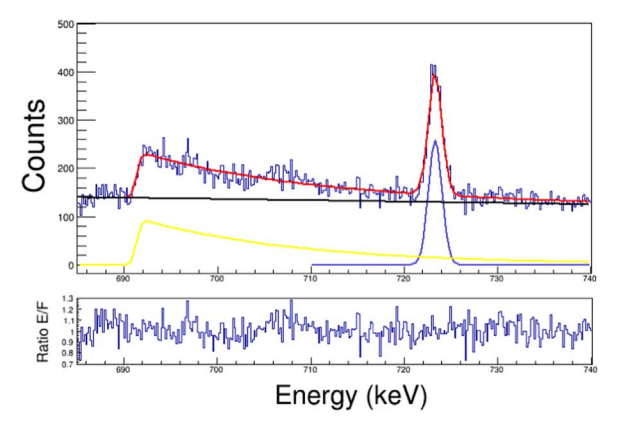


Fig. 4. The part of gamma spectrum in region around the 691 keV Ge(n,n') gamma peak with the 7 mm of PVC between the Ge-detector and the ^{252}Cf source and the Cd envelope around detector. The lines show the fitting results for the $^{72}Ge(n,n')$ and background peak (upper graph). Down graph – ratio of experimental spectra to fitting function.

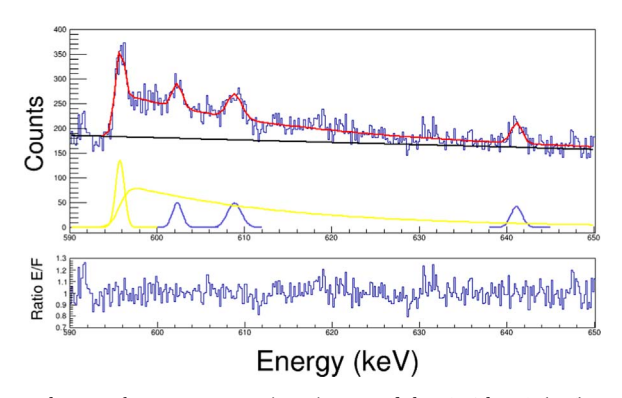


Fig. 5. The part of gamma spectrum in region around the 595.8 keV Ge(n,n') gamma peak with 7 mm of PVC between the Ge-detector and the ^{252}Cf source. The lines show the fitting results for the $^{74}Ge(n,n')$, $^{73}Ge(n,\gamma)$ and background peaks (upper graph). Down graph – ratio of experimental spectra to the fitting function.

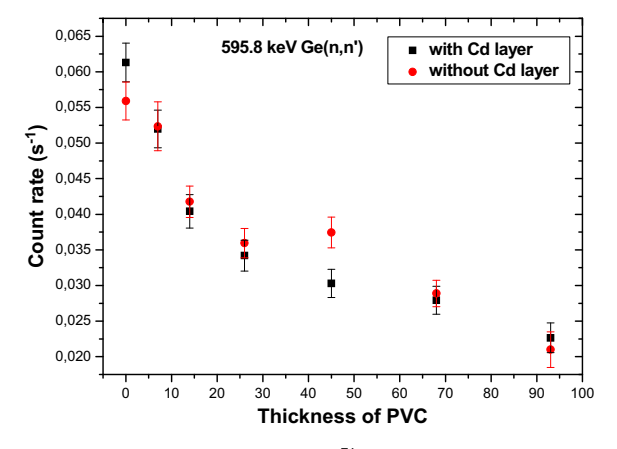


Fig. 6. Detected intensity of the $595.8\,\mathrm{keV}^{-74}\mathrm{Ge}(n,n')$ gamma peak for different thickness of PVC plastic with and without Cd layer around the HPGe detector.

measured for different thicknesses of the plastic plates located between the neutron source and the HPGe detector, has an apparent decreasing trend. As mentioned above, the same trend was observed in analysis of 846.8 keV ⁵⁶Fe(n,n') gamma peak (Fig. 3). Considering that only fast neutrons can initiate the (n,n') reaction, presence of the Cd envelope has no influence on the obtained intensities of the separated long tail peak.

To check the obtained results, comparison with the detected intensity of the 691 keV 72 Ge(n,n') gamma peaks was performed. The intensity of the 691 keV gamma peak decreases with the increase of plastic thickness, as expected. There are no significant differences

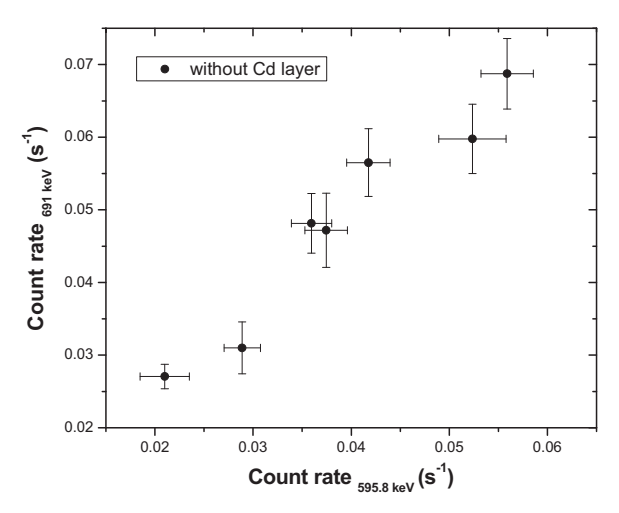


Fig. 7. Correlation between measured intensities of 691 keV and 595.8 keV peaks (without Cd layer around the HPGe detector).

between the measurements done with and without the Cd envelope. Considering that the 691 keV gamma line was frequently used in estimation of the fast neutron fluence [8], let us consider whether it is possible to do the same using the long-tail component of the 595.8 keV gamma peak. Fig. 7 presents a scatter graph showing correlation between the intensities of the two mentioned peaks recorded in this experiment.

The results in Fig. 7 shows strong linear correlation between the $595.8 \, \mathrm{keV}^{73} \mathrm{Ge}(n,\gamma)$ and $691 \, \mathrm{keV}^{72} \mathrm{Ge}(n,n')$ gamma peaks with linear slope coefficient 1.24(4). This means that the $595.8 \, \mathrm{keV}$ can be also used as a standard for the determination of the fast neutron fluence.

3.3.1. $Ge(n,\gamma)$ component of 595.8 keV gamma peak

The intensity of the 595.8 keV 73 Ge(n, γ) gamma peak, obtained by deconvolution, has an almost constant value, not dependent on the plastic thickness (Fig. 8). The constant trend of the measured intensities, depicted in Fig. 8 can be expected considering the results obtained by the measurements of the cadmium gamma peaks (Fig. 2). It is evident that the simple experimental setup used in this experiment can provide different values of thermal neutron fluence at the very place of the detector dipstick.

Very similar results were obtained when the 139.9 keV line was used to estimate the thermal neutron fluence. Results are presented on Fig. 9.

Although experimental setup in this experiment did not allow us to provide different values of thermal neutron fluence at the place of the active volume of the HPGe detector to be able to compare neutron

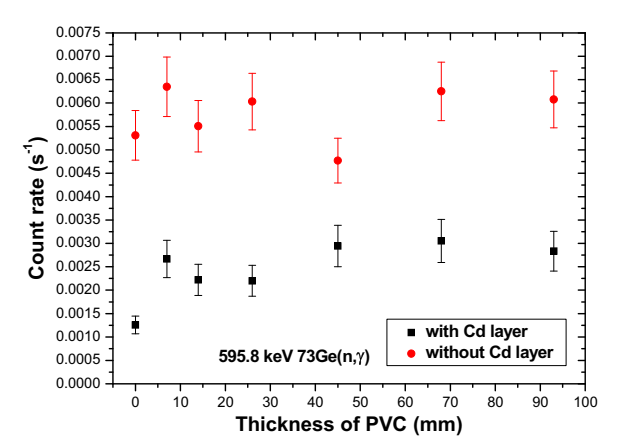


Fig. 8. Detected intensity of the 595.8 keV 73 Ge(n, γ) gamma peak for different thickness of PVC plastic with and without Cd layer around the HPGe detector.

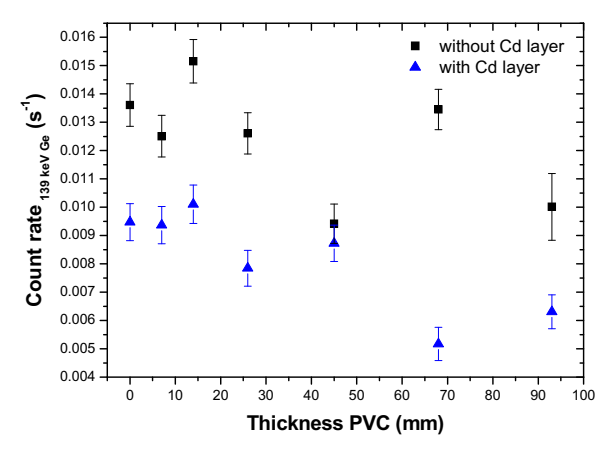


Fig. 9. Detected intensity of the 139.9 keV 74 Ge(n, γ) gamma peak for different thickness of PVC plastic with and without Cd layer around the HPGe detector.

fluence estimation by the 139.9 keV and the (n,γ) component of the 595.8 keV gamma peak, there is still one possible indicator. We have also calculated the ratio of contribution of thermal neutrons to detected intensity of $Ge(n,\gamma)$ peaks using the following equation:

$$R(\%) = 100\% \left(1 - \frac{N_{withCd}}{N_{withoutCd}} \right)$$
 (2)

where N_{withCd} and $N_{withoutCd}$ are the intensities of gamma peaks measured with and without Cd envelope respectively. The obtained mean radio R (for different thicknesses of PVC) for the 139.9 keV and 595.8 keV peak were 33(16)% and 57(12)%, respectively. This result can be a kind of an indication that the thermal neutrons have a stronger influence on creation of the 595.8 keV peak, than on the 139 keV one. Unfortunately, uncertainties are relatively large and for more exact confirmation that the 595.8 keV gamma line has some advantage over the 139.9 keV one, more investigations should be done.

4. Conclusions

In this work we have measured the gamma spectra using the low-background Ge-spectroscopy system in an iron shield, in the presence of the ²⁵²Cf neutron source. A spontaneous fission neutron spectrum was moderated by PVC plastic plates placed between the HPGe detector and the neutron source. In our experimental setup it was possible to analyze several characteristic gamma peaks originating from the interactions of the neutrons with the isotopes of Ge and couple more surrounding materials. Special care was paid to the 595.8 keV peak because it contains records of simultaneous interaction of the thermal and fast neutrons with the Ge detector.

Preliminary results presented in this paper are quite encouraging: the 595.8 keV peak can be used in the estimation of the neutron fluence at the place of the active volume of the Ge detector. In the high energy region, above the threshold of the Ge(n,n') nuclear reactions, very good coincidence between the long-tail component of the 595.8 keV and the 691 keV gamma peaks, usually used for the estimation of fast neutron fluence, was observed. Simple experimental setup unfortunately could not provide us with the variety of thermal neutron fluencies at the place of detector, however it was observed that even in these circumstances

intensity of the sharp gamma peak at the beginning of the long-tail 595.8 keV peak, obtained in neutron capture process, shows a similar trend to the intensity of the 139.9 keV peak. Measured intensities of both mentioned peaks follow the same trends as the gamma peaks obtained in the $^{113}\text{Cd}(n,\gamma)^{114}\text{Cd}$ reaction. It can be expected that the (n,γ) part of the 595.8 keV peak has a potential to be used for estimation of the thermal neutron fluence.

Let us review some noticeable disadvantages and advantages of the method for estimation of neutron fluence based on the measurement of the 595.8 keV peak in gamma spectra. The structure of the 595.8 keV gamma peak is not simple and a sophisticated fit procedure has to be employed. However, the shapes of the sharp Gauss-like gamma lines and the long-tail peak are well known. Moreover, it was noticed that the intensity of the (n,γ) part of the 595.8 keV peak is about two times lower that intensity of the 139.9 keV gamma line, which could introduce some uncertainty, especially if the cases of low thermal neutron fluencies. Significant advantage of the suggested method based on the 595.8 keV gamma peak is the fact that both fast and slow neutron fluence can be determined using just one energy peak. For some rough estimation of thermal to fast neutron fluence ratio, not even the relative energy efficiency of detector needs to be calculated.

Considering that in our experiment no measurements in different fields of thermal neutrons were possible, it is valuable to repeat similar measurements in some other experimental setups. This is especially important in order to confirm the assumption that the intensity of the Gauss-like part of 595.8 keV gamma peak is less dependent on fast neutrons than the usually used 139.9 keV one.

References

- [1] G. Heusser, Nucl. Instrum. Methods A 369 (1996) 539.
- [2] R. Wordel, et al., Nucl. Instrum. Methods A 369 (1996) 557.
- [3] E. Gete, et al., Nucl. Instrum. Methods A 388 (1997) 212.
- [4] N. Jovancevic, M. Krmar, Phys. Procedia 31 (2012) 1-190.
- [5] S. Croft, et al., Nucl. Instrum. Methods A 505 (2003) 536–539.
- [6] Da Silva, et al., Nucl. Instrum. Methods Phys. Res. A 354 (1995) 553.
- [7] Y. Feige, et al., J. Geophys. Res. 73 (1968) 3135-3142.
- [8] G.P. Škoro, et al., Nucl. Instrum. Methods A 316 (1992) 333.
- [9] N. Jovančević, M. Krmar, Appl. Radiat. Isot. 69 (2011) 629-635.
- [10] N. Jovančević, et al., Nucl. Instrum. Methods A 612 (2009) 303–308.
- [11] A. Dragić, et al., Phys. Procedia 59 (2014) 125.
- [12] G. Heusser, Background in ionizing radiation detection, in: M. Garcia-Leon, R. Gracia-Tenorio (Eds.), Low-Level Measurements of Radioactivity in the Environment, Word Scientific, Singapore, 1994, pp. 69–112.
- [13] G. Heusser, Annu. Rev. Nucl. Part Sci. 45 (1995) 543–590.
- [14] M. Krmar, et al., Nucl. Instrum. Methods A 709 (2013) 8-11.
- [15] M. Krmar, et al., Appl. Radiat. Isot. 70 (1) (2012) 269–273.
- [16] S. Niese, Underground laboratories for low-level radioactivitymeasurements, in: P.P. Povinec (Ed.)Analysis of Environmental Radionuclides, Elsevier, Amserdam, 2008, pp. 209–239.
- [17] I. Bikit, et al., Nucl. Instrum. Methods A 606 (2009) 495.
- [18] C.W. Mannhart et al., 1989, IAEA Technical Report INDC(NDS)220/L, p.305, IAEA, Vienna.
- [19] W.V. Schröder, et al., Z. Phys. 239 (1974) 57.
- [20] The ENDF. Evaluated Nuclear Data File, $\langle https://www-nds.iaea.org/exfor/endf. htm <math display="inline">\rangle$ (on 4/9/2016).
- [21] G. Fehrenbacher, et al., Nucl. Instrum. Methods A 372 (1996) 239.
- [22] T. Siiskonen, H. Toivonen, Nucl. Instrum. Methods A 540 (2005) 403.
- [23] NCRP Report 79, Neutron contamination from medical electron accelerators (1984).
- [24] Study of the optimal performance of a neutron activation analysis facility based on a DD neutron Generator. In: Proceedings of Neutron Generators for Analytical Purposes, IAEA Radiation Technology Reports Series No. 1, Vienna (2012).
- [25] ROOT cern, (https://root.cern.ch) (on 4/9/2016).



PAPER • OPEN ACCESS

VERITAS: a high-flux neutron reflectometer with vertical sample geometry for a long pulse spallation source

To cite this article: S. Mattauch et al 2016 J. Phys.: Conf. Ser. 711 012009

View the article online for updates and enhancements.

You may also like

- A short history of my life in science Joseph R Manson
- Recent Progress in Cu Electrodeposition for TSV (Through Silicon Via)
 Jae Jeong Kim, Myung Jun Kim, Seunghoe Choe et al.
- Vortex states in *de fact*o mesoscopic Mo₈₀ Ge₂₀ pentagon plates
 Ho Thanh Huy, Masaru Kato and
 Total and Tota



Journal of Physics: Conference Series **711** (2016) 012009

VERITAS: a high-flux neutron reflectometer with vertical sample geometry for a long pulse spallation source

S. Mattauch¹, A. Ioffe¹, D. Lott², A. Menelle³, F. Ott³, Z. Medic⁴

E-mail: s.mattauch@fz-juelich@de

Abstract.

An instrument concept of a reflectometer with a vertical sample geometry fitted to the long pulse structure of a spallation source, called "VERITAS" at the ESS, is presented. It focuses on designing a reflectometer with high intensity at the lowest possible background following the users' demand to investigate thin layers or interfacial areas in the sub-nanometer length scale. The high intensity approach of the vertical reflectometer fits very well to the long pulse structure of the ESS. Its main goal is to deliver as much usable intensity as possible at the sample position and be able to access a reflectivity range of 8 orders of magnitude and more. The concept assures that the reflectivity measurements can be performed in its best way to maximize the flux delivered to the sample. The reflectometer is optimized for studies of (magnetic) layers having thicknesses down to 5Å and a surface area of 1x1cm². With reflectivity measurements the depth-resolved, laterally averaged chemical and magnetic profile can be investigated. By using polarised neutrons, additional vector information on the in-plane magnetic correlations (off-specular scattering at the µm length scale, GISANS at the nm length scale) can be studied. The full polarisation analysis could be used for soft matter samples to correct for incoherent scattering which is presently limiting neutron reflectivity studies to a reflectivity range on the order of 10^{-6} .

1. Introduction

The European Spallation Source (ESS) will provide neutron pulses with a width of τ =2.84ms and a repetition rate of 14Hz. Though the average flux at the ESS (with its TDR moderator) will be practically equal to the one at the ILL, the time structure of the neutron beam allows for a drastic gain in intensity for time-of-flight instruments due to the 25 times higher peak intensity of the ESS [1]. The

¹ JCNS at MLZ, Forschungszentrum-Jülich GmbH, 85747 Garching, Germany

²Helmholtz Zentrum Geesthacht, 21502 Geesthacht, Germany

³Laboratoire Léon Brillouin CEA/CNRS, CEA Saclay, 91191 Gif sur Yvette, France

⁴ Faculty of Sciences, University of Novi Sad, Trg Dositeja Obradovića 3, 21000 Novi Sad, Republic of Serbia

Content from this work may be used under the terms of the Creative Commons Attribution 3.0 licence. Any further distribution of this work must maintain attribution to the author(s) and the title of the work, journal citation and DOI.

Journal of Physics: Conference Series 711 (2016) 012009

doi:10.1088/1742-6596/711/1/012009

natural resolution of the instrument using the full pulse width is τ/L and defined by the choice of the instrument length L. On the other hand, the artificial narrowing of the pulse width by pulse shaping choppers allows to increase the resolution at the cost of intensity. This opens an exciting opportunity to design a next-generation reflectometer to meet the increasing demand and anticipated scientific challenges. The research topics that will benefit from this reflectometer comprises a wide range of scientific disciplines, ranging from thin film magnetism and novel topological phases in confined geometries, the functionality and properties of hybrid materials in the field of soft and hard matter to the structural biology of membrane proteins. Though the proposed vertical sample geometry excludes the examination of liquid-liquid or liquid-gas interfaces, it nevertheless provides sufficient advantages for soft matter samples that do not require such interfaces and can be measured on the vertical reflectometer with the appropriate sample environment without compromises. Full polarisation analysis will allow measurements of those sample types that were not possible before by making it possible to correct for incoherent background.

The instrument concept presented here, called "VERITAS" the ESS, focuses on designing a reflectometer with high intensity and low background following the high demand of the users to investigate thin layers or interfaces in the sub-nanometer length scale. The high intensity approach of the vertical reflectometer fits very well to the long pulse structure of the ESS. Its main goal is to deliver as much usable intensity as possible to the sample position and be able to access a reflectivity range of 8 orders of magnitude and more.

The concept assures that the reflectivity measurements can be performed in its best way to maximize the flux delivered to the sample. The reflectometer is optimized for studies of (magnetic) layers having thicknesses down to 5\AA and a surface area of $1\text{x}1\text{cm}^2$. With reflectivity measurements the depth-resolved, laterally averaged chemical and magnetic profile can be investigated. By using polarised neutrons, additional vector information on the in-plane magnetic correlations (off-specular scattering at the μm length scale, GISANS at the nm length scale) can be studied.

The instrument will furthermore be capable to work with a higher wavelength resolution down to 1%. Depending on the operational mode of the instrument, different detector configurations will be used. The detector area will be highly configurable and optimised for the different needs of the specular, off-specular and GISANS-modes.

The design of the vertical reflectometer is based on well-tested components that will be very robust and bear no unpredictable risks for a reliable operation.

1. General philosophy: relaxed Q-resolution machine

The proposed instrument is primarily designed for the investigations of thin interfaces from several nm down to the sub nm range. The main goal is therefore to deliver as much usable intensity as possible at the sample position to be able to access a reflectivity range of 8 orders of magnitude and more. Fig. 1 shows the specular reflectivity curves simulated for a thin Fe-layer for a perfect and relaxed Q-resolutions, respectively. Comparing the two cases it can be noticed that only the minima of the interference pattern are slightly smeared out in the latter case, thus the resolution for the measurement can be drastically relaxed for thin interfacial structures without any loss of information. With a relaxed resolution the neutron intensity on the sample is increased to obtain a detectable signal from an extremely small amount of the scattering material of a thin layer, particularly if it is required to measure the reflectivity up to high Q values.

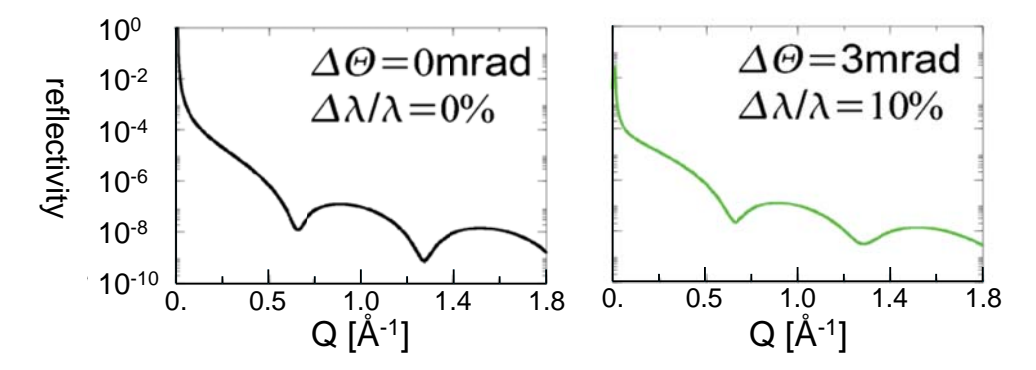


Fig. 1: Simulated reflectivity curve of 10Å thin Fe layer on a Ag substrate for ideal resolution/collimation and for relaxed wavelength resolution/collimation.

The pulse width τ and the instrument length L from the moderator to the detector impose physical limits on the main instrument parameters – the natural λ -resolution and the wavelength band $\Delta\lambda$, are both directly determined by the choice of τ and L:

$$\frac{\Delta\lambda}{\lambda} \propto \frac{\tau}{T} \propto \frac{\tau}{L} \qquad \Delta\lambda \propto \frac{1}{L} \tag{1}$$

(T- the time of flight of neutrons from the moderator to the detector). To achieve a resolution of 10% for τ =2.86ms at the ESS and to use a maximum of neutrons from the spectrum centered around a wavelength of 3Å, the instrument length L is fixed at about 36m. When L is chosen no further relaxation of the wavelength resolution is possible while the increase in the resolution can be achieved by a shortening of the pulse length. In turn the repetition rate of 14Hz and the choice of instrument length defines the wavelength band of the instrument to $\Delta\lambda$ =8Å.

2. General instrument layout

The general layout of the instrument is depicted in Fig. 2, the schematic diagram of the instrument is shown in Fig. 3. The overall length up to the detector position is 36m allowing a wavelength resolution of 10% (see above) by making use of the full length of the ESS pulse.

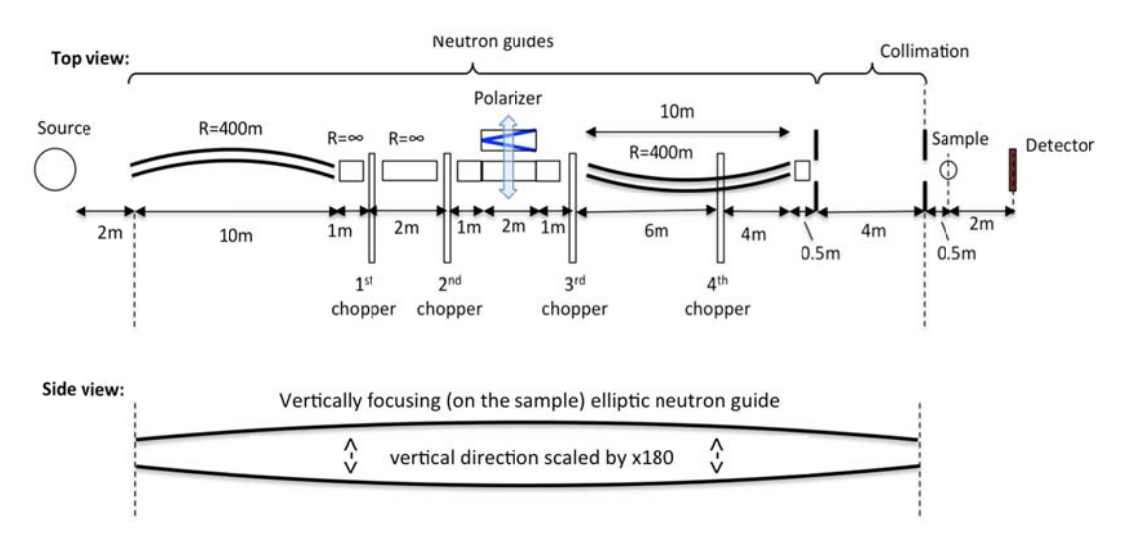


Fig. 2: The top and side view of VERITAS. The moderator is on the left hand side.

2.1. Neutron guide design:

The instrument guide is S-shaped and made of two curved neutron guides (R=400m) with a 7m long straight neutron guide at the inflection point (see Fig. 2). The use of the S-shaped neutron guide prevents the direct line-of-sight of the primary and secondary radiation sources. The movable parts (choppers, polariser changer, etc.) are positioned downstream of the neutron beam beyond the biological shielding and thus can be freely accessed during the operation of the ESS. The basic guide parameters are listed in Table 1. The neutron guide width of 30mm is chosen to allow the complete filling of the phase space of the guide for a moderator width of 10cm. To increase the incident neutron intensity for reflectivity measurements on small samples, the incident neutron beam is focused along the vertical direction onto the sample using a focusing elliptical neutron guide. A comparison of the intensities at the sample position (for a sample size of 1x1 cm²) of such a setup to a straight guide with a cross section of 3 x 12 cm² and mirrors with m=2 coating shows a clear increase in the beam intensity by at least a factor of 4 for the elliptical focusing option (see Fig. 3).

An elliptical guide (see Table 1 for the shape) with the same length and m=3 coating for the last 4m will be used.

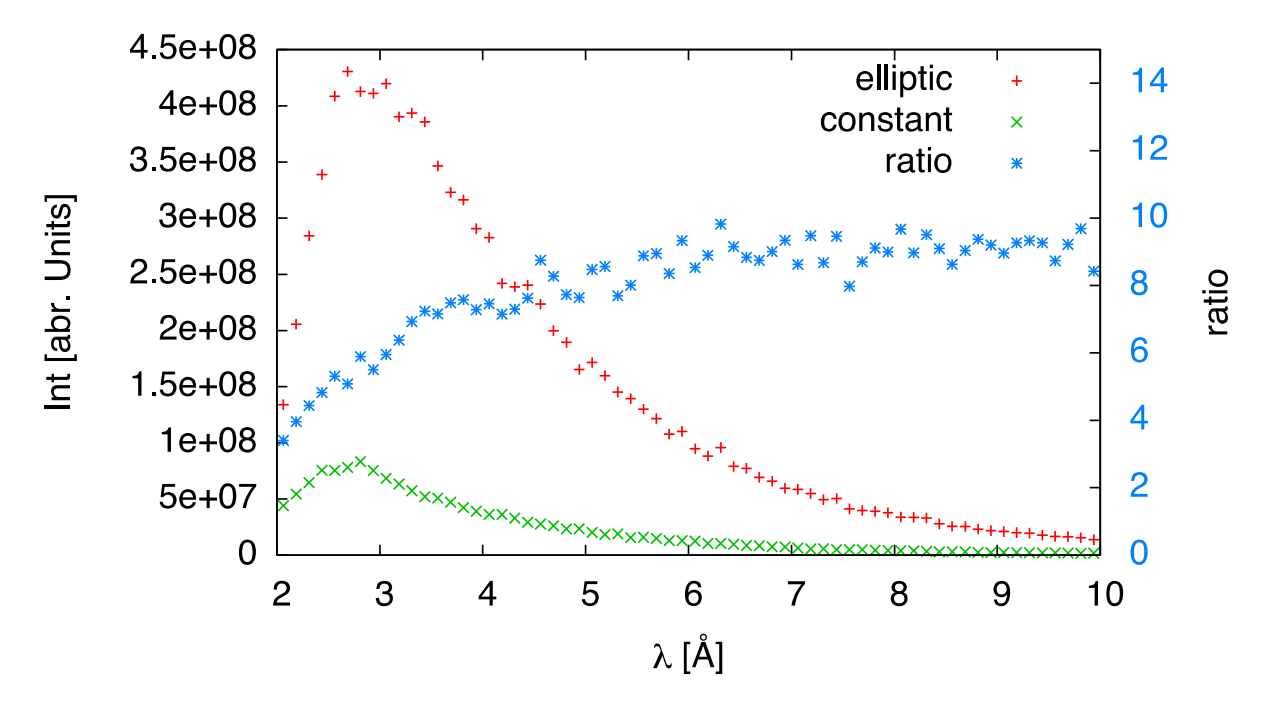


Fig. 3: Comparison of the intensity at the sample position with a sample size of 1x1cm² for elliptical and constant cross section neutron guides.

2.2. Chopper design:

The time-distance diagram for the low resolution mode is shown in Fig. 4a. The first chopper at 13m is the band selection chopper selecting an 8Å broad wavelength band. The band from 2 to 10Å will provide the highest intensity. The wavelength band can be selected arbitrarily in a range between 2 and 32Å. This is important in the case one wants to adjust the reciprocal space to a specific scientific question, e.g. separating the off-specular scattering signal from the direct beam or in the GISANS mode for separating reflections from each other. The additional choppers ((2) at 15m, (3) at 19m and

PNCMI 2014 IOP Publishing

Journal of Physics: Conference Series **711** (2016) 012009 doi:10.1088/1742-6596/711/1/012009

(4) at 25m) serve as frame overlap choppers to prevent contaminations of very high wavelength neutrons of more than 50Å.

	gth				Exit height	Exit width	ng		Coating left	Coating right
1	10.0m	+400m	95.8mm	30mm	194.5mm	30mm	m=3.0	m=3.0	m=3	m=4
2	1.0m	8	194.5mm	30mm	198.5mm	30mm	m=3.0	m=3.0	m=3	m=3
3	2.0m	∞	198 . 5m m	30mm	202.7mm	30mm	m=3.0	m=3.0	m=3	m=3
4	4.0m	00	202 . 7m m	30mm	202.5mm	30mm	m=3.0	m=3.0	m=3	m=3
5	6.0m	-4 00m	202 . 5m m	30mm	180.5mm	30mm	m=3.0	m=3.0	m=4	m=3
6	4.0m	-400m	180.5mm	30mm	145.5mm	30mm	m=3.0	m=3.0	m=4	m=3
7	0.5m	8	145.5mm	30mm	140.0mm	30mm	m=3.0	m=3.0	m=3	m=3
8	4.0m	8	140.0mm	30mm	54.0mm	30mm	m=3.0	m=3.0	absorber	absorber

Table 1: Basic guide design parameters. To avoid the depolarization of the neutron beam, all guides after the polarizing cavity (from section 4) are coated with non-magnetic supermirrors. Geometric parameters of the elliptic guide were selected to maximize the brilliance transfer, while keeping the guide's cross-section reasonably small for a practical chopper design.

In order to achieve a high wavelength resolution for the proposed design, the natural pulse width has to be reduced according to Eq. (1). Technically the sub-pulse duration will be defined by a pulse-shaping chopper installed at 13m from the source. Each sub-pulse will provide neutrons arriving at the detector during a certain time interval (time sub-frame) and covering a certain wavelength band (wavelength sub-frame), see Fig. 4b. For the optimal use of all neutrons from the long ESS pulse, a sequence of sub-pulses will be selected that the wavelength band of subsequent sub-frames will overlap. Then the available wavelength band from 2 to 10Å will be completely covered thus avoiding gaps in Q. It is necessary, however, that the time sub-frames of these sub-pulses are well separated to avoid ambiguity in the wavelength (i.e. in Q) determination. The high-resolution choppers will be installed just behind Ch.1 and Ch.3 (see Fig. 4b).

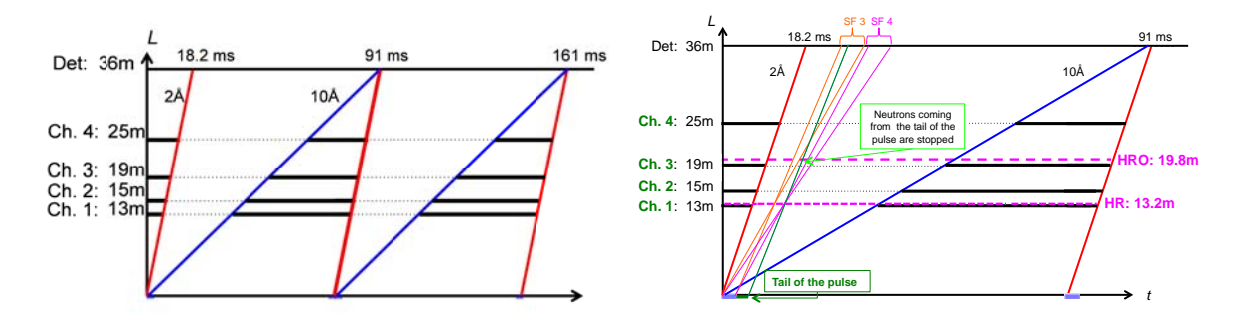


Fig. 4: Time-distance diagrams of the (a) low and (b) high resolution mode

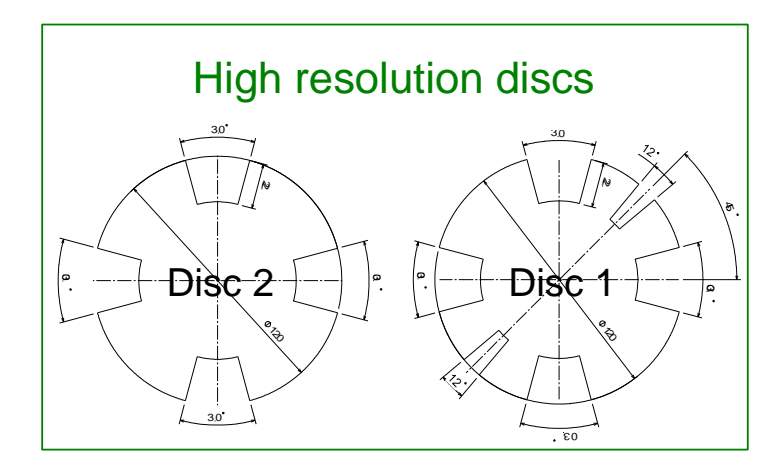


Fig. 5: A double disc chopper allowing different openings by setting an offset angle between the discs.

Different resolutions require a variable opening of the pulse-shaping high-resolution chopper. Therefore we use a double disc chopper (see Fig. 5) that will allow different openings by setting an offset angle between the discs. For a 1% wavelength resolution mode, an offset angle of 45° will result in two openings of 10°. In the 3% and 5% modes, the offset angles will be set between -12.5° and +12.5°, leading to 4 windows and a variable opening from 0-25°. The frequency of the sub-pulses has to be an integer multiple of the frequency of the ESS source, otherwise the timing of the sub-pulses will continuously shift relative to the ESS pulses. The simulated time and wavelength intensity distributions for the 1, 3 and 5% resolution modes show a clear separation of the time sub-frames and an overlap of the wavelength sub-frames (see Fig. 6). It is important to note that in all three modes, the $\Delta\lambda/\lambda$ value is not constant because the pulse length, whether directly from the ESS or from the HM-chopper, is always constant, while the λ values change.

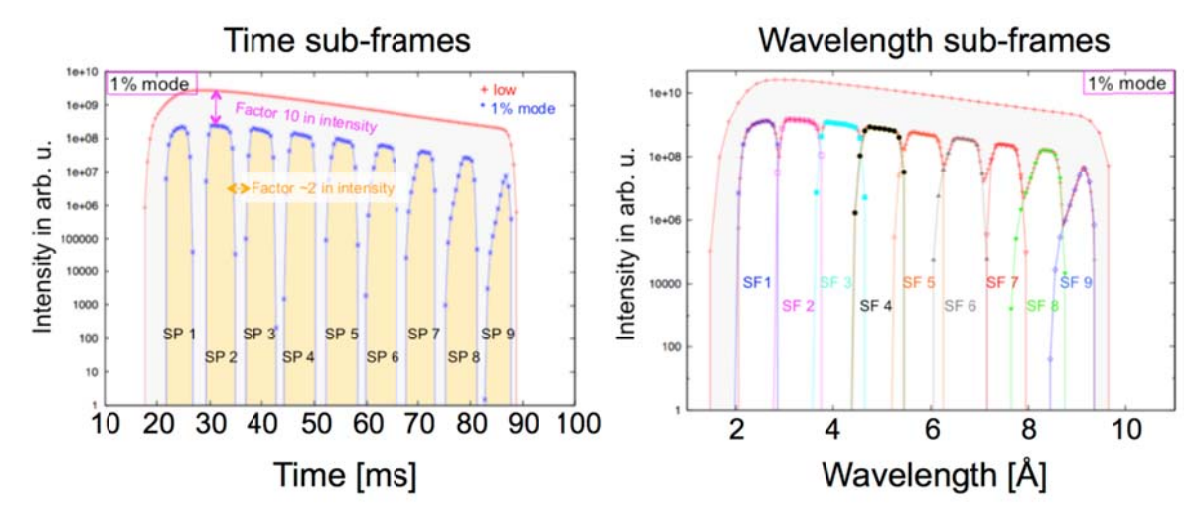


Fig. 6: The simulated time and wavelength intensity distributions for the 1% wavelength resolution modes. The low wavelength resolution curves ($\Delta\lambda/\lambda=10\%$) are shown as envelops.

2.3. Polarization option:

In the polarized mode, the central 2m long piece of the guide (see Fig.2) will be replaced by another one equipped with a polarizing cavity which is built upon thin, 0.3mm thick, Si wafers coated with m=5 Fe/Si supermirrors working in transmission [2]. This solution leads to high values of neutron beam polarization (see Fig. 7) with small intensity losses over the whole wavelength band and allows practically for instant-switch between polarizing and non-polarizing operation modes without affecting the overall beam propagation. Even higher polarization of the neutron beam of more than 99% can be achieved using an optional ³He neutron spin filter with a wide band neutron adiabatic RF-flipper, resulting in a drop of the beam intensity of about 25%. It should be noted that all sections after the polarizer will be coated by non-magnetic supermirrors.

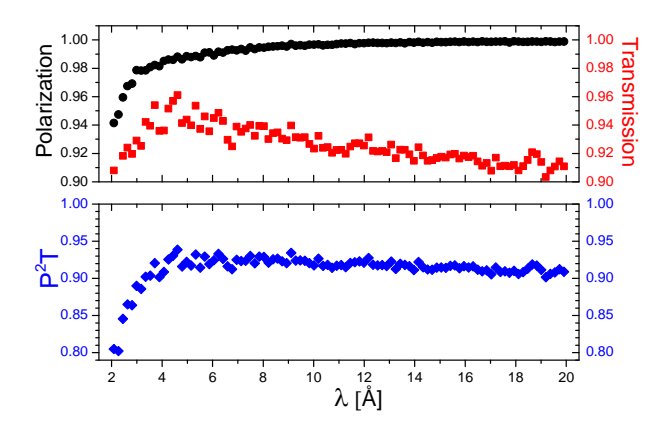


Fig. 7: Polarization P, transmission T of the selected spin component and the figure of merit P²T of the polarizing cavity setup.

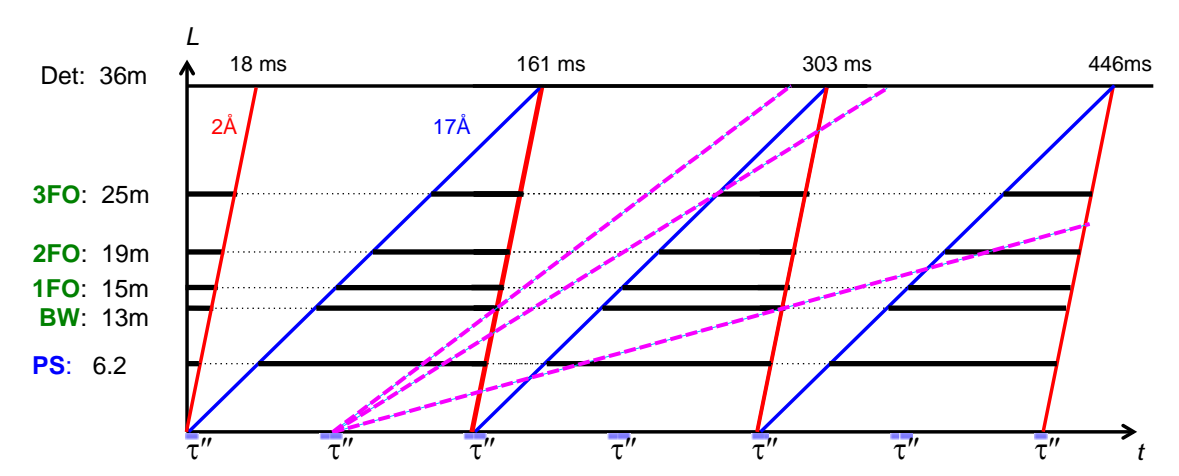


Fig. 8: Time-distance diagram for the kinetic mode of the 1 pulse skipping mode (7Hz), i.e. skipping every second pulse of the ESS source.

2.4. Kinetic mode:

For kinetic measurements it is desirable to cover a large Q-range for a single angular setting to allow measuring of the kinetic processes on time scales of one second and less. The design of VERITAS enables one to extend the Q range beyond the ratio of Qmax/Qmin≈5 in the basic chopper mode by

skipping one or more pulses. This can be easily realized by placing one additional chopper (PS) at 6.2m distance from the source blocking the neutrons coming from the second (7Hz mode), third (4.7Hz) or fourth (3.5Hz) pulse as depicted in the time-distance diagram in Fig. 8 for the 1 pulse skipping mode. The corresponding choppers' settings are listed in Table 2, and e.g. the 3 pulse skipping mode and enables one to measure a complete reflectivity curve in a Q range from $0.0075\text{\AA}-1$ (total reflectivity plateau) up to 0.12Å^{-1} .($\sim10^{-5}$ level depending on the sample) in one shot with a time resolution of 286ms as shown in Figure 9.

Mode	PS[°]	BW[°]	1FO[°]	2FO[°]	3FO[°]	f[Hz]	Time[ms]	Q-ratio
1 pulse	-66.2	-84.9	97.1	121.1	156.4	7	143	9
2 pulse	-40.9	-79.0	-90.3	-112.6	-145.3	4.7	212	12
3 pulse	-39.4	-76.0	-86.9	-108.3	-139.7	3.5	286	16

Table 2. The different parameters of the chopper settings used in the pulse skipping mode.

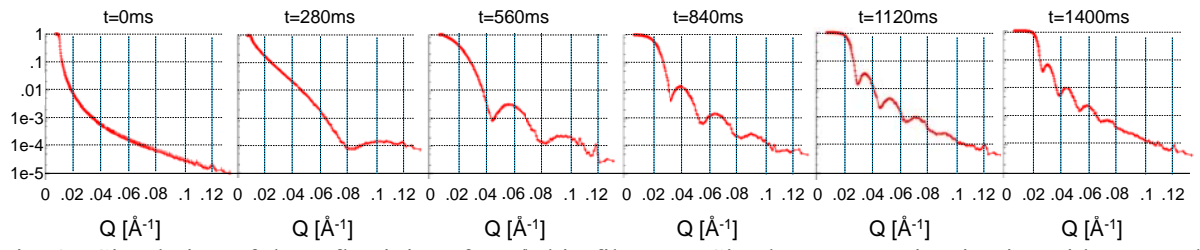


Fig. 9: Simulation of the reflectivity of a Ni thin film on a Si substrate growing in-situ with a growth rate of 28.5Å/s inside an MBE and recorded in a time interval of 280 ms on a 1cm² sample. The parameters are taken for the low resolution mode in the 3 pulse skipping mode.

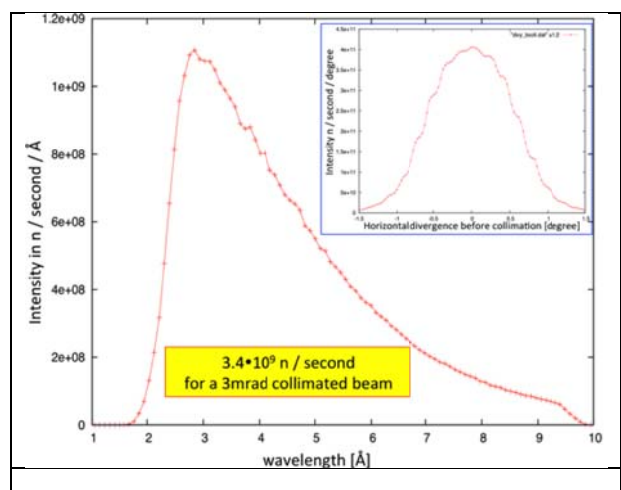
3. Performance of the setup.

Taking the basic setup, the intensity-wavelength distribution is simulated for the proposed 10% wavelength resolution (see Fig. 10). The intensity scale is shown for a measurement time of one second and a beam collimation of 3mrad (2mrad Gaussian equivalent) at a spot size of 1x1cm². The integrated intensity over the full wavelength range amounts to 2.4x10⁸ n/cm² for each single pulse of the ESS. For the integrated intensity per second this value has to be multiplied by the repetition rate of the ESS (14Hz) leading to 3.4x10⁹ n/cm²/s (see Fig. 10). The horizontal divergence profile is depicted in the inset of Fig. 10 showing a smooth distribution and demonstrating that the setup accepts the full divergence of the beam through the collimation. The slight wiggles in the profile are due to the polygonal structure used for the simulation of the curved guide. They will disappear by the use of continuously curved sections at the real instrument. In the GISANS mode the vertical focusing is disabled for a perfect collimation based on a fixed collimation length of 4m. The resolution can be adapted to the needed values in the vertical and horizontal direction. Fig. 11 shows the resulting intensity and the vertical divergence distribution (inset) at the sample position. A total flux of 1.0x10⁸ n/cm²/s at 3mrad collimation (2mrad in Gaussian approximation) in both direction is available with a clean vertical divergence profile. The integrated intensity over the full wavelength band will amount to $1.0 \cdot x10^8 \text{ n/cm}^2/\text{s}.$

PNCMI 2014 IOP Publishing

Journal of Physics: Conference Series **711** (2016) 012009

doi:10.1088/1742-6596/711/1/012009



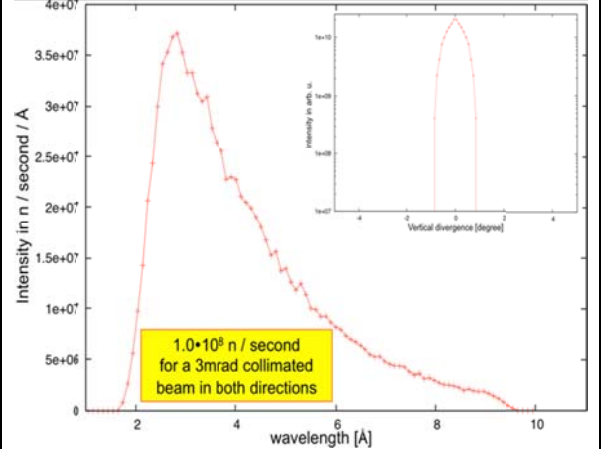


Fig. 10: Spectrum and divergence profile for the low resolution setup of the reflectometer in the lowest wavelength band from 2-10Å and a beam collimation of 3mrad (Boxcar)). The inset shows the horizontal divergence profile in front the collimation.

Fig. 11. Spectrum and divergence profile for GISANS setup in the low resolution setup of the reflectometer in the lowest wavelength band from 2-10Å and a beam collimation of 3mrad (Boxcar)). The inset shows the vertical divergence profile.

The suggested reflectometer will provide an extremely high flux, exceeding the flux which is currently achievable at the best reflectometers in the world. A 25 times gain is expected in comparison with D17 at the ILL [3]. The simulations above are supported by simple estimations: (i) the average flux at the ILL and ESS is about equal, the chopping of the beam will result in the losses of the useful neutron intensity because of the blocking of the neutron beam between the neutron pulses produced by the choppers; (ii) the opening time is defined by the ratio of the pulse width to their period that is approximately equal to 1/25; (iii) such pulse structure is naturally produced by the ESS, thus no losses related to the time structuring of the neutron beam will occur. Therefore, assuming that other beam parameters are similar, the expected gain is about 25.

4. Conclusions

The instrument concept presented above allows to design a very flexible vertical sample reflectometer for specular reflectivity and off-specular scattering as well GISANS investigations (in the pinhole geometry) at a modern long pulse source. An elliptically focusing neutron guide gives a gain of a factor 4 in intensity compared to a straight guide.

As the length of the instrument depends on the pulse structure of the source and the resolution of the instrument, VERITAS is designed for the ESS, delivering a maximum flux centered around 3Å with 10% wavelength resolution. It results in a stunning flux of 3.4×10^9 n/cm²/sec at the sample position for a 3mrad collimated beam (scattering plane) that is 25 times higher than one can achieve with an equivalent instrument at the ILL (e.g. D17). The wavelength resolution can be increased to e.g. 1%, 3% or 5% by using pulse-shaping choppers. Besides the reflectometry mode, VERITAS can be switched into the GISANS mode in seconds, preserving the gain of 25 over an equivalent instrument at the ILL. The huge neutron flux available at the sample position enables one to investigate systems where the sensitivity to a small amount of material or the resolution of small length scales around interfaces in thin film materials is required, something that is not feasible today.

The reflectometry mode as well as the GISANS mode can be further easily combined with a polarizer/analyzer system as well as with the kinetic mode of VERITAS. The need for the polarizer and analyzer system follow the increasing demand in the research field of magnetic nanoparticles (e.g.

Journal of Physics: Conference Series 711 (2016) 012009

doi:10.1088/1742-6596/711/1/012009

assembled in thin films), magnetism, ferroelectricity and superconductivity at interfaces or novel topologically protected magnetic states (e.g. skyrmions) besides many other topics. In addition the polarizer/analyzer system can be used to measure precisely the incoherent background of soft matter samples, increasing the dynamic range of reflectivity and GISANS studies in this science area.

The VERITAS concept at the ESS (or adapted to any other long pulse source with similar strength or even steady reactors like PIK at the PNPI, Russia) allows one to push the limits in thin film science in all directions, making a huge step forward in the instrumentation, particularly for exploiting the full potential of the new spallation sources supporting the users in performing cutting edge science.

Acknowledgements

The authors would like to acknowledge the fruitful discussions with F. Cousin (LLB), R. Cubitt (ILL), Th. Brückel (FZJ), M. Lösche (CMU), F. Henrich (CMU) and Th. Gutberlet (HZB). We also would like to thank S. Manoshin (JINR, Dubna) for the support with VITESS and D.M. Rodriguez (ESS) for the initial VITESS simulations.

References

- [1] http://eval.esss.lu.se/DocDB/0002/000274/015/TDR online ver all.pdf
- [2] Th Krist, C Pappas, A Teichert, C Fehr, D Clemens, E Steichele and F Mezei, Journal of Physics: ConferenceSeries 251 (2010) 012081
- [3] R. Cubitt, G. Fragneto, Appl. Phys. A 74 [Suppl.], S329–S331 (2002)





Available online at www.sciencedirect.com

ScienceDirect

Physics Procedia

Physics Procedia 59 (2014) 71 - 77

GAMMA-2 Scientific Workshop on the Emission of Prompt Gamma Ray in Fission and Related Topics

Applicability of the $Ge(n,\gamma)$ reaction for estimating thermal neutron flux

J. Nikolov^{a,*},Ž. Medić^a, N. Jovančević^{a,b}, J. Hansman^a, N. Todorović^a, M. Krmar^a

^aUniversity Novi Sad, Physics Department, Faculty of Sciences,Trg Dositeja Obradovica 4, 21000 Novi Sad, Serbia ^bEuropean Commission, Joint Research Centre, Institute for Reference Materials and Measurements, Retieseweg 111, 2440 Geel, Belgium

Abstract

A simple experimental setup was used to measure gamma lines appearing in spectra after interactions of neutrons with Ge in the active volume of a high-purity germanium detector placed in a low-background shield. As source of neutrons a 252 Cf spontaneous fission source and different thicknesses of PVC plates were used to slow down neutrons. A cadmium envelope was placed over the detector dipstick to identify the effect from slow and fast neutrons. Intensities of several characteristic γ -lines were measured, including intensity of the 139.9 keV γ -line from the reaction 74 Ge(n, γ) 75m Ge, usually used for estimation of thermal neutron flux. Obtained results signify that only a part of the detected 139.9 keV γ -rays originate from thermal neutron capture. Some preliminary results indicate that in our detection setup thermal neutron capture contributes with 30% to 50% to the total intensity of the 139.9 keV γ -line, depending on the thickness of the PVC plates.

© 2014 The Authors. Published by Elsevier B.V. This is an open access article under the CC BY-NC-ND license (http://creativecommons.org/licenses/by-nc-nd/3.0/).

Selection and peer-review under responsibility of Guest Editor: Mr. Stephan Oberstedt - stephan.oberstedt@ec.europa.eu

Keywords: thermal neutron flux monitor; neutron capture; ⁷⁴Ge;

^{*} Corresponding author. Tel.: +381-21-459-368; fax: +381-21-459-367. E-mail address: jovana.nikolov@df.uns.ac.rs.

1. Introduction

Reduction of gamma-background has been always a crucial matter of concern in all low-background measurements using gamma spectroscopy. Sometimes the only practical method for improving detection limits of rare processes is reducing the number of background events. Neutrons are an unavoidable source of background events, even in well-shielded detectors. Detailed understanding of the various aspects of neutron production and interactions with detection systems is one of the most important requirements of contemporary low-background experiments.

In experiments, where a high-purity germanium (HPGe) detector is exposed to neutrons, five natural isotopes of germanium interact with it producing gamma radiation. The most probable interactions are inelastic scattering with fast neutrons and thermal neutron capture. When inelastic scattering and capture reactions take place in the active volume of an HPGe detector characteristic γ-lines arise in the spectrum. After inelastic scattering typical broad and asymmetric gamma peaks showing a high-energy tail appear; 596.4 keV $(^{74}\text{Ge}(n,n')^{74}\text{Ge})$ and 691.4 keV $(^{72}\text{Ge}(n,n')^{72}\text{Ge})$ are the most prominent ones. The most intensive γ -lines following neutron capture are at 139.9 keV (74 Ge(n, γ) 75m Ge) and 198.4 keV (70 Ge(n, γ) 71m Ge) having standard Gaussian shapes. Both types of γ-peaks can be used in order to characterize the neutron field, especially in low-background detection systems. A reduction of background events detected is sometimes the only method for improving detection limits in experiments following effects of rare decay processes (Heusser, 1994; Heusser, 1995; Guiseppe et al., 2009; Haines et al., 2011). Neutrons are an almost unavoidable source of nondesired background even in very sophisticated data acquisition systems used in gamma spectroscopy. There are several sources of neutrons: spontaneous fission of U or Th, (α,n) reactions (Feige et al., 1968), neutrons created through cosmic muon capture, muon-induced spallation reactions, photo-nuclear reactions etc. (Gaisser, 1990; Da Silva et al., 1995; Kudryavtsev et al., 2003; Croft et al., 2003). In order to improve the performance of low-background detection systems, the flux of neutrons and all effects associated with neutron interactions should be well known.

The intensity of the 139.9 keV γ-line was usually used for estimating the thermal neutron flux at the position of an HPGe-detector (Škoro et al., 1992; Niese 2008). There are several ways to classify neutrons according to their energy, from cold to relativistic. Theory says that neutrons in thermal equilibrium with the surroundings are thermal neutrons. Per definition the energy of thermal neutrons is 0.025 eV, and at 20°C the Maxwell distribution of thermal neutrons extends to about 0.2 eV. In practice, the simplest way to distinct neutrons in energy groups can be carried out by the use of a cadmium filter. Neutrons below cadmium cut-off (about 0.4 eV) are called slow neutrons. The cadmium isotope ¹¹³Cd can separate neutrons in two groups because the neutron capture cross section has a prominent peak at energies below 0.4 eV. However, for most other nuclides, including several natural germanium isotopes, the neutron capture cross section in in the eV-region is uniformly decreasing with increasing energy without steep changes as it is in the case of ¹¹³Cd. It means that some sharp changes in the neutron capture of ^{nat}Ge between thermal (slow) and other neutrons having higher energies (epithermal) cannot be expected. Final consequence is that the 139.9 keV radiation, usually used for estimating the thermal neutron flux, can be emitted after capture of thermal as well as epithermal neutrons.

This paper presents an attempt in estimating to what extent epithermal neutrons contribute to the total intensity of the 139.9 keV γ -line detected after the exposure of a HPGe detector to fission neutrons emitted by ²⁵²Cf following spontaneous fission.

2. Experimental setup

A simple experimental setup was designed for the measurements shown in Fig. 1. An n-type, coaxial closed end HPGe detector with horizontal dipstick and relative efficiency of 22.3 %, was used in the experiment. The detector is located in a 1 m³ wide iron chamber having 25 cm thick walls. The chamber was made of 20 tons of pre-World War II iron.

The HPGe detector was exposed to neutrons from the reaction 252 Cf(sf). A large Marinelli container (inner diameter 10.6 cm, outer diameter 16.0 cm, height 20.5 cm, top thickness 3.0 cm) made of 2 mm thick PVC was filled with melted paraffin and located (top down) below the HPGe crystal as shown in Fig. 1. The 252 Cf source was placed in the Marinelli container. The distance between the 252 Cf source and the detector was about 25 cm. The neutron source emitted 4.5×10^3 neutrons per second into 4π sr. When the measurements were carried out the 252 Cf source was very old and a 2 cm thick iron disc was placed on top to attenuate gamma radiation of accumulated fission products. At the open end of the Marinelli container, between 252 Cf source and HPGe crystal, PVC plates were laid down up to a maximal thickness of 9.3 cm. The purpose of PVC plates was to slow down neutrons arriving from the 252 Cf source to the detector. Six different thicknesses of PVC were chosen. For any thickness two spectra were recorded: one with the naked detector and one with the detector crystal canned in a 1 mm thick nat Cd tin. The Cd-cap prevented thermal neutrons to reach the active volume of the HPGe detector.

Characteristic measurement times for one spectra reached up to 160×10^3 s (two days), because the used 252 Cf source was weak at the time of measurements. The GENIE program package was used to calculate intensities of gamma lines appearing in measured spectra.

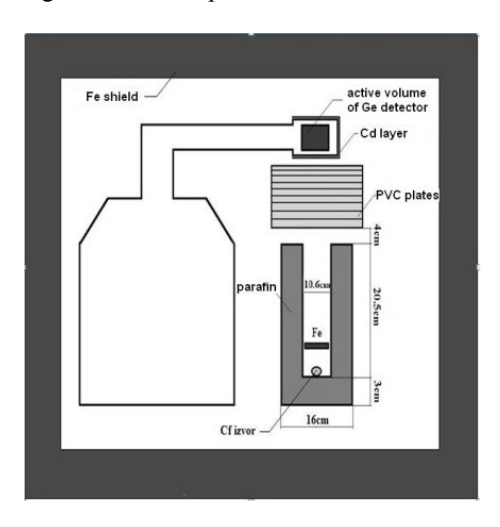


Fig. 1. Scheme of the experimental setup

3. Results and Discussion

A number of γ -lines were detected and identified in the collected spectra. Besides characteristic γ -radiation emitted after neutron capture or inelastic scattering on germanium nuclei, prominent gamma lines at 2223 keV ($^{1}\text{H}(n,\gamma)^{2}\text{H}$), 846.8 keV ($^{56}\text{Fe}(n,n^{2})^{56}\text{Fe}$), 517 keV ($^{35}\text{Cl}(n,\gamma)^{36}\text{Cl}$) appeared in all spectra. It is interesting to note that intensities of γ -lines originating from neutron capture in PVC showed an increasing trend with

increasing PVC thickness. In spectra measured with Cd-cap covering the detector, the 558.5 keV and 651.3 keV γ -lines following ¹¹³Cd(n,γ)¹¹⁴Cd reaction are found. The γ -line at 558.5 keV is even the most prominent.

The primary task of PVC plates inserted was to slow-down neutrons and to reduce their energy through elastic scattering. Figure 2 shows dependence of $691.3 \text{ keV} \gamma$ -peak on PVC thickness (black squares show measured intensity without Cd envelope and red circles are intensities of $691.3 \text{ keV} \gamma$ -peak measured with Cd cap). Fast neutrons non-elastically scattered at ⁷²Ge nuclei produce this line. It can be seen that the intensity of the asymmetric γ -line at $691.3 \text{ keV} \gamma$ measured with maximum thickness of PVC is about 2.5 times lower than without PVC. A similar trend is observed for the intensities of other asymmetric peaks originating from (n,n') reactions. It means that PVC reduced the number of fast neutrons able to excite germanium nuclei through inelastic scattering by about 2.5 times. Most probable mechanisms can be slowing-down of energetic neutrons and removal from the beam by off scattering. The intensity of (n,n') peaks shows that the Cd can has no significant influence on the general trend.

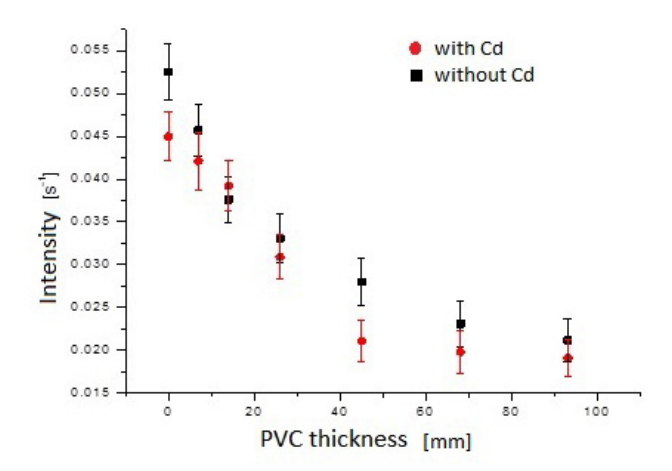


Fig. 2. Intensity of the 691.3 keV gamma peak as a function of the PVC thickness

A similar analysis was performed for the 558.5 keV and the 651.3 keV γ -lines from neutron capture in ¹¹³Cd. The obtained results are presented in Fig. 3.

Having in mind a large difference between the thermal neutron capture cross-section and the resonance integral for ¹¹³Cd (Gryntakis, Kim, 1974) it can be supposed that the 558.5 keV and 651.3 keV γ-lines are produced by thermal neutron capture mostly. From results presented in Fig. 3 it can be concluded that the intensities of of both γ-lines did not depend on PVC thickness at all. It means that the number of thermal neutrons at the detector (with Cd tin) was constant. The number of thermal neutrons is a result of some dynamic balance: thermal neutrons are produced by slowing-down and thermalizing in the PVC plates and other low Z materials, and at the same time, thermal neutrons were captured by all surrounding materials. Results presented in Fig. 3 show that adding PVC plates in our experimental setup can reduce the number of fast neutrons at the place of the detector by a factor 2.5. However, it leaves the number of thermal neutrons constant, i.e. the number of thermalized neutrons compensates the number of thermal neutrons captured.

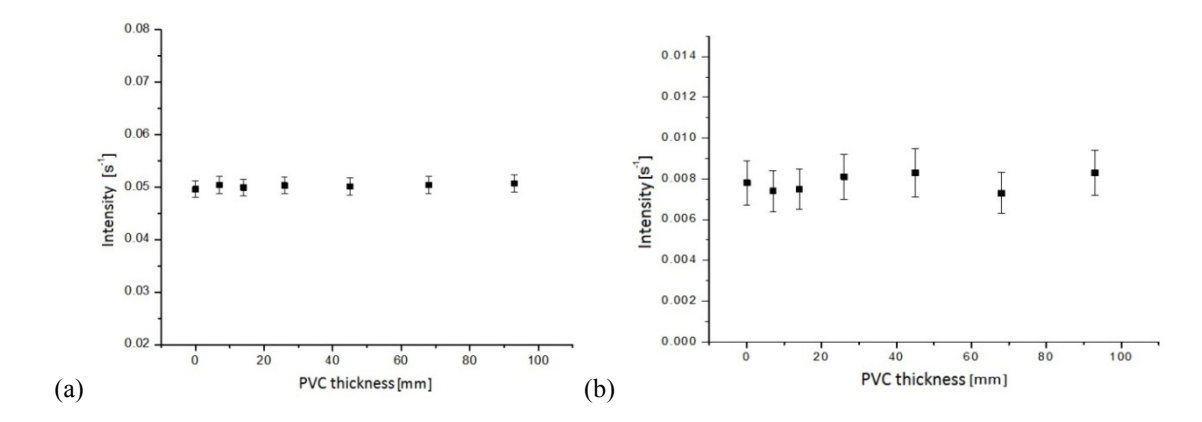


Fig. 3. Dependence of line (a) 558.5 keV and (b) 651.3 keV on PVC thickness

It should be interesting to analyze intensity of 139.9 keV γ -line in the light of the fact that the number of thermal neutrons at the detector is constant and not dependent on the thickness of the PVC layer. 139.9 keV photons are emitted after transition from the exited isomer state ($T_{1/2} = 47.7$ s) to the ground state of ⁷⁵Ge produced by neutron capture. Obtained values of 139.9 keV γ -intensities are shown in Fig. 4. Evidently, in both measurement geometries, with and without Cd shield, the intensity of the 139.9 keV line shows a mildly decreasing trend.

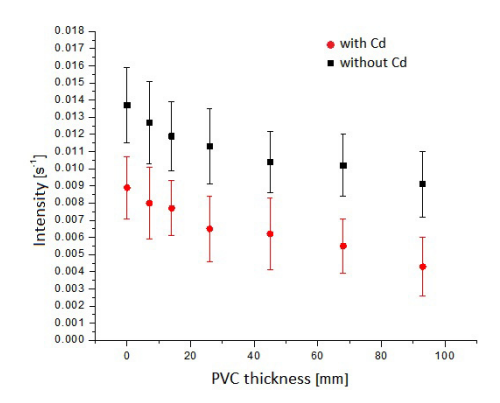


Fig. 4. Intensity of the 139.9 keV gamma line as a function of PVC thickness

In the simplified model where the Cd shield stops all thermal neutrons, the 139.9 keV γ -line measured with Cd cap was supposed to originate from capture of fast neutrons by ⁷⁴Ge. In spectra recorded without Cd cap, capture of both slow and fast neutrons produce the 139.9 keV radiation. Contribution of thermal neutron capture to the total intensity of the 139.9 keV gamma line, for some chosen thickness of the PVC, can be obtained by simple subtraction of the measured 139.9 keV γ -yield measured with Cd cap from that measured without Cd envelope. The result of this subtraction is shown at Fig. 5.

It can be seen that part of the intensity of the 139.9 keV γ-line originating from capture of thermal neutrons is not dependent on the thickness of the PVC layer. It is in very good agreement with results presented in Fig.

3. If thermal neutron flux at the detector is not dependent on plastic thickness, as it illustrates the γ -lines of 114 Cd, it can be expected that the contribution of thermal neutron capture to total intensity of the 139.9 keV γ -line should be constant (cf. Fig. 5).

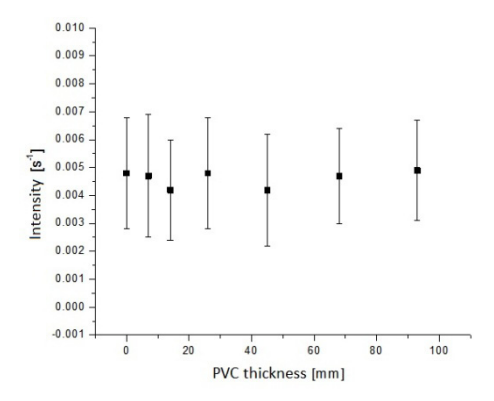


Fig. 5. Calculated intensity of the 139.9 keV gamma line originating from capture of thermal neutrons only as a function of PVC thickness.

Data presented in Fig. 5 shows the count rate into the 139.9 keV γ -line from thermal neutron capture on ⁷⁴Ge to be about 0.005 s⁻¹. In the measurement without PVC plates the total intensity into that γ -line measured without Cd envelope is about 0.015 s⁻¹. We conclude that thermal neutron capture contributes to about 30% to the total intensity of the 139.9 keV γ -line. However, additional plastic plates reduced number of fast neutrons (cf. Fig. 2). In the case of maximum thickness of the PVC layer the contribution of thermal neutrons to the total intensity at E₁ = 139.9 keV is about 50%.

4. Conclusion

We measured γ -lines appearing in spectra after interactions of neutrons with germanium and other materials surrounding the HPGe detector. Source of neutrons was 252 Cf(sf), and PVC plates were used to slow-down neutrons before interacting with the detector. Intensities of γ -lines appearing in spectra after inelastic scattering of fast neutrons on natural isotopes of germanium showed that in this simple setup the number of fast neutrons can be reduced more than 2.5 times. A Cd cap placed over the detector was used to eliminate thermal neutrons before reaching the active volume of the HPGe detector. By standard technique used in neutron activation analysis, where detectors are exposed to neutrons with and without Cd envelope, influence of fast neutrons is subtracted and contribution of slow neutrons on the total intensity of 139.9 keV γ -line was estimated. In the case when fission neutrons from 252 Cf reach detector without slowing-down in PVC plates, slow neutrons contribute to just about 30 % to the intensity of the 139.9 keV γ -line. For a maximal thickness of the PVC used in this experiment (9.3 cm) thermal neutrons contribute to about 50% to the total intensity of the 139.9 keV γ -line.

Acknowledgements

The authors acknowledge the financial support of Ministry of Education, Science and Technological Development of Serbia, within projects No. 43007 and No. 171002.

References

Croft, S., Bourva, L.C.A., Nucl. Instr. and Meth. A505 (2003) 536.

Da Silva, A. et al., Nucl. Instr. and Meth. A354 (1995) 553.

Feige, Y., Oltman, B. G., Kastner, J., J. Geophys. Res. 73 (1968) 3135, doi:10.1029/JB073i010p03135.

Geiser T., Cosmic Rays and Particle Physics, Cambridge Univ. Press, Cambridge (1990).

Gryntakis, E.M. and Kim, J.I., Journal of Inorganic Chemistry 36 (1974) 1447-1452.

Guiseppe, V. E. et al., Phys. Rev. C, 79(5) 054604 (2009).

Haines, D.K. et al., Nucl. Instr. and Meth. A 652 (2011) 326.

Heusser, G., Background in ionizing radiation detection, In: Garcia-Leon, M., Garcia-Tenorio, R. (Eds.), Low-Level Measurements of Radioactivity in the Environment, Word Scientific, Sigapore (1994) 69.

Heusser, G., Ann. Rev. Nucl. Part. Sci. 45 (1995) 543.

Kudryaytsev, V.A., Spooner, N.J.C., McMillan, J.E., Nucl. Instr. and Meth. A 505 (2003) 688.

Niese, S., Analysis of Environmental Radioactivity, Elsevier (2008) 209.

Škoro, G.P. et al., Nucl. Instr. and Meth. A316 (1992) 333.